Vol. 25 No. 3
September 2022

ISSN: 1301-9724
e-ISSN: 2146-1511
https://dergipark.org.tr/tr/pub/ijot

International Journal of Thermodynamics

Abstracting and Indexing:

Chemical Abstracts Services, Copernicus, DOAJ, EBSCO, Emerging Sources Citation Index, Engineering Index, Google Scholar, Scopus, and ULAKBIM

International Centre for Applied Thermodynamics

International Journal of Thermodynamics

https://dergipark.org.tr/tr/pub/ijot

Editor-in-Chief

Associate Editor-in-Chief

Associate Editor

Editorial Board

International Journal of Thermodynamics

https://dergipark.org.tr/tr/pub/ijot

Journal Contacts

Editor-in-Chief

Prof. Dr. Lütfullah Kuddusi
ISTANBUL TECHNICAL UNIVERSITY
kuddusi@itu.edu.tr
+902122931300/2452
Department of Mechanical Engineering
Istanbul Technical University
Gumussuyu, 34437 Istanbul Turkey

Volume: 25

Issue: 3

Web: https://dergipark.org.tr/tr/pub/ijot

International Journal of Thermodynamics (IJoT)

ISSN:1301-9724 / e-ISSN:2146-1511

International Journal of Thermodynamics

https://dergipark.org.tr/tr/pub/ijot

ISSN 1301-9724 / e-ISSN 2146-1511

Volume: 25 / No: 3 - September / 2022

CONTENTS

International Journal of Thermodynamics (IJoT)
ISSN 1301-9724 / e-ISSN 2146-1511
https://dergipark.org.tr/en/pub/ijot

Vol. 25 (No. 3), pp. 001-010, 2022
doi: 10.5541/ijot.1017174

Static Dielectric Constants, Densities, Refractive Indices and Related Properties of Binary Mixtures at Various Temperatures Under Atmospheric Pressure

Navarkhele A.V[2], Navarkhele V.V.*[1]

[1]Department of Physics, Dr. Babasaheb Ambedkar Marathwada University, Aurangabad - 431 004, India
[2]Chanabasweshwar College of Pharmacy Latur
Email: [1]vvn_bamu@yahoo.co.in

Received 1 November 2021, Revised 8 February 2022, Accepted 4 April 2022

Abstract

Experimental dielectric constants at (293.15, 298.15, 303.15) K, densities and refractive indices at 293.15 K are reported for water- ethanol and water- n-butanol binary mixture systems over the entire volume fraction range and atmospheric pressure. From the experimental dielectric data, the excess dielectric constant, effective Kirkwood correlation factor, Bruggeman factor and from density and refractive index data various parameters and their excess properties like excess density, excess refractive index, excess molar polarization, and excess molar volume were estimated and reported in the study. The static dielectric constant of the studied binary mixtures decreases with increase in temperature and volume fraction of the solutes. The density values are decreasing and refractive indices are increasing with increasing volume fraction of ethanol and n-butanol in water. Excess molar volumes values of ethanol and n-butanol are negative over the entire volume fraction range shows the presence of intermolecular interaction and hydrogen bonding in both the binary mixtures.

***Keywords**: Static dielectric constant; density; refractive index; excess properties; polar binary mixtures.*

1. Introduction

The dielectric constant of the material is a measure of solvent's efficiency for separating the electrolytes into the ions; this physical property is influenced by interatomic and intermolecular attractions. Solvents with high dielectric constants encourage complete dissociation of the electrolytes whereas in solvents of low dielectric constant considerable ion pairing occur [1]. The variation in this physical property with composition, frequency and temperature gives important data about intermolecular interactions, hydrogen bonding and the molecular structure. There are a wide range of possible interactions between the components of a mixture, such as hydrogen bonding, molecular associations, charge transfer, dipole-dipole and dipole induced dipole interactions [2].

Ethanol is an alcohol produced from grains and agricultural products. It is a clear, colorless alcohol made from a variety of biomass materials. Ethanol is also called as ethyl alcohol, grain alcohol which dissolves in water and organic compounds readily. It is an important solvent and extractant that is widely used in the production of beverages. It is also an ingredient in number of beauty and personal care products. It has excellent solubility to many organic compounds. The solute n- butanol is also known as 1- butanol or butyl alcohol produced by fermentation of sugars derived from corn or petrochemical process. It is also used in a number of beverages, food and in an artificial food flavoring. It is also used in plastic, polymers, lubricants, synthetic rubber and brake fluids. The knowledge of the thermophysical properties of these liquids and their corresponding liquid mixtures has been employed in different fields including pharmaceutical and analytical sciences and they affect many pharmaceutical processes like design, synthesis, extraction, purification, absorption and distribution in body fluids [3]. However, reports are available about the thermophysical properties of ethanol and n-butanol with other compounds. Dielectric constants of water, methanol, ethanol, butanol and acetone: measurement and computational study was reported using low pass filter by M. Mohsen- Nia et al [4]. Excess properties of alcohol - water systems at 298.15 K were also reported by Hülya Yilmaz [5]. Dielectric and acoustic properties of binary liquid mixtures of cyclohexane with n-butanol at 308 K temperature were reported by Maharolkar et al [6].

Here we present the static dielectric constants ($\in_s$) of the binary mixtures of water - ethanol and water - n-butanol at 293.15, 298.15 & 303.15 K temperatures and densities (ρ), refractive indices (n) at 293.15 K temperature over the entire volume fraction range. The related properties like excess dielectric constant (ε^E), effective Kirkwood correlation factor (g^{eff}), Bruggeman factor (f_B) , atomic polarization, electronic polarization, permittivity at higher frequency, molar volume, molar refraction, polarizability, solvated radii, molar polarization, deviation in molar refractivity, and the excess properties like excess density (d^E), excess refractive index (n^E), molar polarization $(P_m)^E$, excess molar volume (V^E), were estimated from the experimental data using appropriate equations to confirm molecular interactions, hydrogen bonding between the components of the mixtures.

---

*Corresponding Author

2. Materials and Methods

2.1 Chemicals and Sample Preparations

The chemicals used in the present investigation are of spectroscopic grade with 99.9% purity and were used without further purification. The solutions were prepared by mixing ethanol with water and n-butanol with water at eleven different stages of a mixture of water plus ethanol and water plus n-butanol as 0 to 100% in steps of 10%. All mixtures were prepared just before the measurement.

2.2 Measurement of Dielectric Constant

The static dielectric constants of the binary mixtures were measured using a wet sensor make by Delta-T Devices Ltd. UK, which is based on the principle of frequency domain reflectometry technique. The measurements were recorded with a calibrated meter which is connected to the wet sensor. Measurement of each sample was repeated at least five times and the average value of that reading was taken as a dielectric constant of that mixture. The details of the apparatus have been described in our earlier paper [7]. The uncertainty in measurement of the dielectric constant is ± 3%. The temperature controller arrangement with water bath has been used to sustain the constant temperature within the correctness limit of ± 1 °C. The sample cell used in the measurement system was surrounded by a heat protecting container through which the water of stable temperature was circulated using a temperature controller system**.**

2.2.1 Study of Excess Permittivity (ε^E)

Excess dielectric constant- permittivity provides qualitative information about the formation of new structure in the binary mixtures and that may be obtained from the excess properties of the mixtures [8]. Excess dielectric constant is estimated by the equation:

$$\varepsilon^{\mathrm{E}} = \left(\varepsilon_{\mathrm{O}}\right)_m - \left[\varepsilon_{\mathrm{A}} \cdot \Phi_{\mathrm{A}} + \varepsilon_{\mathrm{B}} . \Phi_{\mathrm{B}}\right] \tag{1}$$

In above equation Φ is the volume fraction and suffix m, A, B represents a mixture, liquid A (water) and liquids B (ethanol) first system and A (water) and liquids B (n-butanol) second system respectively. Excess permittivity provides qualitative information about the formation of new structure in the mixtures as follows:

i) $\boldsymbol{\varepsilon}^{\mathbf{E}} = 0$: indicates that solution A and B do not interact or it is pure liquid.

ii) $\boldsymbol{\varepsilon}^{\mathbf{E}} < 0$: indicates that solution A and B interact is in such a way that the effective dipole moment gets reduced.

iii) $\boldsymbol{\varepsilon}^{\mathbf{E}} > 0$: indicates that solution A and B interact in such a way that the effective dipole moment increases.

2.2.2 Study of Kirkwood Correlation Factor

The Kirkwood correlation factor (g) provides information about the orientation of the electric dipoles in polar liquids [9]. The modified form of Kirkwood correlation factor that is, effective Kirkwood correlation factor (g^{eff}) given by [10, 11] was estimated by the equation:

$$\frac{4\pi N}{9kT}\left(\frac{\mu^2{}_M \rho_M}{M_M} X_M + \frac{\mu^2{}_F \rho_F}{M_F} X_F\right) g^{eff} = \frac{\left(\varepsilon_{0m} - \varepsilon_{\infty m}\right)\left(2\varepsilon_{0m} + \varepsilon_{\infty m}\right)}{[\varepsilon_{0m}\left(\varepsilon_{\infty m} + 2\right)^2]} \tag{2}$$

Where "g^{eff}" is the Kirkwood correlation factor for the binary mixtures.

2.2.3 Study of Bruggeman Factor

Molecular interactions in polar binary mixtures can be confirmed from the Bruggeman mixture formula. The static dielectric constant (ε_{sm}) of two binary mixtures is related to this formula with the volume fraction of solute (ε_{sB}) that proves the interaction between the solute (ε_{sB}) and solvent (ε_{sA}) of the mixtures by the equation [12]:

$$f_{BM=}\left[\frac{\varepsilon_{sm} - \varepsilon_{sB}}{\varepsilon_{sA} - \varepsilon_{sB}}\right]\left[\frac{\varepsilon_{sA}}{\varepsilon_{sm}}\right]^{\frac{1}{3}} = 1 - V, \tag{3}$$

In the above equation (V) is the volume fraction. According to this equation a linear relationship is expected in Bruggeman factor **(**f_{BM}) and (V), and deviation from this linear relation indicates presence of molecular interaction and hydrogen bonding in the mixtures. When both solute and solvent are polar liquids, the Bruggeman equation has to be modified as:

$$f_{BM} = 1 - [a - (a - 1)V\,]\,V, \tag{4}$$

In the above equation (a) is the interaction factor.

2.3 Measurement Refractive index

The refractive indices values of the studied binary mixtures were measured using digital pocket refractometer PAL- RI, make by Atago-Japan. The apparatus measures the refractive index in the range of 1.3306 to 1.5284**.** The uncertainty in the measurement of refractive indices given by the manufacturer is of ± 0.0003.

2.4 Measurements of Density

The densities of the binary mixtures were measured using an Anton Paar oscillation U-tube densitometer (model DMA- 35, Austria), calibrated with double-distilled water and air. The densities of pure liquids and their mixtures were carried at a single temperature, since there is no facility of temperature variation for the said model. The density values have a standard uncertainty given by the manufacturer is of $\pm 10^{-3}$ g·cm^{-3}.

2.5 Molar Refraction, Atomic Polarization, Permittivity at Higher Frequency, Polarizabilty, Solvated Radii, Molecular Polarization and Deviation in Molar Refraction

From experimental densities (d) and refractive indices (n) of pure substances and mixtures, the molar refraction (R) is calculated from the equation [13, 14]:

$$\boldsymbol{R} = \left(\frac{\mathbf{n}^2 - 1}{\mathbf{n}^2 + 2}\right)\mathbf{V} = \mathbf{P_A} + \mathbf{P_E} = \mathbf{P_T} = \mathbf{P_D} \tag{5}$$

Where "n" is the refractive index of the liquid and V = (M/d) is molecular volume, in this 'M' and 'd' is the molecular weight and the density of the pure liquids respectively. The right hand side of equation (5) is equal to the summation of both atomic polarization (P_A) and electronic polarization (E_P) and that is equal to the distortion polarization (P_D).

The atomic polarization (P_A) was calculated from the refractive indices (n) of pure substances and mixtures by the equation [15]:

$$\mathrm{P_A} = 1.05\ \mathrm{n}^2 \tag{6}$$

The permittivity at higher frequency (ε_∞) is the square of the refractive index and it was calculated by the equation:

$$\varepsilon_\infty = \mathrm{n}^2 \tag{7}$$

Where (n) is the refractive index of the binary mixture.

The molecular dipole polarizability (α) was calculated from the experimental densities and refractive indices of pure substances and mixtures using Lorentz- Lorentz formula [16]:

$$\left(\frac{\mathrm{n}^2-1}{\mathrm{n}^2+2}\right) = \left(\frac{4}{3}\right)\Pi \mathrm{n}'\alpha \tag{8}$$

Where $n' = \frac{N}{V}$, N is Avogadro's number, and V is molar volume, (n) is the refractive index of the binary mixture.

Considering spherical form of the solvated molecules, the solvated radii of the pure solvents and binary mixtures were calculated using the equation [17]:

$$\mathrm{V} = \left(\frac{4}{3}\right)\Pi \mathrm{r}^3 \tag{9}$$

From experimental dielectric constants and densities of pure substances and mixtures the molecular polarization (Pm) was estimated using the equation [18]:

$$\mathrm{P_m} = \mathrm{V}\left(\frac{\varepsilon-1}{\varepsilon+2}\right) \tag{10}$$

Where (ε) and (V) is the static dielectric constant and molecular volume of the binary mixtures.

From the experimental density and refractive index data, the deviation in molar refraction was calculated using the well-known equation [19]:

$$\Delta_\mathrm{R} = \mathrm{R_m} - \textstyle\sum_\mathrm{i} \emptyset_\mathrm{i}\mathrm{R_i} \qquad \text{where i= 1, 2,} \tag{11}$$

In the above equation (R_m) is the molar refractivity of the mixtures (φi) and (Ri) are volume fraction and molar refractivity of pure liquids 1 and 2 respectively.

2.6 Excess Parameters (Excess Density (d^E), Excess Refractive Index (n^E), Excess Molar Polarization $(P_m)^E$ and Excess Molar Volume $(V)^E$)

The excess density (d^E) was measured from the experimental density data (d), and it was calculated using the equation:

$$\mathrm{d^E} = \mathrm{d_{mix}} - (\Phi_1 \mathrm{d}_1 - \Phi_2 \mathrm{d}_2) \tag{12}$$

Where d_{mix} are the values of densities of mixtures, Φ_1, Φ_2 d_1, d_2 are the volume fractions and densities of the first and second liquids respectively.

The excess refractive index (n^E) was estimated from the experimental refractive index (n) using the equation:

$$\mathrm{n^E} = \mathrm{n_{mix}} - (\Phi_1 \mathrm{n}_1 - \Phi_2 \mathrm{n}_2) \tag{13}$$

Where n_{mix} are the values of refractive indices of the mixtures and Φ_1, Φ_2, n_1 , n_2 are the volume fractions and refractive indices of the first and second liquids respectively.

The excess molar polarization $(P_m)^E$ of the binary mixtures was determined by the equation:

$$(P_m)^\mathrm{E} = (P)_m - \left[(P_m)_A \cdot \Phi_\mathrm{A} + (P_m)_B . \Phi_\mathrm{B}\right] \tag{14}$$

Where (P_m) is the polarization of the mixtures, $(P_m)_A$, $(P_m)_B$, the molar polarization and $\mathbf{\Phi_A}$, $\mathbf{\Phi_B}$ the volume fraction of liquid A and B respectively.

From the experimental density data of the binary mixtures, the excess molar volume $(V)^E$ was estimated by using the equation [20]:

$$\mathrm{V^E} = \mathrm{V} - \textstyle\sum_{\mathrm{i}=1}^{\mathrm{n}} \Phi_\mathrm{i}\, \mathrm{V_i} \qquad \text{Where i} = 1, 2 \text{ ----} \tag{15}$$

Where V is the molar volume of the mixtures, Φ_i represents volume fraction and V_i is the molar volume of the components 1 and 2 respectively.

3. Results and Discussion

3.1 Static Dielectric Constant

The experimental values of the static dielectric constant of the binary mixtures of water - ethanol and water - butanol are given in Table 1 and graphically illustrated in Figure 1 and 2 respectively. The dielectric constants of the binary mixtures decrease with an increase in temperature (the decrease in dielectric constant with increase in temperature is around 0.20 to 0.55 per degree Celsius for ethanol and 0.15 to 0.40 per degree Celsius for n- butanol respectively) and volume fraction (the decrease in dielectric constant with an increase in volume fraction is around 0.30 to 0.60 for 1 % volume fraction of ethanol and 0.50 to 0.65 for 1 % volume fraction of n- butanol respectively) of ethanol and n-butanol in water for the studied temperatures. The decrease in dielectric constant with an increase in temperature may be due to rapid fall in orientation polarization, because the increased thermal motion reduces the alignment of the permanent dipoles [21]. The decrease in dielectric constant with an increase in volume fraction may be due to increase in size and shape of the complex molecules after hydrogen bonding interaction. This could be attributed to the decrease in the number of dipoles in the complex**,** which may lead to decrease in the volume of the rotating molecules [22, 23].

From Figure 1 and 2 it is also observed that, variation in dielectric constants is non- linear with increasing concentration of ethanol and butanol in water. In mixtures of polar liquid, if molecules are interacting a non-linear variation in dielectric constant with concentration was observed, and the same is confirmed from Figure 1 and 2. The variation in R- square values of dielectric constant of the studied binary mixtures of water - ethanol and water - butanol at different temperatures is graphically illustrated in Figure 3 and 4 respectively**.** From Figures, it is observed that there is non-linear variation in dielectric constants with concentration. This proves that the intermolecular association is taking place in the studied polar binary systems. Similar results have been reported by Lone et al for methanol – ethanol binary mixtures using TDR method, in that study they have claimed such type of non linear variation in dielectric constant [24]. Similar results were reported by Navarkhele et al on the binary mixture study of formamide with butylene glycol using high frequency TDR technique, in that study the authors have reported the non-linear variation in the binary mixtures with concentration [25].

Table 1 *Variation in experimental values of static dielectric constants of water - ethanol and water – n-butanol binary mixture systems at different temperatures.*

Ethanol Volume (%)	Static dielectric constant T=293.15K	Static dielectric constant T=298.15K	Static dielectric constant T=303.15K
00	81.46	79.72	77.81
10	78.21	75.36	73.41
20	72.42	70.05	67.81
30	66.05	64.34	62.17
40	60.92	59.01	56.54
50	54.89	52.26	50.43
60	48.04	46.92	45.14
70	42.77	41.38	39.88
80	37.68	36.12	34.54
90	32.51	30.76	29.24
100	27.16	25.80	23.95
n-butanol volume (%)			
00	81.46	79.72	77.81
10	75.26	73.36	71.14
20	69.02	67.05	65.04
30	62.41	60.74	58.59
40	56.08	54.14	52.10
50	49.55	47.65	46.00
60	43.10	41.52	40.21
70	37.10	35.75	34.65
80	31.45	30.45	29.16
90	26.11	25.21	23.65
100	20.52	19.68	17.94

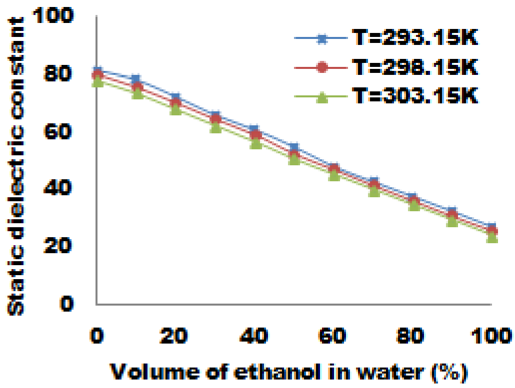

Figure 1*. Variation in static dielectric constant of the binary mixture of water - ethanol at different temperatures.*

The experimental density data of water - ethanol and water- butanol binary mixtures at 293.15 K temperature is given in Table 2. The density of the binary mixtures decreases with an increase in volume fraction of ethanol and n-butanol in water. This may be due to the addition of the concentration of ethanol and n-butanol in water, that may weaken the intermolecular bonds and may results in new bonds between similar and dissimilar molecules, that may increase the volume of the mixture consequently density is reduced. Similar results have been recorded by Nasim et al for the binary mixtures of poly(ethylene glycol) 300 + 1,2-ethanediol, 1, 2-propanediol, 1,3- propanediol, 1,3-butanediol, or 1,4-butanediol [26]

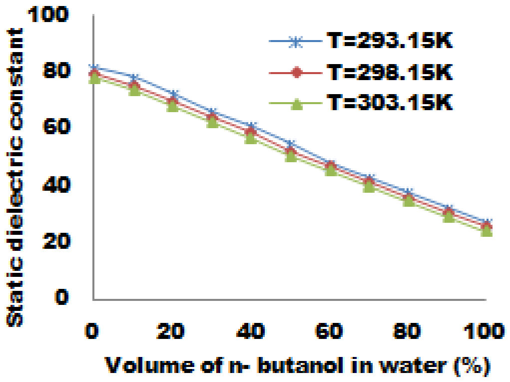

Figure 2*. Variation in static dielectric constant of the binary mixture of water - n-butanol at different temperatures.*

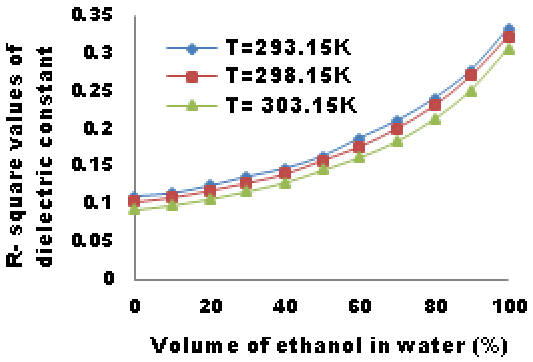

Figure 3 *Variation in R- square values of dielectric constants of the binary mixture of water - ethanol at different temperatures.*

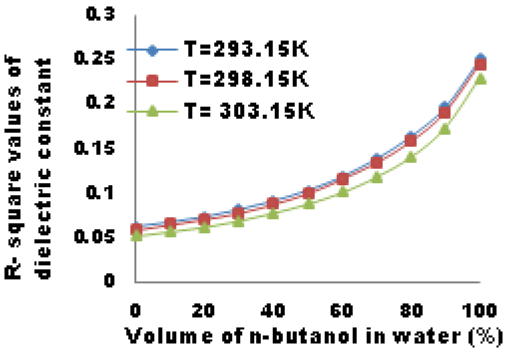

Figure 4 *Variation in R- square values of dielectric constants of the binary mixture of water - n-butanol at different temperatures.*

From density data, it is also seen that, there is nonlinear improvement in the density data of the binary mixtures; this is because of the increment of mass fraction of ethanol and n-butanol. It is observed that by adding hydroxyl groups to water over the entire volume fraction range, the density of the binary mixture is reduced Similar results have been observed by Nasim et al for the binary mixtures of poly(ethylene glycol) 300 + 1,2-ethanediol, 1, 2-propanediol, 1,3- propanediol, 1,3-butanediol, or 1,4-butanediol [26].

The refractive index gives valuable information regarding molecular rearrangement on mixing. The refractive indices values of the binary mixtures of water - ethanol and water - butanol are given in Table 2. From the experimental data, it is observed that the refractive indices of both the binary mixture increases with an increasing volume fraction of ethanol and butanol in water. This may be due to decrease in density and number of dipoles per unit volume in the binary mixtures.

Table 2 *Variation in experimental values of densities and refractive indices of water- ethanol and water – n-butanol binary mixture systems at 293.15 K temperature.*

Ethanol Volume (%)	Density T=293.15K	Refractive index T=293.15K
00	0.9981	1.3338
10	0.9766	1.3363
20	0.9555	1.3392
30	0.9341	1.3418
40	0.9129	1.3445
50	0.8918	1.3474
60	0.8657	1.3500
70	0.8494	1.3527
80	0.8281	1.3556
90	0.8070	1.3582
100	0.7862	1.3612
n-butanol Volume (%)		
00	0.9981	1.3338
10	0.9782	1.3383
20	0.9590	1.3449
30	0.9400	1.3515
40	0.9211	1.3581
50	0.9021	1.3647
60	0.8831	1.3713
70	0.8640	1.3779
80	0.8450	1.3844
90	0.8261	1.3910
100	0.8071	1.3980

3.2 Excess Dielectric Constant (ε^E)

Excess dielectric constant of both the binary mixtures was calculated using equation (1) and it is tabulated in Table 3. The excess dielectric constant of water-ethanol binary mixtures is positive in water rich region that is 0 to 50% volume fraction of ethanol and negative in ethanol rich region that is 60 to 100% volume fraction of ethanol for the studied temperatures. The positive trend of (ε^E) indicates that, in the mixtures the solutions interacts in such a way that the effective dipole moment increases. The positive values of excess dielectric constant suggest that the effective number of dipoles in the mixture is greater than the corresponding average number in pure liquids; this may be due to the formation of new structure leading to a higher macroscopic permittivity. Similar results have been reported by Navarkhele et al in dielectric relaxation study of formamide-propylene glycol using time domain reflectometry, in the study the authors have reported that, the values of (ε^E) are negative up to 55% of mole fraction of PLG and positive for the rest of the mole fraction of PLG in the liquid mixtures [27].

Table 3 *Variation in estimated values of excess dielectric constants of water- ethanol and water – n-butanol binary mixture systems at different temperatures.*

Ethanol Volume (%)	Excess dielectric constant T=293.15K	Excess dielectric constant T=298.15K	Excess dielectric constant T=303.15K
00	0.00	0.00	0.00
10	2.18	1.02	0.98
20	1.82	1.11	0.72
30	0.88	0.79	0.51
40	1.88	0.85	0.27
50	0.58	-0.50	-0.45
60	-0.84	-0.44	-0.35
70	-0.68	-0.59	-0.22
80	-0.34	-0.46	-0.18
90	-0.08	-0.43	-0.09
100	0.00	0.00	0.00
n-butanol Volume (%)			
00	0.00	0.00	0.00
10	-0.10	-0.35	-0.68
20	-0.25	-0.66	-0.79
30	-0.76	-0.96	-1.25
40	-1.00	-1.56	-1.76
50	-1.44	-2.05	-1.87
60	-1.79	-2.17	-1.67
70	-1.70	-1.94	-1.25
80	-1.25	-1.23	-0.75
90	-0.50	-0.47	-0.27
100	0.00	0.00	0.00

Negative values of excess dielectric constant of water - ethanol and water with n-butanol binary mixtures show that, in the mixture the solutions interacts in such a way that the effective dipole moment decreases. Negative trend of (ε^E) indicates that the effective number of dipoles in the mixture might be smaller than the corresponding average number in the pure liquids that indicates the formation of new structure leading to a lower macroscopic permittivity. Similar results have been reported in the study of p-fluorophenylacetonitrile–methanol binary mixtures using time-domain reflectometry technique by Hosamani et al, in that study the authors are reported that when the values of (ε^E>1) the excess permittivity is positive, and (ε^E < 1) the excess permittivity is negative [28].

3.3 Kirkwood Correlation Factor

The estimated effective Kirkwood correlation factor values of water- ethanol and water-butanol binary mixtures were estimated using equation (2) and tabulated in Table 4 and graphically illustrated in Figure 5 and 6 respectively. From Figures 5 and 6 it is also observed that, there is small bump in (g^{eff}) values at 40% volume fraction of ethanol and n- butanol in water, that may be an experimental error. From Figure 5 and 6 it is also observed that the effective

Kirkwood correlation factor values of both the binary mixtures are greater than 1 ($g^{eff} > 1$) over the entire volume fraction range. This indicates that in the mixtures the dipole pairs have been formed and their orientation is parallel over the entire volume fraction range of the binary mixtures for the studied temperatures. In the study of p-fluorophenylacetonitrile–methanol binary mixtures using time-domain reflectometry technique by Hosamani et al reported that when the values of $g^{eff} > 1$, the dipoles are formed and their orientation is parallel and when $g^{eff} < 1$, their orientation is antiparallel [28].

Table 4 *Variation in estimated values of effective Kirkwood correlation factor of water- ethanol and water – n-butanol binary mixture systems at different temperature.*

Ethanol Volume (%)	Kirkwood correlation factor T=293.15 K	Kirkwood correlation factor T=298.15 K	Kirkwood correlation factor T=303.15 K
00	5.00	4.95	4.91
10	5.13	5.02	4.97
20	5.12	5.04	4.95
30	5.07	5.02	4.93
40	5.11	5.03	4.90
50	5.08	4.91	4.81
60	4.95	4.91	4.80
70	4.98	4.89	4.78
80	5.03	4.90	4.75
90	5.10	4.89	4.71
100	5.16	4.97	4.66
n-butanol Volume (%)			
00	4.98	4.95	4.91
10	4.99	4.95	4.87
20	5.01	4.94	4.87
30	4.99	4.94	4.84
40	5.00	5.05	4.80
50	5.00	4.88	4.78
60	4.99	4.88	4.80
70	5.05	4.94	4.86
80	5.20	5.11	4.96
90	5.50	5.39	5.11
100	5.96	5.79	5.31

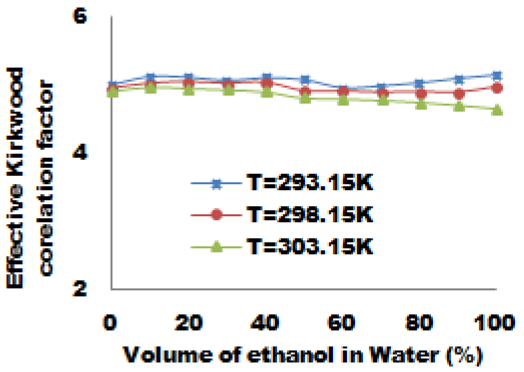

Figure 5*. Variation in estimated values of effective Kirkwood correlation fator of the binary mixture of water - ethanol at different temperatures.*

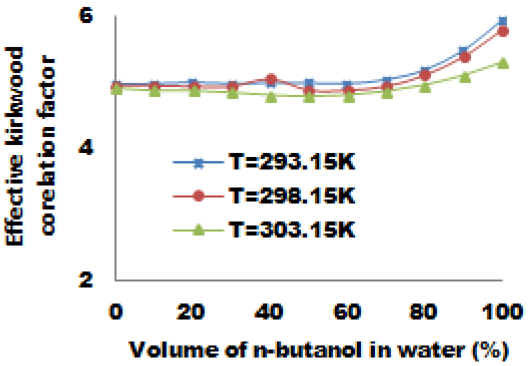

Figure 6*. Variation in estimated values of effective Kirkwood correlation fator of the binary mixture of water - n-butanol at different temperatures.*

3.4 Bruggeman Factor

Bruggeman factor values of water - ethanol and water-butanol binary mixtures were estimated using equation (3) that is noted in Table 5, and graphically illustrated in Figure 7 and 8 respectively. From figures it is observed that, there is deviation from the linear relation has been taking place in both the studied binary mixtures for the three different temperatures, which give the evidence of presence of molecular interaction and hydrogen bonding in the binary mixtures.

Table 5 *Variation in estimated values of Bruggeman factor of water- ethanol and water - n-butanol binary mixture systems at different temperatures.*

Ethanol Volume (%)	Bruggeman factor T=293.15K	Bruggeman factor T=298.15K	Bruggeman factor T=303.15K
00	1.00	1.00	1.00
10	0.95	0.93	0.93
20	0.86	0.85	0.85
30	0.76	0.76	0.76
40	0.68	0.68	0.67
50	0.58	0.56	0.56
60	0.45	0.46	0.47
70	0.35	0.35	0.36
80	0.25	0.24	0.25
90	0.13	0.12	0.13
100	0.00	0.00	0.00
n-butanol Volume (%)			
00	1.00	1.00	1.00
10	0.92	0.91	0.91
20	0.84	0.83	0.83
30	0.75	0.74	0.74
40	0.66	0.65	0.65
50	0.56	0.55	0.55
60	0.45	0.45	0.46
70	0.35	0.34	0.36
80	0.24	0.24	0.25
90	0.13	0.13	0.14
100	0.00	0.00	0.00

Table 6 *Estimated values of molar volume (V), molar refraction (R), polarizability (α), solvated radii (r), molar polarization (Pm), deviation in molar refractivity (Δ_R) , atomic polarization (P_A), electronic polarization (P_E) and permittivity at higher frequency (ε_∞) of water- ethanol and water – n-butanol binary mixture systems at 293.15K temperature.*

Ethanol Volume (%)	V (cm^3/mol)	R (cm^3/mol)	α (10^{-24}) cm/molecule	(r) A^0	(Pm) (cm^3/mole)	Δ_R	(P_A)	(P_E)	ε_∞
00	18.049	3.720	1.47	1.62	17.400	0.000	1.86	1.85	1.77
10	21.319	4.424	1.75	1.72	20.521	-0.221	1.87	2.54	1.78
20	24.726	5.171	2.05	1.80	23.729	-0.399	1.88	3.28	1.79
30	28.296	5.959	2.36	1.89	27.048	-0.536	1.89	4.06	1.80
40	32.026	6.793	2.69	1.96	30.499	-0.627	1.89	4.89	1.80
50	35.930	7.679	3.04	2.04	34.035	-0.666	1.90	5.77	1.81
60	40.254	8.661	3.43	2.12	37.840	-0.609	1.91	6.74	1.82
70	44.329	9.604	3.80	2.19	41.359	-0.591	1.92	7.68	1.82
80	48.857	10.664	4.22	2.26	45.163	-0.456	1.92	8.73	1.83
90	53.611	11.778	4.67	2.33	48.569	-0.267	1.93	9.84	1.84
100	58.598	12.971	5.14	2.40	52.274	0.000	1.94	11.02	1.85
n-butanol Volume (%)									
00	18.049	3.720	1.47	1.62	17.400	0.000	1.86	1.85	1.77
10	24.152	5.039	1.99	1.79	23.214	-0.525	1.88	3.15	1.79
20	30.485	6.473	2.56	1.93	29..198	-0.935	1.89	4.57	1.80
30	37.070	8.007	3.17	2.06	35.344	-1.246	1.91	6.08	1.82
40	43.922	9.647	3.82	2.18	41.653	-1.450	1.93	7.11	1.84
50	51.066	11.402	4.52	2.30	48.095	-1.540	1.95	9.44	1.86
60	58.518	13.277	5.26	2.40	54.626	-1.509	1.97	11.30	1.88
70	66.306	15.283	6.06	2.51	61.218	-1.347	1.99	13.28	1.89
80	74.436	17.419	6.90	2.60	67.760	-1.056	2.01	15.40	1.91
90	82.931	19.703	7.81	2.70	74.080	-0.616	2.03	17.67	1.93
100	91.846	22.164	8.78	2.79	79.611	0.000	2.05	20.11	1.95

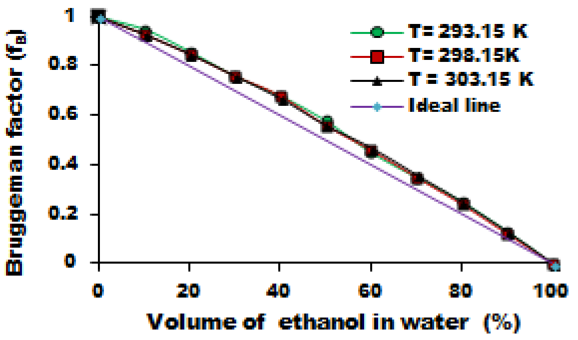

Figure 7. *Variation in estimated values of Bruggeman factor of the binary mixture of water – ethanol at different temperatures.*

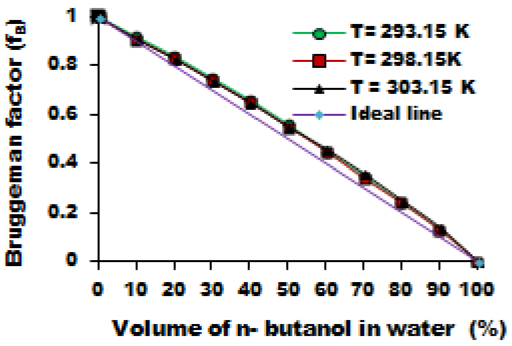

Figure 8. *Variation in estimated values of Bruggeman factor of the binary mixture of water – n-butanol at different temperatures.*

3.5 Molar Volume (V), Molar Refractions (R), Polarizabillty (α), Solvated Radii (r), Molar Polarization (P_m), Deviation in Molar Refraction (Δ_R), Atomic Polarization (P_A), Electronic Polarization (P_E) and Permittivity at Higher Frequency (ε_∞)

The calculated values of the molar volume (V), molar refractions (R), polarizabillty (α), solvated radii (r), molar polarization (P_m), deviation in molar refraction (Δ_R), atomic polarization (P_A), electronic polarization (P_E) and permittivity at higher frequency (ε_∞) of water-ethanol and water- butanol binary mixtures are given in Table 6. From the data it is observed that, all these parameters are increasing with volume fraction of ethanol and n-butanol in water and their trend is similar to that of refractive index. This means that as the refractive index increases, the solute-solvent interaction increases and so the molar volume, molar refraction, polarizabilities, molar volumes, solvated radii, atomic polarization, electronic polarization and permittivity at higher frequency increase. Since the molar refraction is a measure of volume occupied with an atom or molecule and depends on the refractive index, it was noticed that the molar refractions of the studied binary mixtures increases as the molar volume and refractive index increase and the same is noticed from Table 6 and 2. Similar results have been reported by Farid for selected binary protic-protic, aprotic-aprotic, and aprotic-protic systems at temperatures from 298.15 K to 308.15 K, in that study the author reported that, as the refractive index increases the solute-solvent interaction increases and so the molar volume, molar refraction, polarizabilities, solvated radii and molar polarization increases. In the same study the author also reported that the molar refraction is a measure of volume occupied with an atom or molecule and depends on the refractive index and temperature, it was noticed that the molar refractions of the studied binary mixtures increases as the molar volume and refractive index increase. [13].

3.6 Excess Density, Excess Refractive Index, Excess Molar Polarization and Excess Molar Volume

The estimated values of excess density excess (d^E), excess refractive index (n^E), excess molar polarization **(**$P_m)^E$ and excess molar volume (V^E) of water-ethanol and water-butanol binary systems are tabulated in Table 7. From the Table it is observed that, excess density values are negative over the entire volume fraction range of the binary mixtures at the studied temperature. This may be due to increase in molar volume of the binary mixtures.

Table 7 *Variation in estimated values of excess density* $(d)^E$*, excess refractive index* $(n)^E$*, excess molar polarization* $(P_m)^E$ *and excess molar volume*(V^E) *of water- ethanol and water – n-butanol binary mixture systems at 293.15 K temperature.*

Ethanol Volume (%)	$(d)^E$	$(n)^E$	$(P_m)^E$	(V^E)
00	0.0000	0.0000	0.000	0.00
10	-0.0003	-0.00031	-0.366	-0.71
20	-0.0002	-0.00022	-0.645	-1.16
30	-0.0004	-0.00043	-0.814	-1.37
40	-0.0004	-0.00044	-0.850	-1.37
50	-0.0003	-0.00035	-0.802	-1.20
60	-0.0052	-0.00526	-0.484	-0.88
70	-0.0003	-0.00037	-0.452	-0.61
80	-0.0004	-0.00048	-0.136	-0.31
90	-0.0005	-0.00039	-0.217	-0.08
100	0.0000	0.00000	0.000	0.00
n-butanol Volume (%)				
00	0.0000	0.00000	0.000	0.00
10	-0.0008	-0.00192	-0.407	-1.17
20	-0.0009	-0.00174	-0.644	-1.91
30	-0.0008	-0.00156	-0.719	-2.25
40	-0.0006	-0.00138	-0.631	-2.25
50	-0.0005	-0.00120	-0.410	-1.99
60	-0.0004	-0.00102	-0.100	-1.55
70	-0.0004	-0.00084	0.270	-1.02
80	-0.0003	-0.00076	0.591	-0.52
90	-0.0001	-0.00058	0.690	-0.14
100	0.0000	0.00000	0.000	0.00

From Table 7, it is also observed that the excess refractive indices of both the binary mixture are negative over the entire volume fraction range at the studied temperature. The excess refractive indices and the binary mixtures interactions depend on the nature of the solvent and its physical properties such as the dielectric constant, dipole moment and the donor number. The results are in agreement with the earlier results of Farid, in the same study the author Farid reported that the values of excess refractive indices indicates maximum solvent- solvent interaction and depends mainly on the different physical properties of the solvents such as the dielectric constant, dipole moment donor number, chemical structure.

The estimated values of excess molar polarization of both the binary mixtures are given in Table 7. From the data it is noticed that for water- ethanol binary mixtures the excess molar polarization is negative over the entire volume fraction range and for water- butanol binary mixture it is negative in water rich region and positive in n-butanol rich region.

The estimated values of excess molar volume of water-ethanol and water - butanol binary mixtures are given in Table 7 and graphically illustrated in Figure 9 and 10 respectively.

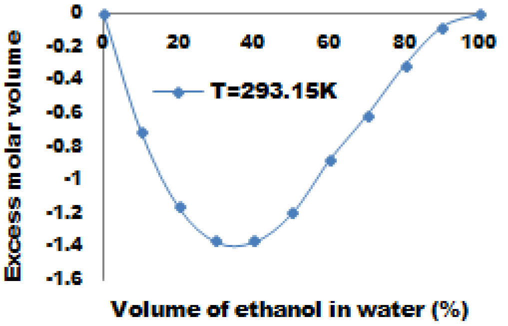

Figure 9*. Variation in estimated values of excess molar volume of the binary mixture of water – ethanol at 293.15K temperature.*

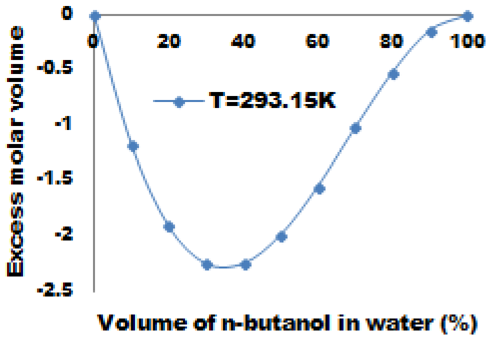

Figure 10*. Variation in estimated values of excess molar volume of the binary mixture of water – n-butanol at 293.15K temperature.*

From figures it is observed that, the values of excess molar volumes are negative over the entire volume fraction range for both the binary mixtures at the studied temperature. The negative behavior of excess molar volume over the entire concentration range may be due to the volume contraction after mixing. Excess molar volume is generally used as a signal of non-ideal behavior of real mixtures. Negative values of excess molar volumes show strong intermolecular interaction and formation of hydrogen bonds, charge transfer complexes and other complex forming interactions including strong dipole-dipole interactions between the component molecules in the mixtures. In the study of Density, Viscosity, Refractive Index, and Speed of Sound in Binary Mixtures of Pyridine and 1-Alkanols (C6, C7, C8, C10) at 303.15 K by A. Ali, the authors had reported similar results. In the study the authors reported that, the negative deviations in $\mathbf{V^E}$ values over the entire composition range for all the binary systems suggest the presence of strong interactions between pyridine and 1-alkanol molecules and that the strength of interaction follows the order: 1-hexanol > 1-heptanol > 1-octanol > 1-decanol. [29].

4. Conclusions

The static dielectric constant of binary mixtures decreases with increase in temperature and volume fraction of ethanol and n-butanol in water.

The variation in R- square values in dielectric constant of the studied binary mixtures show a non-linear variation with concentration, that shows the intermolecular association is taking place in the studied binary systems.

Densities of the studied binary mixtures decrease and the refractive indices increase with increase in volume fraction of ethanol and n-butanol in water.

Excess dielectric constant of water - ethanol binary mixture is positive in water rich region and negative in ethanol rich region. In case of water- butanol binary mixtures the excess dielectric constant is negative over the entire volume fraction range of n- butanol.

In both the studied binary mixtures the dipole pairs are formed and they orient in parallel direction over the entire volume fraction range of ethanol and n-butanol in water that is confirmed from the (g^{eff}) values.

The Bruggeman factor study of both the binary mixture systems shows that there is deviation from linear relations, which gives strong evidence of presence of molecular interactions and hydrogen bonding in the binary mixture systems.

Molar volume, molar refraction, polarizability, solvated radii, molar polarization, atomic polarization, electronic polarization, optical permittivity values increases with increasing volume fraction of ethanol and n-butanol in water.

Excess density, excess refractive index, and excess molar volume values of the binary mixtures is negative over the entire volume fraction range of ethanol and n-butanol. In water- butanol binary mixtures the excess molar polarization values are negative in water rich region and positive in butanol rich region.

Negative values of excess molar volume over entire volume fraction range of the studied binary systems confirm the presence of intermolecular interaction and hydrogen bonding between the binary systems.

Acknowledgements

The authors are thankful to head, Department of Physics, Dr. Babasaheb Ambedkar Marathwada University-Aurangabad (M.S.) India, for providing the experimental facility for the said work.

Nomenclature

Symbol	***Variable***
D	*Density*
d^E	*excess density*
f_{BM}	*Bruggeman factor*
g^{eff}	*effective Kirkwood correlation factor*
n	*Refractive index*
n^E	*excess refractive index*
P_A	*Atomic polarization*
P_E	*Electronic polarization*
P_M	*molar polarization*
$P_m{}^E$	*excess molar polarization*
R	*Molar refraction*
r	*Solvated radii*
V	*Molar volume*
V^E	*excess molar volume*
Greek	
Δ_R	*Deviation in molar refraction*
α	*Polarizabilty*
ε	*Dielectric constant*
ε_∞	*Permittivity at higher frequency*
$\boldsymbol{\varepsilon^E}$	*excess dielectric constant*
Superscript	
E	*Excess*
eff	*Effective*
Subscripts	
BM	*Bruggeman*
M	*Molar*
A	*Atomic*
E	*Electronic*
∞	*Higher Frequency*
Abbrevations	
r^2	*Coefficient of determination*

References

[1] R. Day and A. Underwood, "*Quantitative Analysis*, New Jersey: Prentice-Hall 1991.

[2] H. Yilmaz and S. Guler, "Excess properties of methanol-water binary system at various temperatures," *II Nuovo Cimento, 20D,* 1853-1851, 1998.

[3] A. Jouyban, S. Shahla and H. Chan, "A simple relationship between dielectric constant of mixed solvents with solvent composition and temperature,"*International Journal of Pharmaceutics, 269,* 353- 360, 2004. doi: 10.1016/j.ijpharm.2003.09.010.

[4] M. Mohsen- Nia, H. Amiri, B. Jazi, "Dielectric constant of water, methanol, ethanol, butanol, and acetone: measurement and computational study," *J. Solu. Chem., 39*, 701-708, 2010. DOI 10.1007/s10953-010-9538-5.

[5] Hülya Yilmaz, "Excess properties of alcohol- water systems at 298.15K," *Turk, J. Phys., 26*, 243-246, 2002.

[6] A.P. Maharolkar, A. Murugkar, P.W. Khirade, S.C. Mehrotra, "Study of Dielectric and Acoustic Properties of Binary Liquid Mixtures of Cyclohexane with n-Butanol at 308 K," *Russian Journal of Physical Chemistry A, 95*, S56-S61, 2021. DOI:10.1134/S0036024421140120.

[7] V. V. Navarkhele, *"*Dielectric and Excess properties of glycol with formamide at different temperatures,*" Russian Journal of Physical Chemistry A, 92*, 1417-1422, 2018. *DOI*: 10.1134/S0036024418070191.

[8] R. J. Sengwa, S. Sankhla and S. Shinyashiki,. "Dielectric Parameters and Hydrogen Bond Interaction Study of Binary Alcohol Mixtures," *J. Sol. Chem., 37*, 137-153, 2008. DOI 10.1007/s10953-007-9230-6.

[9] J. G. Kirkwood, "The dielectric polarization of polar liquids", *J. Chem. Phys., 7*, 911-919, 1939.

[10] A.C. Kumbharkhane, S.M. Puranik, S.C. Mehrotra, “Dielectric relaxation of tert- butyl alcohol–water mixtures using a time-domain technique”, *J. Chem. Soc. Faraday Trans., 87*, 1569-1573, 1991. https://doi.org/10.1039/FT9918701569.

[11] A.C. Kumbharkhane, S.M. Puranik, S.C. Mehrotra, “Dielectric relaxation studies of aqueous N, N dimethylformamide using a picoseconds time domain technique”, *J. Sol. Chem., 22*, 219-229, 1993. https://doi.org/10.1007/BF00649245

[12] D. A. G. Bruggeman, *Ann. Phys (Leipz.), 24*, 636-646, 1935.

[13] Farid I.EI-Dossoki, “Refractive index and density measurements of selected binary protic-protic, aprotic-aprotic, and aprotic and protic syatems at temperatures from 298.15K to 308.15 K”, *J. Chinese Chem. Society, 54*, 1129-1137, 2007.

[14] C. M. Trivediand V. A. Rana, “Static permittivity,refractive index, density,and related properties of binary mixtures of pyridine and 1-propanol at diffenent temperatures”, *Indian journal of pure & applied Physics, 52*, 183-191, 2014.

[15] E.R. Mongnaschi and L.M. Laboranti, “Association of pure polar liquids: Dielectric properties of docosanoic acid”, *J. Chem..Soc. Faraday Trans., 92(18),* 3367-3369, 1996.

[16] S. K. Rays, J. Rath and C. Dwivedi, “ Excess Molar polarization in binary mixtures of polar liquids,” *Physics and Chemistry of Liuids., 39,* 227-237 2001. https://doi.org/10.1080/00319100108030341

[17] J. I. Kim, “A Critical Study of the Ph_4AsPh_4B Assumption for Single Ion Thermodynamics in Amphiprotic and Dipolar-Aprotic Solvents; Evaluation of Physical Parameters Relevant to Theoretical Consideration,” *Z. Phys, Chem. Neue Folge, 113,* S.129-150, 1978.https://doi.org/10.1524/zpch.1978.113.2.129

[18] S. Oswal, “Studies on density, viscosity, dielectric constant, and refractive indices of binary mixtures of ester in benezen and carbon tetrachloride”, *Can. J. Chem., 66*, 111-116, 1988.

[19] Fisnik Aliaj, Naim Syla, Ardita Kurtishaj, Njomza Elezaj, Tahir arbneshi, Arber Zeqiraj, “Densities, refractive indices, and derived properties of binary mixtures of ethanol with benzene and pyridine at various temperatures under atmospheric pressure”, *International journal of Thermophysics,41*, 49-55, 2020. doi.org/10.1007/s10765-020-02632-9

[20] E. J. Gonzalez, P.F. Requejo, F. M. Maia, A. Dominguez and E. A. Macedo, “Solubility, density and excess molar volume of binary mixtures of aromatic compounds and common ionic liquids at $T = 283.15$ K and atmospheric pressure”, *Physics and Chemistry of liquids, 53*, 419-428, 2015. doi.org/10.1080/00319104.2013.782546

[21] N.E. Hill, W.E. Vaughan, A.R. Price and M. Davies, *Dielectric properties and Molecular behavior, Van* Nostrand Reinhold: London -1969.

[22] A.C. Kumbharkhane, S. M. Puranik, S.C. Mehrotra, *“*Structural study of amide-water mixtures using dielectric relaxation technique”, *J. of Mole. Liqs, 51*, 261-277, 1992. doi.org/10.1016/0167 7322(92)80088-Y

[23] V. V. Navarkhele, M. K. Bhanarkar, “Microwave dielectric response of binary mixture of N, N dimethylformamide with propylene glycol using TDR method,” *Molecular Physics, 107*, 1823-1830, 2009. http://dx.doi.org/10.1080/00268970903084912

[24] B. G. Lone, P.B. Undre, S. S. Patil, P.W. Khirade and S.C. Mehrotra, “Dielectric study of methanol- ethanol mixtures using TDR method. Journal of Molecular Liquid”, *J. of Mole. Liqs, 141*, 47-53, 2008. doi:10.1016/j.molliq.2008.03.001.

[25] V. V. Navarkhele and M.K. Bhanarkar, “High-frequency dielectric response of the binary mixture formamide–butylene glycol,” *Physics and Chemistry of Liquids, 48*, 89-98, 2010. http://dx.doi.org/10.1080/00319100802688360

[26] A. Nasim, K. Movagharnejad, P. Mohsenand K. Mahnam, “Densities, Viscosities, and Refractive Indices of Poly(ethylene glycol) 300 + 1,2-Ethanediol, 1,2-Propanediol, 1,3-Propanediol, 1,3-Butanediol, or 1,4-Butanediol Binary Liquid Mixtures,”. *Journal of Chemical Engineering Data, 65,* 3448-3462, 2020. https://dx.doi.org/10.1021/acs.jced.9b01189

[27] V. V. Navarkhele and M.K. Bhanarkar, “Dielectric relaxation study of formamide–propylene glycol using time domain reflectometry”, *Physics and Chemistry of Liquids, 49*, 550-559, 2011. DOI: 10.1080/00319104.2010.508041.

[28] M.T. Hosamani, R.H. Fattepur, D.K. Deshpande and S. C.Mehrotra, “Temperature-and Frequency –Dependent Dielectric studies of PFluorophenylactetonitrile –Methanol mixtures using the Time domain reflectrometry”, *J. Chem. Soc. Faraday Trans., 91*, 623-626, 1995. https://doi.org/10.1039/FT9959100623

[29] A. Ali, M. Tariq, F. Nabi and Shahajahn, “Density, Viscosity, Refractive Index, and Speed of Sound in Binary Mixtures of Pyridine and 1-Alkanols (C6, C7, C8, C10) at 303.15 K”, *Chinese Journal of Chemistry, 26*, 2009-2015, 2008. https://www.researchgate.net/publication/315750205.

International Journal of Thermodynamics (IJoT)
ISSN 1301-9724 / e-ISSN 2146-1511
https://dergipark.org.tr/en/pub/ijot

Vol. 25 (No. 3), pp. 12-20, 2022
doi: 10.5541/ijot.1024316

Exergy Cost Accounting Analysis of New Hybrid Solar Organic Rankine Cycle-MSF Desalination System for Pasabandar Region in Gwadar Bay

Mojtaba Babaelahi[1*], Somayyeh Sadri[2]

[1*]Department of Mechanical Engineering, University of Qom, P.O. Box 6765-1719, Qom, Iran
[2]Thermal cycles and Heat Exchangers Department, Niroo Research Institute, Tehran, Iran
Email: [1*]m.babaelahi@qom.ac.ir

Received 16 November 2022, Revised 17 May 2022, Accepted 2 June 2022

Abstract

An energy system affordable plan selection using renewable energy is a significant problem for designing and manufacturing these systems. The fault detection and thermoeconomic diagnosis in the combined solar Rankine cycle and multi-stage flash (MSF) desalination system is analyzed. In the suggested energy system, the linear parabolic solar collector is utilized as a heat source for the organic Rankine cycle, the domestic hot water, and the multi-stage-flash desalination system. First, the energy balances and exergy analysis are implemented in the considered system, the energy value and exergy parameter are calculated. The exergy cost parameters are calculated for all parts and streams with the thermoeconomic and exergy cost accounting investigation. Finally, the thermoeconomic diagnosis is performed, and the malfunction of each component is evaluated, and the effect of each component's irreversibility on the other part is investigated. Results show that the linear parabolic solar collector has the maximum malfunction. Still, the condenser in the organic Rankine cycle is the most effective component on irreversibility increment among its counterparts..

Keywords: *Desalination; exergy cost accounting; hybrid solar; malfunction; organic rankine cycle.*

1. Introduction

Nowadays, a decrease in fossil-fuel consumption is one of the significant challenges. Consequently, the investigation of supplementary strategies for reaching the United Nations Sustainable Development Goals on energy has long been initiated. As the fundamental source of renewable energy globally, solar energy is the primary source of all available energy on the earth. Same other energies, it can be converted into different energy types (like heat and electricity). Many research types have been performed in recent years, identifying the importance of replacing fossil fuels with renewable energy.

Omar et al. [1] presented a review of the solar Rankine cycle and its characteristics. In their research, the influence of different working fluids and utilizing solar energy were considered. The investigation of the solar energy potential for providing electricity and desalinated water in UK domestic applications was done by James et al. [2]. In the research, the authors presented a life-cycle analysis of the system and according to the total electrical power output and cost, the annual performance of the system was evaluated. They found that tracking concentrating parabolic-trough (PTC) collectors were to be very similar in performance to non-tracking non-concentrating evacuated-tube (ETC) collectors with an average power output of 89 W vs. 80 W.

John et al. [3] reviewed the various solar energy technologies used in different water desalination systems. In their study, the authors compared the direct and indirect solar desalination technologies and selected the direct solar-desalination systems as the best efficient system. Baltasar et al. [4] proposed the best solar desalination system design for given ranges of about 1000–5000 m^3⁄day. In their proposed system, the reverse osmosis desalination system and the solar organic Rankine cycle were combined. Guanghui et al. [5] proposed reverse osmosis (RO) desalination system operated by wind energy and a solar-powered organic Rankine cycle (ORC). In their study, the authors presented that the condenser temperature and turbine inlet pressure have an essential role in water production. Agustin et al. [6] suggested the different recommendations for combined ORC and solar RO desalination system (SORC). In their paper, the authors found that the linear solar collectors (linear Fresnel concentrators or parabolic troughs) were suitable for incrementing overall thermal performance. The feasibility of using solar desalination in Iran was studied by Shive et al. [7]. In their study, the topography, climate, and water shortage status in Iran were considered, and some of the solar water desalination technology was investigated. The results showed that the fossil fuels used as the heat source for water desalination in the desalination plants centralized in the southern coastal regions. Ratha et al. [8] analyzed a tri-generation system driven by solar energy. The analysis was done with IPSEpro software and verified with experimental data. The tri-generation arrangement produced about 1MW electricity, 234 tons⁄day of distilled water, and 194 Ton of refrigeration. Nafey et al. [9] performed the combined solar ORC and RO process's design and performance analysis. In their research, the effect of various working fluids on exergy and cost factors was studied. Diab et al. [10] studied the integrated Rankine cycle and solar-based multi-stage flash (MSF)desalination. The results showed that the significant part (about 75 percent) of exergy destruction was related to

*Corresponding Author

the MSF unit. Mohamed et al. [11] evaluated a multi-stage flash brine recycled distillation process (MSF-BR) driven by solar energy and performed the thermo-economically analysis.

Exergy cost accounting was one of the important ways to analyze energy systems used in their manuscript. Valero et al. [12-13] have introduced this approach. In this method, Valero proposed the exergy cost accounting and the thermoeconomic method for energy system analysis. In [1], Valero showed the fundamental necessities for calculating the exergy costs and thermoeconomic costs of energy systems. In the next paper [13], Valero presented thermoeconomic analysis applications in energy systems. In the other research, Sajjad et al. [14] studied the energy systems malfunctions and faults and suggested an energy systems thermoeconomic diagnosis nominated Thermoeconomic Input-Output Analysis(TIOA). Alicia et al. [15] presented a thermoeconomic investigation for the cement manufacturing process. In their study, the most inefficient processes were identified and tried to overcome this problem.

This paper proposes a new novel combined energy system, including the organic Rankine cycle, domestic hot water producer, and seawater desalination system. In this system, the linear parabolic solar collector is utilized as a heat source, and energy storage is employed to stabilize the system's stable operation. Therefore, in this manuscript, the linear parabolic solar collector is chosen as a heat source for power, domestic water, and desalinated water production in one of the proper cities in Gwadar Bay. The Pasabandar, one of the small regions of Chabahar in Gwadar bay, is selected for the installation of this proposed system. The exergy and energy analysis for all of the components is performed to evaluate the combined energy system. Exergy destruction in energy systems reduce the overall efficiency. In this study, the thermoeconomic diagnosis method is implemented to detect each component's inefficiencies in the proposed designs. Thus, the amount of inefficiencies and their location is present with the thermoeconomic diagnosis method. Other techniques zoom on each component's irreversibility and endeavor to reclaim it. Each component's hidden effects on other components' irreversibility are examined in this manuscript. Thus, the governing results offer a suitable method for identifying significant unknown inefficient components.

2. Modelling

2.1 System Description

The suggested hybrid solar system schematic is shown in **Error! Reference source not found.**. The proposed system consists of the solar cycle, Organic Rankine cycle, Multi-stage flash distillation cycle, and domestic heat water producer. In the basic solar cycle (5-6-7-8-9-10), Therminol-66 is used as the working fluid, and thermal storage is forecasted for steady-state operation in different solar conditions. The working fluid is heated by the solar energy unit and then stored in the tank. The heat from the exhaust gases from the combustion of the turbine inside a heat exchanger is added to the operating fluid, and this heat is used to increase the temperature of the water used in the residential units as well as to produce fresh water in the MSF units. For domestic hot water production (17-18), a heat exchanger uses to heat the feed water (to 60°C). In the Organic-Rankine cycle (1-2-3-4), the water-ammonia mixture is used as a working fluid, and a heat exchanger provided the required thermal energy. For desalination of seawater, the multi-stage-flash desalination system (MSF) is proposed. One heat exchanger provided the requires heat for seawater vaporization in different stages. The Pasabandar, one of Chabahar regions in Gwadar bay, is selected for the proposed cycle location. The detailed information about Pasabandar is presented in Table 1. The required analyses of each component are

Table 1. The detail of Pasabandar region.

parameter	value
Longitude	25°04′01″N
Latitude	61°24′44″E
population	1093

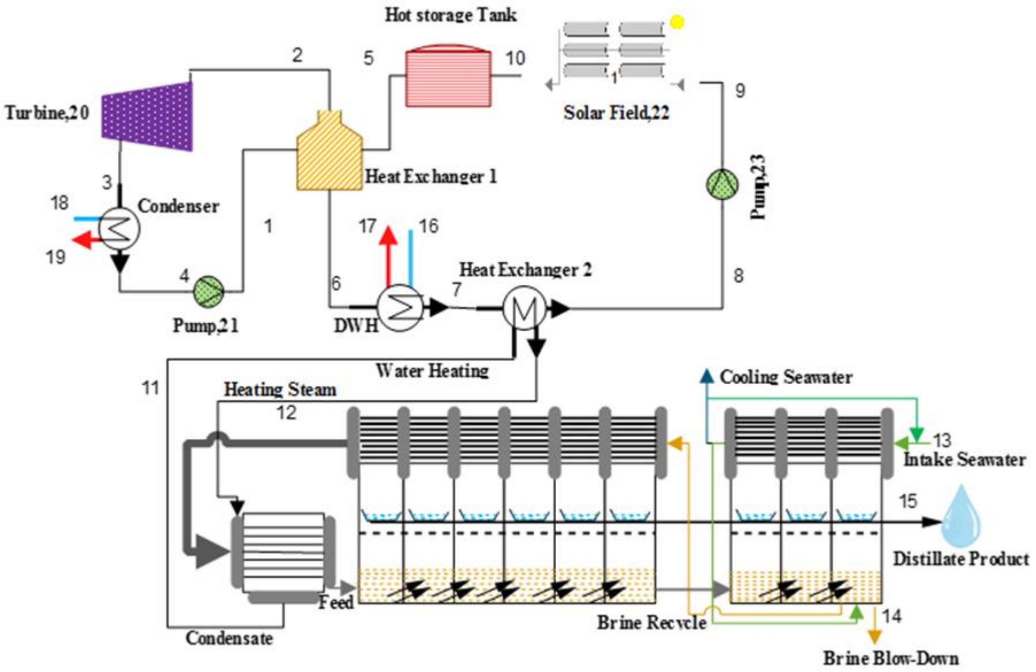

Figure 1. Schematic of the hybrid system

2.2 Energy Analysis

- Therminol Cycle (Solar Circuit)

In the Therminol-66 cycle, the linear parabolic solar collector is used as the heat absorber. Detailed information about these types of collectors can be found in [16], and in this section, only the required formulation is considered. In general, the absorbed solar heat in a linear parabolic collector can be calculated with Eq.(1).

$$Q_u = E_R A_u [S - \frac{A_{re}}{A_0} U_L (T_{10} - T_0)] \tag{1}$$

The absorbed solar radiation per unit of aperture area, the un-shaded area, and the area of the receiver can be calculated respectively, as bellow:

$$S = I_{ap} \tau \rho \alpha \tag{2}$$

$$A_u = (w - D) l \tag{3}$$

$$A_{re} = \pi D_0 l \tag{4}$$

The heat removal factor is calculated from the next equation:

$$E_R = \frac{\dot{m} c_{pr}}{A_r U_L} [1 - \exp\left(\frac{A_{re} U_L F'}{\dot{m} c_P}\right)] \tag{5}$$

Where,

$$F' = \frac{\frac{1}{U_L}}{\frac{1}{U_L} + \frac{D_O}{H_{te} D_i} + (\frac{D_O}{2k} ln \frac{D_O}{D_i})} \tag{6}$$

The heat losses in hot storage can be presented in the unit area of the tank surface as below:

$$\dot{Q}_{hs} = U (T_{11} - T_0) \tag{7}$$

For heat exchangers used in the organic Rankine cycle, domestic heat water, and desalination systems, the following energy balance equations can be used:

$$\dot{m}_{sc} (h_5 - h_6) = \dot{m}_{rc} (h_2 - h_1) \tag{8}$$

$$\dot{m}_{sc} (h_6 - h_7) = \dot{m}_w (h_{18} - h_{17}) \tag{9}$$

$$\dot{m}_{sc} (h_7 - h_8) = \dot{m}_r (h_{12} - h_{11}) \tag{10}$$

- Organic-Rankine cycle

In the organic Rankine cycle, the primary energy balance equation used in the classic steam cycle can be applied. The output power from the steam turbine, the input power to the pump, and total net power is calculated as below:

$$\dot{W}_t = \dot{m}_{rc} (h_2 - h_3) \tag{11}$$

$$\dot{W}_p = \dot{m}_{rc} (h_1 - h_4) \tag{12}$$

$$\dot{W}_{net,rc} = \dot{W}_{t,rc} - \dot{W}_{p,rc} \tag{13}$$

The isentropic turbine efficiency is defined as below:

$$\eta_t = \frac{(h_2 - h_3)}{(h_2 - h_{3s})} \tag{14}$$

The absorbed heat rate in the heat exchanger 1 and the rejected heat rate in the condenser are given by:

$$\dot{Q}_{boil} = \dot{m}_{rc} (h_1 - h_2) \tag{15}$$

$$\dot{Q}_{cond} = \dot{m}_{rc} (h_3 - h_4) \tag{16}$$

- Desalination system

MSF is one of the thermal desalination technologies that used widely in the world. The brine recirculation type of this technology is used for seawater desalination in this manuscript. In brine recirculation MSF, the hot brine can flow freely and flash in a set of effects. The required heat for the brine heating of feed-water is provided from the Therminol cycle. The hot brine flashes in the stages, and the formed vapor's latent heat recovers by feed and brine recycle flow in the condenser. The surplus heat given to the system is rejected to the sea in the condenser.

The feed to distilled water mass flow ratio can be examined as the function of thermal and mechanical parameters as below [17],

$$\frac{M_f}{M_d} = \frac{L_v}{c_P \Delta F} + \frac{N-1}{2N} \tag{17}$$

Where the flashing temperature range, $\Delta F$is given by:

$$\Delta F = T_h - T_{bN} = (T_{b1} - T_{bN}) \frac{N}{N-1} \tag{18}$$

The maximum brine concentration limits the rate of external feed per unit of product (M_f / M_d) as bellow:

$$\frac{M_f}{M_d} = \frac{y_{bN}}{y_{bN} - y_f} \tag{19}$$

The total required heat for water desalination can be calculated by:

$$\frac{\dot{Q}_{des}}{M_d} = \frac{M_r}{M_d} c_P (T_h - T_0) = L_v \frac{T_h - T_0}{\Delta F} \tag{20}$$

Where,

$$\dot{Q}_{des} = \dot{m}_{sc} (h_8 - h_7) \tag{21}$$

2.3 Exergy Analysis

The highest available work that can be obtained from the particular flow is named exergy. This idea is used in the assessment of irreversibility in any system. For the particular flow, the exergy can be computed as following [18]:

$$e_f = (h - h^*) - T_0 (s - s^*) + \sum_{i=1}^{n} y_i (\mu_i^* - \mu_i^0) \tag{22}$$

The first two terms show the physical exergy, and the next term indicates the chemical exergy. For a control volume, the exergy equation is represented as bellow:

$$\frac{dE}{dt} = \sum \left(1 - \frac{T_0}{T}\right) Q + \left(W - P_0 \frac{dv}{dt}\right) + \sum \dot{m}_i e_i - \sum \dot{m}_e e_e - \dot{E}_D \tag{23}$$

Based on fuel and product exergy, the exergy destruction in each component is evaluated:

$$\dot{E}_D = \dot{E}_{fuel} - \dot{E}_{product} \tag{24}$$

Table 2. Exergy equations of each component in the system.

Component	Fuel exergy (kW)	Product exergy (kW)
Solar field	$\dot{E}_{22}$	$\dot{E}_{10} - \dot{E}_9$
Hot storage tank	$\dot{E}_{10}$	$\dot{E}_5$
Heat exchanger 1	$\dot{E}_5 - \dot{E}_6$	$\dot{E}_2 - \dot{E}_1$
DWH	$\dot{E}_6 - \dot{E}_7$	$\dot{E}_{17} - \dot{E}_{16}$
Heat exchanger 2	$\dot{E}_7 - \dot{E}_8$	$\dot{E}_{12} - \dot{E}_{11}$
Solar pump	$\dot{E}_{23}$	$\dot{E}_9 - \dot{E}_8$
Desalination unit	$\dot{E}_{12} + \dot{E}_{13}$	$\dot{E}_{14} - \dot{E}_{15}$
Turbine	$\dot{E}_2 - \dot{E}_3$	$\dot{E}_{20}$
Condenser	$\dot{E}_3 - \dot{E}_4$	$\dot{E}_{19} - \dot{E}_{18}$
Rankine pump	$\dot{E}_{21}$	$\dot{E}_1 - \dot{E}_4$

The above definitions describe that each component exergy balance equations in steady-state condition are determined and mentioned in Table 2

Exergetic efficiency is one of the essential parameters for irreversibility evaluation that defined based on the fuel-product definition as bellow:

$$\varepsilon = product/fuel \tag{25}$$

2.4 Thermoeconomic Diagnosis and Exergy Cost Accounting

The thermoeconomic analysis is a fundamental idea that combines the irreversibility and cost principles for evaluating thermal systems. Thermoeconomic variables can be determined based on the investment costs and thermodynamic irreversibilities. The necessary data for thermoeconomic evaluation is obtained from the economic and thermodynamic model, physical structure, and productive system. The physical system defines the components, thermodynamic process (feed or product), mass, heat, and workflows. In the thermoeconomic theory, the economic study as the function of investment, operation, and fuel cost are applied to exergy and energy equations. One of the essential parameters in thermoeconomic evaluation is unit exergy consumption (k), equal to the inverse of exergetic efficiency.

The exergy cost ($\dot{E}_i^*$) is another parameter defined as the amount of exergy resources utilized for specific flow production [19]. This parameter can be employed for the evaluation of resource consumption in various exergy flow. The unit exergy cost is defined as follows, based on the above definition:

$$c_i = \dot{E}_i^*/\dot{E}_i \tag{26}$$

The calculations mentioned above are the primary action for the diagnosis of energy systems and thermoeconomic analysis.

In the fuel-product (FP) table definition, the residue and product streams should be determined. Each element ($\dot{E}_{ij}$) describes the product exergy for the component (i) and the fuel exergy of the component (j). After the FP table accounting, the product, P, and irreversibility, I, can be determined. The incoming flows from the environment and other elements are defined as the resources of this component. In the productive and dissipative units, respectively, the cost of fuel and product is calculated as below:

$$C_{F,i} = \dot{E}_{i0}^* + \textstyle\sum_{j=1}^{n} \dot{E}_{ji}^* \tag{27}$$

$$C_{P,i} = \dot{E}_{0i}^* + \textstyle\sum_{j=1}^{n} \dot{E}_{ij}^* \tag{28}$$

$$C_{P,i} = R_{i0}^* \tag{29}$$

The cost of residues related to the *j*th productive component is estimated by:

$$C_{R,j} = \textstyle\sum_i R_{ij}^* \tag{30}$$

Each component product cost is calculated as follows:

$$C_{P,i} = C_{F,i} + C_{R,i} \tag{31}$$

The external resources cost, $C_{e.i}$, is determined by:

$$C_{e,i} = \dot{E}_{i0}^* = \dot{E}_{io} \tag{32}$$

The product unit exergy cost can be decomposed as:

$$c_P = c_P^e + c_P^r \tag{33}$$

The variety of the malfunction (MF), the unit exergy consumption (Δk), and the fuel impact (ΔF) are the essential indicators for diagnosis evaluation. The parameters can be determined as follows: [20]

$$\Delta k = k_{op} - k_{ref} \tag{34}$$

$$MF = \Delta k \times \dot{E}_{ref} \tag{35}$$

$$\Delta F = c_F \times \Delta k \times \dot{E}_{ref} \tag{36}$$

The malfunction parameter (MF) shows the exergetic performance variation between reference and operating conditions in any element and can deliver negative or positive values [21]:

$$MF > 0 \rightarrow \left[\left(\frac{1}{\varepsilon}\right)_{op} - \left(\frac{1}{\varepsilon}\right)_{ref}\right] \times \dot{E}_{ref} > 0 \rightarrow \varepsilon_{op} < \varepsilon_{ref} \tag{37}$$

$$MF < 0 \rightarrow \left[\left(\frac{1}{\varepsilon}\right)_{op} - \left(\frac{1}{\varepsilon}\right)_{ref}\right] \times \dot{E}_{ref} < 0 \rightarrow \varepsilon_{op} > \varepsilon_{ref} \tag{38}$$

The extra fuel consumption in each element can be calculated by the fuel impact (ΔF) for anomaly detection in the various segments. In the process, dysfunction by the malfunction of other elements that created the consumption of the more local source to achieve the different generation required by the other elements is given by [12]:

$$DF_i = (k_i - 1)\Delta P_i \tag{39}$$

3. Results & Discussion

The hybrid solar configuration consists of organic Rankine cycle, domestic heat water producer and multi-stage-flash (MSF) desalination method is suggested for the Pasabandar area in Gwadar bay. The design variables for MSF are presented in Table 3.

Table 3. Proposed hybrid system input parameters.

parameter	value
Ambient pressure , bar	1.013
Ambient temperature , ℃	15
Feed water salinity, ppm	35000
Top brine temperature, ℃	82
Sun temperature, ℃	5505

Based on the above input variables, the computation has been completed, and the derived conclusion is displayed in Table 4. The mathematical calculation has been performed using Matlab code and Ebsilon software based on the above input parameters. The compression of results is presented in Table 4, too. Matlab code results have a good agreement with Ebsilon simulation. The results show that, the proposed system delivered 12 m^3/day distillated water, 338 kW electrical power, 0.5581 kg/s domestic hot water (60^{oc}) and 11.36 kg/s industrial feed hot water.

The exergy cost investigation results for the different components are shown in Table 5. Results confirm that the MSF system has the highest unit exergy consumption and is the most ineffective element. Based on these conclusions, the elements can be arranged from efficient to the inefficient as condenser, thermal storage, heat exchanger 2, turbine, pump, heat exchanger 2, solar field, domestic heat water producer, solar pump and desalination system.

The exergy cost in the various elements is displayed in Figure 2. The conclusions confirm that the solar field affects each element's exergy cost and the MSF desalination has the highest exergy cost.

This preliminary investigation introduces the MSF desalination as the origin of irreversibility, but advanced evaluation should be implemented for precise ineffective element detection. For this precise advance analysis, the changes in the concentration of ammonia-water mixture in organic Rankine cycle should be applied. One of this changes that called operation condition is shown in Table 6 .

Table 4. The results of energy balance equations.

Parameter	Value		
	Code	Ebsilon Simulation	Error
Distillated water production, $\dot{m}_d$ (kg/s)	0.1488	0.1522	2.233
Power production, w_{out} (kW)	337.5	337.5081	0.002
Domestic water heating, $\dot{m}_{DWH}$ (kg/s)	0.5581	0.5604	0.417
Industrial water heating, $\dot{m}_w$ (kg/s)	11.36	11.3631	0.027

Table 5. The exergy cost analysis for different equipment.

Equipment	Turbine	Heat exchanger 1	ORC-pump	thermal Storage	Solar Field	Solar Pump	Heat Exchanger 2	Desalination	Condenser	Domestic Heat Water Producer
Product [kW]	337.5	512	7.7	1133	1160.6	0.1	45.4	0.6	150.5	7.4
Fuel [kW]	368.1	1062.3	9.5	1161	2782	0.4	48.4	63.7	151.6	22
Irreversibility [kW]	30.6	550.3	1.8	28	1621.4	0.3	3	63.2	1.1	14.6
Unit Exergy Consumption	1.090	2.075	1.237	1.025	2.397	3.830	1.066	109.824	1.007	2.982

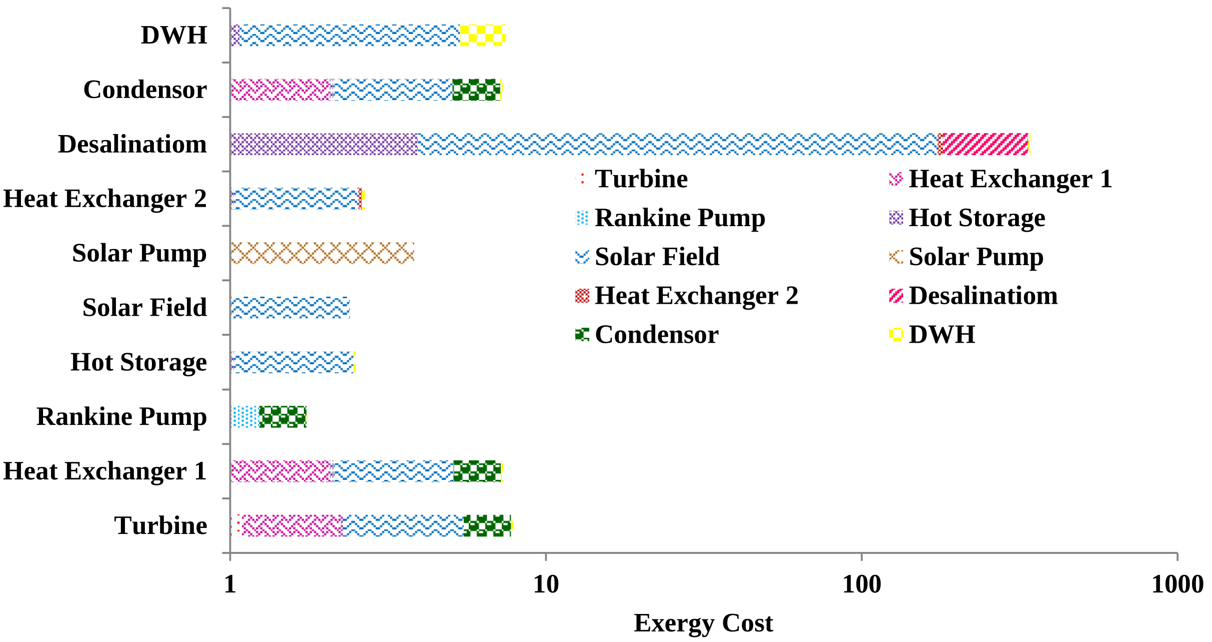

Figure 2. The exergy cost decomposition for different component in reference system.

Table 6. Modeling result of operation system.

Parameter	Value
Ammonia-Water Concentration	0.5
Distillated water production, $\dot{m}_d$ (kg/s)	0.1488
Power production, w_{out} (kW)	101.6
Domestic water heating, $\dot{m}_{DWH}$ (kg/s)	0.5581
Industrial water heating, $\dot{m}_w$ (kg/s)	5.213

At reference and operating conditions, the comparison of exergy cost parameters are collected in Table 7. Results present that decreasing in ammonia-water concentration in organic Rankine cycle decreased the irreversibility in the turbine, heat exchanger, Rankine pump, thermal storage and solar field, effectively.

The amount and location of anomalies that produced the exergetic efficiency decrease are the thermoeconomic diagnosis's main object. Based on the definition of malfunction and irreversibility, these parameters can be determined for each element from equation (35) to assess the anomaly's impacts.

The thermoeconomic diagnosis conclusions for the suggested hybrid arrangement is shown in Table 8. Conclusions confirm that the unit exergy cost in the operating state is lower than the reference state, and thus, the variation in ammonia-water concentration decreased the resource consumption in the operating arrangement. For a better comparison between the various element's malfunction values, the proper diagram is displayed in Figure 3. Considering Table 8 and Figure 3 reveal that the malfunction of the heat exchanger 1, the turbine and Rankine cycle's pump have negative values. These negative values confirm that these elements have better efficiency in operating condition. In general, results confirm that the fuel impact in the operating system is decreased about -1280 kW compared to the reference system and fewer resources are utilized in the new system.

The malfunction decomposition is the important parameter that specifies the effect of each component on total malfunction. This parameter is displayed in Figure 4. Conclusions displayed that the environment has the most effect on the positive malfunction in the solar field. With the same analysis, the hot storage tank has the major role on malfunction decrement in heat exchanger 1; the heat exchanger 1 has the major role in malfunction increment in the condenser.

Table 7. The operating and reference system Irreversibility and unit consumption.

Process	I [kW] Reference scenario	I [kW] Operation scenario	K Reference scenario	K Operation scenario
Turbine	30.6	8.9	1.0907	1.0876
Heat exchanger 1	550.3	105.	2.0748	1.3986
Rankine Pump	1.8	1.3	1.2371	1.2133
Thermal Storage	28.0	13.8	1.0247	1.0314
Solar Field	1621.4	1051.5	2.3970	3.3238
Solar Pump	0.3	0.3	3.8299	3.8299
Heat Exchanger 2	3.0	3.0	1.0658	1.0658
Desalination	63.2	63.2	109.8235	109.8235
Condenser	1.1	90.2	1.0073	2.3061
DWH	14.6	14.6	2.9815	2.9815

Another necessary index that defines the detailed irreversibility increase in different elements (produced by malfunctions of another element) is dysfunction. Figure 5 confirms that the condenser makes a 635.6 kW irreversibility increase in the solar unit, but the solar unit has adverse impacts on the other element's irreversibility. These issues confirm that the irreversibility in the solar unit can be reduced significantly by condenser improvement. Figure 5 reveals that 829.6 kW irreversibility decrease in the solar unit is produced by the heat exchanger 1.

Table 8. The thermoeconomic diagnosis result for different component.

Process [kW]	Turbine	Heat exchanger 1	Rankine Pump	Hot Storage	Solar Field	Solar Pump	Heat Exchanger 2	Desalination	Condenser	DWH	Total
Malfunction	-1	-346.2	-0.2	7.6	1075.6	0	0	0	195.5	0	931.2
Irreversibility variation	-21.7	-445.3	-0.5	-14.2	-569.9	0	0	0	89.1	0	-962.6
Total Product variation	-235.9	0	0	0	0	0	0	0	-81.5	0	-317.4
Malfunction cost	-16	-1187	-0.2	25.4	1075.6	0	0	0	916.5	0	814.3
Total Product variation cost	-1208.9	0	0	0	0	0	0	0	-885.4	0	-2094.2

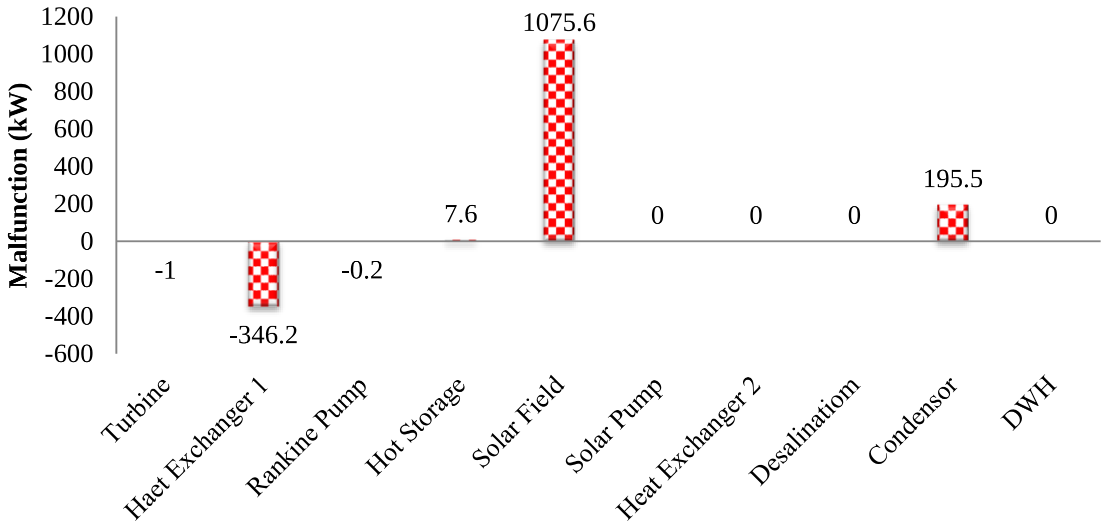

Figure 3. The different components Malfunction of the proposed cycle

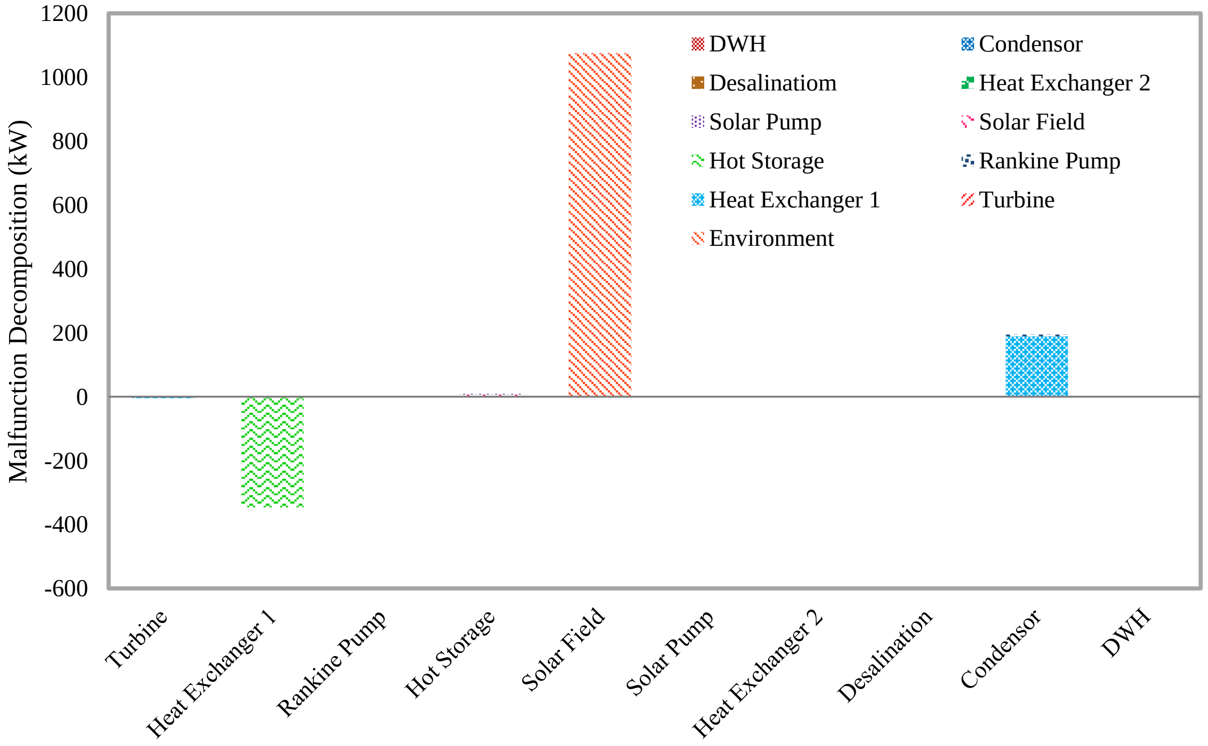

Figure 4. The malfunction decomposition.

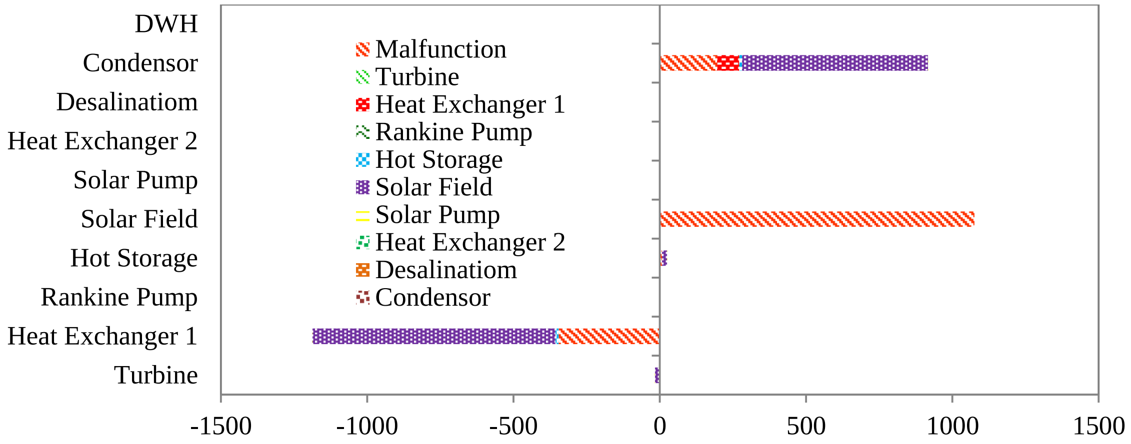

Figure 5. Dysfunction analysis of the system.

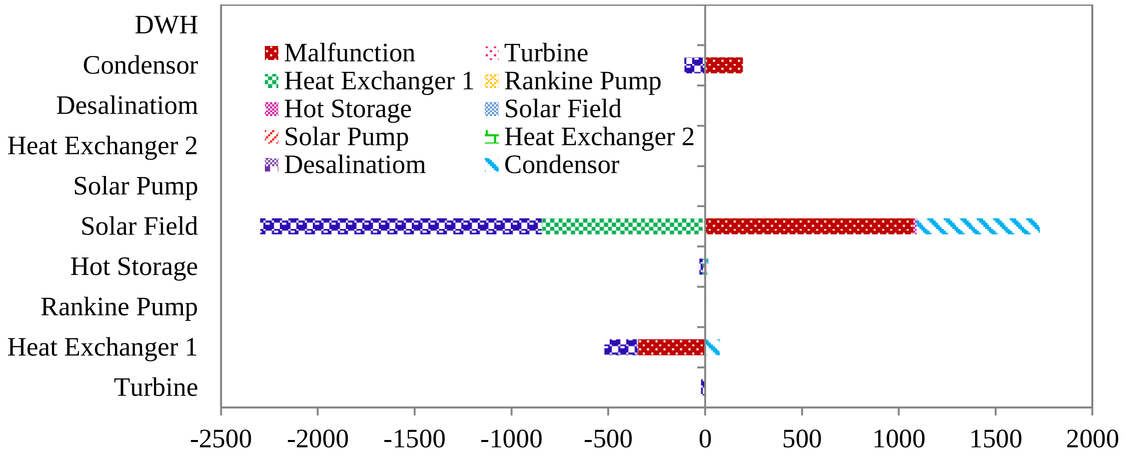

Figure 6. Dysfunction and malfunction analysis.

For a better study, the malfunction and dysfunction indications are connected together and are shown in Figure 6. Conclusions confirm that, in the solar field, 635.4 kW irreversibility increase is generated by malfunction of the condenser and about 830 kW irreversibility decrement related to the heat exchanger 1. The adverse irreversibility in the solar unit, condenser, and heat exchanger 1 shows that the malfunction reduced the additional resource consumption in these elements.

4. Conclusion

In this research, one of the applicable hybrid solar systems consists of an organic Rankine cycle, domestic heat water producer and multi-stage-flash desalination system is proposed for Pasabandar, a region in Gwadar bay. The exergy cost accounting and malfunction diagnosis are implemented to assess different components in the suggested system. Unlike the exergoeconomic method that specifies the inefficient component based on its irreversibility; these indexes examine the hidden impact of each element on irreversibility increase and extra fuel consumption in other elements; thus can introduce the actual inefficient equipment. A large amount of the malfunction calculated in the solar field presents that there is some diagnosis in this equipment. Conclusions present that the condenser has the minimum unit exergy cost, but malfunction-dysfunction analysis shows that this component has the major impact on the irreversibility increment in the other equipment. Thus, the condenser is the main contributor for total malfunction increasing in the system and for the better performance, this component should be improved.

Nomenclature

A_{re}	area of the receiver (m^2)	F	Exergy of fuel (kW)
A_u	unshaded area of the concentrator aperture (m^2)	H_{te}	heat transfer coefficient inside the tube (W/m^2 K)
C	Total Exergy Cost of the flow (kW)	I	Irreversibility (kW)
c	Total unit exergy cost of the flow (kW/kW)	I_{ap}	the effective incident radiation (W/m^2)
Ce	Exergy cost of flow due to irreversibilities (kW)	K	conductivity (W/m K)
c_e	Unit exergy cost of flow due to irreversibilities (kW/kW)	k	Unit Consumption F/P (kW)
c_F	Unit exergy cost of fuel (kW/kW)	L_v	average latent heat of vaporization (kJ/kg)
c_P	Unit exergy cost of product (kW/kW)	l	concentrator length
c_p	mean specific heat (kJ/kg K)	M_d	mass rate of distillate (kg/h)
$c_{P,e}$	Unit production cost due to irreversibility (kW/kW)	M_f	mass rate of feed (kg/h)
$c_{P,r}$	Unit production cost due to residues (kW/kW)	M_r	mass rate of recirculated brine (kg/h)
Cr	Exergy cost of flow due to residues (kW)	$\dot{m}$	mass flow rate (kg/s)
c_r	Unit exergy cost of flow due to residues (kW/kW)	MF	Malfunction (kW)
D	absorber envelope outer diameter (m)	MF*	Malfunction cost (kW)
D_i	absorber inside diameter (m)	N	total number of stages or effects

D_o	absorber outside diameter (m)	P	Exergy of product (kW)
DF	Dysfunction (kW)	R^*_{ij}	cost of the residue dissipated by the ith component that is related to the jth component production
DI	Irreversibility variation (kW)	R^*_{i0}	cost of waste
DPs	Total Product variation (kW)	S	absorbed solar radiation per unit of aperture area (W/m^2)
DP*	Total Product variation cost (kW)	T	temperature (K)
$\dot{E}$	Exergy of flow (kW)	U_L	overall heat transfer coefficient (W/m^2 K)
$\dot{E}^*_{i0}$	cost of the external resources entering the component	w	width of receiver (m)
$\dot{E}^*_{0i}$	cost of the final products of the system	y	mass fraction of salts in brine
	Greek letters		
α	absorptivity	τ	effect of angle of incidence
ρ	specular reflectance of the concentrator	ε	Exergetic efficiency
	Subscript		
b	brine	r	recirculated brine
b1	brine in first effect	rc	Rankine cycle
bN	brine in last effect	ref	reference
f	feed	sc	Solar cycle
op	operating	0	Environment

References

[1] O. Aboelwafa, S. K. Fateen, A. Soliman, I. M. Ismail, “a review on solar Rankine cycles: Working fluids, applications, and cycle modifications” Renewable Sustainable Energy Rev., 82, 868–885, 2018.

[2] J. Freeman, K. Hellgardt, C. N. Markides, “an assessment of solar-powered organic Rankine cycle systems for combined heating and power in UK domestic applications”, Appl. Energy, 138, 605–620, 2015.

[3] J. H. Reif, W. Alhalabi, “Solar-thermal powered desalination: Its significant challenges and potential”, Renewable Sustainable Energy Rev., 48, 152–165, 2015.

[4] B. Peñate, L.G. Rodríguez, “Seawater reverse osmosis desalination driven by a solar Organic Rankine Cycle: Design and technology assessment for medium capacity range”, Desalination, 284, 86–91, 2012.

[5] G. Xia, Q. Sun, J. Wang, X. Cao, Y. Yu & L. Wang, “Theoretical analysis of a reverse osmosis desalination system driven by solar-powered organic Rankine cycle and wind energy”, Desalin. Water Treat., 53, 876–886, 2015.

[6] A. M. D. Torres, L.G. Rodriguez, “Design recommendations for solar organic Rankine cycle (ORC)–powered reverse osmosis (RO) desalination”, Renewable Sustainable Energy Rev., 16, 44– 53, 2012.

[7] S. Gorjian, B. Ghobadian, “Solar desalination: A sustainable solution to water crisis in Iran”, Renewable Sustainable Energy Rev., 48, 571–584, 2015.

[8] R. Z. Mathkor, B. Agnew, M. A. Al-Weshahi and F. Latrsh, “Exergetic Analysis of an Integrated Tri-Generation Organic Rankine Cycle”, Energies, 8, 8835-8856, 2015.

[9] A.S.Nafey , M.A.Sharaf, “Combined solar organic Rankine cycle with reverse osmosis desalination process: Energy, exergy, and cost evaluations”, Renewable Energy, 35, 2571-2580, 2010.

[10]D.W. Abueidda and M. Gadalla, “Thermodynamic Analysis of an Integrated Solar-Based Multi-Stage Flash Desalination System”, IMECE, USA, 2012.

[11] M. A. S. Eldean, H.E. Fath,” Exergy and thermo-economic analysis of solar thermal cycles powered multi-stage flash desalination process”, Desalin. Water Treat., 51, 7361–7378, 2013.

[12] A. Valero, L. Serra, J. Uche, “Fundamentals of Exergy Cost Accounting and Thermoeconomics”, Part I: Theory, J. Energy Resour. Technol., 128, 1-8, 2006.

[13] A. Valero, L. Serra, J. Uche, “Fundamentals of Exergy Cost Accounting and Thermoeconomics”, Part II:Applications, J. Energy Resour. Technol., 128 , 9-15, 2006.

[14] S. Keshavarzian, M. V. Rocco, “Emanuela Colombo, Thermoeconomic diagnosis and malfunction decomposition: Methodology improvement of the Thermoeconomic Input-Output Analysis (TIOA)”, Energy Convers. Manage., 157, 644-655, 2018.

[15] A. Valero, A. Abadías, “Thermoeconomic analysis of a cement production plant”, *29th international conference on efficiency, cost, optimization, simulation and environmental impact of energy systems*, Slovenia, 2016.

[16] J.A. Duffie, W.A. Beckman, *Solar Engineering of Thermal Processes*,John Wiley & Sons, Inc., 2006.

[17] S. A. Kalogirou, *Solar Energy Engineering Processes and Syste*ms, Second edition, Elsevier Inc, ISBN–13: 978-0-12-397270-5, 2014.

[18] S. Sadri, R. H. Khoshkhoo, M. Ameri, “Optimum exergoeconomic modeling of novel hybrid desalination system (MEDAD-RO)”, Energy, 149, 74-83, 2018.

[19] A. Valero, S. Usón, C. Torres and W. Stanek, *Theory of Exergy Cost and Thermo-Ecological Cost, chapter 7 of Thermodynamics for Sustainable Management of Natural Resources*, Springer International Publishing, ISSN 1865-3529, 2017.

[20] V.Verda, “Accuracy level in thermoeconomic diagnosis of energy systems”, Energy , 31:32 48–60, 2006.

[21] S. Keshavarzian, M. V. Rocco, E. Colombo, “Thermoeconomic diagnosis and malfunction decomposition: Methodology improvement of the Thermoeconomic Input-Output Analysis (TIOA)”, Energy Convers. Manage., 157, 644-655, 2018.

International Journal of Thermodynamics (IJoT)
ISSN 1301-9724 / e-ISSN 2146-1511
https://dergipark.org.tr/en/pub/ijot

Vol. 25 (No. 3), pp. 22-30, 2022
doi: 10.5541/ijot.1077697

Geothermal Well Exploration in Nigeria Using Remote Sensing and Modified Thermal Equations

M.E. Emetere*

Department of Mechanical Engineering Science, University of Johannesburg, South Africa
Physics Department, Covenant University, Ota, Nigeria
E-mail: emetere@yahoo.com

Received 23 February 2022, Revised 13 April 2022, Accepted 16 May 2022

Abstract

Based on the preliminary evidence of volcanoes, hot springs, and Geysers in parts of Nigeria, it is proposed that deep geothermal wells can be found in Nigeria. This research uses thermal anomalies zones to identify types of geothermal wells in Nigeria, i.e., using remote sensing and modified thermal equations. The remote sensing dataset includes the ground heat flux (GHF) dataset from Modern-Era Retrospective analysis for Research and Applications (MERRA) of 28 years; sediment thickness dataset from EarthData; and surface geology from LANDSAT. The thermal transport model was used to narrow potential locations across Nigeria using the ground heat flux and sediment thickness, while the surface geology was used to confirm the deep geothermal zones. Four GHF patterns were discovered in Nigeria. The research shows that the deep geothermal wells might be located in Plateau, Bauchi, Gombe, Taraba, Ekiti, Kogi, Benue, Nassarawa, and Taraba. Also, the medium-depth geothermal wells may be located in Sokoto, Zamfara, Kastina, Kwara, Oyo, and Jigawa States. It was revealed that the southern parts of Nigeria have lots of shallow geothermal wells. The deep geothermal wells can be found in the Chad Basin and Benue trough, while the medium-depth geothermal wells can be found in the Sokoto basin, Bida basin, and parts of the lower Benue trough. It is recommended that further ground trotting exploration be carried out in the identified geographical locations.

Keywords: *Ground heat flux; geothermal; energy; alternative energy.*

1. Introduction

Based on the preliminary evidence of volcanoes, hot springs, and Geysers in parts of Nigeria, it is logical to agree with the International Geothermal Association report on geothermal energy potential in Nigeria [1]. There are about ten warm springs in Nigeria, including Rafin Rewa Warm Spring, Ikogosi Warm Spring, Lamurde Hot Spring, Keane-Awe Thermal Springs, Akiri Warm Spring, Nike warm spring, Kerang warm spring, Ngeji warm spring, and Wikki Warm Spring. Also, there is a volcanic site in Plateau. Most of the warm spring and volcanic sites are located in the Cretaceous Benue Trough in the northern part of Nigeria [2]. In the southern parts, it has been postulated that the overpressured thick sediment strata are characterized by anomalous temperature gradients, which have influenced heat flow [3]. Detection of anomalous thermal zones to predict potential geothermal energy sites has been adopted in various studies [4]. Since the pioneering research on geothermal energy exploration using remote sensing to detect temperature anomalies [5], many research has followed the same route. The typical challenge in most studies using remote sensing to determine the temperature anomalies is the duplication of false sites due to prevailing climate change. This research seeks to adopt various techniques to streamline the false hot areas to reduce the high cost of unfruitful field exploration.

The geology of geothermal well is as confusing as exploring hydrocarbon deposition in some geographical regions. Geothermal wells found in Madrid between 1985-1990, show that it is usually a dependable reservoir in tertiary clastic host rocks at 1500-2000 m depths [6]. However, it was found that the ultra-deep geothermal horizons are within 3500-5000 m depth. At this point, the source and condensing temperatures are well above 160 oC and 65 oC, respectively. Significant pointers to the geothermal well discovery may occur synonymous with hydrocarbon exploration. For example, the sedimentary basin is usually the first geological pointer to hydrocarbon reservoirs in hydrocarbon exploration. Likewise, the significant geological features in geothermal well detection are synonymous with warm springs' geological features [7,8]. Shallow and medium depth geothermal wells are most times characterized by hydrothermal wells. The main geothermal well is located in the deep and ultra-deep seated geothermal environment. The popular technique for detecting geothermal wells is considering regions near active tectonic plate boundaries where volcanic activity has occurred, such as in Iceland, New Zealand, and the Philippines [9].

The geology of Nigeria is significant, and there are high prospects of discovering geothermal energy sources. Currently, the energy demands in Nigeria have risen high [10]. The primary sources of power (i.e., gas stations and hydroelectricity) in Nigeria may not be sufficient. The proposal for the nation to have main sources of energy across the geopolitical zones (Figure 1) would help reduce the high cost of transferring energy from one region to another. The geothermal energy source exploration is very important in the national energy drive because of the enormous energy

*Corresponding Author

accruable. Geothermal energy source (GES) exploration is very expensive using conventional techniques. Most conventional techniques are plagued with fundamental theoretical flaws [11]. These technical flaws have led to the frequent modification of its techniques when applied to various geological terrains.

The design, model, and optimization of ground heat exchangers depends on the undisturbed ground temperature (UGT), which is directly proportional to the subsurface layer's ground temperatures, which depend on the location's geology. Scientists believe that the thickness of the subsurface layer plays a vital role [12]. However, the geology and the components of the subsurface layer are vital for the thermal conservation and diffusivity of the ground. Over certain earth locations, the thermal inertia of the ground ensures the amplitude of changes in the ground temperature decreases with an increasing depth [13]. Several models have proved the relation between longwave and geothermal parameters. Some scientists have correlated UGT with meteorological parameters [14-15] and detailed models to show the advantage and disadvantages of UGT. Ultimately, the UGC is applied to projected to be essential for space heating via the use of heat pump systems (such as the ground-coupled heat pump systems (GCHPs)) to extract heat from the geothermal energy [16].

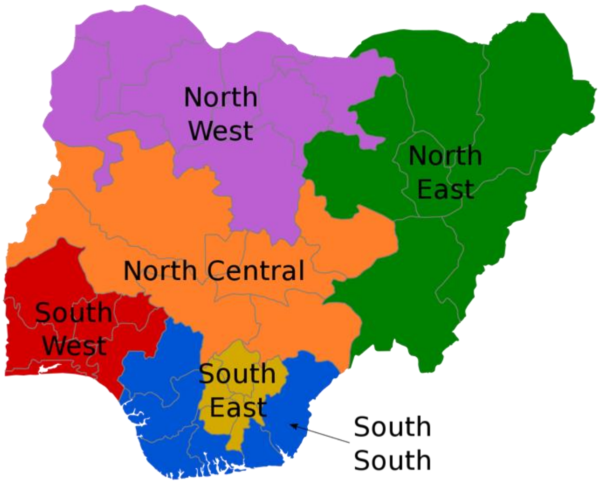

Figure 1. The geopolitical regions of Nigeria.

This study combines remote sensing and mathematical techniques for discovering geothermal wells and ground heat catchments. The limitation of this work is that the lithology is almost assumed to be equal over the same geological basin. The application of this work may be extended to the agricultural sector and planning for ground source heat pump systems.

2. Methodology

The different geology of Nigeria is presented in Figure 2. It has been discovered that the warm springs are located along the cretaceous rock (Figure 2). In this research, the satellite remote sensing technique was adopted. The satellite remote sensing technique (SRST) has shown high prospects for determining the geological features, hydrocarbon deposit, seepage, geothermal heat flux, ground heat flux, latent heat flux, etc. In this research, the ground heat flux was examined. Ground heat flux is an important component of the energy balance at the land surface, particularly over the relatively dry land surface and over a daily time scale. It is a reliable parameter that accounts for how the earth gives off and absorbs heat. The dataset was obtained from the NASA MERRA. The ground heat flux dataset for 1990-2017 was used for this study. Modified thermal equations were used to estimate geothermal temperatures in suspected GES in Nigeria.

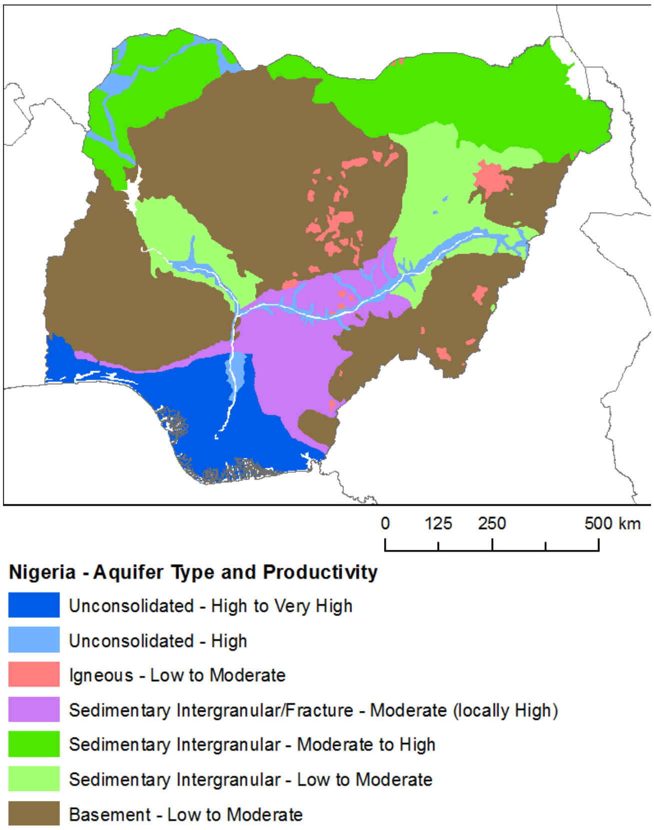

Figure 2. The geology of Nigeria.

The geothermal energy well stores heat in two major forms. The earth's surface acts as a very large collector of solar energy, where the energy radiated from the sun is stored below the earth's surface. Secondly, there is heat transferred from the belly of the earth's crust to the earth's surface. Therefore, one of the appropriate techniques to understand the heat variations in the aforementioned heat sources is the use of ground heat flux.

The power generation from this type of enhanced geothermal system is given as [17]:

$$E_w = \phi\left[\frac{h_w(\rho_i,\theta_i)}{v_w(\theta_i)} - \frac{h_w(\rho_f,\theta_f)}{v_w(\theta_f)}\right] = \left[\frac{h_{wi}}{v_{wi}} - \frac{h_{wf}}{v_{wf}}\right] \tag{1}$$

where h is the liquid enthalpy, i is the initial term, f is the final term, v is the liquid specific volume, p is reservoir pressures, ϕ is the porosity. The ground heat flux will give insight into the different enthalpy. Hence, the mathematical formula of ground heat flux is given as [18]:

$$H_G = -k\frac{\partial T}{\partial z} = \frac{\rho c \kappa A}{DRe\{1+i\}\exp(i\omega t)} = \rho c(\kappa\omega)^{0.5} A\cos(\omega t + \frac{\pi}{4}) \tag{2}$$

where T is the temperature of the ground (◦C); k is thermal diffusivity of the ground (m^2/s), z is the position coordinate, t is the time, ρ is the density of the medium, A is the amplitude of daily average temperature of the ground surface, ω is the frequency of temperature fluctuations.

The ground heat flux clearly shows the heat transfer and temperature distribution depends on the geological features (which includes rock conductivities). The conductivity is a composite rock (with grains arranged in parallel orientation (equation 3) and layered sequence perpendicular (equation 4) to the direction of heat flow) is given by [19]

$$K_p = n_1 K_1 + n_2 K_2 + n_3 K_3 + \cdots .... \qquad (3)$$

$$\frac{1}{K_s} = \frac{n_1}{K_1} + \frac{n_2}{K_2} + \frac{n_3}{K_3} + \cdots ..... \qquad (4)$$

Where K_p is the bulk parallel rock conductivity, n is the fractional volumes of mineral phases and K is the conductivities of minerals.
Hence, the sum of bulk series and parallel conductivities is given as [19]:

$$K_{ps} = \frac{1}{2}\left(K_p + K_s\right) \qquad (5)$$

The modified geothermal temperature T(z) can be estimated under steady-state conditions as [20]:

$$T(z) = T_s + \frac{q_s}{k} z - \frac{\rho A}{2k} z^2 \qquad (6)$$

where q_s is the ground heat flux, Ts is the surface temperature, A is the radioactive heat production, z is the depth, ρ density of medium and k is the thermal conductivity (3.138 $\text{Wm}^{-1\text{o}}\text{C}^{-1}$).

3. Results and Discussion

Figure 3a shows that high ground heat flux is observed in the northern region of Nigeria. However, a significant amount of ground heat flux was domiciled in the cretaceous rocks with possible extension into the neighboring Precambrian basement. This discovery may prove that the ground heat flux was more from within the earth's crust than the heat trapped by solar energy. Also, the warm spring locations were found to have high ground heat flux. Figure 3b shows a reversed ground heat flux pattern where southern Nigeria is found to have higher heat flux than northern Nigeria. This image shows the earth's crust ground heat signatures.

Figure 3c shows that the ground heat flux is diffuse with time from the region of higher ground heat flux signatures to regions of lower ground heat flux. It is noted that the geological cross-sectional profile of Nigeria allows for heat transfer with high convenience. Figure 3d showed a combination of the two sources of ground heat flux (GHF). Like Figure 3a, a significant amount of ground heat flux was found to be domiciled in the cretaceous rocks with possible extension into the neighboring Precambrian basement. Like Figure 3b, the GHF diffuses from the northern belt to the southern belt (Figure 3e). The GHF trend was found to repeat in Figures 3f -3i. Figures 3j and 3k had the same GHF trend but different patterns. The area of coverage was central Nigeria, which is mainly cretaceous. This result is the second GHF pattern in Nigeria. The GHF diffusion had the same pattern (Figure 3i). Figures 3l-3p had different GHF patterns that suggest sustained storage of solar energy. However, it is observed that the pattern is mainly in northern Nigeria. This result is the third GHF pattern in Nigeria. Figure 3q reveals the GHF diffusion towards the southern parts, while Figure 3r shows the higher GHF in the south. The geological possibility of this unique GHF pattern can be traced to the geological cross-section between Lagos and Port Harcourt (Figure 4) [21]. The profile is mainly Cenozoic, upper cretaceous, and lower cretaceous. This profile converges between Ondo and Delta states (Figure 1). Figures 3s-3x show the fourth GHF pattern where the GHF diffusion pattern is from south to northern Nigeria. Figures 3y-3ab show that the GHF activities are mainly in the central part of Nigeria. The central part includes Ekiti, Kogi, Benue, Nassarawa, and Taraba (Figure 1). Three of the identified warm spring lies in the Benue trough.

Therefore, with the GHF analysis of Nigeria, the first type of deep geothermal wells may be located in the following states, i.e., Plateau, Bauchi, Gombe, and Taraba. The second type of deep geothermal wells may be located in the following states i.e., Ekiti, Kogi, Benue, Nassarawa, and Taraba. Shallow geothermal wells mainly characterize the southern parts of Nigeria. Medium depth geothermal wells may be located in Sokoto, Zamfara, Kastina, Kwara, Oyo, and Jigawa.

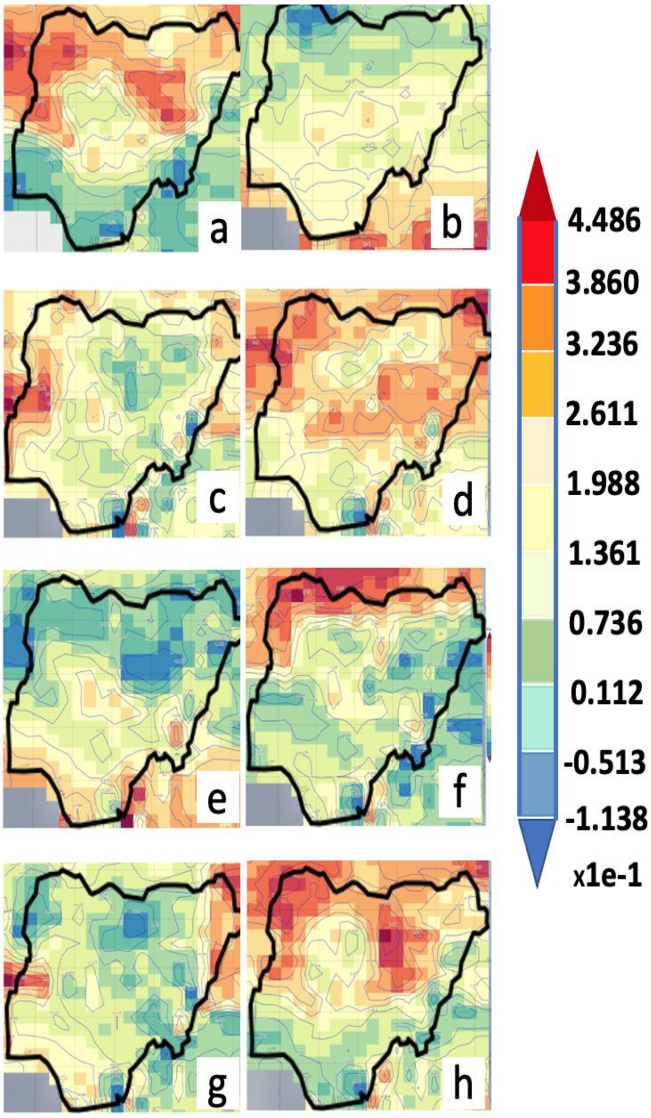

Figure 3. Ground heat flux analysis over Nigeria (1990-2017).

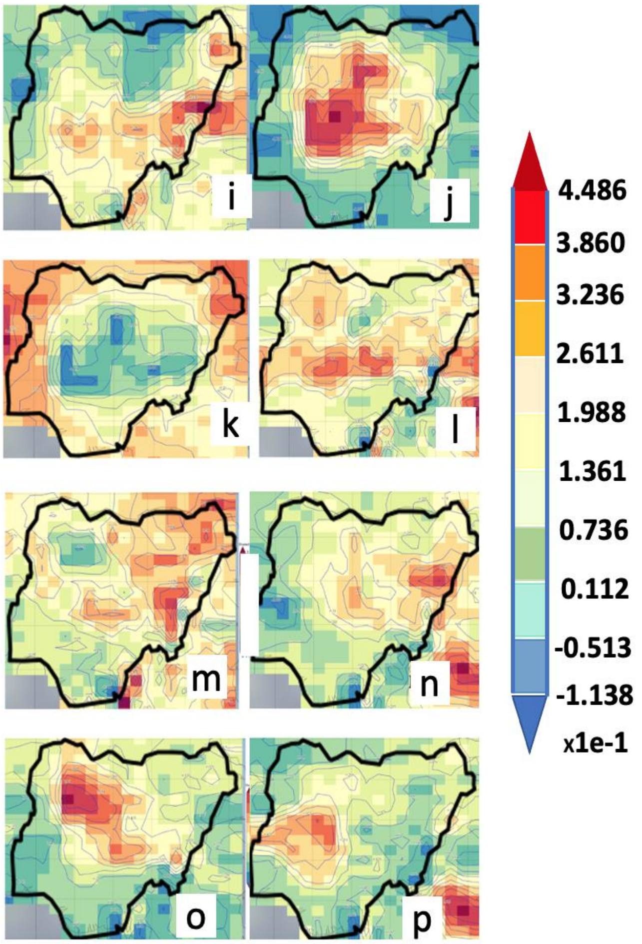

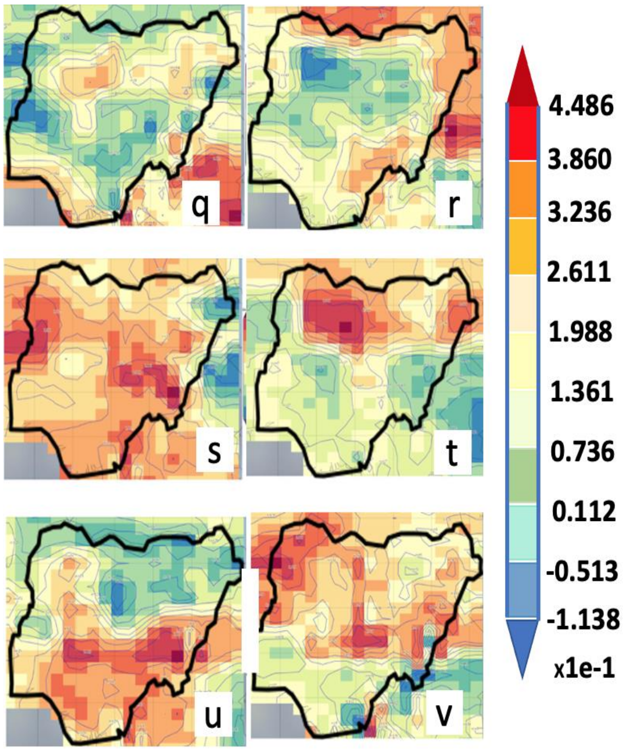

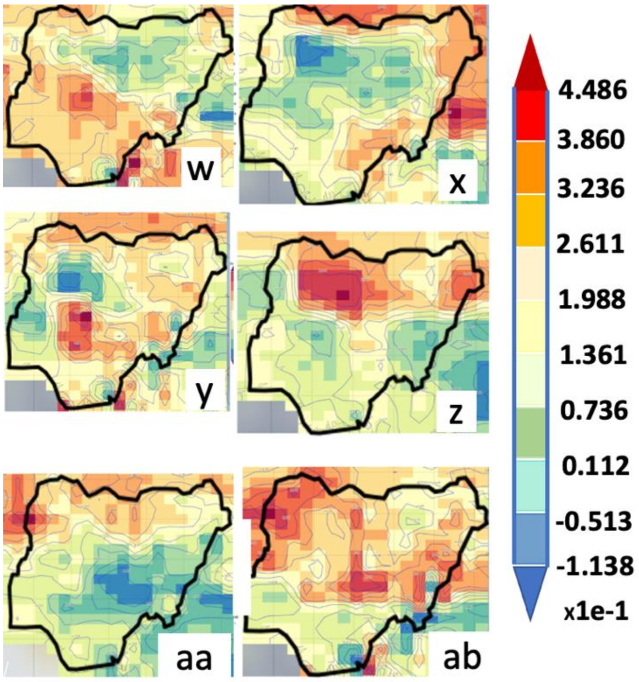

Figure 3. Ground heat flux analysis over Nigeria (1990-2017) (continue).

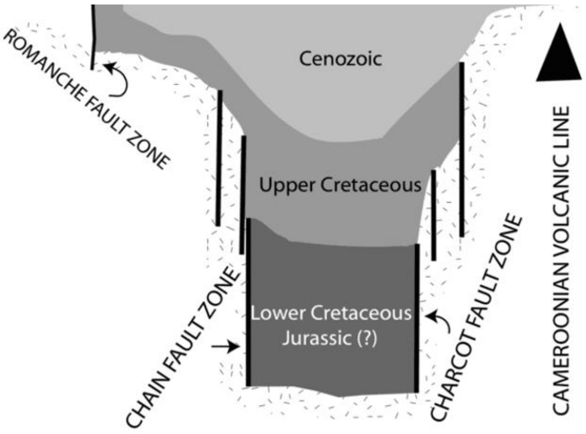

Figure 4. Geological cross-section of the lower south of Nigeria [21].

The geology of Nigeria is made up of four groups i.e., basement complex (Migmatite-Gneiss, schist belts, and pan-African Granitoids), Younger Granites (complexes of Triassic), sedimentary rocks and Tertiary volcanic rocks [22]. In most parts, the Schist belts are in-folded into the older Migmatite-Gneiss Complex in the southwestern part of Nigeria. Though, a small extension of the schist belts can be found in the southeastern part of Nigeria [23]. Also, schist belts of Nigeria are best developed in the northwest and southwestern portions of the country [24]. Hence, the connection of Ekiti and Ogun state in the league of geothermal wells in Nigeria. The Ogun geological profile includes porphyroblastic (Augen) gneiss, hornblende-biotite gneiss, banded gneiss and quartz schist [25]. Zamfara state has quartz-grain, very coarse-grained and fine-grained granitic rocks [26]. Sokoto state, which sits on the Sokoto basin (Figure 5), is characterized by: the Gundumi formation in the Lower Cretaceous; limestone in Kalambaina formation; clay beds in the Dange formation; fine gray sand of the Wurno formation; dark gray clay of the Taloka formations; and clay shale of the Dukamaje formation [27]. The Gundam formation has sedimentary rocks.

Generally, the Cretaceous and Tertiary formations in the Sokoto Basin are northeasterly and dip about 20 feet per mile to the northwest [27]. Bauchi and Jigawa states sit on the Chad basin (Figure 5). It is comprised of: shale and sandstone in the Bima formation; sandstones and bluish-black shale (calcareous) in the Gongila formation; Cretaceous sediments in the Kerri-Kerri formation [28]. The composition of the Kerri-Kerri formation includes coarse-grained sandstones, clayey grits, siltstones and clay stones. The Gombe sandstone is mainly folded at the end of the Cretaceous [29]. The geological of Kogi state is made up of migmatite and mica schist, granitic suite (i.e. fine- medium-grained granite, granodiorite and porphyritic granite) [28].

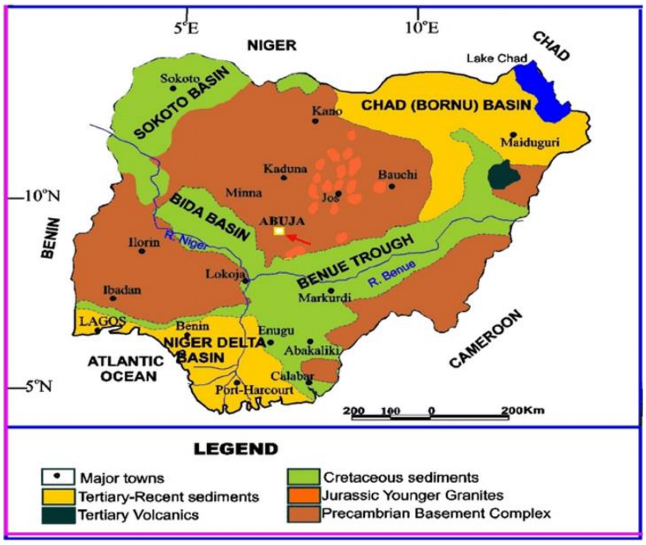

Figure 5. The basins and trough in Nigeria [30].

The rock formation in Kwara includes migmatitic gneiss, quartzite, quartz-mica schist, talc-tremolite schist, porphyroblastic granite, porphyritic granite, coarse-grained alkali granite, medium-grained granodiorite, medium-grained alkali granite, alkali syenite, pegmatite/aplite and vein quartz [21, 31]. Taraba and Benue state sits on the Benue Trough. It is characterized by: volcanic rocks (basalts suite, olivine basalt, and trachyte basalt); shallow subsurface structures (faults and dykes); and basaltic intrusions [32]. These formations support locations in the Benue trough (such as Benue and Taraba States) as places of potential deep geothermal wells. Via the connection in the Gongola sub-basin and the Benue trough (Figure 5), it is easy to understand the inclusion of Gombe state as a place of potential deep geothermal wells. Plateau state is reported to have rock formations such as alkaline feldspar granites, rhyolites, vom microgranite, biotite suite, shen hornblende – fayalite granite, minor gabbros and syenites [33, 34]. More so, this results from sub-volcanic intrusive complexes of ring dykes and related annular and cylindrical intrusions [35]. The basement complex in Nassarawa State has the following rock formations: Pelitic schist - amphibolite, granodiorite gneiss, plagioclase feldspar, quartz, muscovite, biotite, lepidolite and tourmaline [36].

The analysis of the geothermal temperature across the geological basins over Nigeria was calculated as presented in Figure 6. The sediment thickness was adopted in place of depth.

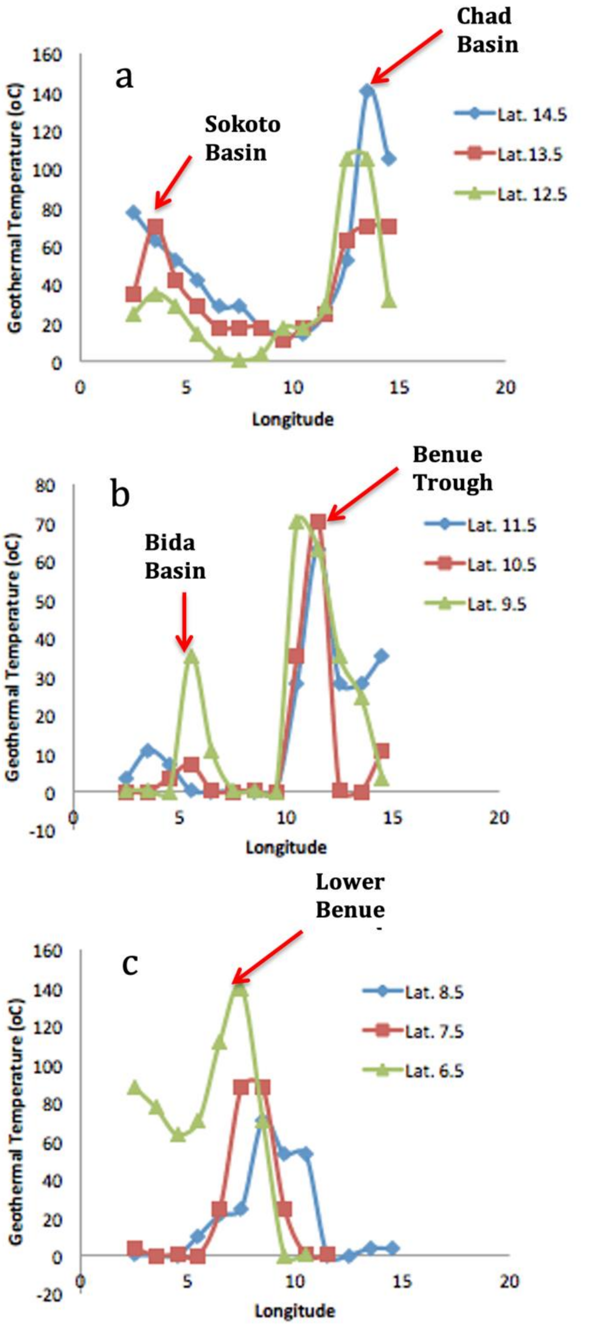

Figure 6. Analysis of geothermal temperature in Nigerian basin (a) Sokoto basin, (b) Bida basin, (c) Lower basin.

The sediment thicknesses over the Nigerian basin were obtained from the Marine Geoscience Data System. It is salient to note that the sediment thickness can be used to find the minimum geothermal temperature, not the exact temperature. This result is because the conductivities of the rock formations over the location are quite important to estimate the exact geothermal energies. In this calculation, q_s = 1.674, Ts =26.8^{o}C, A =0.28, ρ =0.68 kg/m^3 and k = 1.24 Wm^{-1o}C^{-1}. Figure 6a affirmed that States in the Chad and Sokoto basins would have a geothermal well. However, States in the Chad basins are likely to have deep geothermal wells, while States in the Sokoto basin may have medium-depth geothermal wells. These results agree with the remote sensing results presented above. Figure 6b affirmed that States in the upper Benue trough and Bida basin would have geothermal wells. While Bida is likely to have medium-depth geothermal wells, the upper Benue trough would certainly have deep geothermal wells. These results agree with the remote sensing results presented above. Figure 6c affirmed that States in the Lower Benue trough would likely have deep and medium-depth geothermal wells. These results agree with the remote sensing results presented above.

4. Landsat imagery of surface geology

Ground temperature at a depth of 2 meters can be used to delineate relatively hot areas or thermally anomalous zones related to subsurface geothermal features [37]. Likewise, the Landsat imageries can be used to determine the hot areas or thermally anomalous zones as they are useful techniques in geology for interpretation of hydrothermal alteration, lithological discrimination, and tectonic setting [38-39]. The imagery was an integration of Landsat 7 (ETM +) and 8 (OLI) outcomes with an accuracy of 95%. The satellite images were obtained from the United States Geological Survey (USGS). Typically, Landsat 8 has 11 image bands taken 250 scenes a day, whereas Landsat 7 only has 8 image bands.

Five locations were considered out of the nine highlighted locations from the previous sections. Figure 7 is the LANDSAT imagery in parts of Gombe. The objective of this section was to determine the thermally anomalous zones related to subsurface geothermal features from the LANDSAT image slicing, as presented in Figures 7-11. In Gombe State, the red arrows identified the thermally anomalous zone at the northeast section of the map. Different authors postulate the various features of the thermally anomalous zones. Garibaldi et al. [40,41] proposed that the thermally anomalous zones lie along the fault and permeable zones. Mao and Li [42] proposed that the thermally anomalous zones lie along the uplift zones.

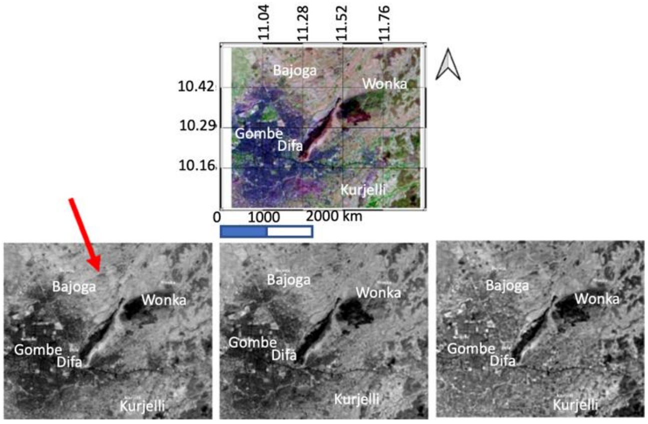

Figure 7. Slice of LANDSAT imagery in Gombe

In addition to the above, the determination of thermally anomalous zones in this section identifies isolated fault zones. Few of the isolated fault zone close to the uplift zone close to the uplift zone was identified as the potential thermally anomalous zones related to subsurface geothermal features. For example, the isolated fault zone was used to determine the thermally anomalous zone in Gombe, Bauchi, and Benue as presented in Figures 7-9.

The isolated fault zones close to uplift zones were used to identify the thermally anomalous zone in Ikogosi (Figure 11). This method was used to identify potential deep geothermal wells close to Pankshin in Plateau State. Figure 10 shows that the location has no significant thermally anomalous zone. In other words, a location may have potential mineral deposits but not have features of geothermal wells. Hence, this section has corroborated the findings highlighted in the previous sections.

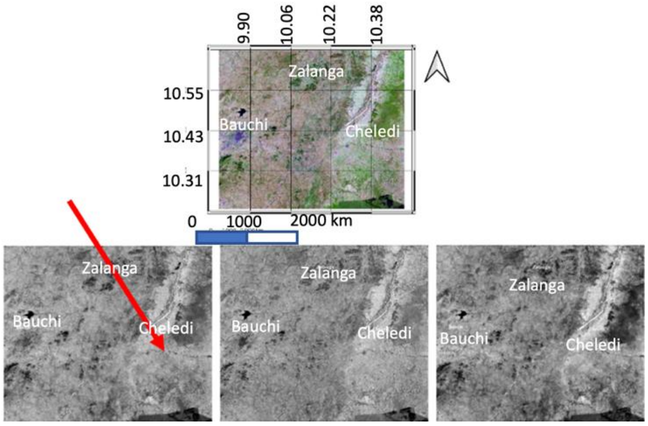

Figure 8. Slice of LANDSAT imagery in Bauchi

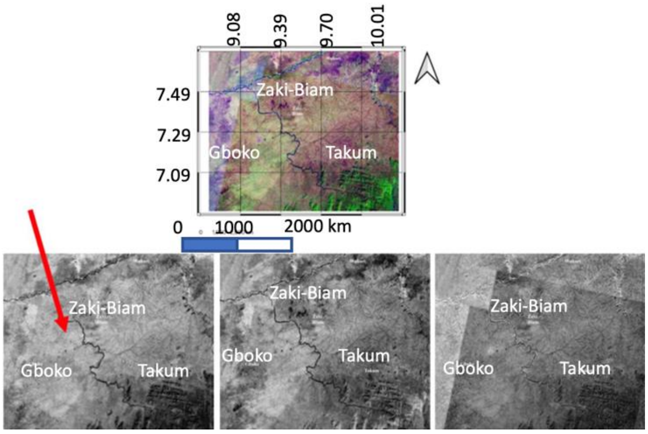

Figure 9. Slice of LANDSAT imagery in Benue

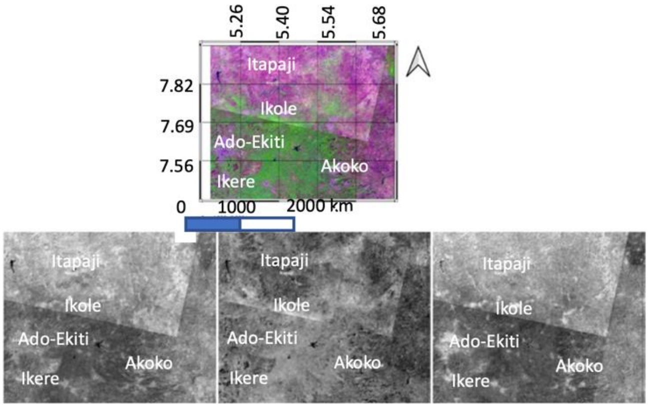

Figure 10. Slice of LANDSAT imagery in Ekiti

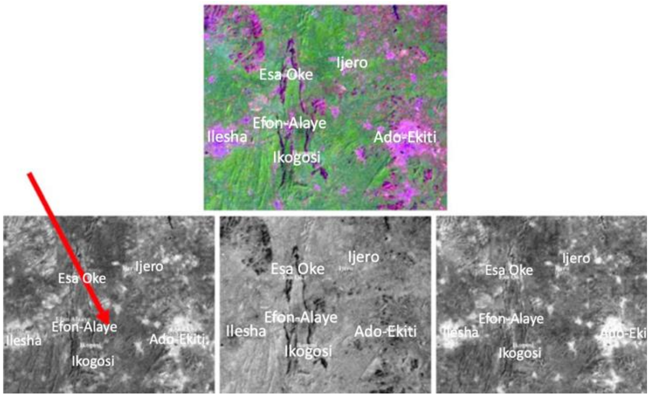

Figure 11. Slice of LANDSAT imagery in Ikogosi

In summary, the twenty-eight years ground heat flux dataset from the MERRA gave insight into surface thermal variability, which is not dependent on the thickness of the subsurface layer alone, but on the near-surface geology of the location. The thicknesses of the sediments in each location were obtained from the NASA satellite. The model was used for geothermal temperature expected at the sediment thicknesses along several transverses of the study location. This procedure helped classify prospective shallow, medium, and deep geothermal across the study location. The LANDSAT imagery was used to differentiate between medium and deep geothermal wells over the study location. The results from the study corroborate existing aeromagnetic over selected locations in the study area, such as Ikogosi [43], Sokoto Basin [44], and Wikki [45].

5. Conclusion

The research has revealed that the shallow, medium-depth and deep geothermal wells can be obtained in various locations in Nigeria. The deep geothermal wells may be located in Plateau, Bauchi, Gombe, Taraba, Ekiti, Kogi, Benue, Nassarawa and Taraba using remote sensing. It was revealed that the southern parts of Nigeria have lots of shallow geothermal wells. The remote sensing results also showed that the medium depth geothermal wells might be located in Sokoto, Zamfara, Kastina, Kwara, Oyo, and Jigawa States. Using the modified thermal equations, it was observed that deep geothermal wells could be found in the Chad Basin and Benue trough, while the medium-depth geothermal wells can be found in Sokoto basin, Bida basin and parts of the lower Benue trough. These results agree with the remote sensing results. It is recommended that further ground trotting exploration be carried out in the identified geographical locations.

Acknowledgements:

The author appreciates NASA for the satellite imagery and the Marine Geoscience Data System for the dataset.

Nomenclature

h	*liquid enthalpy,*
i	*initial term,*
f	*final term,*
v	*liquid specific volume,*
p	*reservoir pressures,*
ϕ	*porosity.*
T	*temperature of the ground (◦C)*
k	*thermal diffusivity of the ground (m^2/s)*
z	*position coordinate*
t	*time*
ρ	*density of the medium*
A	*amplitude of daily average temperature of the ground surface*
ω	*frequency of temperature fluctuations*
K_p	*bulk parallel rock conductivity*
n	*fractional volumes of mineral phases*
K	*conductivities of minerals*
$T(z)$	*modified geothermal temperature*
q_s	*ground heat flux*
Ts	*surface temperature*
A	*radioactive heat production*
z	*depth*
ρ	*density of medium*
k	*thermal conductivity (3.138 Wm^{-1o}C^{-1})*

References:

[1] International Geothermal Association -IGA (2020). *Geothermal outlook in East Africa: Perspective for Geothermal Development. (Presentation by P. Omenda, Director IGA; Consultant).* Available: https://www.irena.org/publications/2020/Nov/Geothermal-Development-in- Eastern-Africa. (accessed October 14, 2020)

[2] E. M. Abraham, E. E. Nikitnam, “Review of geothermal energy research in Nigeria: The Geoscience Front,” *International Journal of Earth Science and Geophysics*, 3, 1 – 10, 2017.

[3] I.M. Okiyi, S.I. Ibeneme, E.Y. Obiora, S.O. Onyekuru, A.I. Selemo, “Evaluation of geothermal energy resources in parts of southeastern sedimentary basin, Nigeria,” *Ife Journal of Science,* 23(1), 195 -211, 2021.

[4] R. G. Vaughan, L. P. Keszthelyi, J. B. Lowenstern, C. Jaworowski, H. Heasler, “Use of ASTER and MODIS thermal infrared data to quantify heat flow and hydrothermal change at Yellowstone National Park,” *Journal of Volcanology and Geothermal Research*, 233–234, 72-89, 2012

[5] D. T. Hodder, “Application of remote sensing to geothermal prospecting,” *Geothermics*. 2, 368-380, 1970.

[6] P. Ungemach, R. Hidalgo, J. S. Sanchez, “Multiple Use Assessment of the Madrid Basin (Spain) Geothermal Potential,” *Proceedings World Geothermal Congress 2010 Bali, Indonesia,* 25-29 2010

[7] A. Chiasson, “The economic, environmental, and social benefits of geothermal use in the eastern United States,” *Geo-Heat Center Quarterly Bulletin*, 30(2), 1-5, 2011.

[8] E.M. Abraham, E.E. Nkitnam, “Review of Geothermal Energy Research in Nigeria: The Geoscience Front,” *Int J Earth Sci Geophys* 3, 15-19, 2017.

[9] Geoscience Australia, *Geothermal Geology,* Available: http://www.ga.gov.au/scientific-topics/energy/resources/geothermal-energy-resources/geothermal-geology (Accessed October 14, 2019)

[10] M.E. Emetere, U. Okoro, B. Etete, and G. Okunbor, “Free energy option and its relevance to improve domestic energy demands in southern Nigeria,” *Energy Reports*, 2, 229–236, 2016.

[11] M.E. Emetere, “Modified satellite remote sensing technique for hydrocarbon deposit detection,” *Journal of Petroleum Science and Engineering*, 181, 106228, 2019.

[12] M. Gwadera, B. Larwa, and K. Kupie, “Undisturbed Ground Temperature—Different Methods of Determination,” *Sustainability*, 9, 2055, 2017.

[13] Y. Li, S. Geng, X. Han, H. Zhang, F. Peng, “Performance evaluation of borehole heat exchanger in multilayered subsurface,” *Sustainability,* 9, 356, 2017.

[14] C.O. Popiel, J. Wojtkowiak, “Temperature distributions of ground in the urban region of Poznan City,” *Exp. Therm. Fluid Sci*., 51, 135–148, 2013.

[15] M. Badache, P. Eslami-Nejad, M. Ouzzane, Z. Aidoun, “A new modeling approach for improved

ground temperature profile determination," *Renew. Energy*, 85, 436–444, 2016.

[16] I. Sarbu, C. Sebarchievici, "General review of ground-source heat pump systems for heating and cooling of buildings," *Energy Build*, 70, 441–454, 2014.

[17] P. Ungemach, M. Papachristou and M. "Antics (2007), Renewability versus Sustainability. A Reservoir Management Approach," *Proceedings European Geothermal Congress*. Available: http://www.geothermal-energy.org/pdf/IGAstandard/EGC/2007/216.pdf

[18] A. J. Purdy, J. B. Fisher, M. L. Goulden, J. S. Famiglietti, "Ground heat flux: An analytical review of 6 models evaluated at 88 sites and globally," *JGR: Biogeosciences*, 121(12), 3045-3059, 2016.

[19] E. C. Robertson, "Thermal Properties of Rocks, United States Department of The Interior Geological Survey," *Virginia, Open-File Report*, 88-441, 1988.

[20] H. N. Pollack, D. S. Chapman, "On the regional variation of heat flow, geothermal, and the thickness of the lithosphere," *Tectonophysics*, 38, 279-296, 1977.

[21] M.L.W. Tuttle, R.R. Charpentier, M.E. Brownfield, "The Niger Delta Petroleum System: Niger Delta Province, Nigeria, Cameroon, and Equatorial Guinea, Africa," Available: https://pubs.usgs.gov/of/1999/ofr-99-0050/OF99-50H/OF99-50H.pdf (Accessed 5th Oct., 2019)

[22] R. Caby, J.M. Boesse, "Pan African Nappe System in southwest Nigeria: The Ife-Ilesha schist belt," *J. Afr. Earth Sci.*, 33, 211-225, 2001.

[23] A. Ibrahim, A. Toyin, Z.J. Sanni, "Geological Characteristics and Petrographic Analysis of Rocks of Ado-Awaiye and its Environs, Southwestern Nigeria," *International Journal of Applied Science and Mathematical Theory*, 1(8), 28-47, 2015.

[24] H.M. Sadiq, A. Zarma, "Depth to Magnetic Sources Using Spectral Analysis of High Resolution Aeromagnetic Data Over Machina and Environs, Northeastern Nigeria," *Journal of Geography and Geology*, 11, 70-78, 2019.

[25] N.G. Obaje, "Geology and mineral resources of Nigeria," *Springer Dordrecht Heidelberg London New York*, 221, 2009.

[26] A.F. Folorunso, E.A. Ayolabi, S. Ariyo, "Geological mapping, petrological study and structural analysis of Precambrian basement complex rocks in part of Ago-Iwoye Southwestern Nigeria," *International Research Journal of Geology and Mining*, 3(1), 19-30, 2013.

[27] A. I. Chinwuko, U.A. Danbatta, I. Shaibu, M.O. Ovwasa, A.M. Shuaibu, "Geological Mapping of Basement Rocks in Federal University Gusau And Its Environs, Zamfara State, Northwestern Nigeria," *IOSR Journal of Applied Geology and Geophysics*, 6(1), 32-42, 2018.

[28] H.R. Anderson and W. Ogilbee, "Aquifers in the Sokoto Basin, Northwestern Nigeria, With a Description of the General Hydrogeology of the Region," *Geological Survey Water-Supply*, 1757, 1-79, 1973.

[29] O.A. Boboye, A.F Abimbola, "Hydrocarbon Potential of the Lithostratigraphic Units in Late Cenomanian-Early Paleocene Shale, Southwestern Chad Basin," *World Applied Sciences Journal*, 7 (5), 567-573, 2009.

[30] Jotscroll (2019), "The Benue Trough and Economic Importance," Available: https://www.jotscroll.com/forums/3/posts/153/the-benue-trough-and-economic-importance.html (Accessed 12th October, 2019).

[31] M.S. Kolawole, M. Onimisi, S.B. Olobaniyi, "Field occurrence and structural characteristics of basement rocks around Kabba-bunu area in part of Kabba-Lokoja-Igarra Schist belt, southwestern Nigeria," *Global Journal of Pure And Applied Sciences*, 23, 263-274, 2017.

[32] J. Ajadi, S.S. Dada, P.N. Nnabo, B.A. Owoeye, "Lithostructural description and metallogeny of Alagbede gold deposit, West Central Nigeria," *Journal of Environment and Earth Science*, 8(5), 115-132, 2018.

[33] E.A. Igwe, J.A. Yakubu, I.U. Ileagu, "Investigation of Mambila Plateau In North Central Part of Nigeria For Potential Minerals Using Aeromagnetic Method," *IOSR Journal of Applied Geology and Geophysics*, 6, 10-22, 2018.

[34] O. I. Ejeh, C.F. Ugbe, "Fracture systems in the younger granite rocks around four, northern Nigeria: Product of residual stress?" *Global Journal of Geological Sciences*, 8, 57-64, 2010.

[35] M. O. Lekdukun, F. A. Akpah and F. X. O. Ugodulunwa, "A Geoelectrical Investigation of Groundwater Potentials in Dorowa and its Environs, Plateau State, North Central Nigeria, Journal of Geography," *Environment and Earth Science International*, 2(2), 65-76, 2015.

[36] I.Y. Tanko, M. Adam, P.D. Dambring, "Field Features And Mode Of Emplacement of Pegmatites of Keffi Area, North Central Nigeria," *International Journal Of Scientific & Technology Research*, 4, 214-229, 2015.

[37] M.F. Coolbaugh, C. Kratt, A. Fallacaro, W.M. Calvin, J.V. Taranik, "Detection of geothermal anomalies using Advanced Spaceborne Thermal Emission and Reflection Radiometer (ASTER) thermal infrared images at Bradys Hot Springs, Nevada, USA," *Remote Sensing of Environment*. 106(3), 350-359, 2007.

[38] J.C. Thouret, "Volcanic geomorphology—an overview," *Earth- Science Rev*, 47 (1–2), 95–131, 1999.

[39] M. Kervyn, F. Kervyn, R. Goossens, S.K. Rowland, G.G.J. Ernst, "Mapping volcanic terrain using high-resolution and 3D satellite remote sensing," *Geol Soc*, 2007, 5–30, 1999.

[40] C. Garibaldi, G.F. Laurent, G.F. Laurent, l. Jean-Marc, P. Ledru, "Thermal anomalies and geological structures in the Provence basin: Implications for hydrothermal circulations at depth," *Bulletin de la Societe Geologique de France*, 181(4), 363-376, 2010.

[41] C. Garibaldi, L. Guillou-Frottier, J-MLardeaux, V. Bouchot, “Combination of Numerical Tools to Link Deep Temperatures, Geological Structures and Fluid Flow in Sedimentary Basins: Application to the Thermal Anomalies of the Provence Basin (South-East France),” *World Geothermal Congress*, 7, 00496212, 2010.

[42] M. Xiaoping and K. Li, “Main Controlling Factors of Regional High Geothermal Anomaly,” *43rd Workshop on Geothermal Reservoir Engineering Stanford University, Stanford, California*, SGP-TR-213, 2018.

[43] M.A. Ema, M.L. Kolawole, C.E. Amobi, A. Owens, A.M. Kehinde, A.L. Aminu, “Spectral analysis of aeromagnetic data for geothermal energy investigation of Ikogosi Warm Spring - Ekiti State, southwestern Nigeria,” *Geothermal Energy*, 2(1), 6, 2014.

[44] T. Suleiman, F. N. Okeke, N.D. Obiora, “Spectral Analysis of High-Resolution Aeromagnetic Data for Geothermal Energy Reconnaissance across Sokoto Basin, Northwest, Nigeria,” *Journal of the Earth and Space Physics*, 46(4), 147-158, 2021.

[45] E.O. Grace, M.L. Kolawole, A.A. Lawal, “Spectral analysis of aeromagnetic data for geothermal investigation of Wikki Warm Spring, north-east Nigeria,” *Geothermics*, 50, 85-90, 2014.

International Journal of Thermodynamics (IJoT)
ISSN 1301-9724 / e-ISSN 2146-1511
https://dergipark.org.tr/en/pub/ijot

Vol. 25 (No. 3), pp. 032-039, 2022
doi: 10.5541/ijot.1085553

Calculation of the Thermodynamic Quantities for Cubic Gauche Nitrogen (cg-N)

H. Yurtseven [1*] and Ö. Akay [1, 2]

[1]Department of Physics, Middle East Technical University, 06531, Ankara-Turkey
[2]Department of Mechatronics Engineering, Faculty of Technology, Marmara University, Istanbul, -Turkey
E-mail: *hamit@metu.edu.tr

Received 10 March 2022, Revised 23 May 2022, Accepted 21 June 2022

Abstract

This work aims to investigate the thermodynamic properties of the cubic gauge nitrogen (cg-N) by calculating the relevant thermodynamic quantities as a functions of temperature and pressure. The thermodynamic quantities of volume (V), thermal expansion (α_p), isothermal compressibility (κ_T), bulk modulus(B), and the heat capacity (C_p) are calculated as a function of temperature at constants pressures (0, 35, 125, 250 GPa) for the cg-N structure. Also, the pressure dependences of V, κ_T, α_p, C_p and γ (macroscopic Grüneisen parameter) are predicted at T= 295 K for this structure. This calculation is caried out by the thermodynamic relations using some literature data. From our calculations, we find that the κ_T, α_p and also B exhibit anomalous behavior as the temperature lowers below about 100 K at constant pressures studied. This is an indication that cg-N transforms to a solid phase at low temperatures (below about 100 K). Experimental measurements can examine this prediction when available in the literature for the cg-N phase. Also, our predictions of the κ_T, α_p, C_p and γ at various pressures (T= 295 K) can be examined experimentally for the cg-N phase. This calculation method can be applied to some other structures.

Keywords: *Thermodynamic quantities; cubic gauche nitrogen; macroscopic Grüneisen parameter.*

1. Introduction

A number of molecular solids are known to undergo a transition to a nonmolecular phase under high compression [1]. Among those structures, nitrogen consists of molecules with the two atoms which are strongly triple-bonded [2]. Higher pressure transitions with the diatomic molecular state have been studied [3-5] as pointed out previously [6]. In particular, pressure-volume relations, thermal expansion coefficients, phase transition pressures and temperatures have been determined by the Monte Carlo method [3]. It has been indicated that in the pressure region of 10-100 GPa by the Raman, infrared and x-ray measurements the structural properties depend on the kinetics of the experiment and on the P_T path [5]. Pressure-induced dissociation forming a polymeric phase called cubic-gauche (cg-N) was found [2], which is a three-dimensional network structure with the $I_{2,3}$ symmetry as predicted by the theoretical calculations[7,8] as reported in an earlier study [6]. Monte Carlo calculations have been caried out for the atomic, molecular, and compressed forms of the nitrogen [8] and for the calculations of the molecular and nonmolecular structures of nitrogen, the local- density- functional method has been used [9] and the cg-N has been observed experimentally [1,7,9-11]. At high pressures and temperatures, T-P phase diagram including the phases θ and i solid nitrogen has been obtained experimentally [10]. Also, experimental measurements have been conducted to determine the P-T path [11]. It has been indicated that the cg-N represents a new class of single-bonded nitrogen material with unique properties such as energy capacity [2]. It has also been indicated that polymeric nitrogen with a cg- structure grows in single crystals if the pressure-temperature conditions are close to the boundary of molecular nitrogen cg-N [12]. As pointed out previously[13], the predicted [7] transition pressure (50 ± 15 GPa) for the formation of polymeric cg-N from molecular nitrogen falls within the region of metastability, cg-N will persist at low pressures and temperatures. Compared to the simple cubic (sc) structure which was found to be mechanically unstable over the entire pressure range considered, the cg structure was found to be metastable over a pressure range up to 360 GPa [13]. Experimentally, by the x-ray diffraction of nitrogen at pressures up to 170 GPa it has been pointed out that the transformation of the diatomic phase into the single-bonded(polymeric) phase, which is the cg-N structure proceeds as a first order transition with the volume change [4]. Also, by the x-ray diffraction, it has been shown that the amorphous nature of the semiconducting nonmolecular material transforms to the crystalline cg-N phase on heating above 2000K, this indicates a sequence of transitions associated with the molecular to atomic transition of solid nitrogen [14].

Regarding the thermodynamic properties of the cg- N high-pressure phase diagram of nitrogen has been calculated [15]. This connects the observed molecular to cg-N polymer phase transition in the solid at 110GPa, to a liquid-polymer phase line which was obtained from the shock cooling measurements. For the polymeric structures of nitrogen(cg-N), calculation of the variation of enthalpy with the pressure up to 90 GPa [6]and 400 GPa[16] has been reported. Also, the coexistence line of molecular and polymeric cg-N has been predicted and, the phase transition parameters, latent heat, volume and entropy jumps have been calculated [17].

---

*Corresponding Author

Table 1. Values of the coefficients for the volume V(T) and for the bulk modulus B(T) according to Eqs.(1) and (6), which were fitted to the thermal expansivity $V_0(T)$ and the bulk modulus K_0 (T) data [18], respectively, at P=0 for the cg-N, as also given in our previous study[20].

V(T) ($Å^3$)	V_0 ($Å^3$)	$-\alpha x10^{-6}$ ($Å^3/K$)	$\beta x10^{-7}$ ($Å^3/K^2$)	B(T) (GPa)	κ_0 (GPa)	$-\alpha' x10^{-3}$ (GPa/K)	$-\beta' x10^{-5}$ (GPa/K^2)
Eq.(1)	52.47	4.73	7.63	Eq.(6)	298.28	9.1	1.3

Regarding more recent studies on the cg-N structure, unusual high- pressure cg-N was experimentally synthesized and the first-principle calculations were performed [21]. Molecular and polymeric cg has been predicted by the equations of state, and the phase transition parameters (latent heat, volume and entropy) were calculated [22]. In relation to the cg-N structure, another nitrogen-based solid of N_8 molecular crystal (stable at ambient pressure) has been predicted [23]. Several phases of nitrogen including highly energetic phase, covalently bound cg-N have been studied by density functional theory (DFT)[24].Polymeric cg-N phase has been studied by the molecular dynamics and metadynamic simulations [25]. Also, using the first-principle calculations the thermodynamic and kinetic stabilities in polymorphs and cg-N have been investigated [26]. Experimentally, x-ray diffraction measurements of nitrogen also for the cg covalent solid have been performed [27]. Using DFT, single-bonded 3D nitrogen allotrope (cg-N) has been studied [28]. Experimentally study on the phase transition from cg-N to LPN (post-layered polymeric nitrogen) has been reported [29]. Very recently, solid nitrogen and nitrogen- rich compounds [30], cg phase in highly compressed nitrogen solid has been studied [31].

Over the years, various aspects of the cg-N have been studied both experimentally and theoretically as stated above. However, the thermodynamic properties of the cg-N structure have been explained to some extend in some earlier studies as stated above, when compared to the well-known solid phases (α,β,γ at low temperatures and ε, δ, υ, ξ at high pressures) of N_2 in the P-T phase diagram [10]. This has motivated us to study the cg-N phase exhibiting interesting features regarding its thermodynamic quantities which differ from those in the solid phases of N_2. From this point of view, by using some literature data, those thermodynamic quantities of interest are calculated at various temperatures and pressures for the cg-N structure. Regarding some earlier studies [18,20], the present work gives the calculation method of those thermodynamic quantities at higher pressures as well as their temperature dependence at zero pressure in the cg-N structure. Considering the pressure effects which changes the critical behavior of those thermodynamic quantities (mainly κ_T, α_p and B) at various temperatures in the cg-N phase, their pressure dependence has not been investigated extensively in the earlier works [18,20]. The pressure dependence as studied here, is also the principal improvement and contributions to the thermodynamic properties of the cg-N structure. For the high-pressure studies, it is important to achieve the cg-N structure as the most stable phase which has been obtained experimentally [2,12]. Thus, it was obtained experimentally that by the existence of the stable cg-N phase, the transition from the molecular phase to the polymeric form of nitrogen was realized. This states that investigation of the thermodynamic properties of the cg-N phase becomes important, particularly, at high pressures. This is the main objective of the present study. In particular, due to the literature data available our interest is focused on the calculation of the temperature and pressure dependence of the volume (V), thermal expansion (α_P), bulk modulus (B), isothermal compressibility (κ_T), specific heat (C_P) and the macroscopic Grüneisen parameter (γ) in the cg phase of nitrogen. For this calculation, the thermodynamic data obtained at constant pressures(0,35, 125 and 250 GPa) at 295 K [18] and for the V-P calculation (T=295 K) the experimental data [12] are used.

2. Calculation Methods

The temperature and pressure dependence of the volume for the cg-N was analyzed by using the thermodynamic data to calculate the thermodynamic quantities in this system. Our hypothesis for this calculation was to write the temperature and pressure dependence of the volume for the cg-N phase in the simplest functional form in order to explain the experimental measurements of V(T) and V(P). Therefore, they were expressed in the quadratic form. Also, our hypothesis was to use the quadratic form for the other thermodynamic quantities, namely, bulk modulus B(T) and heat capacity $C_v(T)$ to describe the cg-N phase

2.1 Temperature dependence of the thermodynamic quantities

The temperature dependence of the volume for the cg-N can be analyzed at constant pressures according to

$$V(T) = V_0 + \alpha T + \beta T^2 \tag{1}$$

where V_0 , α and β are constants. In Eq.(1), those constants represent nonlinear variation of the volume with the temperature (in the quadratic form). So that V_0 is the volume at the absolute temperature(T=0), α and β are the linear and nonlinear (quadratic) variations of the volume with the temperature, respectively (α is the volume per degree and β is the volume per degree squared). By means of the definition of the thermal expansion, in thermodynamics as $\alpha_P \equiv (1/V)\,(\partial V/\partial T)_P$, its temperature dependence is obtained from Eq.(1),

$$\alpha_P = \frac{\alpha + 2\beta T}{V_0 + \alpha T + \beta T^2} \tag{2}$$

Also, the temperature dependence of the isothermal compressibility κ_T can be obtained from the definition of the slope dP/dT of the transition line in the P-T phase diagram for the cg-N in the polymeric phase using the thermodynamic identity

$$dP/dT = \alpha_P/\kappa_T \tag{3}$$

By knowing the V, α_P and κ_T ,the temperature dependence of the heat capacity C_P can be obtained through the thermodynamic relation,

$$C_P = C_V + TV\,({\alpha_P}^2/\kappa_T) \tag{4}$$

This gives rise to the macroscopic Grüneisen parameter by the definition in the thermodynamics as

$$\gamma= (V/C_V)(\alpha_P/\kappa_T) \tag{5}$$

The temperature dependence of the isothermalcompressibility K_T (=1/B) which is the inverse bulk modulus B and the temperature dependence of the specific heat C_V can be analyzed by expressing

$$B(T) = \kappa_0 + \alpha' T + \beta' T^2 \tag{6}$$

And

$$C_V(T) = e_0 + e_1 T + e_2 T^2 \tag{7}$$

respectively, where $\kappa_0, \alpha', \beta'$ and e_0, e_1, e_2 are constants. In Eq.(6), the constants κ_0 defines the bulk modulus B(T) at the absolute zero(T=0), the coefficients α' and β' represent per unit degree (linear variation) and B(T) per unit degree squared (quadratic variation), respectively. Similarly, for the heat capacity C_v(T) in Eq.(7), e_0 is the C_v at T=0, e_1 and e_2 are the coefficients of the C_v per degree and per degree squared, respectively, as for the nonlinear terms of V(T) (Eq.1) and B(T) (Eq.6). On the basis of the experimental measurements of the V(T), α_p(T), dP/dT, C_p(T) and B(T) through the expressions (Eq. 1,2,3,4 and 6), those constants and variables become significant, and they need to be determined. The temperature dependence of the C_p, isothermal bulk modulus K(T) and thermal expansion α(T) have been given in the polynomial form for the melting of β-quartz previously [32]. However, their expressions for those thermodynamic quantities include terms such as T^{-1}, T^{-2} etc., which characterize rather different behavior for melting. We have given our relations (Eqs. 1,6 and 7) with the thermodynamic relations (Eq.4) for the cg-N phase in our earlier study [20].

2.2 Pressure dependence of the thermodynamic quantities

Pressure dependence of the thermodynamic quantities can also be analyzed for the cg-N at room temperature. As we stated for the V(T), B(T) and C_v, the pressure dependence of V(P) and k_T , our hypothesis was to express them in the simplest functional form. Thus, by writing the V(P) in quadratic form, the pressure dependence of the α_p, C_p and γ were obtained in order to describe the experimental measurements of those quantities accordingly n the cg-N phase. We have also given Eqs.(8) and (11) for the cg-N structure in our previous study [20]. Volume can be expressed as a function of pressure as

$$V(P) = b_0 + b_1 P + b_2 P^2 \tag{8}$$

where b_0, b_1 and b_2 are constants. In this equation, the coefficient b_0 is the volume at zero pressure (P=0), b_1 and b_2 are the volume per unit pressure and the square of the pressure, respectively. Those constants (b_0, b_1 and b_2) are also significant as determined from the V-P measurements in the cg-N structure. Thus, from the V-T measurements through Eq.(1) and also using V(P) relation (Eq.8) the P-T phase diagram with the slope dP/dT (Eq.3) can be determined in the cg-N phase. Thus, from Eq.(8) the isothermal compressibility κ_T can be obtained by using the definition $\kappa_T \equiv (-1/V)\,(\partial V/\partial P)_T$ as

3. Results

For the temperature dependence of the thermodynamic quantities, the volume was first analyzed according to Eq.(1), as also analyzed previously with the values given [18] at

$$\kappa_T = -\frac{b_1+2b_2P}{b_0+b_1P+b_2P^2} \tag{9}$$

Also through Eq.(3), the pressure dependence of the thermal expansion can be written as

$$\alpha_P = -(dP/dT)\left(\frac{b_1+2b_2P}{b_0+b_1P+b_2P^2}\right) \tag{10}$$

This provides the pressure dependence of C_P-C_V according to the thermodynamic relation (Eq.4). Finally, by knowing the pressure dependence of those quantities Eq.(4), macroscopic Grüneisen parameter (γ) can be calculated at various pressures (Eq.5).

Table 2. Values of the thermal expansion (α_p),bulk modulus (B), the slope dP/dT in the P-T phase diagram and the macroscopic Grüneisen parameter γ at T=295 K (P=0) for the cg-N. We also give the values of the volume V calculated from the equations indicated at constant pressures (T= 295 K).

P=0	α_px10^{-5} (K^{-1})	B (GPa)	(dP/dT)x10^{-3} (GPa/K)	γ	T= 295 K	V(Å^3) P=0	V(Å^3) P=35 GPa	V(Å^3) P=125 GPa
T=295 K	0.81	294.46	2.385	3.35	Eq.(1)	7.44	6.00	5.54
					Eq.(8)	6.77	6.08	5.14

Table 3 Values of the coefficients e_0, e_1 and e_2 for the specific heat $C_V(T)$ according to Eq.(7) which was fitted to the C_V-T data [18] at the pressures indicated for the cg-N.

P (GPa)	$-e_0$ (J/mol.K)	e_1 (J/mol.K^2)	$-e_2 x10^5$ (J/mol.K^3)
0	18.72	0.16	5.77
5	18.41	0.18	7.72
25	19.06	0.21	10.3
50	16.59	0.22	11.9

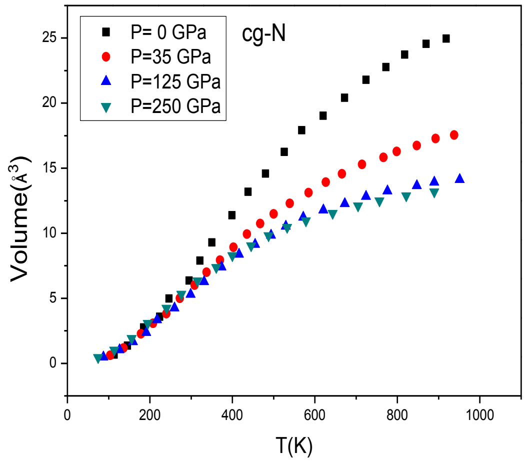

Figure 1 Volume as a function of temperature according to Eq.(5) through Eq.(3) using the C_v data [18] for the cg-N.

various temperatures (P=0) for the cg-N. For this analysis and in the simulations, we used the computer programme of OriginLab. Values of the coefficients of V(T) are given in Table 1, as also given in our previous study [20]. The temperature dependence of the bulk modulus (B) (=1/κ_T) was then analyzed according to Eq.(6) as also analyzed in our previous work [20] by using the bulk modulus K_0 data [18] (P=0) with the coefficients determined (Table 1) in the cg-N phase. This provided us to determine the slope value of dP/dT (Eq.3) in the P-T phase diagram of the cg-N phase by using the values of α_P and B at P=0, T=295 K. The values of the thermal expansion α_P , bulk modulus B and the dP/dT value at T=295 K (P=0) are given in Table 2. By analyzing the C_V(T) data [18] at P= 0 according to Eq.(7), the coefficients e_0, e_1 and e_2 , were determined, as given in Table 3. Also, by analyzing the V(P) data [12] at T=295 K according to Eq.(8) the values of b_0, b_1 and b_2 were obtained. (Table 4). This enabled us to evaluate the macroscopic Grüneisen parameter γ (Eq.5) by using the values of V(=b_0), C_V and dP/dT (Table 2) at P=0 (T=295 K), which we is given in Table 2.

At constant pressures of 35, 125 and 250 GPa, the γ values were also evaluated(Eq.5) by using the V(P) [12] and the C_V data [18] with constant dP/dT value (Table 2). For this calculation, the C_V data were analyzed according to Eq.(7) for the pressures considered with the coefficients of e_0, e_1 and e_2 which were determined , as given in Table 3. By means of the γ values determined, the temperature dependence of the volume V(T) was then calculated using the C_V data with the constant dP/dT (Table 2) at the pressures of 0, 35, 125 and 250 GPa, as plotted in Figure 1. Values of the coefficients for V(T) for constant pressures studied according to Eq.(1), are given in Table 5. From the temperature dependence of the volume V(T) (Figure 1), the thermal expansion α_P was obtained according to Eq.(2) as a function of temperature at the pressures of 0, 35, 125 and 250 GPa, as plotted in Figure 2. This also gave us the temperature dependence of the isothermal compressibility κ_T (Eq.3) where dP/dT value (Table 2) was used, and the bulk modulus B(T) was obtained at constant pressures, as plotted in Figures 3 and 4, respectively. By knowing the temperature dependence of V(T), α_P and κ_T (Eq.3) and using the C_V(T) data , the specific heat C_p was then predicted at constant pressures of 0, 35, 125 and 250 GPa according to Eq.(4) for the cg-N, as plotted in Figure 5.

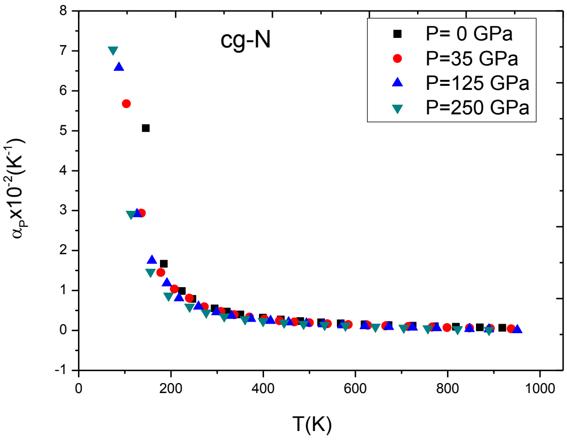

Figure 2 Thermal expansion α_P as a function of temperature (Eq.2) at the pressures indicated for the cg-N.

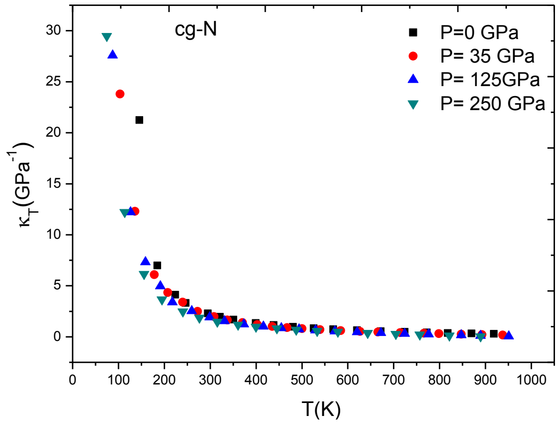

Figure 3 Isothermal compressibility κ_T as a function of temperature (Eq.3) at constant pressures indicated for the cg-N.

Regarding the pressure dependence of the thermodynamic quantities for the isothermal compressibility of the cubic structure a/a_0 lattice parameter data [18] were used at various pressures (at T=295 K) for κ_T as defined above with the a/a_0 using

$$\kappa_T/\kappa_0 = b_0{}' + b_1{}'P + b_2{}'P^2 \qquad (11)$$

where $b_0{}'$, $b_1{}'$ and $b_2{}'$ are constants, the pressure dependence of the volume can be then calculated according to

$$lnV(P) = -\int_0^{P_0} b_0{}'\,dP - \int_0^{P_0} b_1{}'\,PdP - \int_0^{P_0} b_2{}'\,P^2 dP \qquad (12)$$

Table 4 Values of the coefficients b_0, b_1 and b_2 of the volume V(P) which was fitted to the V-P data [12] at T=295 K according to Eq.(8). The coeffcients b_0', b_1' and b_2' of the isothermal compressibility κ_T/κ_0 (normolized) were obtained by fitting Eq.(11) to the lattice parameter a/a₀ data [18] at T=295 K for the cg-N.

V(P) (Å³)	b_0 (Å³)	$-b_1x10^{-2}$ (Å³/GPa)	b_2x10^{-5} (Å³/ GPa²)	κ_T/κ_0	b_0'	$-b_1'x10^{-4}$ (GPa⁻¹)	$b_2'x10^{-6}$ (GPa⁻²)
Eq.(8)	6.77	2.22	7.35	Eq.(11)	0.99	7.4	1.06

where P_0=250 GPa. The lattice parameter (a/a₀) data were then analyzed for the normalized κ_T/κ_0 with the coefficients determined (Table 4), as also given in our previous work [20]. In Figure 6, the volume V(P) deduced from κ_T/κ_0(Eq.11) is plotted according to Eq.(12) with the observed V-P data [12] at 295 K. With the constant dP/dT value (Table 2), the pressure dependence of the thermal expansion α_P (Eq.3), and the bulk modulus B were obtained. α_P and κ_T are plotted as a function of pressure (T=295 K) in Figures 7 and 8, respectively. Similarly, from the pressure dependence of V, α_P, κ_T and the C_V data, the specific heat C_P was calculated (Eq.4) at constant pressures of 0,35,125 and 250 GPa, as plotted in Figure 9. Finally, the macroscopic Grüneisen parameter γ was calculated at those constant pressures according to Eq.(5) using the calculated values of V, α_P, κ_T and the C_V data , as plotted in Figure 10. Note that for the analysis of the B(T) (Eq.6), C_V(T)(Eq.7), V(P) (Eq.8) and κ_T/κ_0(Eq.11), we also used the programme (OriginLab) in our simulations.

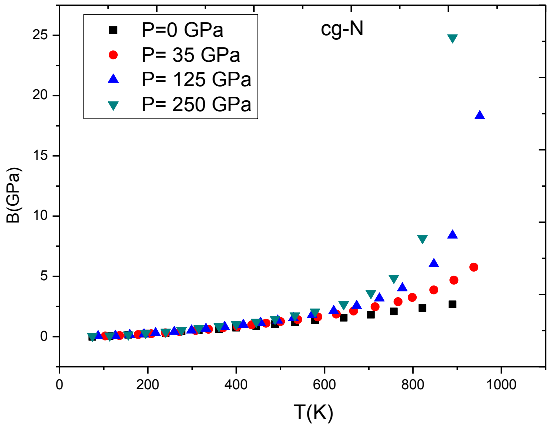

Figure 4 Bulk modulus B(T) as a function of temperature according to B(T)=1/κ_T (Eq.3) at the pressures indicated for the cg-N.

4.Discussion

Volume V(T) which was calculated at various temperatures, decreases as the pressure increases for the cg-N (Figure 1). Pressure effects considerably from 0 to 35 GPa, whereas its effect becomes insignificant above 125 GPa for the cg-N. Above the room temperature (T=295 K), the volume values are separated considerably as the pressure increases up to 125 GPa (Figure 1). The temperature dependence of the thermal expansion α_P(Figure 2) and isothermal compressibility κ_T (Figure 3)at the pressures of 35 ,125 and 250 GPa, exhibit similar critical behavior as in the zero pressure for the cg-N. They decrease as the temperature increases up to 1000K. An abrupt decrease in the α_P and κ_T occurs just above about 100K in the cg-N at constant pressures indicated (Figures 2 and 3). Since a constant slope value of dP/dT (Table 2) was considered in the P-T phase diagram of the cg-N according to Eq.(3), the same critical behavior was obtained at the pressures of 0, 35, 125 and 250 GPa as expected. As shown in Figures 2 and 3, calculated α_P and κ_T, decreasing with increasing temperature exhibit similar critical behavior which is independent of the pressures (0, 35, 125 and 250 GPa) for cg-N. This is also expected since the temperature increases the volume and it decreases the compressibility of the structure in the cg phase of nitrogen, as also indicated previously [18].Also, at ambient pressure and low temperature nitrogen freezes into a diatomic solid where strongly covalent (N≡N) N_2 molecules are weakly (van der Waals) bonded to each other as stated in an earlier study[13]. On the other hand, the bulk modulus B and the specific heat capacity C_P increase as the temperature increases as shown in Figures. 4 and 5, respectively. An abrupt increase of B occurs at about 900 K (Figure 4). The pressure does not effect on the B(T) up to about 600 K above which the diverging behavior seems to occur with the larger values as the pressure increases (Figure 4). Instead of anomalous behavior of the α_P (Figure 2) and κ_T (Figure 3) and B (Figure 4), the heat capacity C_p increases monotonically as the temperature increases with the larger C_p values at higher pressures (Figure 5).

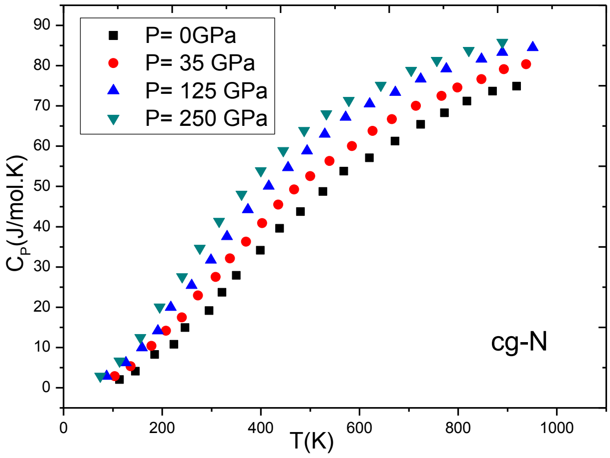

Figure 5 The specific heat as a function of temperature (Eq.4) by using the V(T) values (in this study) and the C_V(T) data[18] at the pressures indicated for the cg-N.

Our value of dP/dT= 2.385x10⁻³ GPa/K for the cg-N which we obtained, can be compared with the experimental value of dT_m/dP=35K/GPa or dP/dT_m=0.029 GPa/K up to 50 GPa for the melting temperature of the solid-liquid transition in nitrogen [33]. We see that our calculated value of dP/dT for the cg-N phase is much smaller (one order of magnitude) than the experimental value of the melting point in nitrogen.

Regarding the pressure dependence of the volume V (Figure 6), κ_T/κ_0(Figure 7), α_P(Figure 8), and γ (Figure 10), calculations indicate that they decrease whereas C_P (Figure 9) increases with the pressure increasing from 0 to 250 GPa at T=295 K in the cg-N. As pointed out previously [18] under the compression, crystalline atomic structure develops and the formation of nonmolecular single bonded polymorphs involves the dissociation of the extremely strong triple N≡N bond into three weaker single N-N bonds [12]. This is in accordance with the theory which predicts dissociation of the molecule and formation of monatomic phases similar to those observed in group V elements such as phosphorus and arsenic, as also pointed out in an earlier study [13]. At extremely high pressures nitrogen is predicted to occur in the simple cubic structure instead of cg-N structure[13]. Since the α_P, κ_T , C_P and γ were calculated by using the C_V data at constant pressures of 0,35,125 and 250 GPa (T=295K), plots (Figures 7-10) were restricted to the four data points only, which still give the general trend. As seen from Figure 6, the volume calculated (Eq.12) as a function of pressure at T= 295 K agrees with the observed data [12]. In this plot, the curve represents the best fit to the experimental data according to Eq.(8) with the coefficients determined (Table 4). Note that in Figure 7, the isothermal compressibility κ_T was normalized (κ_T/κ_0) since the κ_T was analyzed by using the normalized lattice parameter data normalized (a/a_0)[18] for the cg-N at 295 K. As in the case of the normalized isothermal compressibility (Figure 7), the pressure dependence of the α_P(Figure 8) and C_P (Figure 9) can be compared when the measured thermodynamic data become available in the literature for the cg-N. This examines whether our calculated thermodynamic quantities (κ_T/κ_0, α_P, and C_p) at various pressures (T=295 K) for the cg-N structure are adequate which also validate our simulations procedure. For the calculation of κ_T/κ_0, α_P, and C_p, we started with the V(P) relation (Eq.12) which was fitted to the observed volume data [12) satisfactorily (Figure 6). On the basis of the experimental data as our reference, decreasing κ_T/κ_0,(Figure 7) and α_P (Figure 8), and increasing C_p (Figure 9) with the increasing pressure (T= 295 K) are then expected for the cg-N. Regarding the temperature dependence of the thermodynamic quantities, we started with the calculation of V(T) at constant pressures(0, 35,125, 250 GPa), as plotted in Figure 1. The V(T) calculation was also based on the experimental V(P) data [12] which were fitted (Eq.8) as stated above (Figure 6). By obtaining the temperature dependence of the thermodynamic quantities (C_v, α_P, κ_T and γ) , V(T) was calculated through Eq.(5) at constant pressures studied as plotted in Figure 1. The calculated volume V(T=295 K) at P=0, 35 and 125 GPa (Figure 1) can be compared with those V(P) at T=295 K (Figure 6). They were deduced from Eqs. (1) and (8) with the values in Tables 5 and 4, respectively, as given in Table 2. Those volume values are comparatively close to each other with the errors of 0.67 (P=0), 0.08 (P= 35 GPa) and 0.39 Å^3 (P=125 GPa). This small discrepancy between our calculated V(T) values at constant pressures (0, 35,125 and 250 GPa) and the observed V(P) data (T=295 K) [12], as shown Figures. 1 and 6, respectively, indicates that our results are validated for the cg-N structure.

Regarding the temperature dependence of α_P, κ_T, B and C_p, as plotted in Figures 2,3,4 and 5, respectively, they were originally extracted from the V(T) which was calculated at constant pressures studied (Figure 1), as stated above. Because of the fact that our calculated V(T) at P=0 (Figure 1) agrees with the observed V(P) at T= 295 K (Figure 6), predicted values of those thermodynamic (α_P, κ_T, B and C_p) should be acceptable at P=0. At higher pressures (35,125 and 250 GPa), our calculated values should also be reasonably well as compared with the experimental measurements for the cg-N structure when available in the literature. Our predictions are therefore important in the sense that they give an initiative for the experimental measurements to describe the cg-N structure thermodynamically.

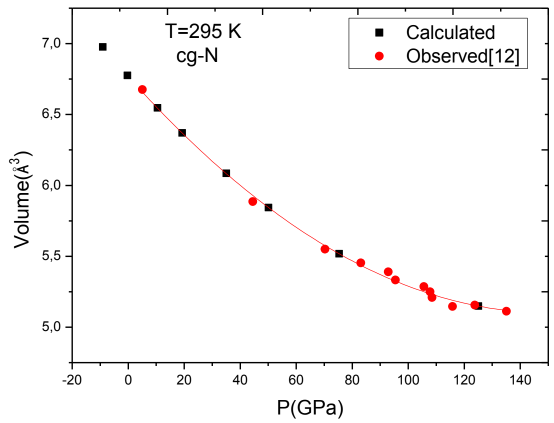

Figure 6 Volume V(P) at various pressures (Eq.12) using the (a/a_0) lattice parameter data [18] for the cg-N (T= 295 K). Solid line represents the best fit to the observed data [12] as shown (Eq.8) with the coefficients determined (Table 4).

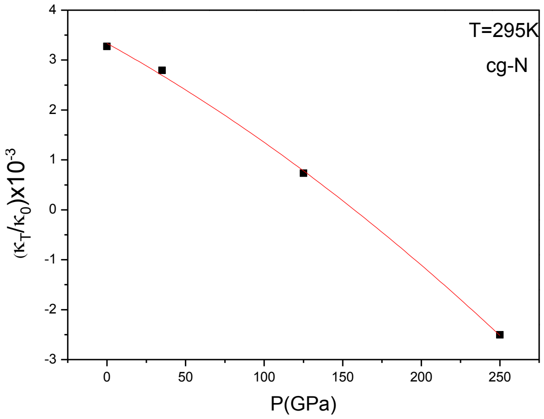

Figure 7 The isothermal compressibility κ_T/κ_0 (normalized) as a function of pressure (T=295 K) according to Eq.(11) for the cg-N. Solid line represents the best fit to the κ_T/κ_0 values with the coefficients determined (Table 4).

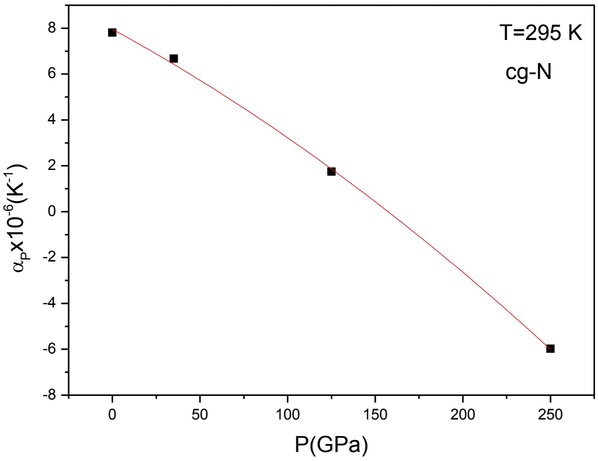

Figure 8 Thermal expansion α_p as a function of pressure (T=295 K) according to Eq.(3) from the normalized isothermal compressibility κ_T/κ_0 for the cg-N. Solid line represents the best fit to α_p values.

As mentioned above for the V(P) at T=295 K (Figure 6), our fit (Eq.8) to the observed data [12] is reasonably good. Similar fit was conducted for the powder and single crystal of the cg-N structure by using the Birch-Murnaghan (BM) equation of state (EOS) [12]. This shows that our V(P) calculation on the basis of the P-V measurements, can be compared with the Birch-Murnaghan EOS for the cg-N structure.

On the basis of the V(P) fit to the experimental data (Figure 6), the pressures dependences of κ_T/κ_0 (Figure 7), α_P(Figure 8), C_P (Figure 9) and γ (Figure 10), which we predicted for the cg-N structure, are expected to agree with the experimental measurements (the macroscopic Grüneisen parameter should be calculated from the measured V, C_p, α_P, κ_T according to Eq.5) when available in the literature, as stated above.

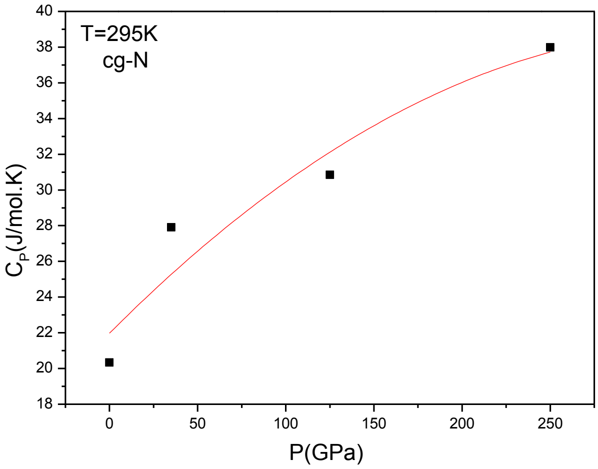

Figure 9 Specific heat C_P calculated as a function of pressure at T=295 K (Eq.4) using the C_V data [18] for the cg-N. Solid line represents the best fit to the C_P values (Eq.4).

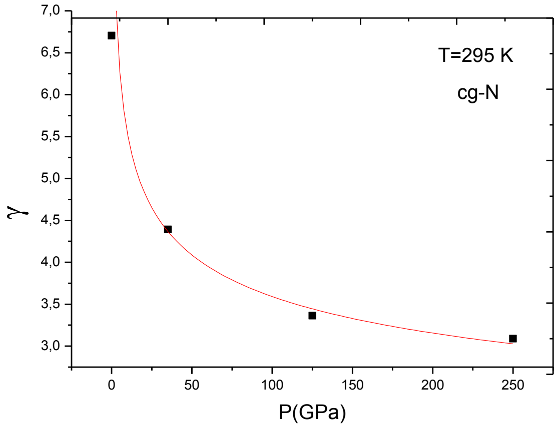

Figure 10 Macroscopic Grüneisen parameter as a function of pressure (Eq.5) using the C_V-P data [18] at T=295 K for the cg-N.

5.Conclusions

Temperature dependence of the thermodynamic quantities the volume (V), thermal expansion (α_P), isothermal compressibility (κ_T) bulk modulus (B), heat capacity (C_P) and the macroscopic Grüneisen parameter (γ) were calculated at constant pressures (0,35,125 and 250 GPa) for the cg-N. The pressure dependences of the κ_T, α_P and C_p and γ were also calculated at room temperature (T=295 K) for this structure. By assuming the polynomial (quadratic) form of V(T) and V(P), those calculations were performed through the thermodynamic relations using the thermodynamic data from the literature, in particular, for the V(T), B(T) at zero pressure and C_v(T) at constant pressures which were considered for the cg-N phase.

Our results show that the increase in the V(T) at the higher pressures, tends to lower as compared to the V(T) at P=0. Additionally, the temperature dependence of α_P and κ_T decreases anomalously starting from nearly T= 100 K at constant pressures studied. This indicates that the cg-N phase undergoes to a solid phase at low temperatures (below~100 K). Calculated thermodynamic quantities which were obtained in this study can be compared with the measured thermodynamic data for the cg-N when available in the literature.

As we started from the V(T) at zero pressure to calculate the temperature dependence of the thermodynamic quantities at constant pressures, which were presented in this study also by starting from the V(P) at room temperature, those thermodynamic quantities can be calculated at higher constant temperatures for the cg-N structure by the same calculation method given here. This can be considered as a future work for the cg-N phase. This method of calculating the thermodynamic quantities can be applied to some other structures.

Nomenclature

B	bulk modulus
C_p	heat capacity
C_v	specific heat capacity
K	bulk modulus
P	pressure
T	temperature
V	volume
κ_T	isothermal compressibility
α_P	thermal expansion
γ	macroscopic Grüneisen parameter

Greek letters

α , β, γ, ε, δ, υ, ξ	phases of solid nitrogen

References:

[1] A.F. Goncharov, E. Gregoryanz, H.K. Mao, Z. Liu and R.J. Hemley, “Optical Evidence for a Nonmolecular Phase of Nitrogen above 150 GPa,” *Phys.Rev.Lett.*, 85, 1262-1265, 2000.

[2] M. I. Eremets, A. G. Gavriliuk, I. A. Trojan, D. A. Dzivenko and R. Boehler, “Single-bonded cubic form of nitrogen,” *Nat. Mater.*, 3, 558-563, 2004.

[3] J.Belak,R.Lesar and R.D. Etters, “Calculated thermodynamic properties and phase transitions of solid N_2 at temperatures 0≤*T*≤300 K and pressures 0≤*P*≤100 GPa,” *J.Chem. Phys.*, 92, 5430-5441,1990.

[4] M. I. Eremets, A. G. Gavriliuk,N.R. Serebnianaya, I. A. Trojan, D. A. Dzivenko,R. Boehler, H.K. Mao and R.J. Hemley, "Structural transformation of molecular nitrogen to a single-bonded atomic state at high pressures," *J.Chem. Phys.*, 121, 11296-11300, 2004.

[5] E.Gregoryanz,A.F. Goncharov,R.J. Hemley, H.K. Mao,"Raman spectra and lattice dynamics of cubic *gauche* nitrogen," *Phys.Rev. B*,64, 0520123-1-4, 2001.

[6] R.Caracas and R.J. Hewley, "New structures of dense nitrogen: pathways to the polymeric phase," *Chem Phys. Lett.*, 442, 65-70,2007.

[7] C.Mailhiot,L.H. Yang and A.K. McMahan, "Polymeric nitrogen,"Phys.Rev. B, 46 ,14419-14435,1992.

[8] L.Mitas and R.M. Martin, "Quantum Monte Carlo of nitrogen: Atom, dimer, atomic, and molecular solids," Phys. Rev. Lett., 72, 2438-2441,1994.

[9] R.M. Martin and R.J. Needs, "Theoretical study of the molecular-to-nonmolecular transformation of nitrogen at high pressures," Phys. Rev. B, 34,5082-5092,1986.

[10] E. Gregoryanz,A.F. Goncharov, R.J. Hemley, H.K. Mao, M. Somayazulu and G. Shen, Raman, "infrared, and x-ray evidence for new phases of nitrogen at high pressures and temperatures," Phys. Rev. B ,66, 224108-1-5, 2002.

[11] M. I. Eremets, R.J. Hemley, H.K. Mao and E. Gregoryanz, "Semiconducting non-molecular nitrogen up to 240 GPa and its low-pressure stability," Nature, 411, 170-174, 2001.

[12] M. I. Eremets, A. G. Gavriliuk and I. A. Trojan, "Single –crystalline polymeric nitrogen," Appl.Phys.Lett., 90 ,171904-1-4,2007.

[13] T.W. Barbee III, "Metastability of atomic phases of nitrogen," Phys.Rev. B, 48, 9327-9330, 1993.

[14] E.Gregoryanz, A.F. Goncharov, C.Sanloup, M.Somayazulu, H.K. Mao and R.J. Hemley, "High P-T transformations of nitrogen to 170 GPa,", J. Chem. Phys., 126, 184505-1-5, 2007.

[15] M.Ross and F.Rogers, "Polymerization, shock cooling, and the high-pressure phase diagram of nitrogen,", Phys. Rev. B, 74, 024103-1-6, 2006.

[16] Y. Ma, A.R. Oganov, Z.Li, Y. Xie and J. Kotakaski, "Novel High Pressure Structures of Polymeric Nitrogen," Phys. Rev. Lett., 102, 065501-1-4, 2009.

[17] L.N. Yakub, "Phase transition line of solid molecular nitrogen into the cubic gauche-polymeric phase," Low Temp. Phys., 37, 431-434, 2011.

[18] R.Caracas, "Raman spectra and lattice dynamics of cubic gauche nitrogen," J. Chem. Phys., 127, 144510-1-7, 2007.

[19] O.Akay and H. Yurtseven, "Investigation of vibrational, elastic and dielectric properties of cubic gauche nitrogen (cg-N)", Optik, 236 ,166481-1-9, 2021.

[20] H.Yurtseven,O.Tiryaki and O.Tari , "Pippard relations for cubic gauche nitrogen,"Anadolu Univ. J. Sci. Tech.Appl. Sci. Eng., 17, 741-746, 2016.

[21] X.Q.Chen, C. L. Fu, and R. Podloucky , "Bonding and strength of solid nitrogen in the cubic gauche (cg-N) structure", Phys. Rev. B, 77, 064103-1-6, 2008 .

[22] Yakub, L.N, "Phase transition line of solid molecular nitrogen into CG-polymeric phase.", Fizika Nizkikh Temperatur, 37(5), 543-546, 2011.

[23] Hirshberg, B., Gerber, R. & Krylov, A. "Calculations predict a stable molecular crystal of N8". Nature Chem., 6, 52–56 , 2014.

[24] N. Capel, B. Devang, and M. Sergei, "A Comparative Density Functional Theory and Density Functional Tight Binding Study of Phases of Nitrogen Including a High Energy Density Material N8" Computation 3, 574-585, 2015.

[25] D. Plasienka and R. Martonak, "Transformation pathways in high-pressure solid nitrogen: From molecular N2 to polymeric cg-N" , J. Chem. Phys. ,142, 094505-1-10, 2015.

[26] T.Yu, W. P. Lai, Y. Z. Liu, B. Wu, Z. X. Ge, J. H. Bu, "The outlook for platonic and cubic gauche nitrogens", Computational Mater. Sci. 123, 31-39, 2016.

[27] G. Weck, F. Datchi, G. Garbarino, S. Ninet, J.A. Queyroux, T. Plisson, M. Mezouar, and P. Loubeyre, "Melting Curve and Liquid Structure of Nitrogen Probed by X-ray Diffraction to 120 GPa", Phys. Rev. Lett. 119 , 235701-1-5, 2017.

[28] S.V. Bondarchuck and B. F. Minaev, "Super high-energy density single-bonded trigonal nitrogen allotrope—a chemical twin of the cubic gauche form of nitrogen" Phys. Chem. Chem. Phys., 19, 6698-6706, 2017.

[29] L.Lei, Q.Q. Tang, F. Zhang, S. Liu, B.B. Wu, C.Y. Zhou, "Evidence for a New Extended Solid of Nitrogen", Chin. Phys. Lett.,37, 068101-1-4, 2020.

[30] Y. Yao and A. O. Adeniyi, "Solid nitrogen and nitrogen-rich compounds as high energy density materials", Phys. Status Solidi B,258, 2000588-1-15, 2021.

[31] E.S. Yakub and L.N. Yakub, "Polymorphic transitions in highly compressed molecular nitrogen. Application of Mayer group expansion for solids" Low. Temp. Phys., 48, 165-169, 2022.

[32] P.Hudon, I.H. Jung and D.R. Baker, "Melting of β-quartz up to 2.0 GPa and thermodynamic optimization of the silica liquidus up to 6.0 GPa", Phys. Earth and Planetary Interiors 130, 159-174, 2002.

[33] G.D.Mukherjee and R.Boehler, "High-pressure melting curve of nitrogen and the liquid-liquid phase transition," Phys.Rev.Lett., 99, 225701-1-4, 2007.

International Journal of Thermodynamics (IJoT)
ISSN 1301-9724 / e-ISSN 2146-1511
https://dergipark.org.tr/en/pub/ijot

Vol. 25 (No. 3), pp. 041-045, 2022
doi: 10.5541/ijot.1102511

Research Article

Optimal Regime for Growth of Epitaxial Germanium Layers from the Liquid Phase Based on Thermodynamic Calculations

[1]*A. Sh. Razzokov, [2]Kh. O. Eshchanov

[1] Department of Physics, Urgench State University, Urgench, Uzbekistan
[2] Department of Chemistry, Urgench State University, Urgench, Uzbekistan
E-mail: [1]*razzokov.a@bk.ru

Received 12 April 2022, Revised 5 July 2022, Accepted 9 August 2022

Abstract

Thermodynamic calculations were performed to determine the optimal conditions for the growth of germanium epitaxial layers from a Ge-Sn solution (system) to a germanium substrate. The determination of the optimal conditions was based on the change in the Gibbs energy values of the system during the crystallization process and the size of the crystal-forming nanoclusters. Based on the results obtained, we determined the optimal conditions for obtaining low-dislocation, crystalline perfect germanium epitaxial layers from a liquid tin solution, and recommended starting the crystallization process at 923 K and finishing at 800 K. When the temperature drops below 800 K, the formation of $Ge_{1-x}Sn_x$ epitaxial layers from the Ge-Sn solution was observed.

Keywords: *Epitaxial layer; dislocation; nanoclusters; activity coefficients.*

1. Introduction

It is essential to obtain low-dislocation germanium crystals that can be used in detectors of special devices used in IR spectroscopy analysis and in other electronic devices. Numerous studies have been conducted to obtain low-dislocation germanium crystals.

In Germanium single-crystals grown by the Czochralski method, dislocations have been studied to appear continuously from the front during growth and to spread to the crystal mass in specific crystallographic directions [1].

The dislocation structure of single-crystalline germanium crystals grown in the (211) and (110) directions by the Czochralski method has been studied using white light X-ray topography [2].

Obtaining solid semiconductor solutions with micro and nanosized based on group IV periodic systems such as SiGe, SiC, SiSn, GeSn, and SiGeSn is an urgent task due to their specific electrophysical and photoelectric properties. Especially, optoelectronic devices operating in the infrared region of the spectrum are in demand, which is built on the basis of photo and heat-sensitive materials with a narrow band gap.

Semiconductor solid solution $Ge_{1-x}Sn_x$ is a narrow-gap material and has great potential for the development of infrared photodetectors. germanium and tin do not react under ambient conditions, i.e. are sustainable. And also, $Ge_{1-x}Sn_x$ is an attractive semiconductor material for Photonics, but the low solubility of tin in germanium limits its growth. To obtain a high Sn content in $Ge_{1-x}Sn_x$, it is usually grown at a low temperature, which would lead to inevitable dislocations. $Ge_{1-x}Sn_x$ was laterally grown by the fast melting method and the lattice parameter matched the size of the germanium lattice parameters [3].

The possibility of growing single-crystal $Ge_{1-x}Sn_x$ on a silicon substrate was shown in [4] using plasma chemical vapor deposition (PE-CVD). The density of dislocations in the substrate Si-$Ge_{1-x}Sn_x$ film heterointerface was~10^9 cm^{-2} due to the lattice mismatch between them.

A $Ge_{1-x}Sn_x$ alloy with a thickness of 250 nm was grown on a germanium (001) substrate by molecular beam epitaxy at low temperatures. The microstructures of $Ge_{1-x}Sn_x$ samples were studied by transmission and scanning electron microscopes. The results show that defects are mainly localized at the $Ge_{1-x}Sn_x$/Ge interface [5].

It was experimentally established in [6] that the temperature required for crystallization of $Ge_{1-x}Sn_x$ is reduced, and the crystallinity is improved compared to the case of pure germanium. In $Ge_{1-x}Sn_x$ film deposition, there is an optimal tin composition for the best crystalline after relaxation at temperatures $t^o<500°C$, when seed growth prevails over nucleation. Thin films of $Ge_{1-x}Sn_x$ alloys containing up to 8.7 at. % tin grows at low crystallization temperatures of 370~470°C on silicon. The direct band gap is significantly red limit from 0.8 eV for pure germanium to ~0.5 eV for crystalline $Ge_{0.913}Sn_{0.087}$. The authors believe that the obtained highly crystalline $Ge_{0.913}Sn_{0.087}$ thin films on SiO_2 were obtained by the crystallization of a sample of 9.5 at. % tin is an important step towards growing a low defect density close to single-crystal $Ge_{1-x}Sn_x$ on amorphous materials [6].

To obtain plastically relaxed $Ge_{1-x}Sn_x$ layers using the technological method of molecular beam epitaxy to grow on silicon, without using an intermediate germanium buffer layer, a discrepancy was caused due to differences in the lattice parameters of the Si/$Ge_{1-x}Sn_x$ hetero compound materials [7].

*Corresponding Author

Given the narrow band gap of $Ge_{1-x}Sn_x$ can be adjusted by adding tin content, and $Ge_{1-x}Sn_x$ material can be applied to light-emitting devices, including laser and LED. The indirect band gap of $Ge_{1-x}Sn_x$ passes to the direct band gap due to an increase in the concentration of the substituting tin in the germanium lattices [8].

Using ion implantation and pulsed laser melting (PLM), $Ge_{1-x}Sn_x$ layers 0.2 µm thick with different atomic concentrations of 0.5 % to 3.0 % were obtained. The implanted germanium layer becomes amorphous due to bombardment with high kinetic energy tin ions. The re-growth of the $Ge_{1-x}Sn_x$ layer after PLM and the expansion of the lattice were confirmed by X-ray diffraction and micro-Raman spectroscopy. Studying morphology and chemical composition of $Ge_{1-x}Sn_x$, the authors confirmed the single-crystal structure of the alloys [9].

Paper [10] shows the production of $Ge_{1-x}Sn_x$ films by molecular beam epitaxy on germanium (001) substrates. The dependence of growth temperature and the effect of post-growth annealing were studied. We also carried out thermodynamic calculations, during film growth from a solution-melt, and in solid-liquid contact. The energy change of the liquid-solid interface during growth is shown. Dissolved germanium is recrystallization from the volume of the Ge-Sn melts solution by the method of liquid-phase epitaxy.

Increasing the Sn content in the $Ge_{1-x}Sn_x$ alloy improves charge carrier mobility and converts the band gap from indirect to direct. However, the production of $Ge_{1-x}Sn_x$ is limited due to the equilibrium solubility of tin in germanium (no more than 1 at. %). Therefore, the authors of [11] tried to obtain planar $Ge_{1-x}Sn_x$ nanowires catalyzed by tin nanoparticles to overcome this limitation, reaching a nonequilibrium tin concentration of 22 at. %.

In our previous work, we reported that on the basis of experiments we managed to obtain epitaxial layers $Ge_{1-x}Sn_x$ in the temperature range 740÷450ºC [12].

To grow crystalline perfect germanium epitaxial layers, we performed thermodynamic calculations of the Ge-Sn solution. We aimed to determine energy-efficient growth regimes using Gibbs energy calculations and size analysis of crystal-forming nanoclusters.

2. Theoretical Part

To determine the optimal conditions for the growth of $Ge_{1-x}Sn_x$ crystals, calculations were performed based on experimental results. The application of calculations to real processes is of great practical importance. To do this, it is necessary to express the concentrations of tin and germanium components in terms of activity. We relied on the Clausius-Clapeyron and Gibbs–Duhem equations to determine the activity of the tin and germanium components in the system [13, 14].

$$\ln\left(\frac{1}{\gamma_{Ge} X_{Ge}}\right) = \frac{\Delta H_f}{R}\left(\frac{1}{T_c} - \frac{1}{T_l}\right) \tag{1}$$

$$\ln \gamma_{Sn} = -\frac{X_{Ge}}{X_{Sn}}(\ln \gamma_{Ge} - 1) \tag{2}$$

Where *X*- is the concentration (mole fraction) of the component in the system, *γ*- is the activity coefficient, T_c- crystal formation temperature (K), T_l- liquidus temperature (K), ΔH_f is the heat of fusion (J/mol), *R*-universal gas is constant.

Activity (*a*) values were determined based on the determined activity coefficients of the germanium and tin components in the system. Using the activity values, the Gibbs energies of the mixing of germanium and tin components in the system at different temperatures were calculated. This allows you to get closer to the real process situations in the system. The mixing of Gibbs energy was determined using Eq. (3).

$$\Delta G_{mix} = RT(X_{Ge} \ln a_{Ge} + X_{Sn} \ln a_{Sn}) \tag{3}$$

Germanium nanoclusters were thought to be involved in crystal growth in the system.

Germanium nanoclusters in the system are located on the growing surface and form a crystallization process. Therefore, the total Gibbs energy of the crystallization process on the growing surface can be expressed as follows.

$$\Delta G_{system} = \Delta G_{cr} + \Delta G_{mix.then} - \Delta G_{mix.\,first} \tag{4}$$

Depending on the Gibbs energy of crystallization, the size of the 2D bulges that cause dislocations in the growing layer on the base surface is determined. The following equation was used to determine the size of the bumps.

$$\Delta G_{cr} = \frac{4\sigma^2 b V_m}{\Delta G_v} \tag{5}$$

Here σ- nanoclusters are the surface tension at the liquid tin boundary, *b*- 2D is the size of the bulges, V_m- is the molar volume, ΔG_v- is the volumetric Gibbs energy of the crystal.

Eq. (6) can be used to determine the volumetric Gibbs energy.

$$\Delta G_v = \Delta H_f \frac{T_l - T_c}{T_l} \tag{6}$$

Using the above calculation formulas, we will be able to determine the optimal conditions for crystal growth.

3. Experience Part

3.1. Equipment and Materials

Chemically pure samples of tin and germanium (Taizhou ATS Optical Material Co., Ltd.) were used for the experiment. Germanium plate in the <111> direction was used as the substrate. The experiments were carried out in an EPOS-type device (Pd-15T purifier) and in a hydrogen atmosphere at a temperature of 823÷1200 K. 4-Channel Type-K thermometer was used to check the temperature. An AE ADAM NBL 214e (Germany) analytical balance was used to measure the weight of the substances. An SEM EVO MA 10 (Zeiss) device was used to analyze the crystal surface.

3.2. Obtaining Crystals of Germanium

Experiments were carried out in an EPOS-type device (Pd-15T purifier) and in a hydrogen atmosphere at temperatures of 823÷1200 K to determine the solubility of germanium in the tin and to obtain germanium crystals.

The resulting crystal sample was treated with a dilute solution of hydrochloric acid. The surface of the processed crystal sample was examined using a scanning electron microscope.

4. Results and Discussion

The concentrations and activities of the components for the saturated state of the Ge-Sn system at temperatures 823÷1173 K were determined.

Activity coefficients were determined based on Eq. (1) and Eq. (2) based on the concentrations of the components corresponding to different temperatures (Table 1-2).

Table 1. Activity coefficient and activity values of germanium component in Sn-Ge system.

T, K	X_{Ge}	γ_{Ge}	a_{Ge}
1173	0.960	0.924	0.887
1123	0.850	0.882	0.750
1073	0.613	1.016	0.623
1023	0.386	1.317	0.509
973	0.233	1.746	0.407
923	0.166	1.9085	0.318
873	0.116	2.070	0.2415
823	0.085	2.0854	0.1773

Table 2. Activity coefficient and activity values of tin component in Sn-Ge system.

T, K	X_{Sn}	γ_{Sn}	a_{Sn}
1173	0.040	2.4360	0.0974
1123	0.150	0.7500	0.1125
1073	0.387	0.35845	0.1386
1023	0.614	0.30926	0.1896
973	0.767	0.31048	0.2380
923	0.834	0.32326	0.26937
873	0.884	0.33417	0.2952
823	0.915	0.3436	0.31438

Based on the determined results, the Gibbs energy values of the mixing of the components were calculated using Eq. (3).

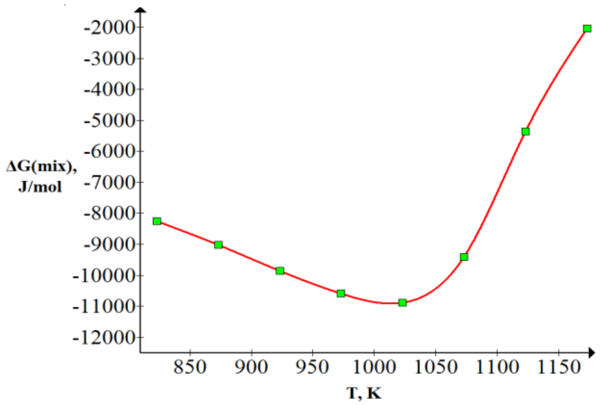

Figure 1. Temperature dependence of the Gibbs energy of mixing in the Ge-Sn system.

If we look at the graph in Figure 1, we can observe that the initial Gibbs energy values of the mixture are high when the temperature is high and decrease to a temperature of 1023 K. It is also observed that mixing the above components at temperatures below 1023 K increases the Gibbs energy values.

At the minimum Gibbs energy value of the mixture, the melting process of the components in the system is observed to be the highest. As a result, the increase in Gibbs energy values above the mixing temperature above 1023 K leads to the conclusion that the melting capacity of the components decreases. However, in the experiment, conversely, as the temperature increases, the solubility of germanium at tin increases. Using the results obtained, the following conclusion can be drawn. The germanium and tin components up to the minimum value of the Gibbs energy of the mixture conform to the basic law. Above 1023 K, a chemical change may be observed in the system.

It has been assumed that the main participants in the formation of germanium crystals from the Ge-Sn system are nano-sized particles. It is important to know the size of the nanoclusters that form germanium crystals. This is because the density of dislocations at the base-film boundary during the growth of $Ge_{1-x}Sn_x$ epitaxial layers on the substrate is directly related to the size of the crystal-forming nanoclusters.

When a large nanocluster is located on the crystal growing surface, it causes various defects to appear on the crystal surface. As a result, the density of dislocations on the surface increases. It is therefore advisable to grow crystals in the presence of small-sized nanoclusters.

Based on data from the literature [15], the sizes of crystal-forming nanoclusters were determined using the following Eq. (7).

$$r = \frac{2\sigma V_m}{\Delta G_V} \qquad (7)$$

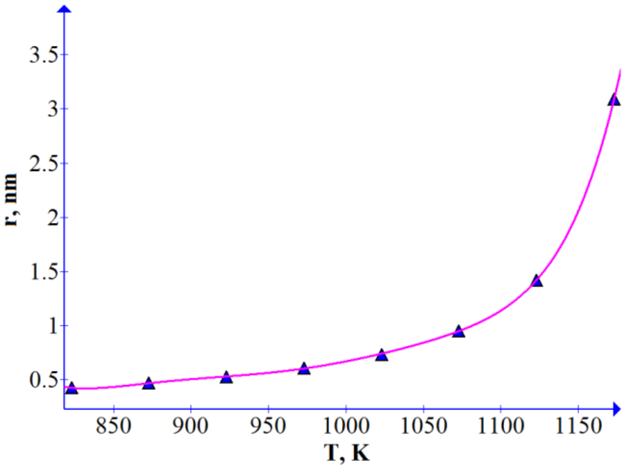

Figure 2. Temperature dependence of the size of germanium nanoclusters.

At low temperatures, the size of germanium nanoclusters involved in crystallization decreases.

The analysis of the results showed that the differences in the size (radius) of the germanium nanoclusters forming crystals below the temperature of 923 K were reduced (Figure 2). Small germanium nanoclusters form low-dislocation and crystalline perfect epitaxial layers.

The formation of germanium nanoclusters involved in the crystallization process is the basis for determining the optimal state of crystal formation in the system by determining the critical Gibbs energies. The critical Gibbs energies of crystal-forming nanoclusters were determined at different temperatures.

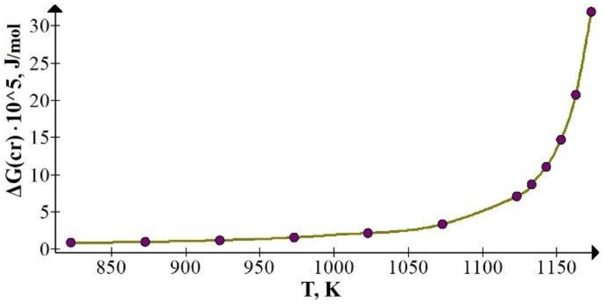

Figure 3. Critical Gibbs energies of germanium nanoclusters.

As can be seen from the graph, the differences between the critical Gibbs energy values of the crystal-forming germanium nanoclusters decrease sharply below a temperature of 923K (Figure 3). That is, the change of critical Gibbs energy values of nanoclusters is linear. It is significant that at temperatures below 923 K the values of the critical Gibbs energy are low and the differences between the values are small. A low value of Gibbs energy means that less work is done to form nanoclusters under the same conditions.

It is very important that the sizes of the nanoclusters involved in the crystal formation are close to each other in the temperature range of the critical Gibbs energy.

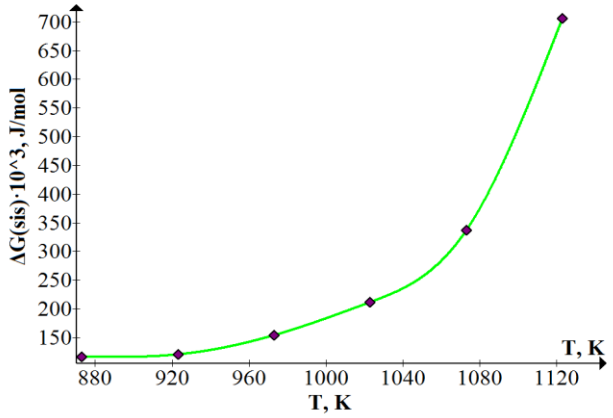

Figure 4. Temperature dependence of the Gibbs energy of a system during crystallization (With the participation of nanoclusters).

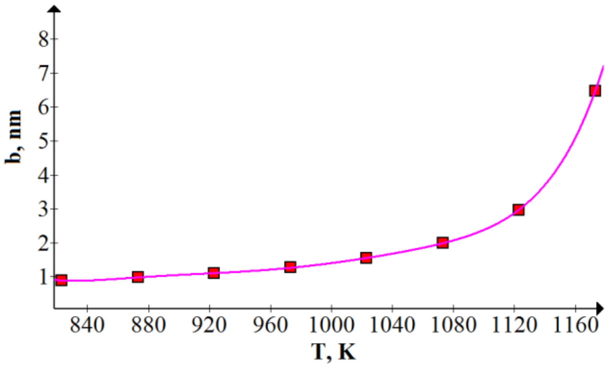

Figure 5. Temperature dependence of the size of the 2D bulges of the germanium crystal growing from the liquid tin solution to the germanium substrate.

As the initial crystallization temperature of the growing germanium crystal in the substrate decreases, the size of the 2D bumps on the growing surface decreases due to the small size of the germanium nanoclusters involved in crystallization. The dimensions of the 2D bumps were calculated using Eq. (5). In the high-temperature ranges of crystallization, the difference between the bulge sizes is large, and the difference between the values decreases with decreasing temperature. As the temperature began to decrease from 923 K, the differences between the values of the 2D bulge sizes decreased sharply (Figure 5). It is desirable that the initial growth temperature be less than 923 K to obtain perfectly crystalline, low-dislocation germanium crystals. If germanium crystals are grown from tin solution at temperatures below 800 K, a solid mixture with an epitaxial layer of $Ge_{1-x}Sn_x$ is formed [12]. The following are images of the $Ge_{1-x}Sn_x$ epitaxial layers formed under these conditions obtained using a scanning electron microscope (SEM) (Figure 6-7).

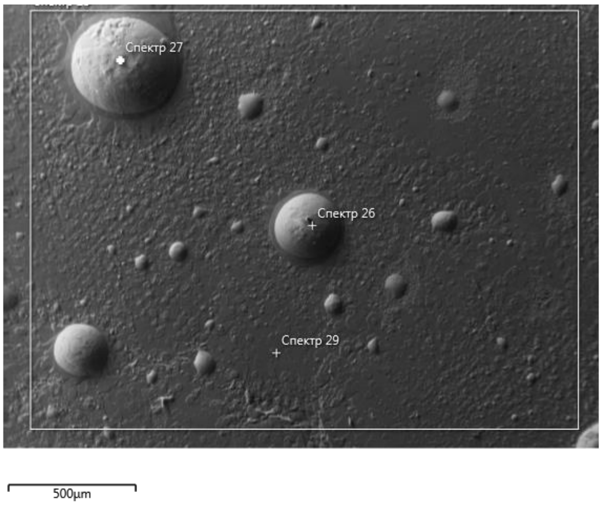

Figure 6. SEM image of the surface of epitaxial layers of $Ge_{1-x}Sn_x$ solid mixture.

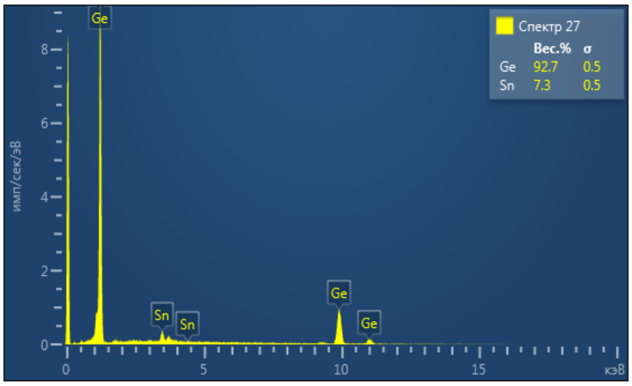

Figure 7. Quantitative composition of elements in the epitaxial layers of $Ge_{1-x}Sn_x$ solid mixture.

The analysis process was performed at SEM EVO MA 10 (Zeiss). The sample obtained for analysis was treated using a hydrochloric acid solution. The purpose of processing is to remove tin particles that are mechanically located on the surface. If we look at the results of the analysis, we can see the data indicating the formation of epitaxial layers of $Ge_{1-x}Sn_x$ solid mixture on the growing surface below a temperature of 800 K. It was found to contain 92.75 % germanium and 7.25 % tin in terms of mass.

5. Conclusion

Based on the results obtained, the optimal conditions for obtaining low-dislocation, crystalline perfect germanium epitaxial layers from a liquid tin solution were determined. The determination of the optimal conditions was based on the change in the Gibbs energy values of the system during the crystallization process and the size of the crystal-forming nanoclusters.

We found that one of the reasons for the relatively high density of dislocations in crystals grown at high temperatures was related to the size of the nanoclusters.

We recommend starting the crystallization process from 923 K and ending at 800 K. At temperatures below 800 K, the formation of $Ge_{1-x}Sn_x$ epitaxial layers is observed.

Nomenclature

a	Activity
γ	Activity coefficient
ΔG_{mix}	The Gibbs energy of mixing, J/mol
ΔG_v	Volumetric Gibbs energy
ΔG_{cr}	Critical Gibbs energy, J/mol
R	Universal gas constant, 8.314 $J \cdot K^{-1} \cdot mol^{-1}$
T	Temperature, K
X	Mole fraction
σ	solid-liquid surface tension, J/m^2
V_m	Molar volume, m^3/mol
ΔH_f	Heat of fusion, J/mol
b	2D is the size of the bulges, m
r	nanocluster radius, m

References:

[1] Y. Smirnov, A. Ivanova, and I. Kaplunov, “Dislocation formation and motion in germanium single crystals,” *Crystallogr. Rep.,* 53(7), 1133–1136, 2008.

[2] K. Gradwohl, M. Roder, A. Danilewsky, and R. Sumathi, “Investigation of the dislocation structure in Czochralski germanium crystals grown in [211] and [110] growth directions,” *Cryst. Eng. Comm.*, 23(23), 4116-4124, 2021.

[3] Z. Liu, H. Cong, F. Yang, C. Li, J. Zheng, C. Xue, Y. Zuo, B. Cheng. and Q. Wang, “Defect-free high Sn-content GeSn on insulator grown by rapid melting growth,” *Scientific Rep.*, 6(1), 38386, 2016.

[4] W. Dou, B. Alharthi, P. Grant, J. Grant, A. Mosleh, H. Tran, W. Du, M. Mortazavi, B. Li, H. Naseem, and S. Yu, “Crystalline GeSn growth by plasma enhanced chemical vapor deposition,” *Opt. Mat. Exp.*, 8(10), 3220, 2018.

[5] G. Zhu, T. Liu, Z. Zhong, X. Yang, L. Wang, and Z. Jiang, “Fabrication of High-Quality and Strain-Relaxed GeSn Microdisks by Integrating Selective Epitaxial Growth and Selective Wet Etching Methods,” *Nanoscale Res. Lett.*, 15(1), 2020.

[6] H. Li, J. Brouillet, A. Salas, X. Wang, and J. Liu, “Low temperature growth of high crystallinity GeSn on amorphous layers for advanced optoelectronics,” *Opt. Mat. Exp.*, 3(9), 1385, 2013.

[7] Y. Sadofiev, V. Martovitsky, M. Bazalevsky, A. Klekovkin, D. Averyanov, I. Vasilevsky, “Ge/GeSn heterostructures grown on Si(100) by molecular beam epitaxy,” *Phy. Tech. of Semi.*, 1, 128-133, 2015.

[8] C. Fang, Y. Liu, Q. Zhang, G. Han, X. Gao, Y. Shao, J. Zhang, and Y. Hao, “Germanium-tin alloys: applications for optoelectronics in mid-infrared spectra,” *Opt. Electr. Adv.*, 1(3), 18000401-18000410, 2018.

[9] K. Gao, S. Prucnal, R. Huebner, W. Skorupa, M. Helm, S. Zhou, “Liquid phase epitaxy of Ge(1-x)Sn(x) alloy using ion-implantation and pulsed laser melting,” *E-MRS 2014 Spring meeting*, Lille, France, 2014.

[10] H. Groiss, M. Glaser, M. Schatzl, M. Brehm, D. Gerthsen, D. Roth, P. Bauer, and F. Schäffler, “Free-running Sn precipitates: an efficient phase separation mechanism for metastable $Ge_{1-x}Sn_x$ epilayers,” *Scientific Rep.*, 7(1), 2017.

[11] E. Azrak, W. Chen, S. Moldovan, Sh. Gao, S. Duguay, Ph. Pareige, and P. Cabarrocas, “Growth of In-Plane $Ge_{1-x}Sn_x$ Nanowires with 22 at. % Sn Using a Solid–Liquid–Solid Mechanism,” *J. Phys. Chem. C*, 122(45), 26236–26242, 2018.

[12] A. Saidov, A. Razzakov, E. Koshchanov, “Liquid phase epitaxy of $Ge_{1-x}Sn_x$ semiconductor films,” *Tech. Phys. Lett.*, 27(8), 698–700, 2001.

[13] K. Matthew, S. Eduardo, “Beyond Clausius–Clapeyron: Determining the second derivative of a first-order phase transition line,” *Am. J. Phys.*, 82(4), 301–305, 2014.

[14] H. DeVoe, *Thermodynamics and Chemistry - 2nd Ed.* Maryland, 2019.

[15] E. Shukin, A. Persov, E. Ameline, *Colloidal chemistry*, -M.: Higher. shk., 2004.

International Journal of Thermodynamics (IJoT)
ISSN 1301-9724 / e-ISSN 2146-1511
https://dergipark.org.tr/en/pub/ijot

Vol. 25 (No. 3), pp. 047-053, 2022
doi: 10.5541/ijot.1105040

Entropy of Open System with Infinite Number of Conserved Links

A. Moldavanov*

2774 Sunnybridge Dr., Burnaby, BC Canada V5A 3V1
E-mail: trandrei8@gmail.com

Received 18 April 2022, Revised 17 June 2022, Accepted 15 July 2022

Abstract

Energy budget of open system is a critical aspect of its existence. Traditionally, at applying of energy continuity equation (ECE) for description of a system, ECE is considered as a declaration of local balance in the mathematical (infinitesimal) vicinity for the only point of interest and as such it does not contribute to entropy. In this paper, we consider transformation of ECE to account the effects in the physical (finite) vicinity with infinite number of energy links with environment. We define parameters of appropriate phase space and calculate Shannon's, differential, and thermodynamic entropy. Shannon's and differential entropies look sufficiently close while thermodynamic entropy demonstrates close character of variation in its functionality being different in its mathematical form. Physical applications to confirm contribution of a new concept to the real-world processes are also discussed.

Keywords: *Information uncertainty; Shannon's entropy; thermodynamic entropy, continuity equation; energy exchange.*

1. Introduction

1.1 Entropy

Information theory was established by Shannon in 1948 [1]. It allowed to introduce a remarkable measure of information – Shannon's (information) entropy [2]. Since that, entropy plays a central role in statistical mechanics, and, as a result, in physics.

A fundamental meaning of new concept was shortly confirmed by existence for a given probability distribution of notable complementary interpretation - quantity of information (after measurement) or uncertainty (before measurement) [3]. Within this way of thinking, Jaynes has seen a statistical mechanics as an application of informational theory, and thermodynamics as a special case of entropy maximization procedure [4].

In recent years, a concept of information entropy was being intensively developed within the framework of both, classic and quantum physics.

These days, we can think of an entropy as a key concept of quantum information theory [5]. In this sense, an entropy of a quantum system is a measure of its randomness and has many applications in quantum communication protocols, quantum coherence, and so on [6-8].

Important role in above development belongs to the so called Bialynicki-Birula and Mycielski (*BBM*) inequality

$$S_{nx} + S_{np} \geq d\lfloor 1 + ln(\pi) \rfloor \qquad (1)$$

which can be considered as a new uncertainty relation in quantum mechanics, where S_x and S_p are entropy for position and momentum. This new relation has a clear interpretation in information theory as a formalism that relates the position and momentum uncertainties, where *d* denotes the dimension of the position and momentum space [9].

The study of Shannon entropy for a spinless non-Hermitian particle in the presence of a magnetic field was conducted in [10]. Numerical analysis demonstrates that Shannon's entropy satisfies the *BBM* relationship for ground and excited states independent of the value of the magnetic field. It was also shown that the magnetic field has an ability to modify the Shannon entropy which satisfies the *BBM* relationship of the model.

Modification of Shannon's entropy and thermodynamic properties under the linear potential action was studied in [11]. It was noted that Shannon's entropy of Majorana fermions satisfies *BBM* for fundamental and excited states. At this, an external force that acts on the Majorana fermions alters Shannon's entropy, however, this alteration still obeys *BBM* relation of the model.

Simulation of a Shannon entropy at abrupt heterojunctions in semiconductor materials in approximation of the soliton-like mass distribution (position-dependent mass) was investigated in [12]. It was shown that for the Hamiltonian operator to be Hermitian, Zhu-Kroemer ordering for the stationary Schrodinger equation can be employed.

Numerical calculation of the Shannon entropies for a rectangular asymmetric multiple quantum well system with a constant total length was fulfilled in [13]. It is demonstrated that the S_x and S_p do not always decrease or increase monotonically with the confined potential depth, but their sum always satisfies *BBM*.

A spherically confined hydrogen atom has been considered using two different confined potentials such as modified Kratzer and non-spherical oscillator potentials. *BBM* has been also tested. It was found that its validity depends on non-extensive parameter [14].

On the other hand, in classic physics, an entropy concept has taken important and prominently deserved place since

---

*Corresponding Author

recognition of its remarkable meaning. However, the new results and fresh views to the well-known facts related to entropy are still being appeared regularly.

As an example, indicate to the recent research which demonstrates that information content and its uncertainty as measured from the file compression procedure can unexpectedly provide new insights like quantifying of hidden order in non-equilibrium physics [15].

Some uses of Shannon's entropy formula in information theory that have confirmed the functionality of this paradigm were considered in [16].

Advent of nanostructures that straddle the border between the molecular and the macroscopic levels of physical understanding, has opened new applications for informational entropy [17].

Analysis of entropy for obtaining of an uncertainty principle by utilizing of fundamental physical paradigm of continuity in the nanoscale level was conducted in [18-20].

New reading of the far from equilibrium thermodynamical concepts was recently achieved due to using of entropic relations [21,22].

Alternative approach to thermodynamic uncertainty relation as well as limitation to entropy variations for non-equilibrium thermodynamical states was considered in [23].

Above results confirm existence of the deep-laid connection between entropy and behavior of physical system. Further, we will be presenting transformation of energy continuity equation (*ECE*) and, on this basis, evaluation of entropy for open system with infinite number of conserved links with environment.

1.2 Extension of energy continuity equation

In this research, we will be using a physical model of the conserved link between system and its environment. By its definition, this link calls for the conserved quantities (*CQ*) that meet generic requirement of conservation [24]. This requirement in differential shape represents balance in the local form and in the non-relativistic approximation for energy is given by an *ECE*

$$\frac{\partial \varepsilon}{\partial t} + \nabla \cdot \mathbf{J} = 0 \qquad (2.a)$$

where **J** is flux of energy, ε is energy volume density, t is time, and ∇ is Nabla operator [25, 26].

So, considered approach contains such exchange scenarios that include an energy dimension. Hence, we only deal with the scenarios in which the change in system state can be described in energy terms irrelevant of the nature of the exchange processes themselves. Further discussion about employed approach can be found in [24].

By default, notation (2.a) appeals to a mathematical (infinitesimal) space-time vicinity (*STV*) for the only point of interest. As a result, (2.a) assumes a predetermined description of an energy exchange process in the only point and eliminates any chance for uncertainty in definition of parameters (2.a). Therefore, (2.a) brings no contribution to entropy.

However, validity of (2.a) becomes questionable if we do step aside from the mathematical to the physical (finite) *STV*, further *PSTV*. Obvious reason of that lies in breaking of the space-time predetermination which inevitably brings randomness, uncertainty, and missing information, *i.e.*, Shannon’s entropy.

To reflect emergence of *PSTV* uncertainty, (2.a) can be extended to the system of infinite number of *ECE*

$$\begin{cases} \dfrac{\partial \varepsilon_1}{\partial t} + \nabla \cdot \mathbf{J}_1 = 0 \\ \dfrac{\partial \varepsilon_2}{\partial t} + \nabla \cdot \mathbf{J}_2 = 0 \\ \ldots \\ \dfrac{\partial \varepsilon_n}{\partial t} + \nabla \cdot \mathbf{J}_n = 0 \\ \ldots \end{cases} \qquad (2.b)$$

where $n \to \infty$ [25].

Below, it is assumed that *PSTV* is surrounded by a permeable boundary that supports the non-zero mass flow, then *PSTV* can be considered as an open thermodynamic system. For description of this system, we combine three kinds of energy flux under common symbol **J**: (a) default heat transfer, (b) work transfer by the transport of *CQ* like charge, momentum, angular momentum, and mass, (c) enthalpy flow via the mass transfer across permeable boundary.

So, we make step from *STV* (2.a) to *PSTV* (2.b), and our aim is to estimate an appropriate increment in entropy that this step can cause.

2. Transformation of *ECE*

In *ECE* (2.a), conduct equivalent mathematical transformation.

So, let *STV* be the closed manifold oriented by inward-pointing normal $\boldsymbol{n}$ at each point of the boundary S. Suppose the direction of d**J** is determined by the unit vector $\boldsymbol{m}$, $\boldsymbol{m} = (\cos\varphi_x, \cos\varphi_y, \cos\varphi_z)$, where $\varphi = \angle(d\mathbf{J}, \mathbf{n})$,

$$\cos\varphi_i = \frac{dJ_i}{dJ}, \qquad (3)$$

dJ_i is i-th component of d**J**, d**S** is a shorthand for $\boldsymbol{n}dS$, $i = \{x, y, z\}$ in the Cartesian system.

Multiply both sides of (2.a) by elementary volume dV and use (3), so we have

$$\frac{dU}{dt} = -dJ(\mathbf{m} \cdot d\mathbf{S}) = -dJ(\mathbf{m} \cdot \mathbf{n})dS \qquad (4)$$

where $\boldsymbol{m} \cdot \boldsymbol{n} = \cos\varphi$, $dU = \varepsilon \cdot dV$.
Divide (4) by $J \cdot dS$ and observe $Q = J \cdot dS\, dt$, so

$$\frac{dU}{Q} = -d(\ln y)\, x \qquad (5.a)$$

or, equivalently,

$$\frac{dU}{\delta Q} = -x \qquad (5.b)$$

where $\delta Q = dJ \cdot dS\, dt$, random $x = \cos\varphi$, deterministic y (energy exchange rate) $= J/J_0$, normalizing constant $J_0 > 0$.

Note that relations (5) explicitly include factor x. At variable nature of x, it naturally accounts an infinite n in *PSTV* approximation (2.b).

3. Factor *x* as indicator of uncertainty

Physically, factor x determines the instantaneous status of an energy exchange pattern between *PSTV* and its environment.

It should be noted that violation of (2.a) leads to widening of the uncertainty interval for quantity (dU/Q) in (5). In this sense, emergence of uncertainty in (5) could be considered as a natural adjustment to get to the higher confidence for the observed results.

Note that in alignment with above, generally, (5) cannot be considered as a *continuity* equation in its conventional meaning anymore.

So, at fixed x, we deal the mathematical *STV* with, and (5) is a regular *ECE* asserting the predefined energy transfer in dependence on y and certain match between the amount of energy brought to the *STV* boundary and that of finally acquired by *STV*, *i.e.*, $dU = Q$.

In contrast to that, in *PSTV* approximation, random x is taken from some range, hence uncertainty is being emerged, and it is no longer mandatory for dU and Q to be the same. In this sense, the set of x controls the set of possible scenarios of energy exchange at every given y, when the particular scenario is realized on the random basis.

We see from above that simple reformulation of x allows us to easily switch between the mathematical (2.a) and the physical (2.b) method of description. In turn, the latter provides a natural way to switch from the only possible scenario of energy exchange to many of them. This switching can be done by just changing of type and value of x.

4. Function Υ as measure of phase volume

By definition, in this model variables x and y are independent, so from (5.a)

$$\int \frac{dU}{Q}\, dy = -\delta\Upsilon(x,y) = -x \cdot \ln y \tag{6}$$

where $\delta\Upsilon(x,y)$ is an instantaneous efficiency of energy exchange with suitable phase space $M \subseteq R^2$ for all possible states (Figure 1).

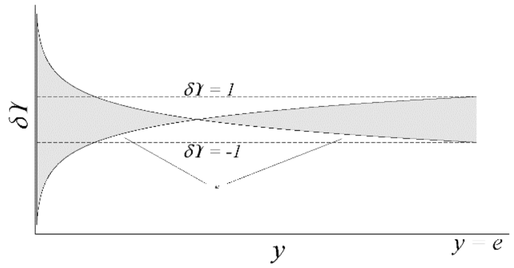

Figure 1. Phase space M for all possible microstates of instantaneous efficiency of energy exchange $\delta\Upsilon$ between PSTV and its surroundings. In the plot, by an abscissa axis a energy rate $y = J/J_0$ is indicated, by an ordinate axis an instantaneous efficiency $\delta\Upsilon$. Space M is marked by a light-grey area (taken from [24]).

Now, introduce function

$$\Upsilon = -\iint_M \delta\Upsilon(x,y) = -\int_{-1}^{1} dx \cdot \int_0^y \ln y \, dy \tag{7}$$

which after integration can be expressed as

$$\Upsilon = y - y \ln y \tag{8}$$

By its appearance, Υ describes the phase volume for random variations of $\delta\Upsilon$.

Function Υ is of maximum in the stationarity point $y = 1$, while its minimum is at the bounds of y-range for energy exchange (Figure 2). In the considered case, these bounds are $[0, e]$, where e is the base of natural logarithm.

Eq. (7) can be rewritten as an identity

$$\int_0^1 dy \int_{-1}^{1} \delta\Upsilon(x,y)\, dx = \left| \int_1^e dy \int_{-1}^{1} \delta\Upsilon(x,y)\, dx \right| = 1 \tag{9}$$

where $|a|$ denotes a modulus of a. Identity (9) can be also written as

$$\begin{cases} \Upsilon(1) - \Upsilon(0) = 1 \\ \Upsilon(1) - \Upsilon(e) = 1 \end{cases} \tag{10}$$

which assumes that the y-ranges $[0,1]$ and $[1,e]$ mandatorily contain the full bunch of *PSTV* exchange scenarios no matter which variations x $(\delta\Upsilon)$ happen. At this, the range $0 \le y \le 1$ deals with the preferable transportation of energy inwards *PSTV*, while the range $1 \le y \le e$ with the opposite transportation of energy outwards *PSTV* [26].

In other words, (7) means that at arbitrary y, the existing phase volume Υ does not guarantee $dU = Q$, however it can guarantee the maximum possible proximity of dU and Q at bidirectional transmission between *PSTV* and environment on the confidence interval $[0, y]$. Generally, this transmission is not the error-free $(\Upsilon \neq 1)$.

Remind that Shannon-Hartley theorem [27] states that theoretically it is possible to provide an error-free transmission through the noisy channel if channel capacity C exceeds the information transmission rate R, *i.e.*, if

$$C \ge R \tag{11}$$

If (11) does not hold, then transmission should include the more or less percentage of errors.

In our case, function Υ can be considered as equivalent of C while y as equivalent of R. Therefore, rewrite (11) as

$$\Upsilon \ge y \tag{12}$$

Using (8), it assumes that theoretically (12) holds in the range $0 \le y \le 1$, and violates in the range $1 < y \le e$. As a result, in the real-world application the probability to observe the error-free energy exchange process is higher in the range $0 \le y \le 1$ compared the range $1 < y \le e$.

In above way, (7,9) directly refers to the context of the theorem [27] as it determines the measure of error occurrence for energy exchange process in the noisy channel (*PSTV* ↔ environment) in terms of volume Υ and bandwidth y. At this, (9) provides conditions to guarantee the lossless $(dU = Q)$ bidirectional transportation of energy through

PSTV boundary, whereas (7) indicates to the minimum portion of errors we should expect in the best case possible.

For example, given $y = 1/e$, then from (8) $\Upsilon = 2/e \approx 0.73$. As $1 - 0.73 = 0.27$, we should expect that about *27%* of transmitted energy is dissipated as a useless heat.

All abovesaid prompts us to use the framework of information theory. So, now we are in a good position to calculate an entropy caused by the *STV* → *PSTV* jump.

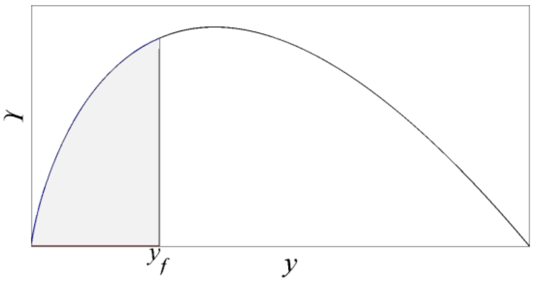

Figure 2. Phase volume Υ for all possible microstates of instantaneous efficiency of energy exchange δΥ. In the plot, designation of the horizontal axis is the same as in the Figure 1, by an ordinate axis the phase volume Υ is indicated. Phase volume at arbitrary $y = y_f$ *is marked by a light-grey area.*

5. Calculation of entropy

5.1 Shannon's entropy

As it was mentioned above, Υ can be interpreted as a phase volume for space *M* (Figure 2). Then in *M*, the maximum number of possible microstates *W* at given rate *y* is $(d\Upsilon/dy)dy$ [28, 29]. Therefore, from (8) and using Gibbs' definition [28], Shannon's entropy up to a constant additive A_0 is

$$\Delta S = \ln W = \ln|\ln y| + A_0 \tag{13}$$

It is important that (13) fully coincides with the main part of differential entropy (16) discussed below.

5.2 Differential entropy

Although differential entropy cannot be considered as the mathematically rigorous extension of information entropy because of the known limitation $\lim_{\Delta\to 0}\ln(\Delta) \to -\infty$ [30], we consider dynamics of its main part yet believing that it may provide useful auxiliary information, where Δ is the size of discretizing for probability density function (*PDF*). Moreover, we are only interested in the difference of differential entropy ΔS^x between adjacent states which obviously lacks above shortcoming. Also, we will consider dynamics of ΔS^x, taking value of S^x at $y = 0$ as the anchor one.

So, let $g(x)$ be the *PDF* for random *x*, *i.e.*

$$g(x) > 0 \;\; for \;\; x \in [-1, 1] \tag{14.a}$$

$$g(x) = 0 \;\; at \;\; x \notin [-1, 1] \tag{14.b}$$

then from (6) at each *y*, *PDF* is

$$f^y(x) = \frac{g(x)}{|\ln y|},\; x \in [-1,1] \tag{15}$$

[31], where $|lny|$ is taken to keep $f^y(x) \geq 0$, *y* is a parameter. Calculation of $f^y(x)$ is done in assumption that *x* is the random at each given deterministic *y*.

Now, introduce an entropy probability distribution for instantaneous random $\delta\Upsilon$ as

$$\Delta S^x = -\int_{-1}^{1} f^y(x)\ln(f^y(x))dx \tag{16}$$

Insert (15) to (16) and simplify, then Shannon's entropy is

$$\Delta S^x = \ln|\ln y| + H_x \tag{17}$$

with the plot shown in Figure 3, where H_x is an entropy probability distribution in the range $[0,\ln 2]$ for *x* on the compact support $[-1, 1]$

$$H_x = -\int_{-1}^{1} g(x)\ln(g(x))dx \tag{18}$$

Now, we can observe meaning of the constant A_0 in (13), *i.e.*, $A_0 = H_x$.

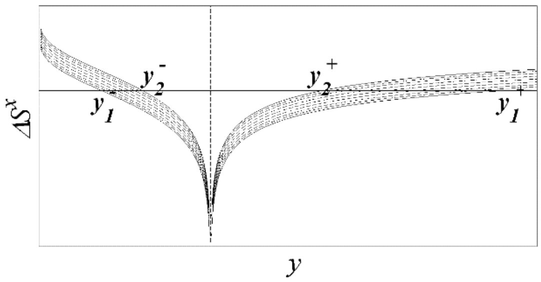

Figure 3. Shannon's entropy ΔS^x *for PSTV. In the plot, designation of the horizontal axis is the same as in the Figure 1, by an ordinate axis Shannon's entropy* ΔS^x *is indicated. The spectrum nodes* $y_1^\pm$ *and* $y_2^\pm$ *match the roots of entropy* ΔS^x*. Allowable* ΔS^x *is located within two dashed area (taken from [24]).*

6. Physical applications of calculated entropy

6.1 Bunch of evolutionary scenarios

As shown in [24], spectrum of Υ at $1/e \leq y \leq e$ becomes discrete

$$y_n = \exp[\pm\frac{1}{n}] \tag{19}$$

where $n = 1,2\ldots$.
Then, from (17), using (19)

$$\Delta S_n = H_x - \ln n \tag{20}$$

and solution for entropy is localized within the area restricted by the roots of ΔS_n (20) for bounds of H_x that, at the same time, are the first and second harmonic of the spectrum (19) as shown in Figure 3 [24].

As the peak of ΔS^x fits to the peak of H_x (18), then according to the principle of maximum entropy production [32], such scenario deals with the most probable and the fastest path of *PSTV* evolution. In Figure 3 appropriate curve crosses the points of the first harmonic of the discrete spectrum, *i.e.*, y_1^- and y_1^+ (Figure 3).

In the same way, minimum ΔS^x fits to the minimum H_x. Then, using [32] one more time, it accommodates requirements for the least probable and the slowest path of evolution. In Figure 3, curve addressing the least probable evolutionary scenario crosses the points of the second harmonic *i.e.*, y_2^- and y_2^+.

The other scenarios fall in the y-range $[y_1, y_2]$ so that the probability of realization decreases from y_1 to y_2.

The more thorough investigation [24] shows that at $y = y_2^\pm$, the probability of evolutionary scenario (assumes quality changes in energy structure of *PSTV*) matches the probability of non-evolutionary scenario (plain mode of receiving and losing of energy). At $|\ln y_1| \geq |\ln y| \geq |\ln y_2|$, probability of the evolutionary scenario is higher, at all other y the non-evolutionary scenario predominates (Figure 3).

6.2 Thermodynamic uncertainty relation

Ratio

$$\Delta E \cdot \Delta(\frac{1}{T}) \geq k_B \tag{21}$$

is known as a thermodynamic uncertainty relation (*TUR*), where k_B denotes the Boltzmann constant, T is temperature, E is energy, and arguments ΔE and $\Delta(1/T)$ could be, generally, replaced with some functions of these arguments [33].

Write $\Delta U = (\Delta U/\Delta T)\Delta T$, then (5.b) can be expressed as

$$\frac{(\Delta U / \Delta T)\Delta T}{Q} = -x \tag{22}$$

Apply to (22) Clausius inequality for entropy [34]

$$\delta Q \leq T\Delta S \tag{23}$$

then it is possible to determine the physical conditions when *TUR* is valid.

6.3 Lower limit for thermodynamic entropy

Recently, the new limiting condition was shaped in nonequilibrium thermodynamics for total entropy rate in Markov jump processes [17,18] dealing with the state arbitrary far from an equilibrium, which could be written as

$$\frac{\dot{S}_t}{2k_B} \geq \frac{<J>^2}{<\delta J>^2} \tag{24}$$

where $\dot{S}_t$ is total entropy rate, $<J>$ is an average flux, $<\delta J>$ is variance of flux fluctuations.

Show that (18) can be stemmed from (2.a,b). So, combine (5.b) with (23), then we obtain

$$\frac{dS}{k_B} \geq \frac{J^2}{2\Delta J^2} \tag{25}$$

Having (25) averaged on the time interval $\tau \sim \Delta t$, and denoting $\dot{S}_t = \Delta S/\Delta t$, we have solution that up to a constant multiple coincides with 24).

So, we see that presented approach (2.b) allows to predict possible way of *PSTV* energy development (section 6.1), provide useful information for working conditions of *TUR* (section 6.2), derive lower entropy constraint in the non-equilibrium thermodynamics (section 6.3). Hence, (2.b) can be considered as a common basis for several physical applications.

7. Discussion

Generalization of physical uncertainties was considered in a number of articles. As shown in [35], in approximation of the highest energies it is possible to bring in to the classic *TUR* an extra term related to the internal energy that causes appearance of the lower boundary for inverse temperature. Technically, eq. (2.b) could be also thought as the consequence of applying to (2.a) some additional uncertainty (energy) which transforms (2.a) to (2.b) and, ultimately, emerges as constraint for Shannon's entropy.

In [36], authors examine collection in which energy E, temperature T and multiplicity N can vary. Then, with the support of non-extensive statistics they suggest interconnection for all varying factors that formalizes the known Lindhard's *TUR* [37]. As it is known, the non-extensive statistics does not use conventional Boltzmann-Gibbs statistical mechanics. The latter seems interesting first of all for study of the objects with complicate structure like nanostructures.

Results [38] presume that an indefinity in the fundamental pattern allows use of the framework of information concept. In this way, it seems acceptable to seek confirmation of uncertainty links using the methods of information concept. We think that it aligned with our analysis in the sections 1.2, 2 where we discussed the "uncertainty" value of (2.b) unlike quite deterministic (2.a).

Presence of resembling entropy limitation was discussed in [17-19,39]. Existence of an uncertainty bound for the small-scale fluctuations in equilibrium thermodynamics, and for the large-scale fluctuations arbitrary far from equilibrium for Markovian processes in non-equilibrium thermodynamics was demonstrated in [17]. In [18], at the nonequilibrium steady states of Markovian processes, a few universal bounds valid beyond the Gaussian regime was derived. Authors [39] declared existence of a new class of thermodynamic uncertainty inequalities, which have revealed that dissipation constrains fluctuations in steady states arbitrarily far from equilibrium. A possible way to come to the identical constraint for the thermodynamic entropy based on (2.b) and Clausius inequality for *PSTV* was demonstrated in [19].

Generalizing the said above in [17-19,39], an entropy constraint for *PSTV* could be given as

$$dS \geq \frac{k_B}{2}\frac{1}{y^2} \tag{26}$$

where $y = <\Delta J>/<J>$.
Integrating (26) on y, we obtain

$$\Delta S \geq -\frac{k_B}{2}\frac{1}{|y|} + C_S \tag{27}$$

where C_S is an integration constant.

Assuming C_S is bounded like H_x in (18), we obtain that solution (27) could also have the quasi-continuous y-

spectrum that in its form (shown in Figure 4) is close to the depicted in Figure 3.

Of course, (17) and (27) are parametrically different equations, however, our purpose is to demonstrate similarity in behavior of these two dissimilar methods.

Novelty of considered approach, primarily, lies in analytic solution of (2.b) and finding of reasonable physical applications for the found solution. Discovered Υ-solution deals with average measure for uncertainty of energy exchange process in open system with infinite number of conserved energy channels with environment, and as such, has natural connection with an entropy. This foundation permits to calculate an increment in Shannon's and differential entropy, as well as study conditions to constrain thermodynamic entropy. Follow this way, it is possible to forecast possible scenarios of energy development in open system, to draw existence of the lower threshold of entropy in the non-equilibrium thermodynamics, and obtain conditions for validity of *TUR*, *i.e.*, describe sufficiently unrelated physical phenomena.

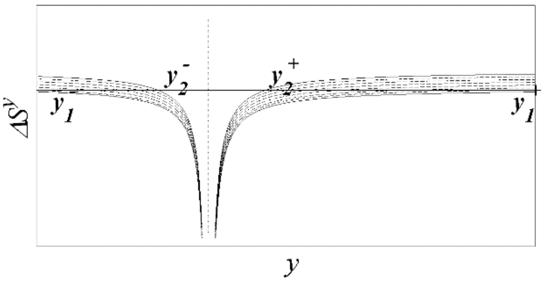

Figure 4. Lower threshold for thermodynamic entropy ΔS^y in PSTV. In the plot, designation of the horizontal axis is the same as in the Figure 1, by the ordinate axis the lower threshold for thermodynamic entropy ΔS^y is indicated. Meaning of the points $y_1^{\pm}$ and $y_2^{\pm}$ is identical to the y-points in the Figure 3.

8. Conclusions

This report presents a nontraditional formalism to Estimate alteration of Shannon's, differential, and thermodynamic entropy in *PSTV* approximation. Found entropy provides a new look at the process of energy exchange in open system with unlimited number of conserved energy links. Generalizing, *PSTV* approximation (2.b) acts as a common basis that demonstrates its value in several dissimilar physical applications.

Nomenclature

ε : *volume energy density[J/m]*^{3}
J : *energy flux* $[J/m^2 \cdot s]$
k_B : *Boltzmann constant [J/K]*
Q : *energy transfer [J]*
t : *time [s]*
T : *absolute temperature [K]*
U : *internal energy [J]*
All other variables are dimensionless.

References:

[1] C. Shannon, "A mathematical theory of communication," *Bell Syst. Tech. J., 27,* 379-423, 1948.

[2] C.E. Shannon, W. Weaver, *The Mathematical Theory of Communication*, v. 1, University of Illinois Press, Urbana, Illinois, 1-131, 1964.

[3] M.A. Nielsen, I.L. Chuang. *Quantum Computation and Quantum Information*, Cambridge University Press, Cambridge, 2000.

[4] E.T. Jaynes, "Information theory and statistical mechanics," *Phys. Rev*., *106 (4)*, 620–630, 1957.

[5] S. Zhang, J. Li. "A bound on expectation values and variances of quantum observables via Renyi entropy and Tsallis entropy*," Int. J. Quantum. Inf., 19,* 2150019, 2021.

[6] J. Acharya, I. Issa, N.V. Shende, A. B. Wagner. "Measuring Quantum Entropy,“ arXiv:1711.00814. 2017.

[7] L. Brillouin, "Science and Information Theory," *Physics Today*, *9(12)*, 39, 1956.

[8] P. Facchi, G. Gramegna, A. Konderak. "Entropy of quantum states," arXiv:2104.12611. 2021.

[9] I. Bialynicki-Birula and J. Mycielski, "Uncertainty relations for information entropy in wave mechanics", *Comm. Math. Phys*. *44*, 129-132, 1975.

[10] F. C. E. Lima, a. R. P. Moreira, c. A. S. Almeida, "Information and thermodynamic properties of a non-hermetian particle ensemble,“ arXiv:2101.04803. 2021.

[11] F. C. E. Lima, a. R. P. Moreira, L.E.S. Machado, A. S. Almeida. "Statistical properties of linear Majorana fermions," *Int. J. Quant. Chem. 121,* e26749, 2021.

[12] F. C. E. Lima. "Quantum information entropies for a soliton at hyperbolic well,|" arXiv:2110.11195. 2021.

[13] R.S. Carrillo, C.A. Gil-Barrera, G.H. Sun, *et al*, "Shannon entropies of asymmetric multiple quantum well systems with a constant total length," *Eur. Phys. J. Plus 136***,** 1060, 2021.

[14] R. Khordad, A. Ghanbari, A. Ghaffaripour.

"Effect of confining potential on information entropy measures in hydrogen atom: extensive and non-extensive entropy," *Indian J. Phys, 94 (12),* 2020.

[15] S. Martiniani, P.M. Chaikin, D. Levine, "Quantifying hidden order out of equilibrium," *Phys. Rev. X 9, 011031*, 2019.

[16] O. Bahadır, H. Türkmençalıkoğlu, "Bilgi Kuramında Shannon Entropisi ve Uygulamaları," Eur. J. Sci. Tech., Special Issue 32, pp. 491-497, 2021.

[13] K.E. Drexler, *Nanosystems: Molecular machinery, Manufacturing, and computation, 1*st *Ed.* Wiley, Hoboken, 576, 1992.

[14] R. Nalewajski, "On entropy/information continuity in molecular electronic states," *Mol. Phys. 114 (1)*, 1225-1235, 2016.

[15] M. Fannes, "Continuity property of the entropy density for spin lattice systems," *Commun. Math. Phys. 31 (4),* 291–294, 1973.

[16] KMR Audenaert, "A sharp continuity estimate for the von Neumann entropy," *J. Phys. A Math. Theor. 40 (28)* 8127-8137, 2007.

[17] T.R. Gingrich, J.M. Horowitz, N. Perunov at al, “Dissipation Bounds All Steady-State Current Fluctuations,” *Phys. Rev. Lett. 116 (12)*, 120601, 2016.

[18] P. Pietzonka P, A. Barato, U. Seifert, “Universal bounds on current fluctuations,” *Phys. Rev., E 93*, 052145, 2016.

[19] A. Moldavanov, “Theoretical Aspects of Radiative Energy Transport for Nanoscale System: Thermodynamic Uncertainty,” *J. Comput. Theor. Trans, 50(3*), 236-248, 2021.

[20] N.W. Tschoegl, *Fundamentals of Equilibrium and Steady-State Thermodynamics*, Elsevier, Amsterdam, 2000.

[21] R. G. Lerner, G.L. Trigg, *Encyclopaedia of Physics 3rd ed.* Wiley-VCH Verlag, Weinheim, 1994.

[22] L.S. Grant, W.R. Phillips, *Electromagnetism, 2nd ed.*, Wiley. Manchester Physics Series, Hoboken, 2008.

[23] R.A. Serway, J.W. Jewett, V. Peroomian, *Physics for scientists and engineers with modern physics. 9th ed*. Pacific Grove: Brooks Cole, 2014.

[24] A. Moldavanov. “Energy Infrastructure of Evolution for System with Infinite Number of Links with Environment,” *BioSystems, 213*, 104607, 2022.

[25] A.V. Moldavanov, “Analytical and Numerical Model for Evolution of Minimal Cell with Infinite Number of Energy Links,”: *Proceedings Mathematical biology and bioinformatics*, Pushino, Russia, *8*, article # e16. doi: 10.17537 /icmbb20.15, 2020.

[26] A. Moldavanov. “Randomized Continuity Equation Model of Energy Transport in Open System,” in *AMSM 2017: Proceedings of the 2017 2nd International Conference on Applied Mathematics, Simulation and Modelling*, 258 – 265, 2017.

[27] D. J. C. MacKay, *Information Theory, Inference, and Learning Algorithms,* Cambridge University Press, Cambridge, 2003.

[28] J.W. Gibbs, *Elementary Principles in Statistical Mechanics*. New York: Dover Publications, 1960.

[29] L. Benguigui, “The different paths to entropy,” arXiv.org Solid State Institute and Physics department Technion Israel Institute of Technology 32000 Haifa. Israel 1-32, 2012.

[30] C. Marsh, “Introduction to Continuous Entropy,” Department of Computer Science, Princeton University.

[31] B.P. Levin, *Theoretical basics of statistical radio engineering. 3rd revised ed.* Radio and communication, Moscow, 1989.

[32] R. Swenson, “Emergent attractors and the law of maximum entropy production: Foundations to a theory of general evolution,” *Syst. Res. 6(3)*, 187–197, 1989.

[33] J. Uffink, J. van Lith. “Thermodynamic uncertainty relations,” *Found. Phys. 29 (5)*, 655-692, 1999.

[34] J.S. Hsieh, *Principles of Thermodynamics*. Washington, D.C.: Scripta Book Company, 1975.

[35] A.E. Shalyt-Margolin, A. Ya. Tregubovich. “Deformed Density Matrix and Generalized Uncertainty Relation in Thermodynamics,” *Mod. Phys. Lett. A. 19(1)*, 71-81, 2004.

[36] G. Wilk, Z. Włodarczyk. “Application of nonextensive statistics to particle and nuclear physics,” *Phys. A: Stat. Mech. Appl. 305 (1-2)*, 227-233. 2002.

[37] J. Lindhard, Complementarity’ between energy and temperature, in *The Lesson of Quantum Theory. edited by de Boer J, Dal E, Ulfbeck O., 99-112,* North-Holland, Amsterdam, 1986.

[38] A. Faigon, “Uncertainty and Information in Classical Mechanics Formulation. Common Ground for Thermodynamics and Quantum Mechanics,” https://arxiv.org/abs/quant-ph/0311153, 2007.

[39] J.M. Horowitz, T.R. Gingrich, ”Thermodynamic uncertainty relations constrain non-equilibrium fluctuations,” *Nat. Phys. 16,* 15–20, 2020.

International Journal of Thermodynamics (IJoT)
ISSN 1301-9724 / e-ISSN 2146-1511
https://dergipark.org.tr/en/pub/ijot

Vol. 25 (No. 3), pp. 055-062, 2022
doi: 10.5541/ijot.1108782

Temperature Dependence of the Entropy and the Heat Capacity Calculated from the Raman Frequency Shifts for Solid Benzene, Naphthalene and Anthracene

H. Yurtseven*, H. Özdemir

Middle East Technical University Physics Depertmant
E-mail: *hamit@metu.edu.tr

Received 25 April 2022, Revised 20 June 2022, Accepted 23 June 2022

Abstract

Temperature dependences of the free energy (F), entropy (S) and the heat capacity (C_v) are calculated (P=0) for the organic compounds (solid benzene, naphthalene and anthracene) by using the quasiharmonic approximation. Contributions to those thermodynamic functions due to the Raman frequencies of lattice modes (solid benzene), librational modes (naphthalene), phonons and vibrons (anthracene) are taken into account in our calculations. We obtain that similar linear increase of F and nonlinear increase of S and C_v, occur with the increasing temperature in benzene and naphthalene. This linear (F) and nonlinear (S, C_v) increase is rather different for anthracene as the molecular structure becomes complex (benzene-naphthalene-anthracene), as expected. Our calculations by the quasiharmonic approximation can be compared with the experiments for those organic compounds.

Keywords: *Quasiharmonic approach; free energy; entropy; heat capacity.*

1. Introduction

Hydrocarbons are the simple organic compounds with the H and C atoms [1] as good fuels occuring naturally. In particular, benzene (C_6H_6) is categorized as the first (elementary) example of the hydrocarbon compounds and in the same family naphthalene ($C_{10}H_8$) and anthracene ($C_{14}H_{10}$) have similar molecular structure as benzene. A number of studies on those hydrocarbons have been published over the years. In particular, for benzene near the phase transitions its thermodynamic properties such as the volume [2-4], specific heat [5-7], thermal expansivity [8] and T-P phase diagrams [3,4,9-11] have been investigated experimentally. We have calculated various thermodynamic functions near the phase changes in benzene as reported previously [12-14]. Spectroscopically, a number of works on the mechanism of phase changes in benzene have been given in the literature. Among those studies, X-ray [3, 4, 15], infrared [4,16-19], fluorescence [20] and Raman [3, 11, 21] spectra of benzene have been obtained experimentally. Raman frequencies near the phase transition in benzene have been evaluated in our earlier studies [22, 23]. Some other theoretical studies and model systems for benzene have been reported [24-28]. More recently, structural properties of solid benzene have been studied experimentally in neutron and x-ray diffraction under high pressure-high temperature conditions and the phase diagram of benzene has been obtained [29]. Also, the solid state structural properties and phase transition (order-disorder) behaviour of benzene derivatives have been studied [30]. Phase diagrams of mixtures of benzene and acetonitrite have been obtained [31]. Very recently, the P-T phase diagram has been constructed to determine the solid, liquid and gaseous states for benzene [32]. Phase transitions in liquid benzene (solid-liquid transition) has been studied by using high-resolution time-resolved Raman spectroscopic technique [33].

Regarding some earlier studies for compounds (naphthalene and anthracene) near the phase changes, measurements of the heat capacity [6, 34, 35] and also Raman [36], neutron scattering [37], X-ray and neutron diffraction [38] studies for naphthalene, have been performed. Using quasi-harmonic approximation, lattice dynamics calculation for naphthalene [39] and the heat capacity prediction using vibration spectra for benzene, naphthalene and anthracene [7] have been made.

For anthracene, some of experimental studies are the following: measurements of thermal conductivity of specific heat [6], pressure dependence of the lattice frequencies [36], wave velocities [40] and determination of the crystalline structure by the high pressure X-ray diffraction [41].

Theoretically, structure and dynamics of anthracene have been studied [42] and using the DFT (density-functional theory) ab initio calculations have been reported [43]. Crystallographic phase transition in anthracene with a large hysteresis has been studied under high pressure [44]. A study on a solid mixture of naphthalene and anthracene at room temperature has also been reported [45]. By differential scanning calorimetry (DSE), a depression of the phase transition temperature was observed [46]. An entropy change in anthracene has been studied [47]. Regarding gas phase of naphthalene, it has been studied at low temperatures [48]. Another study on naphthalene was on its elastic properties, mainly by using the Vinet equation for the P-V phase diagram to obtaine its thermal coefficient [49]. A numerical simulation of naphthalene for the melting and solidification process has been performed [50]. Calculations for the Raman frequencies of naphthalene [51] and anthracene [52] have been reported in our earlier

---

*Corresponding Author

studies. Experimentally, the decomposition of naphthalene, anthracene, pyrene and coronene at high pressures and temperatures have been examined [53]. Ab initio study of the crystal structure, mechanical and acoustic properties of naphthalene and anthracene has been performed [54]. Very recently, anthracene's molecular structure, optical properties and phase transitions have been reviewed [55]. Thermal properties of anthracene-manganese complex have been studied [56]. Also phase transitions in the aromatic naphthalene have been investigated [57].

The three organic compounds (benzene, naphthalene and anthracene) have similar molecular structures and the unit cell parameters which show some differences, can be considered with the differences appearing in the sizes of the molecular units [9]. Structurally, benzene contains Raman active lattice modes and vibrons [3], naphthalene has six librational modes (A_g and B_g) with some other phonon modes [39], similarly anthracene exhibits six phonon modes (A_g and B_g) [36] and nine vibrons [58]. Benzene, naphthalene and anthracene are in the monoclinic phase which changes to another phase as the pressure varies [9]. In both naphthalene and anthracene, decomposition occurs below the triple point whereas in benzene it occurs above that point where the liquid phase meets with the two solid (II and III) phases [2]. Regarding our calculations of the Raman frequencies in our earlier works [51,52], we consiederd the librational modes of $3A_g+3B_g$ as functions of temperature (P=0) and pressure (T=300K) in naphthalene [51]. Also we considered six (A_g+B_g) phonon modes and nine vibrons at various temperatures (P=0) and pressures (T=300K) in anthracene [52]. By means of the mode Grüneisen parameter which relates the vibrational frequencies to the volume changes (with the temperature and pressure), the Raman frequencies of those Raman modes were calculated for both molecular solids (naphthalene and anthracene). By analyzing the observed Raman frequency and volume data from the literature according to the $\vartheta(T,P)$ in the quadratic form, values of the coefficients were first determined. This allowed us to determine the mode Grüneisen parameter for each mode and then the Raman frequencies of those modes were predicted for naphthalene [51] and anthracene [52]. For the solid I-II transition in benzene, similar analysis for the Raman frequencies of the six lattice modes (A,B,C and X,Y,Z) and the volume data from the literature, was conducted to calculate the specific heat C_P of this molecular solid [59]. This calculation of C_P as functions of temperature and pressure was performed by using the thermodynamic relations for benzene. Differently from our earlier studies for the calculation of the Raman frequencies in the naphthalene [51] and anthracene [52], and also the calculation of the specific heat C_P from the Raman frequencies in benzene [59], in the present work by the quasi-harmonic approximation, the vibrational free energy, entropy and the heat capacity are predicted as a function of temperature for those three hydrocarbons (benzene, naphthalene and anthracene). The analysis of the observed Raman frequencies $\vartheta(T)$ from the literature data is performed by using the same functional form (quadratic) with those coefficients determined as given in our earlier publications [51,52 and 59].

This work presents calculation of the thermodynamic quantities (entropy and heat capacity) from the vibrational frequencies of benzene, naphthalene and anthracene by means of the quasi-harmonic approximation. The observed Raman frequencies of those solid systems from the literature, are used to calculate the temperature dependence of the heat capacity as derived from the quasi-harmonic free energy.

Our motivation in this study is to investigate whether those three solid systems (benzene, naphthalene and anthracene) exhibit similar molecular structures thermodynamically. This is of interest for those molecular solids due to increasing complexity of their molecular structures (benzene-naphthalene-anthracene). Our calculations show that the temperature dependence of the free energy, entropy and the heat capacity for benzene and naphthalene behave almost the same, whereas this behaviour is comparatively different for anthracene.

This calculation of S and C_V from the free energy is carried out by using the Raman frequency of the (A,B,C and X,Y,Z) external modes (benzene), six translational A_g and B_g modes (naphthalene) and A_g, B_g modes with the vibrons (anthracene).

Derivation of the entropy and the heat capacity from the free energy is given. By analyzing the experimental Raman data from the literature, entropy and the heat capacity are evaluated at various temperatures for those three substances.

Below, in Section 2, we derive the thermodynamic functions from the free energy by using the Raman frequency shifts. Section 3 gives our calculations. We present discussion in Section 4. Section 5 gives our conclusions.

2. Theory

The method of study is to use the quasi-harmonic approximation for the three hydrocarbons (benzene, naphthalene and anthracene). By considering the vibrational energy which is mainly the frequency dependence of the thermal energy, the temperature dependence of the entropy and the heat capacity can be predicted in those hydrocarbons. Contributions to the free energy due to the vibrational frequencies (Raman frequencies) of various modes in benzene, naphthalene and anthracene are taken into account in the quasiharmonic approximation and those thermodynamic quantities (entropy and heat capacity) can be deduced. Predictions of the free energy, entropy and the heat capacity can be examined by the experimental measurements in those three hydrocarbons.

By using the quasi-harmonic free energy, entropy (S) and heat capacity (C_V) of solid can be obtained at various temperatures Raman frequency shifts of the external modes (benzene), ($3A_g+3B_g$) modes (naphthalene) and, (A_g, B_g) (anthracene) are considered for this calculation.

In general, quasi-harmonic (QH) description of crystals neglects the population driven anharmonic shifts [34]. In particular, we assumed that those three hydrocarbons are harmonic ossilators with the Helmholtz free energy,

$$F = U + \sum_i \frac{h\vartheta_i}{2} + k_B T \sum_i ln\left[1 - exp\left(-\frac{h\vartheta_i}{k_B T}\right)\right] \tag{1}$$

In Eq. (1), i denotes their modes, k_B Boltzmann constant, h is the Planck constant. U is the total potential energy and the second term in Eq. (1) is zero point energy. We represent the frequency dependence of the thermal energy as the third term in Eq. (1), which is the vibrational energy of the crystal.

Thus, the vibrational free energy is defined a

$$F_{vib} = \frac{1}{2}\sum_i h\vartheta_i + k_B T \sum_i ln\left(1 - exp\left(-\frac{h\vartheta_i}{k_B T}\right)\right) \qquad (2)$$

This energy gives rise to the entropy using the definition

$$S = -\left(\frac{\partial F}{\partial T}\right)_V \text{, as}$$

$$S_{vib} = -\left({}^{h}/_{2}\right)\sum_i \left({}^{\partial\vartheta_i}/_{\partial T}\right) + \sum_i \frac{h_{exp}\left(-{}^{h\vartheta_i}/_{k_B T}\right)\left[{}^{\vartheta_i}/_{T} - \left({}^{\partial\vartheta_i}/_{\partial T}\right)\right]}{1-exp\left(-{}^{h\vartheta_i}/_{k_B T}\right)} - k_B \sum_i \ln[1 - exp(-h\vartheta_i/k_B T)] \qquad (3)$$

Also, the C_V (heat capacity) calculated by means of the vibrational entropy S_{vib} (Eq. 3) using the definition

$$C_V = T\left(\frac{\partial S}{\partial T}\right)_V \text{, as}$$

$$C_V = -hc + \sum_i \frac{hexp\left({}^{-h\vartheta_i}/_{k_B T}\right)\left[-\left({}^{2h\vartheta_i}/_{T^2}\right) + {}^{2\left({}^{\partial\vartheta_i}/_{\partial T}\right)}/_{T} - \left({}^{\partial^2\vartheta_i}/_{\partial T^2}\right)\right]}{1-exp\left({}^{-h\vartheta_i}/_{k_B T}\right)} + \sum_i \frac{2hexp\left({}^{-h\vartheta_i}/_{k_B T}\right)\left[{}^{-\left({}^{\partial\vartheta_i}/_{\partial T}\right)}/_{T} + \left({}^{\vartheta_i}/_{T^2}\right)\right]}{1-exp\left({}^{-h\vartheta_i}/_{k_B T}\right)} + \frac{exp\left({}^{-2h\vartheta_i}/_{k_B T}\right)\left({}^{h^2}/_{k_B T}\right)\left[{}^{\vartheta_i}/_{T} - \left({}^{\partial\vartheta_i}/_{\partial T}\right)\right]}{\left[1-exp\left({}^{-h\vartheta_i}/_{k_B T}\right)\right]^2} + \frac{exp\left({}^{-h\vartheta_i}/_{k_B T}\right)\left({}^{h^2}/_{k_B T}\right)\left[{}^{\vartheta_i}/_{T} - \left({}^{\partial\vartheta_i}/_{\partial T}\right)\right]}{1-exp\left({}^{-h\vartheta_i}/_{k_B T}\right)} \qquad (4)$$

3. Calculations and Results

We calculated the temperature dependence of the vibrational free energy (F_{vib}), entropy (S) and the heat capacity (C_V) due to the contributions of the vibrational frequencies (ϑ_i) of benzene, naphthalene and anthracene. For this calculation, we assumed the temperature dependence of the vibrational frequency in the functional form of

$$\vartheta_p(T) = d_0(P) + d_1(P)T + d_2(P)T^2 \qquad (5)$$

where the coefficients d_0, d_1 and d_2 are the pressure dependent in general. By taking those coefficients constant at P=0, they were determined by fitting Eq. (5) to the temperature dependence of the experimental Raman frequencies for benzene, naphthalene and anthracene. This was done for the six lattice modes (A,B,C and X,Y,Z) of benzene by using their observed Raman frequencies [3]. The values of the coefficients d_0, d_1 and d_2 were then determined which we give in Table 1, as also presented in our previous study [59]. By taking $\vartheta_i(T)$ dependence of the six phonon modes of benzene as a sum ($i = 6$) in Eq. (2), we calculated the free energy (F) as a function of temperature as plotted in Figure 1. Similarly, this calculation of the free energy was performed for the six librational modes ($3A_g$+$3B_g$) of naphthalene. By fitting Eq. (5) to the observed Raman frequencies [39] of those modes of naphthalene, we determined the coefficients d_0, d_1 and d_2 as given in Table 2, which we have reported in our earlier study [51]. The vibrational free energy (F_{vib}) was then calculated from the Raman frequencies of the six librational modes of naphthalene as a function of temperature (Eq. 2), which we plot in Figure 1. Also, by determining the coefficients d_0, d_1 and d_2 (Eq. 5) for the six intermolecular (A_g and B_g) and nine intramolecular vibrational modes of anthracene using the observed Raman frequency data [58], which we tabulate in Table 3, as we have given previously [52], we were able to calculate F_{vib} at various temperatures (Figure 1).

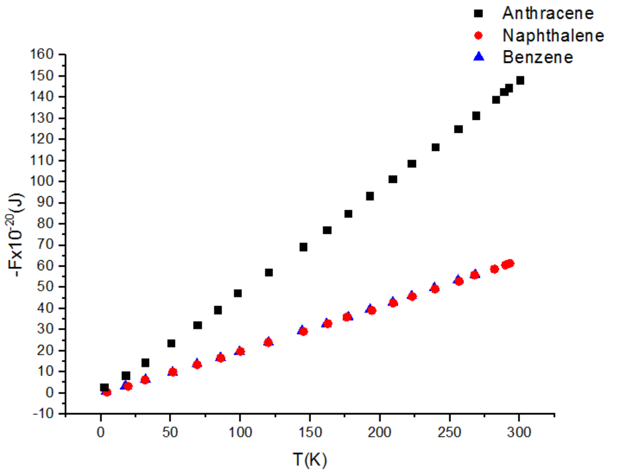

Figure 1. Vibrational free energies calculated as a function of temperature due to of six lattice modes (A,B,C and X,Y,Z) of solid benzene, six librational modes ($3A_g$+$3B_g$) of naphthalene and, six intermolecular (A_g and B_g) and nine intramolecular vibrational modes of anthracene according to Eq. (2).

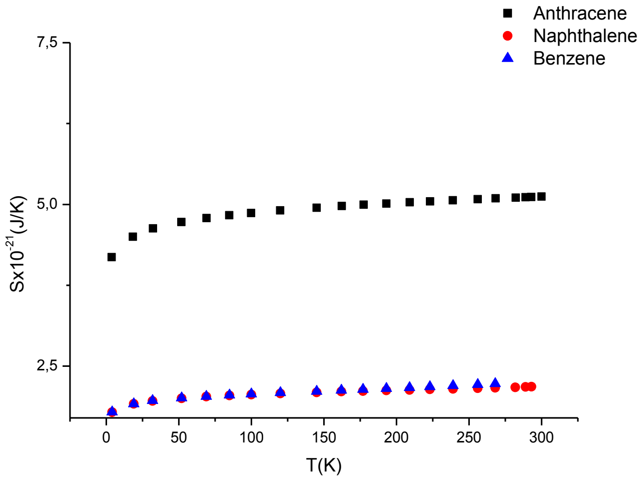

Figure 2. Vibrational entropies calculated as a function of temperature due to of six lattice modes (A,B,C and X,Y,Z) of solid benzene, six librational modes ($3A_g$+$3B_g$) of naphthalene and, six intermolecular (A_g and B_g) and nine intramolecular vibrational modes of anthracene according to Eq. (3).

4. Discussion

Temperature dependences of the vibrational free energy (F), entropy (S) and the heat capacity (C_V) were calculated, as plotted in Figures 1-3, respectively, for the three hydrocarbons studied. We find that the vibrational free energies (F_{vib}) of three hydrocarbons increase linearly and the values of F_{vib} for the anthracene are considerably larger than those of benzene and naphthalene as the temperature increases (Figure 1).

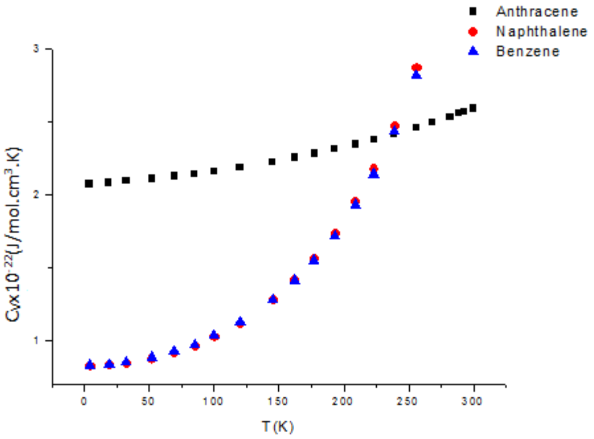

Figure 3. Vibrational heat capacities calculated as a function of temperature due to of six lattice modes (A,B,C and X,Y,Z) of solid benzene, six librational modes (3A_g+3B_g) of naphthalene and, six intermolecular (A_g and B_g) and nine intramolecular vibrational modes of anthracene according to Eq. (4).

Table 1. Values of the coefficients d_0, d_1 and d_2, which were determined by fitting Eq. (8) to the observed Raman frequencies [3] of the modes (A,B,C and X,Y,Z) indicated for the phases I-II of solid benzene (P=0).

Benzene	d_0 $(cm^{-1}/mole)$	$-d_1$ $(cm^{-1}/mole.\mathrm{K})$	$-d_2$ $(cm^{-1}/mole.K^2)$
Mode A	61.42	1.16	2.12
Mode B	70.44	6.46	0.87
Mode C	139.28	6.58	0.23
Mode X	68.79	3.15	0.28
Mode Y	100.30	3.45	2.66
Mode Z	110.91	3.40	2.89

Table 2. Values of the coefficients d_0, d_1 and d_2, which were determined by fitting Eq. (8) to the observed Raman frequencies [39] of the A_g and B_g modes indicated for solid naphthalene (P=0).

Naphthalene	d_0 (cm^{-1})	$-d_1$ $\times 10^{-2}$ (cm^{-1}/K)	$-d_2$ $\times 10^{-4}$ (cm^{-1}/K^2)
Mode A_{g1}	69.35	2.82	1.19
Mode A_{g2}	88.75	1.37	2.64
Mode A_{g3}	121.64	1.24	1.14
Mode B_{g1}	57.36	2.26	0.59
Mode B_{g2}	84.18	1.79	1.05
Mode B_{g3}	142.35	2.65	1.19

Although the F_{vib} increases monotonically, variations of F_{vib} namely, entropy (S) and the heat capacity (C_v) increase non-linearly for the three compounds (benzene, naphthalene and anthracene), with the increasing temperature (Figures 2 and 3). As a result of the larger values of F_{vib} for anthracene compared to those of benzene and naphthalene (Figure 1), the vibrational entropy (S) and the heat capacity (C_v) become significantly larger in magnitude with increasing temperature for anthracene (Figures 2 and 3). Notice that the curves we obtained for benzene and naphthalene in fact overlap for F_{vib}, S and C_v with the lower values in comparison to the anthracene as stated above (Figures 1-3). Thus, the higher values of F_{vib}, S and C_v in anthracene can be considered as in the sequence from benzene and naphthalene towards anthracene in terms of the impact of the increased complexity of molecular structure. This would imply an increase in the number of intramolecular modes of vibration, as also pointed out previously [6], which occurs in anthracene. Changes in the sequence from benzene and naphthalene to anthracene, are large in terms of mass and relatively simple in terms of molecular structure [6]. Depending on the number of atoms (N) per unit cell (N=24, 36 and 48 for benzene II, naphthalene and anthracene, respectively), we considered in our treatment the contributions to the F_{vib}, S and C_v due to the six lattice modes (A,B,C and X,Y,Z) of solid benzene, six librational modes (3A_g+3B_g) of naphthalene and, six intermolecular (A_g *and* B_g) and nine intramolecular vibrational modes of anthracene, as stated above. As shown in Figures (1-3), solid benzene II, naphthalene and anthracene exhibit similar behavior with their simple molecular structures involving one, two and three carbon rings, respectively [6].

Table 3. Values of the coefficients d_0, d_1 and d_2, which were determined by fitting Eq. (8) to the observed Raman frequencies [58] of the intermolecular (A_g and B_g) and intramolecular vibrational modes indicated for solid anthracene (P=0).

Anthracene	d_0 (cm^{-1})	$-d_1$ $\times 10^{-2}$ (cm^{-1}/K)	$-d_2$ $\times 10^{-5}$ (cm^{-1}/K^2)
Intermolecular Vibrational Modes			
A_g	46.26	1.76	2.35
B_g	53.63	1.83	2.57
B_g	81.15	2.93	4.01
A_g	86.76	3.35	4.43
A_g	138.52	4.39	6.37
B_g	149.10	5.04	7.11
Intramolecular Vibrational Modes			
$12A_g$	399.64	0.77	0.50
$10B_{3g}$	523.17	0.24	0.50
$10A_g$	756.61	0.54	1.16
$9A_g$	1011.26	0.48	0.98
$8A_g$	1166.13	0.22	0.56
$7B_{3g}$	1190.35	0.45	1.20
$7A_g$	1265.75	0.97	2.19
$6A_g$	1407.31	0.92	1.84
$4A_g$	1560.26	0.47	1.02

For the calculation of the vibrational F, S and C_v , the quasi-harmonic approximation was used due to the Raman frequency shifts of the vibrational modes of solid benzene, naphthalene and anthracene. The quasiharmonic shifts may be related to the deformation of the lattice known as the deformation shifts and the anharmonicity can also be caused by the phonon-phonon interactions [37]. The anharmonic shift can be determined from the temperature dependence of phonon frequencies at a fixed volume [60], as stated above. It has been obtained experimentally that at ambient pressure and for temperatures up to 300 K, the shifts for most low-frequency modes are dominated by quasi-harmonic effects [37].

In our earlier study [52], we have compared the variation of the Raman frequencies of intramolecular (internal) modes with the intermolecular (external modes) as functions of temperature and pressure in anthracene. This is accompanied with the mode Grüneisen parameter which measures the anharmonicity in a crystalline system, as indicated previously. We have found that the values of the mode Grüneisen parameter for the six intermolecular modes are much larger than those of nine intramolecular vibrational modes of the solid anthracene (between 3 and 4 for the intermolecular modes and between 0.03 and 0.2 for the intramolecular modes) [52]. Thus, the anharmonicity which occurs as the relation between the thermal expansion (isothermal compressibility) and the variation in frequency with temperature (pressure) in anthracene, is dominated by the lower-frequency modes (external modes) as in the benzene and naphthalene.

The heat capacity C_v which we calculated as a function of temperature overlaps for benzene and naphthalene whereas the calculated C_v of anthracene exhibits completely different behaviour although all C_v's increase nonlinearly with the temperature (Figure 3) as stated above. On the other hand, we found that the heat capacity C_p which we calculated [59] for the I-II transition in benzene and naphthalene (P=0) differed from the C_v for those two compounds (Figure 3). For both calculations of C_p and C_v, we used the observed Raman frequencies of six lattice modes (A,B,C and X,Y,Z) of solid benzene [3] and six librational modes ($3A_g$+$3B_g$) of naphthaline [39] at various temperatures. For the calculation of C_p, by means of the temperature-induced Raman frequency shifts of those modes and the volume $V_p(T)$, the isobaric mode Grüneisen parameter (γ_p) at P=0 was determined for the Raman modes studied in benzene and naphthalene [59]. Similarly, the pressure-induced Raman frequency shifts of the modes which were studied and the volume V_T(P), were employed by extracting the isothermal mode Grüneisen parameter (γ_T) to calculate the C_p at various pressures (T=300K) for the I-II transition in benzene and naphthalene [59]. Those pressure-induced frequency shifts are directly related to the large initial compressibility κ_T of benzene as a typical molecular crystal [4]. This also applies to the solid naphthalene and anthracene. It has also been pointed out that under the pressure applied to molecular solids such as benzene, the intermolecular interactions can be compared in magnitude to intramolecular ones [3]. Due to the fact that for the calculation of C_p the change in the slopes of the ϑ-P curves of the modes I,II and III as lattice modes, is significant compared to the internal modes in benzene, which we have reported [61] as also pointed out previously [4], we expect similar behaviour of the C_v for the solid benzene and naphthalene. This is because of the fact that we used in our C_v calculation also the Raman frequencies of six lattice modes (benzene) and six librational modes (naphthalene) as stated above. For the C_v calculation of anthracene since we used the Raman frequencies of six intermolecular (external) and nine intramolecular (internal) vibrational modes, we expect rather different behaviour of C_v as a function of the temperature (Figure 3). Consequently, decrease in the Raman frequencies with the increasing temperature can be attributed to the thermal expansion (α_p) increasing. Also, increase in the Raman frequencies decreases the isothermal compressibility (κ_T) with the increasing pressure by means of the isothermal mode Grüneisen parameter (γ_T). This results in the heat capacity C_p which becomes larger than C_V according to the thermodynamic relation

$$C_p = C_v + TV\left({\alpha_p}^2/_{\kappa_T}\right) \tag{6}$$

for the molecular solids, in particular, benzene and naphthalene.

As we calculated the temperature dependence of the free energy (F), entropy (S) and the heat capacity (C_V) for solid benzene, naphthalene and anthracene from the temperature-induced Raman frequency shifts, the pressure dependence of those thermodynamic functions can also be calculated using the pressure-induced Raman frequency shifts in the three hydrocarbon substances by means of the quasiharmonic approximation. As we calculated F, S and C_V due to the Raman frequency shifts of intermolecular and intramolecular vibrational modes as a function of temperature (P=0), those thermodynamic quantities can also be calculated at various pressures (T=300K). They can then be compared with the measurements for solid benzene, naphthalene and anthracene.

5. Conclusion

Vibrational energy (F_{vib}), entropy (S) and heat capacity (C_v) were evaluated at various temperatures using the Raman data for the external modes (benzene), ($3A_g$+$3B_g$) modes (naphthalene) and, (A_g and B_g) modes and vibrons (anthracene) by means of the quasiharmonic approximation. We find that the vibrational free energy increases linearly, whereas its variation (entropy and heat capacity) increases non-linearly with increasing temperature (P=0) in the sequence of benzene to naphthalene to anthracene.

Our calculated values for the free energy, entropy and the heat capacity by using the quasiharmonic approximation, can be compared with the experimental measurements for solid benzene, naphthalene and anthracene. The quasiharmonic approximation can also be applied to some other hydrocarbons such as the phenanthrene, a more stable isomer of the anthracene.

Using the experimental Raman frequencies, the pressure dependence of the F_{vib}, S and C_v can also be calculated using quasiharmonic approximation for those organic compounds. The quasiharmonic approximation can be applied to some other organic compounds.

Nomenclature

C_v	Heat capacity at constant volume [J/mol.cm^3.K]
F	Free energy [J]
F_{vib}	Vibrational free energy [J]

h	Planck constant [J.s]
k_B	Boltzman constant [J/K]
P	Pressure [Pascal]
S	Entropy [J/K]
T	Temperature [K]
U	Potential energy [J]
ϑ	Frequency $[s^{-1}]$
ϑ_p	Frequency at constant pressure $[s^{-1}]$
γ_T	Grüneisen parameter [-]
κ_T	Isothermal compressibility [J/K]
α_p	Thermal expansion $[K^{-1}]$

Subscript

A_g and B_g	Librational modes
A,B,C and X,Y,Z	Lattice modes
QH	Quasi-harmonic
C	Carbon
H	Hydrogen

References:

[1] G. A. Olah and Á. Molnár, Hydrocarbon Chemistry (Wiley Interscience, Hoboken, NJ, 2003).

[2] P. Figuiere, A. H. Fuchs, M. Ghelfenstein & H. Szwarc, 'Pressure-volume-temperature relations for crystalline benzene.' *Journal of Physics and Chemistry of Solids*, 39, 19-24, 1978.

[3] M. M. Thiery and J. M. Leger. "High pressure solid phases of benzene. I. Raman and x- ray studies of C6H6 at 294 K up to 25 GPa." *The Journal of chemical physics*, 89, 4255-4271, 1988.

[4] L. Ciabini, F. A. Gorelli, M. Santoro, R. Bini, V. Schettino & M. Mezouar, 'High-pressure and high-temperature equation of state and phase diagram of solid benzene.' *Physical Review B*, 72, 1-7, 2005.

[5] R. G. Ross, P. Andersson & G. Bäckström, 'Thermal conductivity and heat capacity of solid phases of benzene under pressure.' *Molecular Physics*, 38, 377-385, 1979.

[6] R. G. Ross, P. Andersson & G. Bäckström, 'Thermal conductivity and heat capacity of benzene, naphthalene and anthracene under pressure.' *Molecular Physics*, 38, 527-533, 1979.

[7] N. Sallamie & J.M. Shaw, 'Heat capacity prediction for polynuclear aromatic solids using vibration spectra.' *Fluid phase equilibria*, 237, 100-110, 2005.

[8] P. Pruzan, D. H. Liebenberg & R. L. Mills, 'Experimental evidence for a second-order transformation prior to melting in ammonia, organic compounds and ice I.' *Journal of Physics and Chemistry of Solids*, 47, 949-961, 1986.

[9] S. Block, C.E. Weir & G. J. Piermarini, 'Polymorphism in benzene, naphthalene, and anthracene at high pressure.' *Science*, 169, 586-587, 1970.

[10] J. Akella & G. C. Kennedy, 'Phase diagram of benzene to 35 kbar.' *The Journal of Chemical Physics*, 55, 793-796, 1971.

[11] F. Cansell, D. Fabre & J.P. Petitet,' Phase transitions and chemical transformations of benzene up to 550 C and 30 GPa.' *The Journal of chemical physics*, 99, 7300-7304, 1993.

[12] H. Yurtseven & E. Sevinç, Pressure dependence of the thermodynamic quantities in phase II of solid benzene. *High Temperature Materials and Processes*, 32, 421-425, 2013.

[13] H. Yurtseven & K. Savaş, Temperature dependence of the thermodynamic quantities near the solid I-II phase transition in benzene. *J Single Mol Res*, 2, 67, 2014.

[14] O. Tari & H. Yurtseven, 'Variation of the molar volume with the temperature and the Pıppard relations near the melting point in benzene.' *Journal of Molecular Liquids*, 220, 883-887, 2016.

[15] E. G. Cox, 'Crystal structure of benzene.' *Reviews of Modern Physics*, 30, 159,1958.

[16] Y. A. Sataty, A. Ron & M. Brith, 'Far-infrared lattice vibrations of crystalline benzene.' *Chemical Physics Letters*, 23, 500-503,1973.

[17] P. Pruzan, J. C. Chervin, M. M. Thiery, J. P. Itie, J. M. Besson, J.P. Forgerit & M. Revault, 'Transformation of benzene to a polymer after static pressurization to 30 GPa.' *The Journal of chemical physics*, 92, 6910-6915, 1990.

[18] L. Ciabini, M. Santoro, R. Bini & V. Schettino, 'High pressure photoinduced ring opening of benzene.' *Physical review letters*, 88, 1-4, 2002.

[19] L. Ciabini, M. Santoro, F. A. Gorelli, R. Bini, V. Schettino & S. Raugei, 'Triggering dynamics of the high-pressure benzene amorphization.' *Nature materials*, 6, 39-43, 2007.

[20] M. Citroni, R. Bini, P. Foggi & V. Schettino, 'Role of excited electronic states in the high-pressure amorphization of benzene.' *Proceedings of the National Academy of Sciences*, 105, 7658-7663, 2008.

[21] Ghelfenstein & H. Szwarc, 'Raman Spectra in Molecular Solids I. A study of Low Frequency Modes as a Funcit of Temperature.' *Molecular Crystals and Liquid Crystals*, 14, 273-281, 1971.

[22] Ö. Tari, H. Yurtseven, 'Raman frequencies calculated at various pressures in phase I of benzene', J. Korean Chem. Soc. 57 ,204-209,2013.

[23] Ö. Tari, H. Yurtseven,'Calculation of the Raman frequencies as a function of temperature in phase I of benzene,' J. Ind. Chem. Soc., 90 ,821-824,2013.

[24] A. Gobbi, Y. Yamaguchi, G. Frenking, H. F. Schaefer, 'The role of σ and π stabilization in benzene, allyl cation and allyl anion. A canonical orbital energy derivative study.' *Chemical Physics Letters*, 244, 27-31, 1995.

[25] A. G. Csaszar, W. D. Allen, H. F. Schaefer III, 'In pursuit of the ab initio limit for conformational energy prototypes,' *J. Chem. Phys.*, doi.org/10.1063/1.476449.

[26] Y. Xie, H. F. Schaefer III, F. A. Cotton,' The radical anions and the electron affinities of perfluorinated benzene,naphthaline and anthracene,' *Chem. Commun.* 20 ,102,2013.

[27] D. Moran, A. C. Simmonett, F. E. Leach, W. D. Allen, P. V. R. Schleyer & H. F. Schaefer, 'Popular theoretical

methods predict benzene and arenes to be nonplanar.' *Journal of the American Chemical Society*, 128, 9342-9343, 2006.

[28] R. Engelke, P. J. Hay, D. A. Kleier, W. R. Wadt, 'A theoretical study of possible benzene dimerizations under high- pressure conditions.' *The Journal of chemical physics*, 79, 4367-4375, 1983.

[29] A. D. Chanyshev, K. D. Litasov, S. V. Rashchenko, Y. Higo, 'High-pressure-high-temperature study of benzene, refined crystal structure and new phase diagram up to 8 GPa and 923 K', *Crystal Growth Design*, doi.org/10.1021/acs.cgd.8b00125.

[30] Y. Zhou, R Patterson., P. A. Williams, B. M. Kariuki, C. E. Hughes, R. Samanta, and K. D. Harris, 'Temperature-dependent structural properties, phase transition behavior, and dynamic properties of a benzene derivative in the solid state', *Crystal Growth & Design*, 19, 2155-2162, 2019.

[31] C. A.McConville, Y. Tao, H. A. Evens, B. A. Trump, J. B. Lefton, W. Xu, A. A. Yakovenko, E. Kraka, C. M. Brown, T. Runcevski, 'Peritectic phase transition of benzene and acetonitrite into a corystal relevant to Titan, Saturn's moon', ChemComm 56, 13520-13523, 2020.

[32] B. Ibrahimoglu, D. Uner, A. Veziroglu, F. Karakaya, B. Ibrahimoglu, 'Construction of phase diagram to estimate phase transitions at high pressures: a critical point at the solid liquid transition for benzene', *Int. J. Hydrogen Energy*, 46, 15168-15180, 2021.

[33] U. Rao, S. Chaurasin, A. K. Mishra, J. Pasley, 'Phase tansitions in benzene under dynamic and static compression', *J. Raman Spectroscopy*, 52, 770-781, 2021.

[34] J.P. McCullough, H.L. Finke, J.F. Messerly, S.S. Todd, T.C. Kincheloe, G. Waddington, 'The low-temperature thermodynamic properties of naphthalene, l-methylnaphthalene, 2-methylnaphthalene, 1, 2, 3, 4-tetrahydronaphthalene, trans-decahydronaphthalene and cis-decahydronaphthalene.' *The Journal of Physical Chemistry*, 61, 1105-1116, 1957.

[35] R.D. Chirico, S.E. Knipmeyer, W.V. Steele, 'Heat capacities, enthalpy increments, and derived thermodynamic functions for naphthalene between the temperatures 5 K and 440 K.' *The Journal of Chemical Thermodynamics*, 34, 1873-1884, 2002.

[36] D.A. Dows, L. Hsu, S.S. Mitra, O. Brafman, M. Hayek, W.B. Daniels, R.K. Crawford, 'Pressure dependence of the lattice frequencies of anthracene and naphthalene.' *Chemical Physics Letters*, 22, 595-599, 1973.

[37] E.F. Sheka, E.L. Bokhenkov, B. Dorner, J. Kalus, G.A. Mackenzie, I. Natkaniec, G.S.Pawley, U. Schmelzer, 'Anharmonicity of phonons in crystalline naphthalene.' *Journal of Physics C: Solid State Physics*, 17, 5893-5914, 1984.

[38] S.C. Capelli, A. Albinati, S.A. Mason, B.T.M. Willis, 'Molecular motion in crystalline naphthalene: analysis of multi-temperature X-ray and neutron diffraction data.' *The Journal of Physical Chemistry A*, 110, 11695-11703, 2006.

[39] R.F. Della Valle, E. Venuti, A. Brillante, 'Pressure and temperature effects in lattice dynamics: the case of naphthalene.' *Chemical physics*, 198, 79-89, 1995.

[40] M. Fukuhara, A. H. Matsui, M. Takeshima, 'Low-temperature elastic anomalies in an anthracene single crystal.' *Chemical Physics*, 258, 97-106, 2000.

[41] M. Oehzelt, G. Heimel, R. Resel, P. Puschnig, K. Hummer, C. A. Draxl, K. Takemura K, A. Nakayama, 'High pressure x-ray study on anthracene.' *The Journal of chemical physics*, 119, 1078-1084, 2003.

[42] C. M. Gramaccioli, G. Flippini, M. Simonetta, S. Ramdos, G. M. Parkinson, J. M. Thomas, 'Structure and dynamics of a new phase of anthracene.' *Journal of the Chemical Society, Faraday Transactions 2: Molecular and Chemical Physics*, 76, 1336-1346, 1980.

[43] K. Hummer, P. Puschnig, C. A. Draxl, 'Ab initio study of anthracene under high pressure.' *Physical Review B*, 67, 1-7, 2003.

[44] R. Resei, M. Oehzeit, K. Shimizu, A. Nakayama, 'On the phase transition in anthraceneinduced by high pressure', *Solid State Commun.*, 129, 103-106, 2004.

[45] D. Liu, J. P. Lang, B. F. Abrahams, ' Highly efficient separation of a solid mixture of naphthalene and anthracene by a reusable porous metal-organic framework through a single-crystal to single crystal transformation', *J. Am. Chem. Soc.*, 133, 11042-11045, 2011.

[46] J. A. Lee, H. Rösner, J. P. Corrigan, Y. Huang, 'Phase transitions of naphthalene and its derivatives confined in mesoporous silicas', *J. Phys. Chem. C*, 115, 4738-4748, 2011.

[47] C. Fontanesi, 'Entropy variation in the two-dimensional phase transition of anthracene adsorbed at the H_g electrode/ethylene glycol solution interface', *Entropy*, 12, 570-577, 2010.

[48] D. S. N. Parker, F. Zhang, Y. K. Kim, A. G. G. M. Treleris, 'Low temperature formation of naphthalene and its role in the synthesis of PAHs (polycylic aromatic hydrocarbons) in the interstellar medium', *PNAS*, 109, 53-58, 2011.

[49] A. V. Likhacheva, S. V. Rashchenko, A. D. Chanyshev, T. M. Inerbaev, K. D. Litasov, D. S. Kilin, 'Thermal equation of state of solid naphthalene to 13 GPa and 773 K: in situ X-ray diffraction study and first principles calculations', *J. Chem. Phys.*, doi.org/10.1063/1.4871741.

[50] L. Yang, H. Peng, X. Ling, H. Dong, ' Numerical analysis on performance of naphthalene phase change thermal storage system in aluminum plate-fin unit', *Heat Mass Transfer*, 31, 195-207, 2015.

[51] H. Özdemir and H. Yurtseven, 'Raman frequency shifts calculated from the volume data in naphthalene.' *Journal of Molecular Structure*, 1090, 65-69, 2015

[52] H. Özdemir and H. Yurtseven, 'Temperature and pressure dependence of the Raman frequency shifts in

anthracene.' *Indian Journal of Pure & Applied Physics*, 54, 489- 494, 2016.

[53] A. D. Chanyshev, K. D. Litasov, A. Shatskiy and I. Sharygin, 'Transititon from melting to carbonization of naphthalene, anthracene, pyrene and coronene at high pressure', *Phys. Earth Planetary Interiors*, doi.org/10.1016/j.pepi.2017.06.011.

[54] T. L. Prazyan, Y. N. Zhuraviev, 'Ab initio study of naphthalene and anthracene elastic properties', *Int. J.Mod.Phys.C*,doi.org/10.1142/S0129183118500249

[55] Y. Hino, T. Matsuo and S. Hayashi, ' Structural phase transitions in anthracene crystals', *Plus Chem*, doi.org/10.1002/cplu.202200157.

[56] Ji-X. Hu, Q. Li, H. L. Zhu, Z. Ni. Gao, Q. Zhang, T. Li, G.-M. Wang, 'Achieving large thermal hysteresis in an anthracene-based manganese (II) complex via photo-induced electron transfer', *Nature Commun*., 13, 1-9, 2022.

[57] W. M. Zoghaib, C. Carboni, M. E. Molla, S. Al-Mahrezi, T. Al-Slahumi, S. Al-Badi, M. Al-Farsi, 'Phase transition investigations of a series of aromatic naphthalene-2-yl-4-(alkoxy) benzoate and naphthalene-1-yl-4-(alkoxy) benzoate materials', *World J. Cond. Matter. Phys.*, 12, 1-7, 2022.

[58] L. Zhao, B. J. Baer, E. L. Chronister, 'High-pressure Raman study of anthracene.' *The Journal of Physical Chemistry A*, 103, 1728-1733, 1999.

[59] H. Yurtseven and H. Özdemir, 'Calculation of the specific heat using the Raman frequency shifts for the solid I–II transition in benzene.' *Journal of Molecular Structure*, 1090, 53-57, 2015.

[60] F. D. Medina, 'Temperature dependence of the far IR spectrum of α- N2.' *The Journal of Chemical Physics*, 72, 5760-5762, 1980.

[61] H. Özdemir and H. Yurtseven, 'Pressure dependence of the Raman frequencies for the modes I, II and III at constant temperatures in phase II of benzene', *Journal of Molecular Structure*, 1080, 117-121, 2015.

International Journal of Thermodynamics (IJoT)
ISSN 1301-9724 / e-ISSN 2146-1511
https://dergipark.org.tr/en/pub/ijot

Vol. 25 (No. 3), pp. 064-073, 2022
doi: 10.5541/ijot.1108911

Entropic Assessment of Sleeping Comfort

D. Kayali[1], Y. Yavuz[2], B. Yilmaz[3], M. Özilgen[4*]

[1,4] Yeditepe University, Department of Food Engineering, 34755 Atasehir, Istanbul, Turkey
[2,3] Yeditepe University, Faculty of Medicine, Department of Medical Physiology, 34755 Atasehir, Istanbul, Turkey
E-mail: [1]denizkayali98@gmail.com, [2]yavuz.yavuz@yeditepe.edu.tr, [3]byilmaz@yeditepe.edu.tr,
[4*]mozilgen@yeditepe.edu.tr

Received 5 May 2022, Revised 17 July 2022, Accepted 18 July 2022

Abstract

In the literature longevity and comfort are evaluated in terms of entropy generation and export rates. When people cannot export entropy, they experience discomfort. Effect of bedding, pajamas and levels of body coverage have been assessed in 270 cases by referring to body weight and height of 25 years old women. By 160 cm tall and 50 kg women, at 0 °C of room temperature, entropy export rates were $6.0\text{x}10^{-3}$ and $7.4\text{x}10^{-3}$ W/kg K, while they were sleeping on their back and on the side, respectively. The results showed that entropy export became more difficult as the body temperature approached the room temperature. Textile properties, including heat transfer and wicking rates of sweat removal were also important while exporting the entropy. The results of this study may be employed while designing beds or beddings, pajamas and comforters to achieve a more comfortable sleeping environment.

Keywords: *Sleeping preferences; metabolic heat generation rate; entropy generation rate; sweating, heat transfer rate; woolen and cotton pajamas.*

1. Introduction

1.1. Physiology of sleeping

Adult humans need approximately 7-8 hours of night sleep to be active during the day and to avoid illness such as cardiovascular diseases, diabetes, stroke and dementia [1]. Organisms live at far-from-equilibrium with their surroundings while maintaining homeostasis, importing exergy and exporting entropy [2]. Homeostatic mechanisms (mechanisms, which keep the internal conditions of the body constant) generate switching impulses to initiate sleep when a person is awake for a long time. In 24 hours of daily cycle, wakefulness and sleep stages are kept in balance with homeostatic effects [3]. Autonomic nervous system (ANS), somatomotor system that control the movements of the body and neuroendocrine systems, e.g., the hormonal system that operate under the effect of the neurons, work in co-ordination to maintain homeostasis. The sleep process consists of the deep sleep (non-rapid eye movement, NREM) and the rapid eye movement (REM) phases [4]. ANS activity regulates switches from the awake to sleep and NREM to REM sleep stages. During the NREM sleep, metabolic needs decrease in connection with the decrease in the biological activity and the ANS reflexes; hence, physiological functions (such as heart rate, respiratory frequency, body temperature and metabolic parameters) fall to the lowest level [5]. In NREM sleep, parasympathetic system is more active than sympathetic system. In the REM sleep, phasic cardiovascular events develop and thermoregulation is suppressed, the ANS becomes unstable because of the phasic changes in sympathetic and parasympathetic discharges. Circadian regulation of sleep and other body functions is processed by neurons located in the hypothalamic suprachiasmatic nucleus (SCN) [5]. Signals from the thermoreceptors are transmitted to the brain that collateralize to the lateral parabrachial nucleus (LPB) in the brain stem and thalamus [6]. Thermal information received in the thalamus is relayed to the somatosensory cortex, where it mediates the perception and discrimination of temperature [7]. Thermal input to the LPB is projected to the neurons in the hypothalamic preoptic area (POA) where thermoregulation is processed to maintain a stable core body temperature [8].

The sleep-wake cycle is associated with heat loss and heat generation during the circadian cycle. In the first half of the night's sleep, energy expenditure and body temperature decrease gradually and then remain constant in the other half. Energy expenditure decreases during sleep, but when the sleep phases are evaluated within themselves, more energy is spent during REM compared to NREM, since the brain activity is higher during REM [5]. Sleep and wakefulness are regulated by different brain regions. The brain-stream-neurotransmitter systems such as noradrenaline, acetylcholine, serotonin and dopamine project to various parts of the brain to support wakefulness [9]. The hypothalamus plays important roles in three basic processes related to sleep. The first includes the SCN and controls the circadian cycle. Secondly, it is the chief regulator of the ANS that controls several vegetative functions including the body temperature [10]. The third role involves production of histamine and orexin neuromodulators that promote wakefulness.

All sensory information is transmitted through thalamus then projects to the brain cortex (except a part of the olfactory sensation that directly feeds to the sensory cortex)

---

*Corresponding Author

[11, 12]. Continuous flow of sensory input to the brain cortex is important to maintain consciousness. During sleep, transmission of sensory information to the brain cortex is reduced.

Changes in the body temperature follow a sinusoidal rhythm, and the core body temperature reaches a minimum value between 04:00-06:00 am under physiological conditions. The transition to sleep is closely related to the core body temperature, and the minimum decrease in core body temperature begins 5-6 hours before falling sleep. Reduction of the core temperature overlaps with maximum sleepiness in circadian rhythm. Wakefulness occurs 1-3 hours after the minimum body temperature begins to rise within the physiological range [13].

Melatonin is an indolamine hormone produced by the pineal gland and released into blood circulation [14]. It has a circadian rhythm and released during the dark phase of the day, reaching a peak between 02:00-04:00am. Serum melatonin levels start to increase 2-3 hours prior to sleep and reaches its maximum level during the middle of sleep. Melatonin secretion decreases after waking up (i.e., when light falls on the retina) and reaches to its minimum levels during the middle of the day [15].

1.2. What is the resting energy expenditure?

More than half of the daily-consumed energy is the resting energy expenditure. In the resting state, energy is used for the maintenance of vital functions. While 20-30% of the energy expenditure is for voluntary activity, 5-10% is spent for thermogenesis. The main methods used in energy expenditure measurement are direct calorimetry, indirect calorimetry and predictive equations. Indirect calorimetry is based on the energy consumed by measuring the amount of oxygen consumed and the amount of carbon dioxide produced. The resting energy expenditure constitutes about 60-75% of the total daily energy expenditure. Energy expended during the rest is spent on basal metabolic processes. The key indicator is the lean mass. For this reason, it is less in women than men are and in the elderly compared to young people. The thermal effect of food and physical activity increase resting energy expenditure [16]. Lean mass consists of bones, skeletal muscles, active organs such as the brain, heart, liver, kidney, and digestive organs. High cardio-pulmonary work increases resting energy expenditure [17]. The time spent in the initiation and in the following stages of sleep affects the metabolism. Energy expenditure and RQ increase during slow wave sleep, NREM's first and second stages, REM and wake after sleep onset. While RQ and carbohydrate oxidation decreases in the first half of sleep, it increases in the second half of sleep [18].

1.3. What is thermoregulation?

Thermoregulation involves both behavioral and autonomic processes. Tremor and sweating are behavioral responses superimposed on the autonomic responses [19]. In order to maintain the core body temperature, heat gain and heat loss must be in balance. During removal of heat from the body, blood flow from the core to the peripheral areas increases. Therefore, heat transfer per unit time increases and a positive thermal gradient occurs. Heart rate and heat production are directly proportional in active state [3]. Prior to sleeping, the core-body temperature declines and heat is dissipated out. Vasodilation (enlargement of the veins) occurs in the arteriovenous anastomoses and blood flow increases and heat is removed from the body. Arteriovenous anastomoses are available intensely in the distal areas of the body, such as hands, feet, nose, ears and lips [15]. They maintain the core body temperature. They are affected by environmental temperature and behavioral factors. While thermoregulation is active in the NREM process, it gradually decreases during the REM process. Responses such as sweating or shivering are generated against environmental conditions. The need to sleep and the first stage of NREM is associated with a decrease in core body temperature and an increase in peripheral body temperature. While awake, proximal temperature is higher than distal temperature. As desire to sleep increases, core temperature declines, distal temperature increases, and the two of them become almost equal and sleep begins at the point where they are equal. Melatonin hormone plays a role in the occurrence of these changes and as a result induces hypothermia (decrease of the body temperature) [20]. It is known that hypothermia occurs also during anesthesia [21].

1.4. Sensory perception of thermal stimulation and central control

Thermoreceptors transform cold and warmth stimuli into action potentials that are transported to the central nervous system [8, 12]. The thermal signals are first transmitted to the spinal cord and projected to the sensory cortex through thalamus. The hypothalamus receives input from the LPB and functions as the brain center that integrates peripheral and visceral thermal signals and maintains the body temperature [3]. Neurons in the POA of the hypothalamus serve as the thermostat that process, regulate heat loss, and heat gain mechanisms.

1.5. Efferent responses

When POA receives an unusual heat input, it generates an error signal and initiates homeostatic responses [3]. Input coming to POA is transmitted to physiological and behavioral effectors via rostral medulla. Neurons originating from the medulla activate peripheral sympathetic and parasympathetic responses. Physiological effectors affected by neurons are brown adipose tissue thermogenesis, control of skin blood flow, tremors and evaporation [8].

1.6. Respiration

At the beginning of sleep, air volume, inspired / exhaled per minute rate (minute ventilation) and tidal volume decrease. During NREM, ventilation is regular, there are no obvious changes, and minute ventilation is gradually reduced. During REM, the respiratory rhythm is irregular [5].

1.7. The effect of ambient temperature on sleep?

Warm environments negatively affect sleep quality [1]. Thermal comfort depends primarily on the microclimate of the bed and secondly on the ambient temperature. Warm environment affects sleep worse than cold environment. The sleeping set reduces the temperature change of the bedding environment and improves the sleep quality [4]. Sleep quality depends on the thermal insulation of the bedding microclimate rather than the ambient temperature. Bedding microclimate with good thermal insulation protects sleep quality [22].

1.8. Effects of cold environment

When the thermal insulation of the bedding environment is insufficient, the cold ambient temperature negatively affects the sleep quality [22].

1.9. Effects of warm environment

High ambient temperature decreases the sleep, the REM, and the slow wave sleep (SWS) times, and increases falling asleep time and awareness. Additionally, adaptation to sleep is low at high temperatures [23].

1.10. Bedding Environment

The sheets used, the clothes worn and the percentage of the body covered by these covers change the total insulation of the bedding system. Therefore, the insulation of the sheets affects the indoor thermal neutral temperature for the sleeping person [23]. Thermal properties of bedding and sleeping clothes should be steady state and permeable to ambient temperature. The microclimate of naked sleeping persons consists of skin and sheet. In the case of wearing sleepwear, there are two microclimates; one is between the skin and the sleepwear and the other is between the sleepwear and the sheet [4]. The human body needs to maintain its core temperature between 36.0 and 37.5 °C for physiological functioning. When the core exceeds this range, eccrine sweat glands begin to produce sweat. When the skin is not clothed, evaporation of the sweat absorbs 2.4 kJ of heat per gram and cools the body. However, when the body is clothed, the sweat may wick into the clothing. In such a case, evaporation slows done, and the cooling efficiency is reduced [24].

1.11. Heat and entropy generation while sleeping

Heat is generated within the body in association with metabolism [25]. The "*entropic age*" concept suggests that ageing related changes in the body, such as loss of molecular functions and overwhelming of the maintenance systems, may be explained in terms of entropy generation [26, 27]. Silva and Annamalai [28] and Annamalai and Silva [29] made significant contribution to this area of research by quantifying the entropy generation related ageing stress on individual organs. Maintaining easy release of $\dot{q}$ has been an active research topic to evaluate human comfort at different temperature and humidity levels [30, 31] by each gender (Molliet and Mady 2021) [32]. Most of the body heat is dispersed into the universe, and the fraction of it, which causes the cellular damage, reveals itself as entropy accumulation [33, 34]**.** Entropy, which is generated this way throughout the life span is called "*life span entropy*" and associated with life expectancy.

1.12. Sweating

Sweating is controlled by the hypothalamus. It allows the body to release excessive heat via evaporative cooling at the skin. Heat absorbed by the blood at the core of the body is transported to the skin and then removed via evaporation. While the body attempts to cool down with evaporative cooling, its response to high temperature is similar to its response to fever [35], where vasodilation and increased heart rate and contractility to support the heat transfer. It has been reported that sweating is less in REM process. In NREM process, the higher the ambient temperature, the higher the skin temperature and the sweating rate [4]. In the present study, effect of sleeping preferences on the caloric expense and entropy generation of 25-year-old women will be evaluated by referring to 270 different cases. The height and the weight of the women will be referred as the biological parameters, sleeping on the back or on the side, room temperature, coverage of the body with woolen or cotton pajamas or comforter and the heat transmission properties of the bed as the sleeping preferences.

2. Methods

Calculations were carried out for 25 years old women, who were 1.60, 1.70 and 1.80 m tall and 50, 55 and 60 kg, respectively. They were covering 30, 50 or 70% of their bodies with 0.8 mm thick woolen pajamas and comforters at 0 and 10 °C and 0.8 mm thick cotton pajamas and comforters at 20 °C. They were wearing cotton pajamas but not using comforters at 30 and 40°C while sleeping. The pajamas had a thickness of 0.80 mm; thermal conductivity of wool was 50.4 mW/m K, heat transfer coefficient 60 W/m^2 K. The thick wool comforter had a thickness of 37.3 mm, thermal conductivity of 39.9 mW/m K, and heat transfer coefficient 10.7 W/m^2 K. Thin cotton comforter had a thickness of 0.8 mm. Temperature of the room, where they slept was 0, 10, 20, 30 or 40 °C and there was no moisture accumulation in the rooms. Heat transfer coefficients of the fabrics were adapted from Holcombe and Hoschke [36]. Natural heat transfer coefficients of different parts of the body were obtained from De Dear et al [37].

At 0, 10, 20 and 30 ℃ Eq 1 was employed to describe heat transfer from the body, under these conditions temperature difference between the body and the environment was the driving force for the heat release from the body and sweating was not an effective heat transfer mechanism at these temperatures. At 40 ℃ environmental temperature was above the body temperature; therefore, evaporative cooling was considered as the dominant mechanism at this temperature. First law of thermodynamics has been employed to describe the energy balance around the sleeping women in (**Figure 1**):

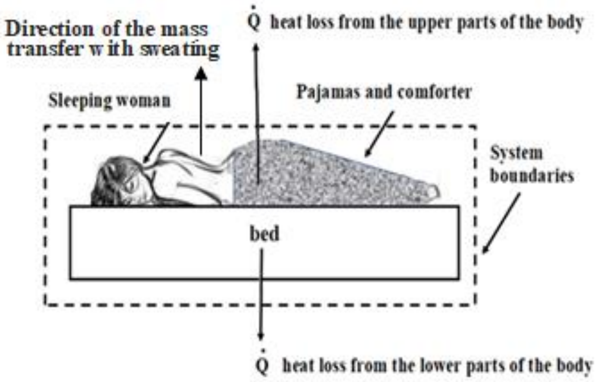

Figure 1. Schematic description of the sleeping woman as a thermodynamic system. In Bed1, Bed2 and Bed3 $\dot{Q}$ pertinent to lower part of the bed is 10%, 20% and 30% of those of the upper parts, respectively.

$$\sum_{\mathrm{in}}[\dot{m}(h+e_p+e_k)] - \sum_{\mathrm{out}}[\dot{m}(h+e_p+e_k)] + \sum \dot{Q} + \dot{W} = \frac{d[m(u+e_p+e_k)]_{\mathrm{system}}}{dt} \qquad (1)$$

In **Figure 1**, $\dot{m_{in}} = \dot{m_{out}}$ and e_p and e_k are negligibly small when compared to u; therefore, equation (1) reduces to the following form:

$$\sum \dot{Q} + \dot{W} = \frac{d[m(u)]_{system}}{dt} \tag{2}$$

When temperature is 30 °C or less, Eq 3 describes the heat removal rate from the body:

$$\dot{Q} = U(A)(\Delta T) \tag{3}$$

Where, U = Total heat transfer coefficient.
A= heat transfer area
ΔT= difference between ambient temperature and body temperature.

Since the surface area, heat transfer coefficients and thermal conductivity of different parts of the body are different, the U values for each part are calculated as:

$$\frac{1}{U(\frac{W}{Km^2})} = \frac{1}{h(\frac{W}{Km^2})} + \frac{x_1(mm)}{k_1(\frac{mW}{Km})} + \frac{x_2(mm)}{k_2(\frac{mW}{Km})} \tag{4}$$

At temperatures 0, 10, 20 and 30 °C equation (1) describes heat loss from the body, and sleeping related entropy transfer rate due to heat transfer through the surface at these temperatures may be described as

$$\dot{s} = \frac{\dot{Q}}{m\,T} \tag{5}$$

when temperature is 40 °C, heat released from the body was adapted from McMurray et al [38], after assuming that all the heat generated in the metabolism is released through sweating. McMurray et al [38] after making a complete review of literature concluded that the mean value for resting metabolic rate was 4.85 W/kg, with 95% confidence limits of 4.79 – 4.91 W/kg. We employed the mean value of the heat released from the body in our calculations.

3. Results and Discussion

Being subject to extremely cold and wet environment causes hypothermia. Shivering is a natural response of the body to hypothermia. When the core body temperature decreases to less than 35 °C shivering heats up the body and relaxes the muscles. Basal metabolic rate of the body may increase to compensate the energy loss. Results presented in this study are valid for the cases that the core body temperature do not fall below 35 °C. The rate of a multi-step cascade-like process would be the same as that of its slowest step [39]. The body temperature is constant, as maintained by the hypothalamus. Height and weight of the women and the apparent heat transfer coefficient U, as described by equation (4), would be influential in determining the heat transfer rates from the body, when conduction and convection are the dominant heat transfer mechanisms. In equation (2) $\dot{W}$ is the internal work performance rate. In the biological systems, work is needed to be done within the system to maintain the essential activities to keep the system living. Work performed by the heart for pumping of the blood or by the lungs for respiration or by the liver for the chemical activities or by the kidneys for re-absorption and secretion processes, along with the electrical work of the nervous system are all regarded as the internal work. In addition, the synthesis of the entire mass of muscles and the bones are some examples to the "i*nternal work*". At environmental temperatures between 0 to 30 °C the body may be able to perform more internal work than that of 40°C in addition to exporting heat. At 40°C, the body may experience a heat shock. The body responds to heat shock by expressing heat shock proteins, to help prevent or reverse protein misfolding and provide an environment for proper folding [40]. At 0, 10, 20 and 30 °C there was heat transfer between the body and the room, however at 40 °C there was mass (sweat) transfer from the body to the room through the pajamas and the bedding, evaporation of the sweat cooled the body.

In the present study, heat removal rate from the surface of the body was regarded as the rate-limiting step. **Figures 2-4** include two different modes of heat transfer from the body. At 0, 10, 20 and 30°C heat removal from the body was achieved via conduction and convection from the skin; whereas at 40°C heat removal was achieved with evaporative cooling from the skin. There was no sweating at 0, 10, 20 and 30°C. Heat transfer with conduction and convection from the skin is a passive process, where the body does not need to perform extra work. However, evaporative cooling is an active process; at 40 °C, heat is transported from the core to the surface with increased rate of blood circulation, which require an additional work performance by the body [41].

Figures 1-4 show that at 40°C substantially higher heat is removed from the body and substantially higher entropy is generated. Pajamas and the beddings considered in this study were made of natural fibers with wicking ability [24]. Those fabrics transport sweat to the surface with wicking and were assumed not to interfere with the heat removal process. The mechanism of the heat transfer would be substantially more complicated and the results of this study would be substantially different, if synthetic fibers, with no wicking ability were employed in this study. At 40 °C, heat release by 25-year-old 160 cm tall, 50 kg women is 242.5 W; by 170 cm tall, 55 kg women is 266.75 W and by 180 cm tall, 60 kg women is 291 W. Specific entropy generation rates by all of these women is constant and $15.57x10^{-3}$ W/kg K.

People generally prefer sleeping on the side [42]. Schrödinger [43], Prigogine and Wiame [44] and Demirel [45], Yildiz et al [2] among many others, argued that organisms live at far-from-equilibrium by up taking energy or exergy, and exporting entropy. Entropy may be regarded as the unusable energy dissipated through molecular vibrations [46] and exporting entropy may be considered as a type of pollution [47]. Both exergy analyses and entropy generation are based on the second law of thermodynamics. Özilgen [48] evaluated the comfort related studies in detail in his review on biothermodynamics and indicated that the pioneers of these studies were air-conditioning engineers. Aoki [49, 50] focused on entropy removal from the environment as the purpose of comfort studies. This approach has been followed by many others. Lucia and Grisolia [51] described in detail that exergy destruction in a process could be calculated as the product of the environmental temperature and the irreversibility related entropy generation. In the present study, we preferred following the Aoki's approach.

Figures 1-4 show that more entropy is exported from the body, when people sleep on their sides. Entropy generation rates by 160 cm tall, 50 kg and 25 years old women are compared in Figure 2. At 0°C of room temperature, entropy generation rate is less in the case of sleeping on the back (Figure 2a) than that of the case of sleeping on the side

(Figure 2b). At 0 degree of room temperature, entropy generation rate is 6.0x10^{--3} W/kg K while the woman is sleeping on her back and 7.4x10^{--3} W/kg K while sleeping on the side. Difference between both sleeping positions is not negligible. As the room temperature increases, entropy generation rates decreased. When the room temperature is reached 30℃, entropy generation rates are nearly same for both sleeping positions and the difference is negligible. At 30℃ of room temperature, entropy generation rate is 1.2x10^{-3} W/kg K while she is sleeping on her back and 1.4x10^{-3} W/kg K while sleeping on her side. As the room temperature increases, entropy generation rates increase for both sleeping positions. When the room temperature reaches to 40℃, entropy generation rates are same in both sleeping positions. At 40℃ room temperature, entropy generation rates are 15.57x10^{-3} W/kg K for both sleep positions.

In Figure 3, comparison is made for different sleeping position and bed preferences for a 170 cm tall, 55 kg, 25-years-old women. In **Figure 3a**, while she is sleeping on her back, entropy generation rate increased as the heat permeability of the bed increased at 0℃ of room temperature. For bed1 with the heat permeability of 0.1, the entropy generation rate is 5.4x10^{-3} W/kg K, and the entropy generation is 6.3x10^{-3} W/kg K in bed3 while heat transfer rate from the bed is 30% of that from the upper sides of the body. Entropy generation rate is 6.3x10^{-3} W/kg K for bed1 while heat transfer rate from the bed is 10% of that from the upper sides of the body and 7.4x10^{-3} W/kg K with bed3. For both sleeping positions, as the room temperature increased, the entropy generation rates decreased, regardless of the bed preferred. When the room temperature is 30℃, entropy generation rates are almost the same, when different beds are preferred in both sleeping positions. At 40℃ of room temperature, entropy generation rate is the same and 15.57x10^{-3} W/kg K for both sleeping positions in all types of beds.

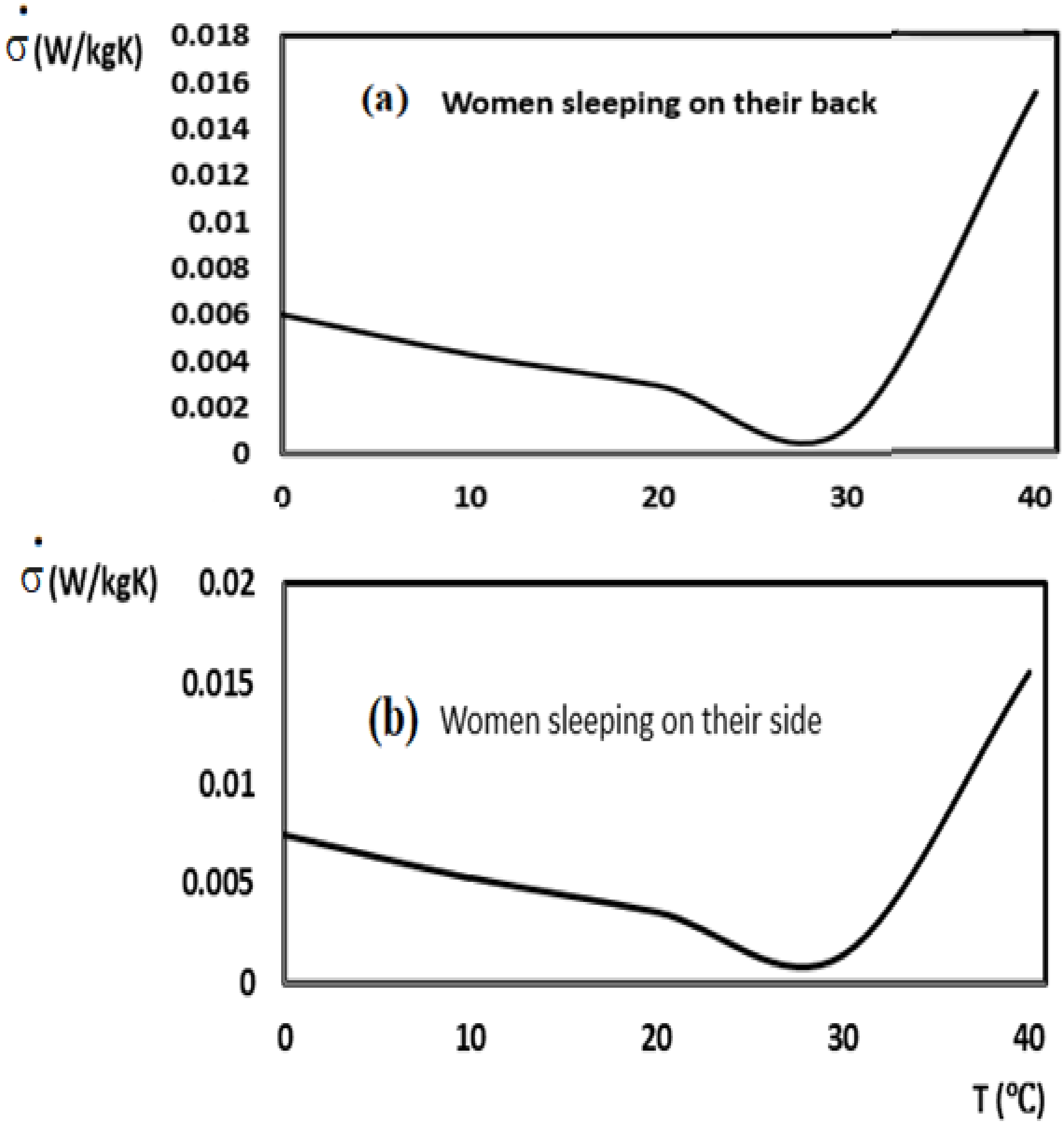

Figure 2. Specific entropy generation rate versus the room temperature, when 160 cm tall, 50 kg and 25-year-old women sleep on their back ***(a)*** *and on their side* ***(b)*** *in bed1 when ϕ=0.30.*

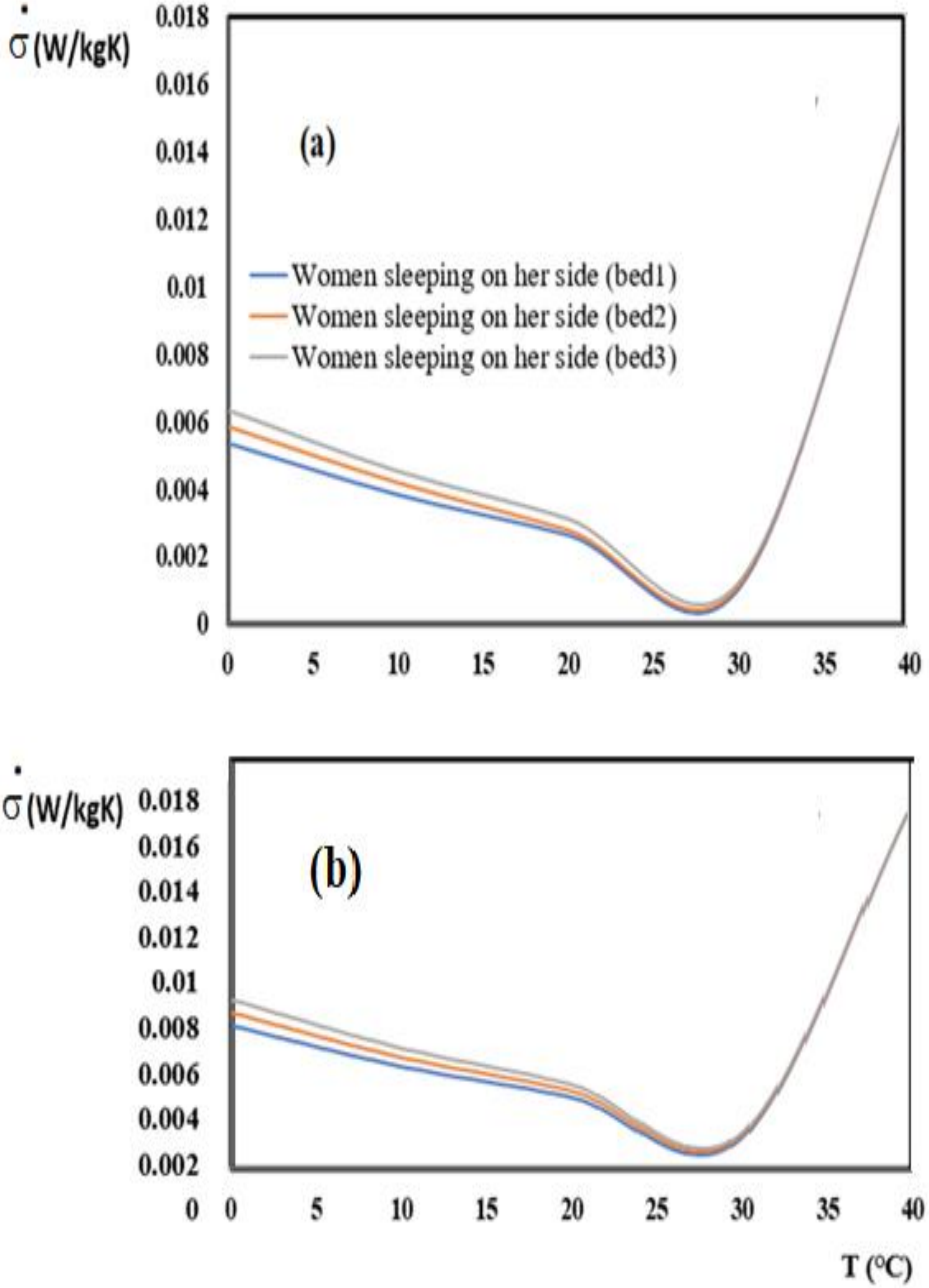

*Figure 3. Specific entropy generation rate versus the room temperature when 170 cm tall, 55 kg and 25-year-old women sleep on their back **(a)** and on the side **(b)**, in bed1, bed2and bed3 when ϕ=0.50.*

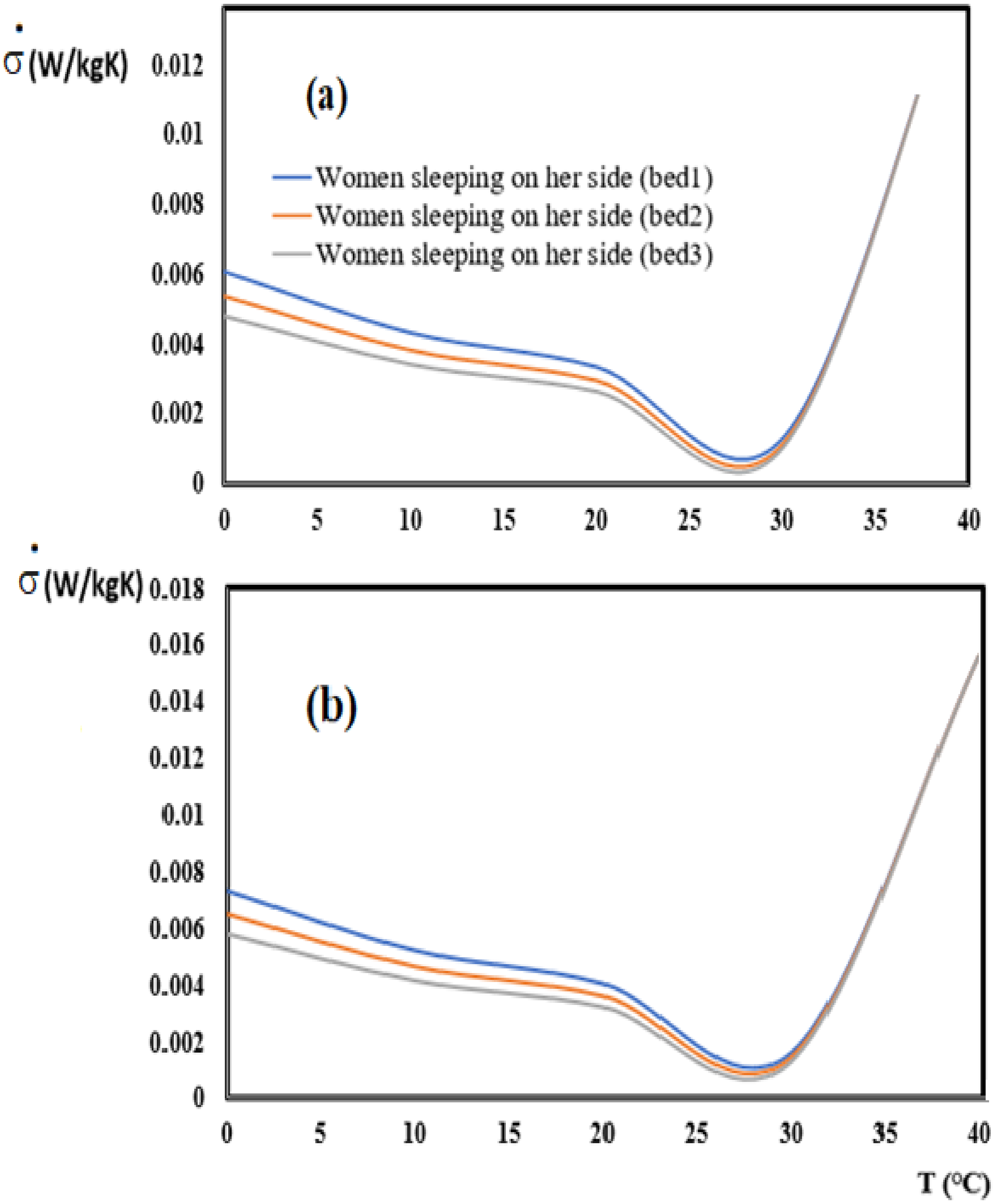

Figure 4. Specific entropy generation rate versus the room temperature, when 25-year-old 160 cm tall, 50 kg, 170 cm tall 55 kg and 180 cm tall 60 kg women sleep on their back ***(a)*** *and on their side* ***(b)*** *in bed3 when ϕ=0.70 (fraction of the body covered).*

Entropy generation rates for 25 years old sleeping women with different body compositions and sleeping positions are compared in Figure 4. At 0°C of room temperature, entropy generation rates decreased as the height and weight of the women increased. For a 160 cm tall and 50 kg sleeping women, entropy generation rate is 6.1x10^{-3} W/kg K and for a 180 cm, 60 kg sleeping women, entropy generation rate is 4.8x10^{-3} W/kg K. The same conditions are valid for sleeping on her side (Figure 4b). As the room temperature increases gradually, entropy generation rates decrease for every body type and sleep positions. Women with higher height and weight have a lower entropy generation rate for both sleeping positions at 30°C of room temperature, but the difference between them is quite small and may be ignored. When the room temperature increased from 30°C to 40°C, entropy generation rate increases. At 40°C room temperature, entropy generation rate is the same, 15.57x10^{-3} W/kg K, for both sleeping positions and all body types.

4. Conclusion

By 160 cm tall old 50 kg old women, at 0 °C of room temperature, entropy exporting rate was 6.0x10^{--3} and 7.4x10^{--3} W/kg K, while the women were sleeping on the back and on the side, respectively. As the room temperature increased, entropy export rates decreased. When the room temperature reached to 30°C, entropy export rates were nearly the same for both sleeping positions. At 30℃ of room temperature, entropy export rates were $1.2\text{x}10^{-3}$ and $1.4\text{x}10^{-3}$ W/kg K while sleeping on the back and on the side, respectively. At 40℃ room temperature, entropy export rates were $15.57\text{x}10^{-3}$ W/kg K for both sleep positions. For a 170 cm tall, 55 kg, 25-years-old women, while she was sleeping on her back, entropy export rate increased with the heat permeability of the bed. For both sleeping positions, as the room temperature increased, the entropy export rates decreased, regardless of the bed preferred. At 40℃ of room temperature, entropy generation rate was the same and $15.57\text{x}10^{-3}$ W/kg K for both sleeping positions in all types of beds. The results of this study may be employed while designing better comforting beds, sleepwear comforters and bed sheets.

Nomenclature

e_p potential energy entering in to the system or leaving out with $\dot{m}_{in}$ or $\dot{m}_{out}$

e_k kinetic energy entering in to the system or leaving out with $\dot{m}_{in}$ or $\dot{m}_{out}$

h enthalpies entering in to the system or leaving out with $\dot{m}_{in}$ or $\dot{m}_{out}$

h heat transfer coefficient of the naked body ($\frac{\mathrm{W}}{\mathrm{Km}^2}$)

k_1 heat transfer coefficient of the pajamas (W/mm

k_2 heat transfer coefficient of the comforter (W7mm)

$\dot{m}_{in}$ input rate of the mass through the system boundaries

$\dot{m}_{out}$ output rate of the mass through the system boundaries (kg)

m weight of the woman (kg)

$\dot{Q}$ = Rate of heat released by the body to the environment ($\mathrm{W/m^2}$)

u chemical energy of the woman (J/kg)

U total heat transfer coefficient from the body $\left(\frac{\mathrm{W}}{\mathrm{m}^2}\right)$

$\dot{W}$ Rate of work performance by the body, since the woman is asleep, the work done equals to the resting metabolic rate.

References:

[1] D. I. Rifkin, M.W. Long, M.J. Perry. "Climate change and sleep: A systematic review of the literature and conceptual framework." *Sleep Med Rev*, 42,3–9, 2018; *https://doi.10.1016/j.smrv.2018.07.007*.

[2] C. Yildiz, V.A. Bilgin, B Yilmaz, M. Özilgen, M. "Organisms live at far-from-equilibrium with their surroundings while maintaining homeostasis, importing exergy and exporting entropy." *Int. J. Exergy,* 31 (3), 287-300, 2020; *https://doi.10.1504/ijex.2020.10027921*.

[3] S.S. Gilbert, C.J. van den Heuvel, S.A. Ferguson, D. Dawson, "Thermoregulation as a sleep signalling system," *Sleep Med. Rev.*, 8(2), 81–93, 2004; *https://doi.10.1016/S1087-0792(03)00023-6*.

[4] O. Troynikov, G.C. Watson, N. Nawaz. "Sleep environments and sleep physiology: A review." *J. Therm. Biol.*, 78(2),192–203,2018; *https://doi.10.1016/j.jtherbio.2018.09.012*.

[5] G. Zoccoli, R. Amici, R. "Sleep and autonomic nervous system." *Curr. Opin. Physiol.*, 15, 128–133, 2020; *https://doi.10.1016/j.cophys.2020.01.002*.

[6] J.L. Hylden, F. Anton, R.L. Nahin, "Spinal lamina I projection neurons in the rat: collateral innervation of parabrachial area and thalamus." *Neuroscience*, 28(1) 27-37, 1989; *https://doi.10.1016/0306-4522(89)90229-7*.

[7] A.D. Craig, A.D., M.C. Bushnell, E.T. Zhang, A. Blomqvist. "A thalamic nucleus specific for pain and temperature sensation." *Nature*, 372(6508), 770-773, 1994; *https://doi.org/10.1038/372770a0*.

[8] L.C. Tan, Z.A. Knight, Z.A. "Regulation of body temperature by the nervous system." *Neuron*, 98(1), 31–48, 2019; *https://doi.10.1016/j.neuron.2018.02.022*.

[9] A.S. Tubbs, H. K. Dollish, F Fernandez, M.A. Grandner, "*The basics of sleep physiology and behavior*." Elsevier, 2019, USA.

[10] S. Tekin, Y. Erden, S. Sandal, E. Etem Onalan, F. Ozyalin, H. Ozen, B. Yilmaz. "Effects of apelin on reproductive functions: relationship with feeding behavior and energy metabolism." *Arch Physiol Biochem*, 123: 9-15, 2017.

[11] L.M. Kay, S.M. Sherman. "An argument for an olfactory thalamus." *Trends Neurosci.* 30(2). 47-53, 407; *https://doi.10.1016/j.tins.2006.11.007*.

[12] J. Hall, M. Hall, M. "Guyton and Hall Textbook of Medical Physiology". 14th Ed., Elsevier, USA, 2020.

[13] R. Szymusiak. Body temperature and sleep. *Handb Clin Neurol.* 156:341-351, 2018.

[14] I. Kuş, B. Yılmaz, B, H. Öner, M. Ögetürk, H. Keleştimur. "Ultrastructural examination of the mutual interrelationship between the pineal gland and the testis in the male rat." *Arch Androl*, 45(2), 119-124, 2000; *https://doi.10.1080/014850100418819*.

[15] L.C. Lack, M. Gradisar, E.J.W. van Someren, H.R. Wright, K. Lushington. "The relationship between insomnia and body temperatures," *Sleep Med. Rev.* 12(4), 307–317, 2008; *https://doi.10.1016/j.smrv.2008.02.003*.

[16] I. Aklan, N. Sayar Atasoy, Y. Yavuz, T. Ates, I. Coban, F. Koksalar, et al. "NTS catecholamine neurons mediate hypoglycemic hunger via medial hypothalamic feeding pathways." *Cell Metab.* 31(2) 313–326.e5, 2020; *https://doi.10.1016/j.cmet.2019.11.016*

[17] D.C. Fonseca, P. Sala, B. de Azevedo Muner Ferreira, J. Reis, R.S. Torrinhas, L. Bendavid, D.L. Waitzberg, D.L. "Body weight control and energy expenditure," *Clin. Nutr. Exp.*, 20, 55-59, 2018; *https://doi.10.1016/j.yclnex.2018.04.001*.

[18] I. Park, M. Kayaba, K. Iwayama, H. Ogata, Y. Sengoku, K. Tokuyama, M. Satoh, M. "Relationship between metabolic rate and core body temperature during sleep in human." *Sleep Med.*, 16(suppl. 1), S186-S187, 2015; *https://doi.10.1016/j.sleep.2015.02.1377*.

[19] R.D. Fealey, R.D. "Interoception and autonomic nervous system reflexes thermoregulation." *Handb. Clin. Neurol.* 117, 79-88 2013; *https://doi.10.1016/B978-0-444-53491-0.00007-9*.

[20] K. Satoh, K. Mishima. Hypothermic action of exogenously administered melatonin is dose-dependent in humans. *Clin. Neuropharmacol.* 24(6), 334-340, 2001; *https://doi.10.1097/00002826-200111000-00004*.

[21] B. Yilmaz, D.P. Gilmore, C.A. Wilson, C.A. "Inhibition

of the pre-ovulatory LH surge in the rat by central noradrenergic mediation: Involvement of an anaesthetic (urethane) and opioid receptor agonists". *Biogenic. Amines*, 12, 423-435, 1996.

[22] K. Tsuzuki, Y. Mochizuki, K. Maeda, Y. Nabeshima, T. Ohata, V. Draganova, V. "The effect of a cold environment on sleep and thermoregulation with insufficient bedding assuming an emergency evacuation." *Energy Build.*, 207(109562), 1-8, 2020; *https://doi.10.1016/j.enbuild.2019.109562*.

[23] L. Lan, K. Tsuzuki, Y.F. Liu, Y.F. Z.W. Lian. "Thermal environment and sleep quality: A review," *Energy Buildings*, 149, 101–113, 2017; *https://doi.10.1016/j.enbuild.2017.05.043*.

[24] K. Hey-sang, S. Michielsen, E. Den Hartog. "Wicking in textiles at rates comparable to human sweating." *Colloids Surf. A Physicochem. Eng. Asp.*, . 622(126726),1-9, 2021; *https://doi.10.1016/j.colsurfa.2021.126726.*

[25] M.E. Öngel, C. Yıldız, C. Akpınaroğlu, B. Yilmaz, M. Özilgen M. "Why women may live longer than men do? A telomere-length regulated and diet-based entropic assessment" *Clin. Nutr.*, 40(3), 1186–1191, 2021; *https://doi.10.1016/j.clnu.2020.07.030*.

[26] L. Hayflick (2007). "Biological aging is no longer an unsolved problem." *Ann. N. Y. Acad. Sci.*, 1100(1), 13, 2007; *https://doi.10.1196/annals.1395.001.*

[27] M.E. Todhunter, R.W. Sayaman, M. Miyano, M. M.A. LaBarge. "Tissue aging: the integration of collective and variant responses of cells to entropic forces over time." *Curr. Opin. Cell Biol.*, 54, 121–129, 2018; *https://doi.10.1016/j.ceb.2018.05.016.*

[28] C. Silva, K. Annamalai, K. "Entropy generation and human aging: Lifespan entropy and effect of physical activity level." *Entropy*, 10,(2), 100–123, 2008; *https://doi.10.3390/entropy-e10020100.*

[29] K. Annamalai, C. Silva. "Entropy stress and scaling of vital organs over life span based on allometric laws." *Entropy*, 14(12), 2550–2577, 2012; *https://doi.10.3390/e14122550.*

[30] H. Caliskan. "Energetic and exergetic comparison of the human body for the summer season." *Energy Convers.* 76, 169-176, 2013*; doi.org/10.1016/j.enconman.2013.07.045.*

[31] C.E.K. Mady, M.S. Ferreira, J.I., Yanagihara, P.H.N. Saldiva, S de Oliveira Jr. "Modeling the exergy behavior of human body." *Energy*, 45(1), 546-553, 2012; *https://doi.org/10.1016/j.energy.2012.02.064.*

[32] D.S. Molliet, CEK Mady, "Exergy analysis of the human body to assess thermal comfort conditions: comparison of the thermal responses of males and females", *Case Stud. Therm. Eng.*; 25(100912), 1-8, 2021*; https://doi.org/10.1016/j.csite.2021.100972*.

[33] F. Mete, E. Kilic, A. Somay, B. Yilmaz. "Effects of heat stress on endocrine functions and behavior in the pre-pubertal rats." *Ind J Med Res.*, 135(2), 233-239, 2012.

[34] C. Yildiz, A.S. Semerciöz, B.H. Yalçinkaya, T.D. Ipek, E. Öztürk-Özışık, M. Özilgen M. "Entropy generation and accumulation in biological systems." *Int. J. Exergy* 33(4), 444-468 2020; *https://doi.10.1504/IJEX.2020.111691.*

[35] C.M. Blatteis. "Fever: pathological or physiological, injurious or beneficial?" *J. Therm. Biol.*, Vol. 28(1), 1-13, 2003; *https://doi.org/10.1016/S0306-4565(02)00034-7.*

[36] B.V. Holcombe, B.N. Hoshke. "Dry heat transfer characteristics of underwear fabrics," *Text. Res. J.*, 53(6), 368–374, 1983; *https://doi.10.1177/004051758305300608*.

[37] R.J. De Dear, E. Arens, Z. Hui, M. Oguro. "Convective and radiative heat transfer coefficients for individual human body segments." *Int. J. Biometeorol.*, 40(3), 141–156, 1997; *https://doi.10.1007/s004840050035.*

[38] R.G. McMurray, J. Soares, C.J. Caspersen, T. McCurdy, T. "Examining variations of resting metabolic rate of adults: A public health perspective." *Med Sci Sports Exerc.*, 46(7), 1352–1358, 2014; *https://doi.10.1249/MSS.0000000000000232.*

[39] M. Özilgen. *"Handbook of Food Process Modeling and Statistical Quality Control,"* CRC Books, 2nd ed. Taylor and Francis, USA, 2011.

[40] J. Weibezahn, C. Schlieker, P. Tessarz, A. Mogk, B. Bukau. "Novel insights into the mechanism of chaperone-assisted protein disaggregation. "*Biol. Chem*. Vol 386(8), 739–744, 2005; *https://doi.10.1515/BC.2005.08.*

[41] J. Karjalainen, M. Viitasalo. "Fever and cardiac rhythm." *Arch. Intern. Med., 14,(*6), 169-171, 1986; *https://doi.10.1001/archinte.1986.00360180179026.*

[42] E.S. Skarpsno, P.S. Mork, T.I.L. Nilsen, A. Holtermann. "Sleep positions and nocturnal body movements based on free-living accelerometer recordings: association with demographics, lifestyle, and insomnia symptoms." *Nat. Sci Sleep*, 9,267-275, 2017; *https://doi.10.2147/NSS.S145777.*

[43] E. Schrödinger. "*What is life? The physical aspects of a living cell.*" Cambridge University Press, Cambridge, 1944.

[44] I. Prigogine, J-M. Wiame. "Biologie et thermodynamique des phénomènes irréversibles." *Experientia* 2(11), 451-453, 1946; *https://doi.org/10.1007/BF02153597.*

[45] Y. Demirel. "Nonequilibrium thermodynamics in engineering and science." *J. Phys. Chem. B*, 108(1), 31–43, 2003; *https://doi.org/10.1021/jp030405g.*

[46] G. Collell, G. J Fauert, J. "Brain and cognition: A connection from thermodynamics and information theory." *Front. Psychol.*, 6(818) 7-11, 2015 *https://doi.org/10.3389/fpsyg.2015.00818.*

[47] J. Lewins, J. "Entropy pollution of the environment: A teaching approach to the second law*." Int. J. Mech. Eng. Educ.* 39(1), 60-67; *https://doi.10.7227/IJMEE.39.1.5.*

[48] M. Özilgen, "Review on biothermodynamics applications: timeline, challenges, and opportunities." *Int. J. Energy. Res.* 41, 1513 – 1533, 2017; *doi:org/10.1007/BF02153597.*

[49] I. Aoki, “Entropy flow and entropy production in the human body in basal conditions.” *J. Theor. Biol.* 141, 11-21, 1989.

[50] I. Aoki, “Entropy production in human life span: A thermodynamical measure for aging.” *Age* 17, 29-31, 1994.

[51] U. Lucia, G. Grisolia. “The Gouy-Stodola theorem: From irreversibility to sustainability - the thermodynamic human development.” *Sustainability*, 13, 3995; 2021; *doi:org/10.3390/su13073995*

International Journal of Thermodynamics (IJoT)
ISSN 1301-9724 / e-ISSN 2146-1511
https://dergipark.org.tr/en/pub/ijot

Vol. 25 (No. 3), pp. 075-095, 2022
doi: 10.5541/ijot.1012365

Techno-Economic and Enviroeconomic Analysis Review of Distinct Passive and Active Solar Distillation Still

Manish Sanserwal[1,2]*, Puspendra Singh[1]

[1]Mechanical Engineering Department, Delhi Technological University, Delhi-110042, India
[2]Mechanical Engineering Department, Galgotia College of Engineering and Technology, Greater Noida, UP -201306, India
Email: *sanserwalmanish@hotmial.com

Received 6 January 2022, Revised 10 March 2022, Accepted 20 May 2022

Abstract

Water scarcity is an issue that stems from the overconsumption and misuse of fresh water supplies, which leads to shortages and decreased quality of life. It most affects developing countries that do not have the infrastructure in place to mitigate these factors. Solar still become most suitable method for water purification in these types of places due to its cheapness and easily made from locally available materials. Current paper concentrate on a detailed techno-economic and enviroeconomic analysis of distinct configurations of active and passive solar distillation stills. Distilled water production, cost per litres, environmental cost comparison has been done between different types of passive and active solar still. Active solar still has a higher system cost compared to passive solar due to the addition of thermal energy by different components and mechanisms. Based on the results, minimum cost per litre is obtained for passive conventional solar still with the spherical ball as heat storage material and in case of active solar still, with PV module, reflectors, air-cooling technique are 0.0136 $/l and 0.0092 $/l, respectively. On the basis of energy, the highest environmental cost was found for AMSSFS air-cooled with evacuated mode (1456.38 $), while the lowest was found for active solar stills with N - Flat Plate Collectors (44 $).

Keywords: *Active solar still; passive solar still; economic and enviroeconomic analysis.*

1. Introduction

As the developing countries moving forward to becoming a developed country and wanted to decrease their dependency on the developed countries, lots of industrialization and urbanization needed and happing in the developing countries. Water act as a one of the main sources for any type of industry (for the production of product) and urban areas (for living and other daily use), due to which demand of clean water increases by 600% over the past 100 years [1]. At present, 47% of the world population living in those areas (among which 73% living in Asia), which suffer water scarcity for a month in a year and it will increase up to 57% by 2050 [2].

Improper irrigation system in agriculture act as a primary driver for the depletion of groundwater worldwide. Presently, more than 30% of world groundwater systems are in trouble [3]. In the last decades, water pollution become worse because of untreated water discharge from industries and lack of sanitation. Over 90% of sewage water discharged untreated in developing countries [4].

For treating or purify wastewater, lots of technologies classified as physical, chemical and energy-intensive methods used [5]. Over the last few decades, the cost of treatment goes significantly down due to improved membrane life (in case of membrane use), enhanced construction materials and low energy consumption [6]. Wastewater treatment is not only important for human health regulations but also for the environmental effects on plants and water bodies on earth.

As the water source and drinkable water availability are depleting in lots of areas of the world, the availability of seawater becomes hope due to which desalination technologies have an emerged market option for providing usable water. This technology continuously growing with a cumulative global capacity of 99.8 million m^3/d and register growth in productivity of almost 25 million m^3/d since 2010 IDA (International Desalination Association) and GWI (Global Water Intelligence). Cost of this technology was quoted around \$0.64 for 0.8/m^3 in mid of 1990 [7] and in the recent decade, it decreases to around \$0.50/m^3 for similar large-scale RO plants [8].

Solar still is an environment-friendly attractive option to obtain fresh water from saline/contaminated water and can be successfully used domestically. Solar still comprises of a water basin, a transparent glass roof and a collecting trough in which water evaporates from the basin due to absorption of sunlight and condenses on the glass cover wall and finally collected in the collecting trough which is discharged in a measuring flask. Further, it can be categorised as passive and active solar still. Passive solar still uses direct sunlight and further categorised as Single basin solar still (wick type, hemispherical, pyramid, triangular, spherical, stepped, tubular, inclined, plastic), multi basin solar still (double basin, pyramid, portable type [9]–[26]. Active solar uses direct and indirect sunlight by integrated it with different solar energy collectors like flat plate collector, evacuated tube collector, hybrid PV/T system, solar pond, Inverted

*Corresponding Author

absorber solar concentrators (parabolic trough collector and heat exchanger) and use for Waste heat recovery (Basin stills, Tubular stills) [27]–[43]. In India, for generating 1 kWh of electricity from a coal-based plant, it is expected that, amount of CO_2 rejected to the environment is approximately 1.58 kg [44]. Recently, some of the reviews were conducted on economic analysis of solar stills, including tubular-shaped solar stills [45], hybrid solar still economics analysis [46], as well as thermal analyses of various solar still filled with nanofluid [47], [48]. However, the recent reviews to the best of our knowledge. The current review of solar still systems deals with the techno-economic and enviro-economic analysis of several configurations of passive and active solar still systems chronologically and help in selecting suitable economic and sustainable designs of solar still systems.

2. Techno-Economic Analysis of the Different Types of Passive Solar Still

Now days, Techno-economic analysis (TEA) is one of the important factors for industries. Based on technological and monetary input variables, most industries perform these kinds of analyses to estimate the economic behaviour of their products and services. Comparative technical detail for different passive solar still provided in Table 1.

V.K. Dwivedi et al. [49] evaluated CO_2 emission, mitigation, and credits earned based on water depth (0.01 m, 0.02 m, and 0.03 m) and life of a double slope passive solar still (DSPSS), using energy and exergy analysis as shown in the Figure 1. In terms of energy, for 20 years of the lifetime of the solar still, the CO2 emission is 952.31 kg for all water depths. Carbon credit earned based on energy for a water depth of 0.01 m is Rs. 9,885.9 and Rs. 26,229.16 for a solar still that lasts for 20 years and 50 years, respectively.

Figure 1. Photograph of DSPSS [49].

Z.M. Omara et.al. [50] investigated finned and corrugated absorbers solar stills and compared them with conventional stills as shown in Figure 2. It is found that, at the same quantity of saline water (30 l) and water depth (50 mm), productivity increased by 40% for finned plate and 21% for corrugated plate compared to conventional ones. Although finned, corrugated and conventional solar stills have about 47.5%, 41%, and 35% daily efficiency respectively, when operated 340 days per year.

T. Arunkumar et.al. [51] done an experimental study on hemispherical solar still with and without the flowing water over the cover as shown in Fig. 3. The efficiency of this still is increased from 34% to 42%. With an output of 4.2 kg/m2/day, cost per litre (CPL) becomes approximately \$0.017/kg water if we include its life of 15 years and an interest rate of 6%. T. Rajaseenivasan et. al. [52] investigates a double slope double basin solar still and also its effect on productivity by varying the water level in both lower and upper basin as shown in Figure 4. From theoretical and experimental results (deviation of 10%), not only the productivity increases by 85% but also fabrication cost of double basin solar still increases by 32% as compared to conventional double slope solar still the results were compared with the single basin still (with same basin area.

The performance of a “V” type solar still with a Cotton Gauze Top Cover Cooling (CGTCC) with and without air flow over the condensation surface (glass cover) are experimentally evaluated by P.U. Suneesh et. al. [53] as shown in Figure 5. The rate at which production increase is less as compared to the increase in cost of still with GCTCC and air flow.

Figure 2. Photograph of conventional, corrugated and finned solar still [50].

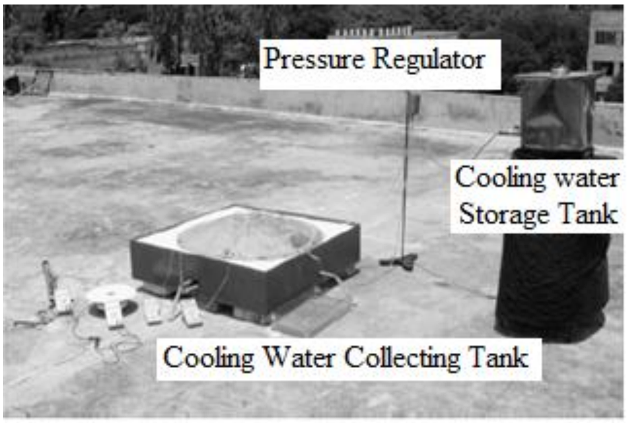

Figure 3. Hemispherical solar still with cooling system [10].

Z.M. Omara et. al. [54] investigate the performance parameters of a solar still with corrugated basin liner (CrSS), using internal reflectors and double wick layer by comparing it with conventional solar still (CSS) as shown in Figure 6. Results shows that, at 1 cm brine depth, productivities increase about 145.5% of CrSS with reflectors and wick as compare to CSS. Whereas, the daily efficiency of CrSS and CSS are 59% and 33% approximately, respectively.

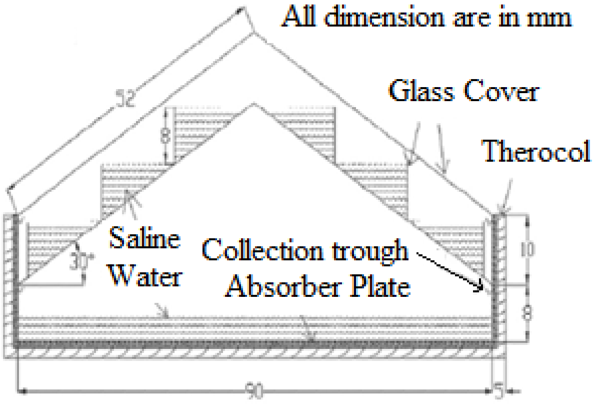

Figure 4. Schematic diagram of double slope double basin solar still [52].

Figure 5. Photographic view of "V" type solar still with CGTCC [53].

Figure 6. Corrugated solar still [54].

Experimental and theoretical analysis are conducted by D.G. Harris Samuel et. al. [55] to find out the performance of CSS using different energy storage material (spherical salt ball and sponge) as shown in Figure 7. Results revealed, payback time of CSS is 4.3 months more as compare to present still. Hence, CSS with spherical ball as heat storage gives us lowest cost of water. Later, Experimental and theoretical performance of a solar still with square (hollow pipe 0.019 × 0.07) and circular fins (circular pipe 0.03 m dia × 0.07) integrated at the base of the conventional solar still (CSS) basin was investigated by T. Rajaseenivasan et. al. [56] with CO_2 mitigation and economic analysis. Daily productivity of the still increases by 26.3 and 36.7% for circular and square finned stills and it changes to 36 and 45.8% for fins covered with wick materials at 1cm water depth.

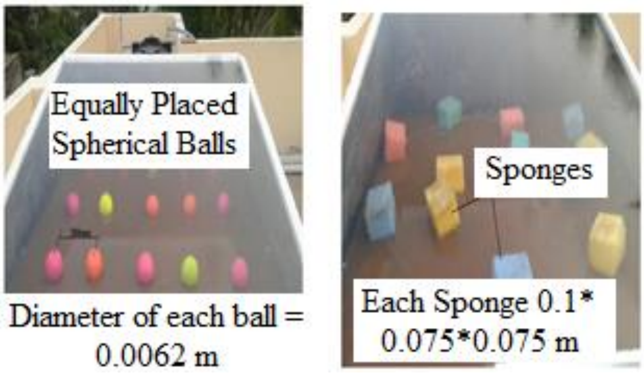

Figure 7. Photograph of CSS with spherical ball (left) salt heat storage and sponge (right)[55].

A modified double slope basin type multi–wick MBDSMWSS (black cotton and jute) solar still have been fabricated and designed to analyse its performance by Piyush Pal et. al. [57]. Maximum daily yield (at 2 cm water depth) and overall thermal efficiency of modified still is 9012 ml; 23.03% for black cotton wick and 7040 ml; 20.94% for the jute wick. In this study, exergy, economic and thermal performance investigated by Samir M. Elshamy et. al. [58] of a tubular solar still (TSS) with two different water basin shapes; semi-circular corrugated (TSS-SC) and flat plate (TSS-FP) as shown in Figure 8. The distilled production enhancement of TSS-SC was about 26.47 % rather than TSS-FP with increment in exergy and thermal efficiencies about 23.7% and 25.9 % respectively.

Figure 8. Photo of TSS with different water basin shapes (left) and different troughs in TSS (right) [58].

Piyush Pal et. al. [59] investigated both experimentally and theoretically a modified multi–wick basin type double slope solar still (MMWBDSSS) with jute and black cotton wicks as show in Figure 9. For jute cotton and black cotton wicks, the CO_2 mitigated per annum has been found to be 7.23 and 0.198 tons at 2cm water depth on the basis of energy; and 0.155 and 0.141 tons at 1 cm water depth, respectively on the basis of exergy; and 0.198 and 0.167 tons at 2cm water depth, respectively on the basis of exergy for year around operations. Tilted wick type and stepped solar stills are well known for increased distillate yield in the day and night conditions due to maximum exposure of solar radiation and sensible heat storage as in case of deep basin stills as compared to conventional solar still.

Figure 9. Photograph of MMWBDSSS [59].

K.S. Reddy et. al. [60] proposed a tilted solar distillation system with wick for treatment of RO reject and domestic sewage water as shown in Figure 10. Heavy metals removing efficiency for RO reject water and sewage water is in the range of 32.9–82.1% and 51.1–70.6%, respectively.

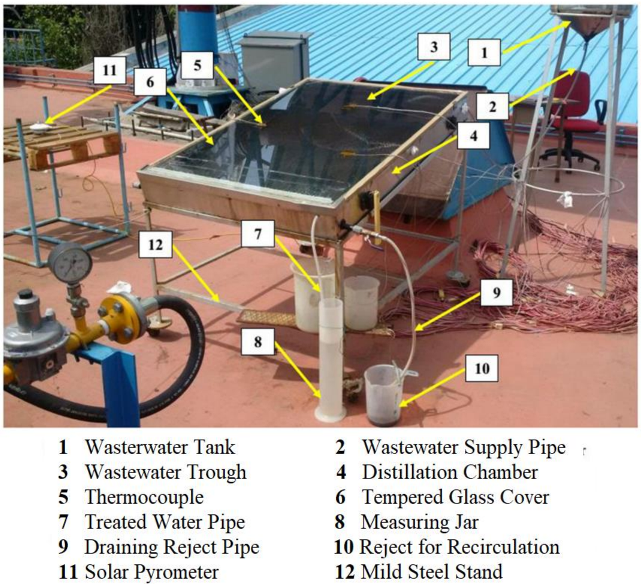

Figure 10. Schematic diagram of tilted solar still [60].

Kalpesh V. Modi et. al. [61] investigate the performance of two similar single-slope double-basin solar stills with the use of two different wick materials namely jute cloth and black cotton cloth in the form of small pile in the lower basin (Figure 11a). The distilled yield for small pile of jute cloth and black cotton was obtained 0.91 L/m^2 and 0.771 L/m^2 respectively at a water depth of 0.01 m, and 0.8287 L/m^2 and 0.6823 L/m^2 respectively for the 0.02 m water depth. Total capital cost per square meter was ₹ 5680 with payback time of 15 months for 250 sunny days in a year. Wen-Long Cheng et. al. [62] carried out experiment with a shape-stabilized phase change material (SSPCM) having solar absorption 0.94 and thermal conductivity 1.50 W/m K by, to replace the metal absorber plate used in CSS (Figure 11b). The experimental and simulation results revealed that, as the thermal conductivity of SSPCM increases from 0.2 to 4 W/mK, the daily productivity of CSS with SSPCM is 42% to 53% higher than that of CSS.

Mohamed S. Yousef et. al. [63] investigated single slope solar still using different absorbing material for analysing (4E) the energetic, exergetic, economic and enviroeconomic. The performance of the three cases, case 1) Traditional solar still (TRD), case 2) with hollow cylindrical pin fins, case 3) with steel wool fibers (Figure 12). In comparison with case 1, the daily cumulative yield of distillate water and average daily exergy efficiency in cases 2 and 3 enhanced by 16% and 25%; and 14% and 23%, respectively. The maximum energy efficiencies of all three cases 1-3 are 42%, 45.5%, and 52.5% respectively.

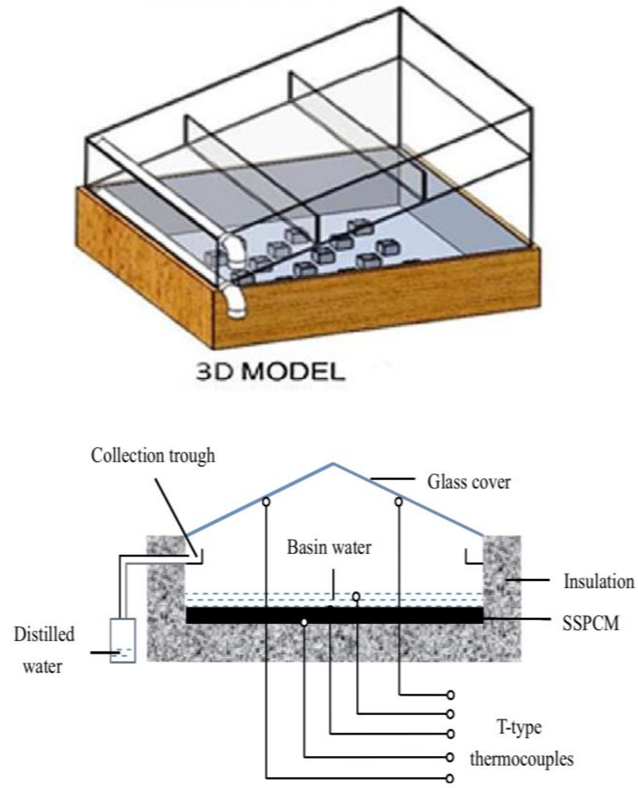

Figure 11. (a) 3D Model of single-slope double-basin solar stills (above) [61] (b) Schematic diagram of pyramid solar still with SSPCM (below) [62].

Figure 12. Photographic view of steel wool fibers and hollow cylindrical pin fins [63].

Table 1. Comparative detail for different passive solar still.

Paper	Type of still	system cost ($)	Daily yield (l/m^2)	Basin area (m^2)	Solar radiation W/m2	place
[50] Z.M. Omara et. al. (2011)	CSS CSS with finned CSS with corrugated	412 490 480	2.5 3.5 3	1	1100	Kafrelsheikh University (31.07°N, 30.57°E), Egypt
[10] T. Arunkumar et. al. (2012)	Hemispherical without cooling with cooling	165 165	3.66 4.2	0.71	732	Coimbatore (11° North, 77° East), India
[52] T. Rajaseenivasan et. al. (2013)	Double slope with Single basin with double basin	93.63 137.27	2.56 4.75	0.63	750	Kovilpatti (9° 11′N, 77° 52′E) Tamil Nadu, India
[53] P.U. Suneesh et. al. (2014)	V type solar still with CGTCC with CGTCC and air flow	200 220 520	3.3 4.3 4.6	1.5	732	Coimbatore (11° North, 77° East), India
[54] Z.M. Omara (2016)	CrSS with wick CrSS with wick and reflecting mirrors	488 520	5 6	1	1100	Kafrelsheikh University (31.07°N, 30.57°E), Egypt
[55] D.G. Harris Samuel et. al. (2016)	CSS CSS with spherical ball heat storage CSS with sponge	68.18 68.18 68.18	2.4 3.7 2.6	1	627	(IITD), New Delhi, India (28°350 N, 77°120 E,
[57] Piyush Pal et. al. (2017)	Double slope with jute wick with black cotton wick	201.08 203.4	4.5 3.52	2	935	Allahabad (U.P.) (25°27′ N)
[58] Samir M. Elshamy et. al.(2018)	Tubulor solar still with SC with FP	100 100	4.3 3.4	0.4	1040	Giza, Egypt (29.9381° N, 30.9140° E)
[61] Kalpesh V. Modi (2019)	Single-slope double-basin solar still with jute cloth with black cotton cloth	81.14 81.14	0.91 0.771	0.25	870	Valsad, Gujarat, India (20.61°N, 72.91°E)
[49] V.K.Dwivedi et. al. (2010)	Double solar still with water depth 0.01 0.02 0.03	- - -	1.66 1.57 1.45	1	627	Greater Noida 28.4572° N, 77.4984° E, India
[56] T. Rajaseenivasan et. al. (2016)	CSS CSS with Square finned still CSS with Circular finned still	121.66 156.67 154.17	3.11 4.25 3.99	1	850	Madurai, Tamil Nadu, India

[59] Piyush Pal et.al. (2018)	Double slope with jute wick with black cotton wick	215.82 218.32	3.52 3.53	-	935	Allahabad (U.P.) (25°27′ N)
[60] K.S. Reddy et. al. (2018)	Tilted solar distillation with RO reject with sewage water	277 277	4.79 4.48	-	867	Chennai (30.08 N 80.27 E) Tamil Nadu, India.
[63] Mohamed S. Yousef et. al. (2019)	TRD TRD with pin fins TRD with steel fibers	190 220 192	3.96 4.65 4.98	1	932	New Borg El-Arab City, Egypt
[64] Pankaj Dumka et. al. (2020)	CSS CSS with ultrasonic fogger & cotton cloth	75.16 83.37	2.7 4.3	1	1050	Guna, Madhya Pradesh, India
[65] H.Sharon (2021)	novel hybrid solar still	520.02	4.59	1 & vertical basin area 3 m^2	860	Chennai, India
[66] Belkheir Benoudina et. al. (2021)	CSS CSS with micro-particle of Al2O3 CSS with Nano-particle of Al2O3	105.87 107.84 109.82	3.02 4.96 6.12	0.25	1010	El Oued, Algeria

The performance of conventional solar still with and without using an ultrasonic atomiser and a cotton cloth was studied and compared experimentally and theoretically by Pankaj Dumka et. al. [64]. Modified solar still (CSS with ultrasonic atomiser and cotton cloth) introduced with the aim of decreasing the excessive fogging issue at low radiation hours, enhance evaporation area and reduce distinctive length of solar still. H.Sharon [65] introduced a novel hybrid solar still (as shown in Figure 13) by combining the effects of conventional solar still with vertical diffusion under reduced ground area under the climatic conditions of Chennai, India. The model is thermodynamically investigated for basin to vertical diffusion area ratio, water depth in basin, shade, vertical still diffusion gap and inlet water flow rate. Belkheir Benoudina et. al. [66] utilizes various concentration of micro-particle and Nano-particle of aluminium oxide in the production of condensate for three types of solar still. In comparison, the first solar still is conventional (CSS), the second one contains micro-particles of aluminium oxide with a concentration ranges of 0.1-0.3%, while the third solar still contains Nano-particles of aluminium oxide with a concentration range of 0.1-0.3%.

3. Techno-Economic Analysis of Different Type of Active Solar Still

A small size portable thermoelectric solar still is proposed by J. A. Esfahani et. al. [67] as shown in Figure 14. All four walls are made up of Plexiglas to make it durable. To evaluate the average daily yield output, experiments were conducted for nine winter days under climate condition of Semnan, Iran. Results show that average annual productivity of fresh water was 620 L/m^2 which is less when compared to portable still and CPL of portable still is calculated on 12% interest rate for 10 year of life.

An evacuated tubular collector integrated solar still (EISS) introduced, not only for getting hot water but also distilled water. Rahul Dev [68] evaluated its performance annually in 2008 as shown in Figure 15.

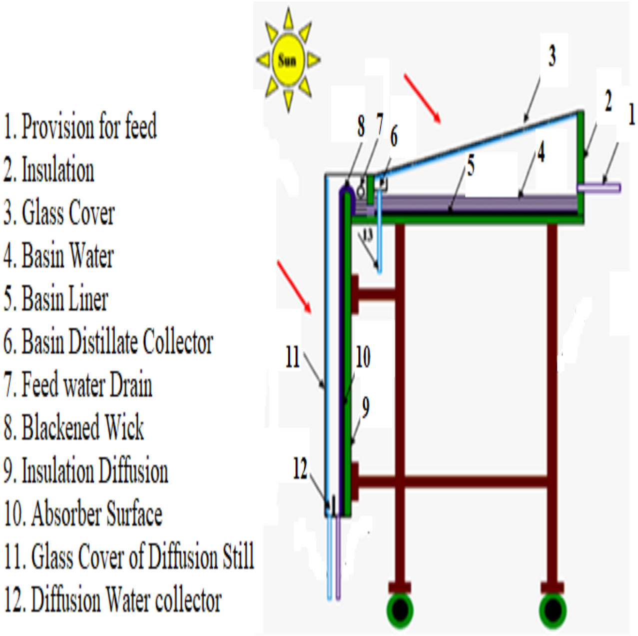

Figure 13. Schematic diagram of hybrid solar still [65.]

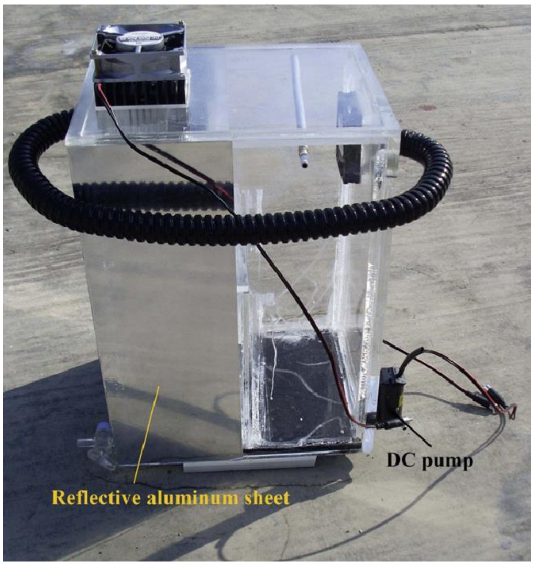

Figure 14. Photograph of portable thermoelectric solar still [67].

Here, heat loss from ETC's (evacuated tubular collector) hot water is used by solar still during the off-sunshine hours and also develop a thermal model to compare it with experimental results. Yearly yield output of EISS and SS system is 630 and 327 kg/m^2, respectively.

Figure 15. Schematic diagram of EISS [68].

Z.M. Omara et. al. [69] presented a hybrid solar desalination system using wicks/solar still and evacuated tubular collector. Various case is studied (Figure16): Single layer plane wick (SLPW), Single- and double-layer lined wick (SLLW/DLLW), Single- and double-layer square wick (SLSW/DLSW) layers; hot water feeding during night and two wick base slope angles of still (20 and 30°). Also verified theoretical analysis through experiments. Yield output for DLSW is increased by 114% as compared to CSS (conventional solar still).

Mohamed A. Eltawil et. al. [70] enhanced the productivity of conventional single slope solar still (CSS) by equipping it with a flat plate solar collector, spraying unit, perforated tubes, external condenser and solar air collector (Figure 17).

Figure 16. Schematic diagram of a) Conventional still b) Double layers wick still c) Single layer wick still [69].

The water either sprayed into developed solar still (DSS) or making upwards fountain by pumping from bottom and a hot air also forced at the bottom of DSS. Results shows that the productivity of DSS (depending upon the type of modification) was 51–148% more in comparison to CSS.

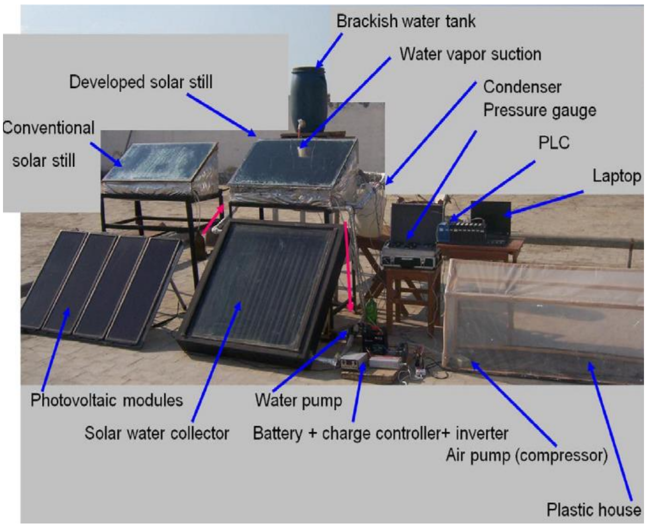

Figure 17. Photograph of Developed solar still [70].

For the first time M.R. Karimi Estahbanati et. al. [71] conducted indoor experiment on 4 similar solar stills with different stages (1–4 stages) effect on the productivity of a multi-effect active solar still (Figure 18). Moreover, compared all four system performances for continuous and non-continuous modes. The experimental result revealed that as the number stage increases, water production also increases in continuous mode compared to non-continuous mode. PPT (payback time) of a four-stage still are 237 and 199 days in non-continuous and continuous modes.

A hybrid (partially covered) photovoltaic thermal (PV/T) flat plat collector (FPC) active solar still has been experimentally studied by D.B. Singh et. al. as shown in Figure 19 [72]. Along with the design and fabrication of the system, a thermal model also developed. Annual water productivity and water production cost of the system have been varying between 120.29% and 883.55%; Rs. 0.19 per kg to Rs. 4.08 per kg, respectively with varying rate of interest between 2% to 10% and life between 30yr. to 50yr. Later B. Praveen kumar et. al. [73] fabricated and experimental studied PV/T solar still with NiCr heater at different water depths of 0.05 m, 0.10 m, and 0.15 m for three consecutive days (Figure 20). Proposed solar still uses saline water for cooling purpose of PV module also which increases its thermal efficiency by 25 % and daily yield by 6 times more as compared to conventional passive still.

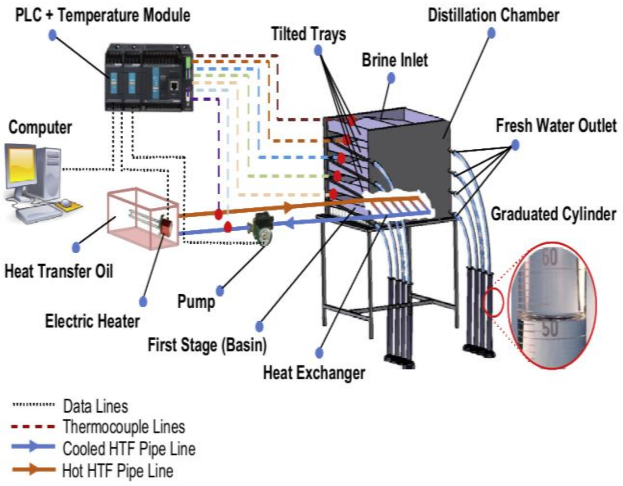

Figure 18. Schema of the 4-stage experimental set-up [71].

Figure 19. Sectional top view of PV/T-FPC active solar still [72].

Omar Bait et. al. [74] developed a numerical simulation and an economic analysis of a multi-stage desalination system and are seeking to promote it as a startup for Batna city. Initially, a general model is involved in the study just to know the global thermal and mass quantities. Investigate the effect of radiation term on temperature as well as yield production in the next step. As a consequence of the variations in the trays, the distillate output for each stage was determined to be: 5.02 kg/day for the first stage, 8.29 kg/day for the three stages, and 8.88 kg/day for all stages.

Multi effect and multistage solar distillation system are widely known for their high rate of distilled water productivity and also capable to fulfil the water requirements in remote and rural areas. In the same scenario, K.S. Reddy et. al. [75] studied the role of number of effects, gap between condensing and evaporating surface, feed water mass flow rate, feed water salinity (0, 5 & 10%), operating pressure of system (normal and evacuated mode) and climatic conditions on distilled water increment of AMEVSS (active multi-effect vertical solar still) by developing mathematical model. Results shows that interest rate (5% to 12%) and salinity of feed water play an important. Later on, Reddy et. al. [76] worked upon AMSSFS (active multiple stage series flow solar distillation unit), which is an improved version of tray type distillation unit with series flow.

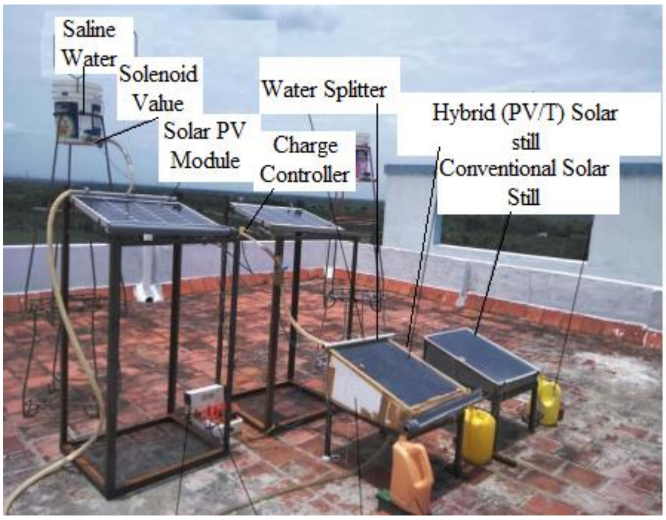

Figure 20. Photograph of proposed hybrid (PV/T) active solar still [73].

Anil Kr. Tiwari et. al. [77] presented an economic analysis of two small single slope solar still plant (FRP single slope solar still and FRP multiple wick solar still) coupled with fountain reservoir to meet 300l/day requirements. The performance of both the plants was analysed theoretically, with the flow of cooled water stored in fountain reservoir over glass cover and compared with CSS plant (without flow). CPL of distilled water for proposed plant-1and plant-2 is 29.2% to 32.5% less than the CSS plant. Annual yield increases for proposed plant-1and plant-2 is 56.4% to 61.4% for, with flow of cooled water over the glass cover.

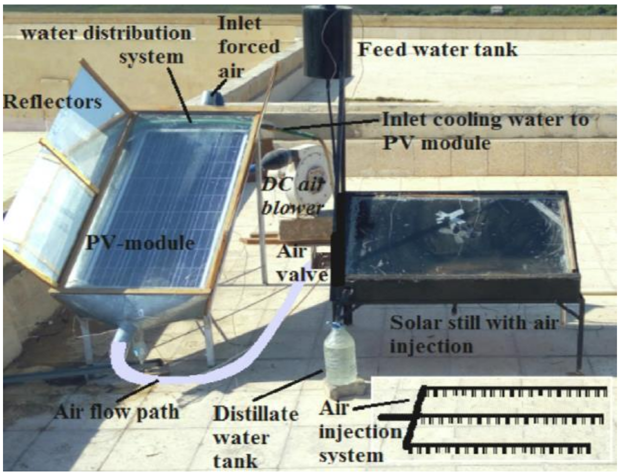

Figure 21. Photographic view of hybrid solar still [78].

Present studies more focused on hybrid use of solar still with PV panel which not only overcome the cleaning problem of PV panel (increases electricity production) but also increase the output of solar still. In the same scenario A.E. Kabeel et. al. [78], proposed a hybrid system (PV panel using reflectors, cooling and air injection) with five operating cases (Figure 21). Only two cases C and E uses cooling air out from PV module into the developed solar still for improving the fresh water productivity (increasing evaporation rate inside the still) by 40.98% and 21.96%, respectively compared to the cases without air injection.

Poonam Joshi et. al. [79] presents an analysis of enviro-economic, energy matrices and exergo-economic of three cases of single slope solar still (same basin area of 2 m^2) integrated with helical coiled copper heat exchanger (Figure 22): (i) and (ii) having N – partially and fully covered Photovoltaic Thermal (PV/T) Flat Plate Collectors, and (iii) N – Flat Plate Collector. Results report that the cost of water is lowest for case (i) followed by case (iii) and then case (ii) at the interest rate of 2% and 5%.

Figure 22. Photographic view of PV/T flat plate collector [79].

Theoretical analysis of double slope solar still (DSSS) integrated with N number of series of identical evacuated tubular collectors (N-ETCs) has been presented by D.B.Singh [80] as shown in Figure 23. Also, the proposed system (N-ETC-DSSS case (i)) has been compared with the different DSSS systems incorporated with case (ii) N identical PV/T flat plate collectors (FPCs), (iii) N identical PVT compound parabolic concentrator collectors (CPCs) and (iv) conventional DSSS on the basis of productivity and enviro- economics parameters. Later on, Omar Bait [81], presented a comprehensive mathematical model of DSSS integrated with a tubular solar collector (TSC) (Figure 24) and also compared it with Conventional DSSS on the basis of economic and enviro-economic parameters. It was revealed from the results that payback time of passive and active solar still was around 7.7 yrs and 21 yrs, respectively.

Emad M.S. El-Said et. al. [82] presented a novel work for increasing the performance and productivity (by heat absorbing capacity) of tubular solar still (Figure 25) by utilizing steel wire mesh porous packing with vibratory excitation system (for transvers harmonic forced vibration to destroy the surface tension and boundary layer of salty water). Yield increment of tubular modified solar still (TMSS) is 34% as compare to tubular conventional solar still (TCSS). CPL of TMSS reduced by 14.39% as compare to TCSS.

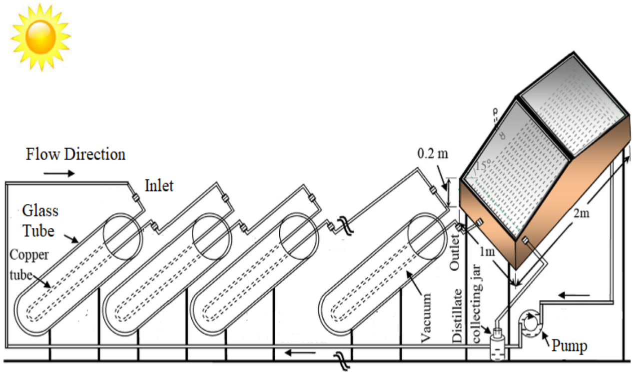

Figure 23. Schematic representation of N-ETC-DS [80].

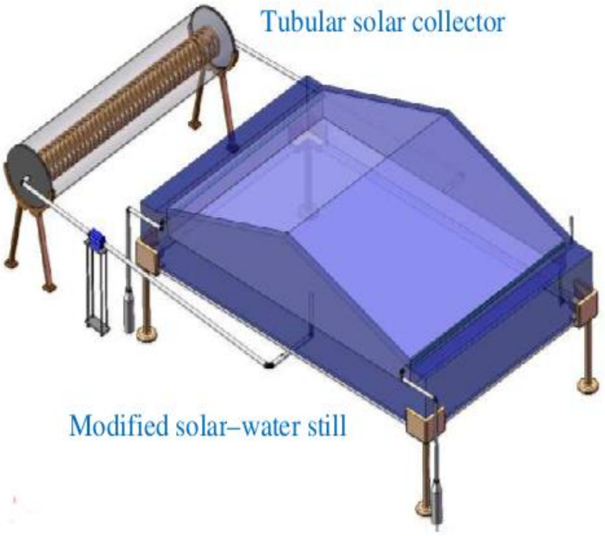

Figure 24. Schematic view of DSSS-TSC [81].

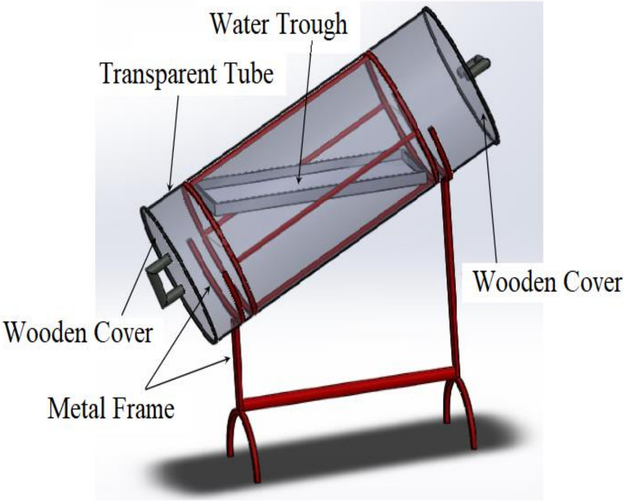

Figure 25. Schematic sketch of TMSS [82].

Hamdy Hassan et. al. [83] investigated single solar slope still in six different ways using parabolic through collectors (PTC), wire mesh (WM) and sand (SD) in the basin (as show in Figure 26). Results revealed that CSS+ SD + PTC in the summer has a higher maximum yield production compared with CSS and CSS+ SD + PTC in the winter by 1.21% and 102.1%, respectively. The maximum increase in energy and exergy in CSS+ SD + PTC as compared to CSS is found to be 216.6% and 325%, respectively.

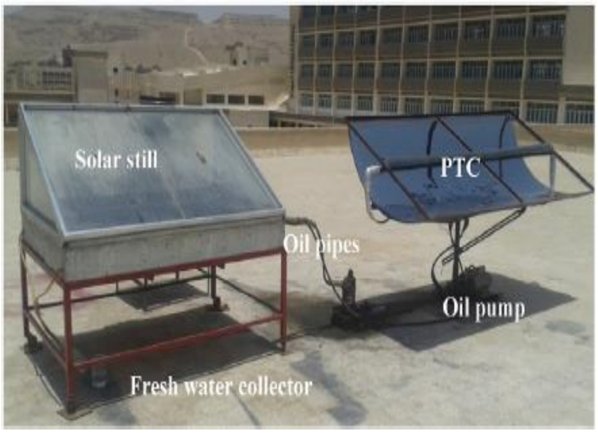

Figure 26. photograph of Solar still with PTC, WM and SD [83].

Rasoul Fallahzadeh et. al. [84] modified a conventional pyramid solar still (MPSS) by incorporating an evacuated tube collector (ETC) containing heat pipes, utilizing two types of fluids, ethanol and water, in three different combinations (as show in Figure 27). When using water as the working fluid at a filling ratio (FR) of 40%, MPSS produces the maximum yield of 6.97 l/m2. Shahin Shoeibi et. al. [85] investigates a double slope still with thermoelectric cooling of the glass cover and heating of basin water simultaneously in order to improve condensation and heating in the climatic conditions of Tehran, Iran.

Figure 27. photograph of modified pyramid solar still (bottom) [84].

Water from the cold side of thermoelectric system flows over the glass, while the hot side passes through a heat exchanger within the basin water of the solar still and on the other hand utilizes wind velocity for cooling of glass cover. Denise Mevada et. al. [86] compares the performance of CSS and modified solar stills (MSS) with fins, evacuated tube collectors (ETC), and a novel air-cooled condenser in the climatic conditions of Gandhinagar, India. The results revealed a 73.45% increase in yield productivity in MSS compared to CSS. Comparative technical detail for different active solar still provided in Table 2.

Table 2. Comparative detail of different active solar still.

Paper	Type of still	Component Incorporated and cost ($)		system cost ($)	Daily yield (l/m^2)	place
[67] Javad Abolfazli Esfahani (2011)	Thermoelectric solar stills	Thermoelectric cooler DC fan DC pump	12.5 8 4	290.5	1.2 winter	Semnan (35° 33′ N, 53° 23′ E), Iran
[68] Rahul Dev (2012)	Single slope	ETC Water pump (AC)	436.8 24.96	694.53	2.5	(IITD), New Delhi, India (28°350 N, 77°120 E
[69] Z.M. Omara (2013)	CSS, DLSW, DLSW with feeding hot brackish water during night	Evacuated solar water heater	450	412 520 1070	2.87 6.29 13.40	Kafrelsheikh University (31.07°N, 30.57°E), Egypt
[70] Mohamed A. Eltawil (2014)	CSS, DSS with condenser, DSS with water solar collector and condenser	Condenser and fan Photovoltaic system Pump Spraying unit Water solar collector Compressor Air solar collector	57 180 10 5 70 7 5	412 760 1348	2.5 4 6	Kafrelsheikh University (31.07°N, 30.57°E), Egypt
[71] M.R. Karimi Estahbanati (2015)	Multi-effect active solar still with 4 stages with non-continuous and continuous modes	Solar collector Circulating pump Heat exchanger	500 50 40	1030	5.95, 8.5, 10.3, 11.45 and 6.2, 8.85, 11.35, 13.55	Sharif University of Technology,Tehran, Iran

[72] D.B. Singh (2016)	Single slope	2PV module Flat Plate collector Motor and pump	253.24 395.69 15.82	807.21	4.25	(IITD), New Delhi, India (28°350 N, 77°120 E,
[74] Omar Bait et. al. (2016)	multi-stage distillation system	solar panel Steel and aluminum metallic structures	30.767 44.637	867.33	5.02	Batna city (35330 N, 6110 E), Algeria
[73] B. Praveen kumar (2017)	CSS CSS with PV/T	nickel-chromium (NiCr) heater powered by solar photovoltaic (PV)	126.62	90.54 145.02	2.9 7.2	KCET, Virudhunagar, Tamilnadu, India (9.5680°N, 77.9624°E)
[77] Anil Kr. Tiwari (2018)	CSS (177 m2) plant-1 (110 m^2) plant-2 (107 m^2)	fountain reservoir Plant installation cost 1089.23 676.92 658.56		11637 8086.1 7888.8	2.98 4.66 4.82	Jodhpur (India)
[78] A.E. Kabeel (2019)	CSS with Case C CSS with Case E	photovoltaic (PV) panel with reflectors and cooling system -		75.42 75.42	6.034 5.22	Tanta, Egypt
[82] Emad M.S. El-Said (2020)	TCSS TMSS	vibratory excitations Wire mesh with aluminium frame	38 17	- 295	3.25 4.2	Fayoum University, Fayoum, Egypt
[75] K.S. Reddy (2016)	AMEVSS with normal with evacuated mode	Flat plate collector DC pump (50 W)	138 58.11	748.27 870.16	9.75 27.80	Chennai (30.08 N 80.27 E) Tamil Nadu, India.
[76] K.S. Reddy (2017)	AMSSFS with Air cooled with Non-evacuated and evacuated AMSSFS with Wetted wick cooled with Non-evacuated and evacuated	Flat plate collector Capillary wick Vacuum pump pump	307.03 15.13 110.53 97.48	1638 1799 1666 1828	10.95 21.13 12.63 44.07	Chennai (30.08 N 80.27 E) Tamil Nadu, India.
[79] Poonam Joshi (2018)	Active single slope solar still with cases (i) case (ii) case (iii)	heat exchanger Photovoltaic Thermal FPC each Motor	28.57 78.57 14.28	2192.8 2192.8 1214.2	5.52 3.68 6	(IITD), New Delhi, India (28°350 N, 77°120 E,
[80] D. B. Singh (2019)	Double slope solar still (DSSS)	ETC Motor and pump	161.53 15.38	295.12	16.71	Greater Noida 28.4572° N, 77.4984° E, India
[81] Omar Bait (2019)	DSSS Modified solar still	tubular solar–water heating system (TSC)	-	63.831 175.62	1.31 1.82	Batna city (35330 N, 6110 E), Algeria

[83] Hamdy Hassan et. al. (2020)	CSS CSS + SD + PTC CSS + WM + PTC	parabolic trough collector steel wire mesh	103.255 14.473	143.79 248.97 261.52	3.96 8.77 8.15	Alexandria, Egypt
[84] Rasoul Fallahzadeh et. al. (2020)	CSS MPSS	heat pipe solar collector	65	82.5 169	3.3 6.97	Mashhad, Iran
[85] Shahin Shoeibi et. al. (2021)	DSSS with air cooled water cooled Modified water-cooled	5 thermoelectric modules PV module 2 DC Pumps	25 75 30	267 300 425	1.41 2.57 3.12	Tehran, Iran
[86] Denise Mevada et. al. (2021)	CSS MSS	Evacuated tubes (6 nos.) Condenser Fins	55 3 3	75 136	2.26 3.92	Gujarat, India

4. Comparison of all Active Solar Still on the Basis of Different Components Incorporated

Till before this sections, different types of active and passive solar still are compared on the basis of their system cost, daily yield and incorporated component cost (in case of active solar still). By the help of tables, it is easier to calculate most yield productive solar still with lowest cost. Further, economic analysis and enviroeconomic is going to be present in next sections for more details. In addition to this, how solar still have been improved with the addition of different organs like reflectors, PV modules, etc in some performance indexes such as water productivity and efficiency as show in the below Figure 28 & 29.

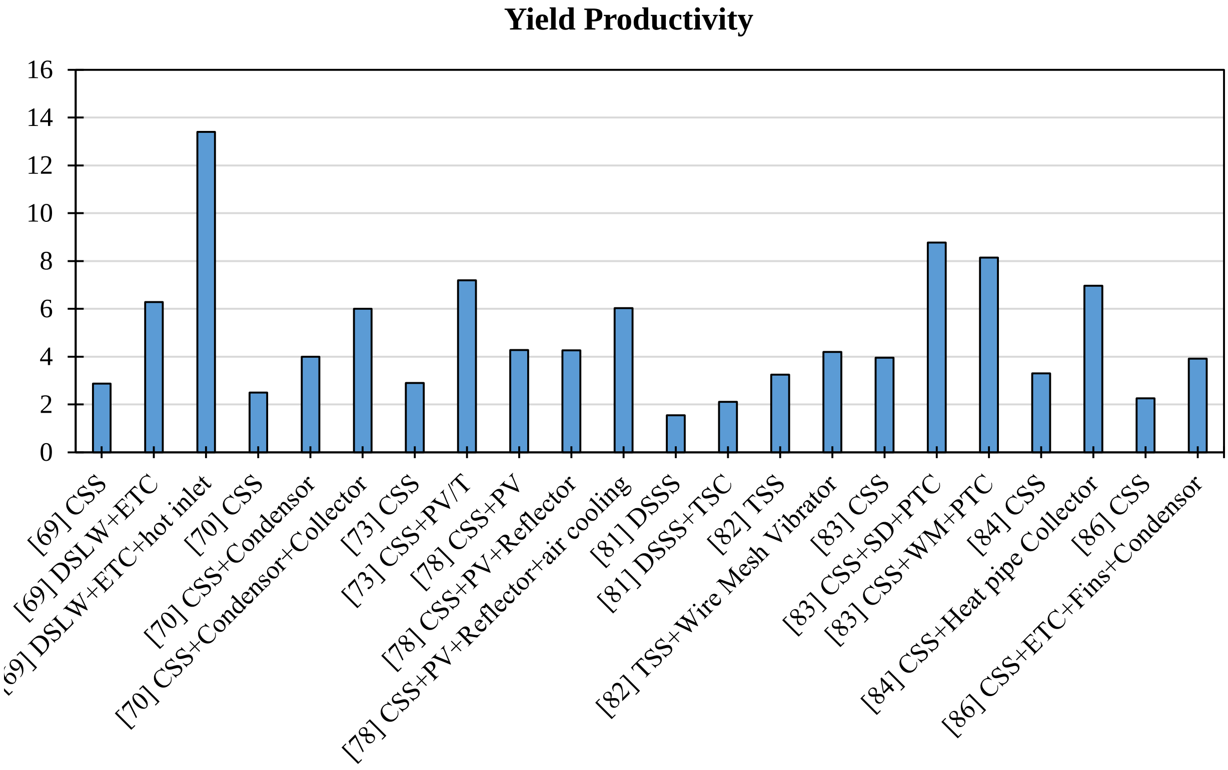

Figure 28. Comparative analysis of active solar still on the basis of yield productivity.

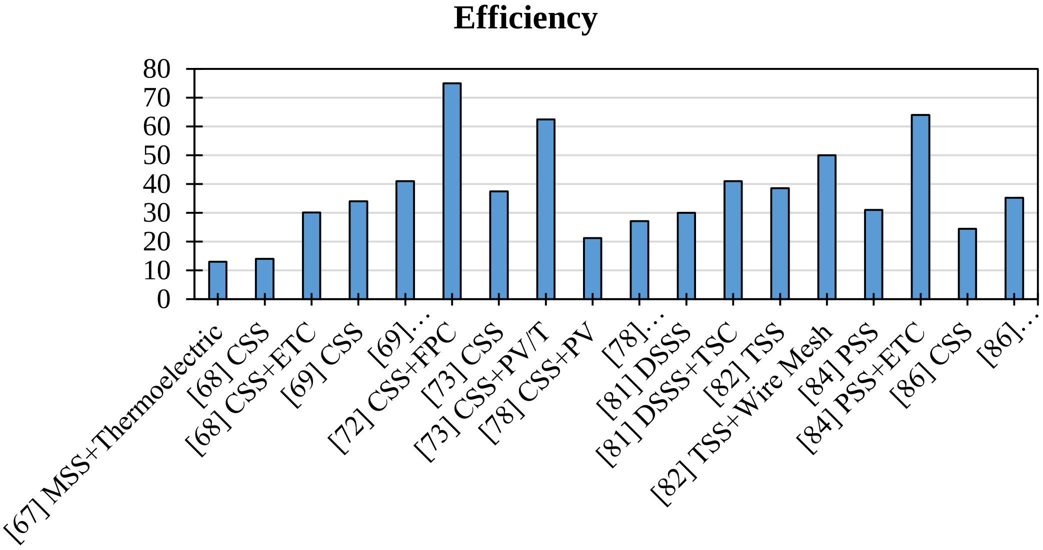

Figure 29. Comparative analysis of active solar still on the basis of efficiency.

5. Economic Analysis of Different Passive and Active Solar Still

In Solar desalination still, the Cost per litre (CPL) of distilled water is calculated in economic analysis. Economic analysis of Solar still initially carried out by Govind and Tiwari [87]. Later Kabeel et al. [88] presented the economic analysis of different configuration passive and active solar still. In this analysis, values of n (number of life years), i (interest per year), sunny days per year and x is assumed as 10, 12%, 260 and 20% respectively and an excel programme was prepared for the calculation. Economic analysis parameters are represented in Table 3 [89]:

Table 3. Economic analysis formulas applied for most of the still system.

Economic Method	Formulas
Present capital Investment (P)	CRF $= i(1+i)^n/[(1+i)^{n-1}]$
Capital recovery factor (CRF)	AFC = P(CRF)
Annual first cost (AFC)	SFF $= (i)/[(1+i)^{n-1}]$
The sinking fund factor (SFF)	ASV = (SFF) × S (Salvage value)
The annual salvage value (ASV)	AC = AFC + AMC – ASV
Annual maintenance cost (AMC) = 15% of AFC	AC/L = AC/M (Annual Yield)
Annual cost (AC)/m^2	AUE = M × 0.65
The annual cost per liter (AC/L)	AC/kWh=(AC/m^2)×AUE
Annual useful energy (AUE)	S = (x × P)
Annual Cost/kWh	
Percentage of degradation rate (x)	
Cost per litres (CPL)	

Table 4. Economic analysis for passive solar still.

Sr. No.	M (L/m2)	CRF	FAC	SSF	S	ASV	AMC	AC	CPL
[50]	650	0.177	72.917	0.057	82.4	4.6955	10.938	79.16	0.1217
[50]	910	0.177	86.722	0.057	98	5.5844	13.008	94.146	0.1034
[50]	780	0.177	84.952	0.057	96	5.4705	12.743	92.225	0.1182
[10]	951.6	0.177	29.202	0.057	33	1.8805	4.3804	31.702	0.0333
[10]	1092	0.177	29.202	0.057	33	1.8805	4.3804	31.702	0.0290
[52]	665.6	0.177	16.571	0.057	18.726	1.0671	2.4857	17.99	0.0270
[52]	1235	0.177	24.295	0.057	27.454	1.5644	3.6442	26.374	0.0213
[53]	858	0.177	35.397	0.057	40	2.2794	5.3095	38.427	0.0447
[53]	1118	0.177	38.937	0.057	44	2.5073	5.8405	42.27	0.0378
[53]	1196	0.177	92.032	0.057	104	5.9264	13.805	99.91	0.0835
[54]	1300	0.177	86.368	0.057	97.6	5.5617	12.955	93.762	0.0721
[54]	1560	0.177	92.032	0.057	104	5.9264	13.805	99.91	0.0640
[55]	624	0.177	12.035	0.057	900	0.775	1.8052	13.065	0.0209
[55]	962	0.177	12.035	0.057	900	0.775	1.8052	13.065	0.0136
[55]	676	0.177	12.035	0.057	900	0.775	1.8052	13.065	0.0193

[57]	1170	0.177	35.591	0.057	40.216	2.292	5.3386	38.637	0.0330
[57]	915.2	0.177	36.00	0.057	40.68	2.318	5.4002	39.083	0.0427
[58]	1118	0.177	17.698	0.057	20	1.1397	2.6548	19.213	0.0171
[58]	884	0.177	17.698	0.057	20	1.1397	2.6548	19.213	0.0217
[61]	236.6	0.177	14.36	0.057	16.228	0.9247	2.1541	15.59	0.0658
[61]	200.46	0.177	14.36	0.057	16.228	0.9247	2.1541	15.59	0.0777
[64]	702	0.177	13.30332	0.057	15.032	0.856824	1.995498	14.44199	0.020573
[64]	1118	0.177	14.75649	0.057	16.674	0.950418	2.213474	16.01955	0.014329
[65]	1193.4	0.177	92.04354	0.057	104.004	5.928228	13.80653	99.92184	0.083729
[66]	785.2	0.177	18.73899	0.057	21.174	1.206918	2.810849	20.34292	0.025908
[66]	1289.6	0.177	19.08768	0.057	21.568	1.229376	2.863152	20.72146	0.016068
[66]	1591.2	0.177	19.43814	0.057	21.964	1.251948	2.915721	21.10191	0.013262

Table 4 presenting the comparative analysis of distinct passive type solar still on the basis of cost of a liter. This study found that the highest cost per liter (CPL) of distilled water production is 0.1217 $/L in traditional solar stills at Kafrelsheikh University, Egypt, and the lowest production cost of distilled water is 0.0132 $/L in CSS with Nano-particles of Al_2O_3 at El Oued, Algeria. Additionally, it is observed that the production price of distilled water is directly proportional to the total price of the still and indirectly proportional to the distilled water produced rate. Furthermore, the choice of material utilized during the construction of the solar still system, while considering overall cost reduction and increased longevity, will result in lower water costs.

Table 5. Economic analysis for active solar still.

Sr. No.	M (L/m2)	CRF	FAC	SSF	S	ASV	AMC	AC	CPL
[67]	312	0.17698	51.4139	0.057	58.1	3.3108	7.712085	55.815	0.1789
[68]	650	0.17698	122.921	0.057	138.906	7.9154	18.43812	133.44	0.2053
[69]	746.2	0.17698	72.9175	0.057	82.4	4.6955	10.93762	79.16	0.1061
[69]	1635.4	0.17698	92.0318	0.057	104	5.9264	13.80476	99.91	0.0611
[69]	3484	0.17698	189.373	0.057	214	12.195	28.40596	205.58	0.059
[70]	650	0.17698	72.9175	0.057	82.4	4.6955	10.93762	79.16	0.1218
[70]	1040	0.17698	134.508	0.057	152	8.6616	20.17619	146.02	0.1404
[70]	1560	0.17698	238.575	0.057	269.6	15.363	35.7862	259	0.166
[71]	5954	0.17698	182.294	0.057	206	11.739	27.34405	197.9	0.0332
[72]	1105	0.17698	142.863	0.057	161.442	9.1996	21.42951	155.09	0.1404
[73]	754	0.17698	16.0241	0.057	18.108	1.0319	2.403622	17.396	0.0231
[73]	1872	0.17698	25.6662	0.057	29.004	1.6528	3.849937	27.863	0.0149
[77]	774.8	0.17698	2059.62	0.057	2327.466	132.63	205.9623	2133	2.7529
[77]	1211.6	0.17698	1431.11	0.057	1617.22	92.156	143.1112	1482.1	1.2232
[77]	1253.2	0.17698	1396.2	0.057	1577.768	89.908	209.43	1515.7	1.2095
[78]	1568.8	0.17698	13.3481	0.057	15.084	0.8595	2.002222	14.491	0.0092
[82]	1092	0.17698	52.2103	0.057	59	3.3621	7.831549	56.68	0.0519
[83]	1029.6	0.17698	25.45083	0.057	28.758	1.639206	3.817625	27.62925	0.026835
[83]	2280.2	0.17698	44.06769	0.057	49.794	2.838258	6.610154	47.83959	0.02098
[83]	2119	0.17698	46.28904	0.057	52.304	2.981328	6.943356	50.25107	0.023715
[84]	858	0.17698	14.6025	0.057	16.5	0.9405	2.190375	15.85238	0.018476
[84]	1812.2	0.17698	29.913	0.057	33.8	1.9266	4.48695	32.47335	0.017919
[85]	366.6	0.17698	47.259	0.057	53.4	3.0438	7.08885	51.30405	0.139946
[85]	668.2	0.17698	53.1	0.057	60	3.42	7.965	57.645	0.086269
[85]	811.2	0.17698	75.225	0.057	85	4.845	11.28375	81.66375	0.10067
[86]	587.6	0.17698	13.275	0.057	15	0.855	1.99125	14.41125	0.024526
[86]	1019.2	0.17698	24.072	0.057	27.2	1.5504	3.6108	26.1324	0.02564

Table 5 shows comparative economic analysis of distinct active type solar stills. In the study, the highest cost for a litre of water was 2.75 $/l when using a solar still with a fountain reservoir plant, while the lowest cost per liter was 0.0092 $/l when using a hybrid solar system with photovoltaics, reflectors and air-cooling systems. Moreover, it is important to use different ways to reduce the cost of construction, to enhance the lifespan of the system and the productivity of the water, with a low-interest rate to lower the price of water production. In addition, solar stills comprising photovoltaic/thermal panels, solar collectors and condenser have a substantial impact on both distillation production and system construction prices.

6. Enviro-Economic Analysis of Different Passive and Active Solar Still

It is a way of providing economic incentives against the reduction amount of emission pollutants and also controlling the quantity of harmful pollutants in the environment. It promotes in developing renewable technologies for better future. It is analysed on the basis of enviro-economic parameter which included the price of CO_2 (Carbon Dioxide) emission and quantity of emitted carbon. From a coal plant, generation of 1 KWh of electricity emitted 980 g CO_2 as per B.K. Sovacool [90]. Therefore, Value of CO_2 mitigates/ annum for solar distillation still on the energy and exergy bases as follow:

$$\Phi_{CO_{2}\text{energy}} = \frac{\psi_{\text{energy}} \times E_{\text{out}}}{1000};\ \Phi_{CO_{2}\text{exergy}} = \frac{\psi_{\text{exergy}} \times G_{\text{ex}}}{1000} \qquad (1)$$

Where, Φ_{CO2} is CO_2 mitigated/ annum (tones CO_2/annum), Ψ_{CO2} is average CO_2 emitted from coal power generation plant (2.08 kg CO_2/kWh), E_{out} and G_{ex} is the annual energy and overall thermal exergy obtained from the solar distillation unit.

In international market, price range of CO_2 mitigated [91] is varies from 3 to 16 $/ton of CO_2. Thus, CO_2 average value taken for the calculation is $14.5/ton CO_2 [92]. So, the environmental cost Z_{CO2} ($/annum) on the bases of energy and exergy expressed as:

$$Z_{CO_{2}\text{energy}} = P_{CO_2} \times \Phi_{CO_{2}\text{energy}};\qquad Z_{CO_{2}\text{exergy}} = P_{CO_2} \times \Phi_{CO_{2}\text{exergy}} \qquad (2)$$

Where, P_{CO2} is carbon dioxide price/ton CO_2. The enviro-economic cost for different passive and active solar still have been shown in Table 6.

Table 6. Enviro-economic analysis of passive and active solar still.

Paper	Type of still	Embodied energy (kWh)	Environmental cost ($) energy and exergy		CO_2 mitigates energy (Tones)	Energy payback time
Passive solar still						
[49] V.K.Dwivedi (2010)	Double solar still with water depth 0.01 0.02 0.03	602.73 602.73 602.73	219.68 206.39 188.66	- - -	9.33 8.76 8.01	1.85
[59] Piyush Pal (2018)	Double slope with jute wick with black cotton wick	1009.99 1032.91	106.86 118.78	2.12 2.71	7.82 8.69	0.692 0.637
[56] T. Rajaseenivasan (2016)	CSS CSS with Square finned still CSS with Circular finned still	320.59 379.62 390.03	280.81 359.42 384.58	- - -	16.13 20.62 22.06	0.65 0.62 0.57
[60] K.S. Reddy (2018)	Tilted solar distillation with RO reject with sewage water	1397.13 1397.13	344.08 319.72	- -	23.73 22.05	1.70 1.82
[63] Mohamed S. Yousef (2019)	TRD TRD with pin fins TRD with steel fibers	235 318 250	179.5 208.9 226.6	- - -	12.38 14.4 15.63	- - -

[65] H.Sharon (2021)	novel hybrid solar still	1915.67	-	-	49.83	1.17
Active solar still						
[75] K.S. Reddy (2016)	AMEVSS with normal with evacuated mode	1228.5 1228.5	344.23 1186.24	- -	23.74 81.81	4.00 1.37
[76] K.S. Reddy (2017)	AMSSFS with Air cooled with Non-evacuated and evacuated AMSSFS with Wetted wick cooled with Non-evacuated and evacuated	6785.12 6698.02 6824.94 6737.84	682.95 1456.38 813.59 3229	- - - -	47.1 100.44 56.11 222.69	3.66 1.92 3.19 0.93
[79] Poonam Joshi (2018)	Active single slope solar still with cases (i) case (ii) case (iii)	14154 14154 7824	103 249 44	26.82 86.56 3.33	7.14 17.20 3.08	4 2 5
[80] D. B. Singh (2019)	double slope solar still (DSSS)	2824.34	5814.35	561.73	400.99	-
[81] Omar Bait (2019)	DSSS modified solar still	1152.605 1584.9 out	33.42556 45.96206	2.552197 4.41875	2.305211 3.169797	7.7 21
[83] Hamdy Hassan et. al. (2020)	CSS CSS + SD + PTC CSS + WM + PTC	603.8 875 930.6	231.42 501.35 464.67	26.37 85.67 76.72	15.96 34.57 32.05	0.756 0.506 0.58
[85] Shahin Shoeibi et. al. (2021)	DSSS with air cooled & water cooled	202.8 843.5	189.79 235.92	1.03 6.51	13.09 16.27	1.49 3.42

Table 6 provides the Embodied energy (kWh), CO_2 mitigated energy (Tones/year) and environmental benefits of various types of solar stills. On the basis of this table, the AMSSFS with wetted wick cooled with evacuated tube collector mitigated the most CO_2 by around 222.69 tons per year. While the DSSS attained the lowest mitigation of CO_2 per year, which was approximately 2.30 tons/year. The lifetime of solar still seems to have a significant impact on environmental cost (enviroeconomic parameters). From the results, the highest environmental cost ($) incurred by double slope solar still with N-identical evacuated tubular collectors during a lifetime of 50 years equalled 5814.35, while the lowest environmental cost ($) incurred by passive double slope solar stills during 30 years was 33.42. Additionally, the embodied energy of the solar still has been inversely impacted on CO_2 mitigates value during stills life time. According to the results, the N-type photovoltaic thermal flat plate collectors' single slope solar stills had the highest embodied energy value in comparison to the other solar stills.

7. Conclusion

The current work effort seeks to analyse the passive and active solar distillation unit on a techno-economic and enviro-economic analysis basis. These analyses play an important role in selecting the suitable solar still based on capital cost, construction material and CPL, environmental cost, and CO_2 mitigates. Based on finding in this work, the following conclusion is as follow:

- Active solar still has a higher system cost compared to passive solar due to the addition of thermal energy by different components and mechanisms.
- CSS with spherical balls of heat storage shows a minimum CPL of 0.0136 $/l due to the lower initial investment cost of 68.18 $.
- On the basis of energy, value of environmental cost of CSS with circular finned still is found to be highest (384.58 $) whereas passive double slope with jute wick solar still having the lowest (106.86 $) among analysed passive solar stills.
- Active solar still with PV modules, reflectors, and forced air cooling has the lowest CPL of 0.0092 $/l, but the active solar still using a fountain reservoir plant has the highest CPL of 2.7529 $/l.
- On the basis of energy, the highest environmental cost was found for AMSSFS air-cooled with evacuated mode (1456.38 $), while the lowest was found for active solar stills with N - Flat Plate Collectors (44 $).
- The study found that CPL increases by decreasing lifetimes and increasing interest rates, and vice versa.
- There are no studies and analyses of cleaning and conservation mechanisms for the particular solar stills as it lacks numerous performing hurdles and automatic maintenances options for whole life functions in the previous literature.
- Several studies have used nanofluids in solar stills in order to increase the temperature of basin water and the evaporation rate of distilled water. Nanofluids could serve as cooling fluids for glass, which would significantly impact distillate production as well as CO_2 mitigates.
- All previous studies considered nominal interest rate in the calculation of cost per liters (CPL). It is necessary to take into account compounded interest rate, effective interest rate, and inflation rate to make the CPL close to reality.

Nomenclature

n	Number of life years
i	Interest per year
x	Percentage of degradation rate
S	Salvage Value
E	Annual energy
G	Overall thermal exergy
Z	Environmental cost
CO_2	Carbon Dioxide
CSS	Conventional solar still
DSSS	Double slope solar still
PV/T	Photovoltaic thermal
ETC	Evacuated tube collector
FPC	Flat plate collector
CPCS	Compound parabolic concentrator collectors
CPL	Cost per liter
Nu	
CGTCC	Cotton Gauze Top Cover Cooling
TSS	Tubular solar still
TISS	Evacuated tubular collector Solar still
Subscript	
ex	Exergy
en	Energy

References:

[1] Y. Wada *et al.*, "Modeling global water use for the 21st century: the Water Futures and Solutions (WFaS) initiative and its approaches," *Geoscientific Model Development*, vol. 9, no. 1, pp. 175–222, Jan. 2016, doi: 10.5194/gmd-9-175-2016.

[2] Audrey Azoulay and Gilbert F. Houngbo, *The United Nations World Water Development Report 3*, vol. 9781849773. Paris: Routledge, 2012. doi: 10.4324/9781849773355.

[3] A. S. Richey *et al.*, "Quantifying renewable groundwater stress with <scp>GRACE</scp>," *Water Resources Research*, vol. 51, no. 7, pp. 5217–5238, Jul. 2015, doi: 10.1002/2015WR017349.

[4] WHO and UNICEF, "Progress on sanitation and drinking water: 2015 update and MDG assessment," 2015. Accessed: Jun. 18, 2021. [Online]. Available: https://www.unwater.org/publications/whounicef-joint-monitoring-program-water-supply-sanitation-jmp-2015-update/

[5] N. P. Cheremisinoff, "Handbook of water and wastewater treatment technonologies," in *Handbook of Water and Wastewater Treatment Technologies*, Elsevier, 2002, p. ix. doi: 10.1016/B978-075067498-0/50001-2.

[6] S. Bhojwani, K. Topolski, R. Mukherjee, D. Sengupta, and M. M. El-Halwagi, "Technology review and data analysis for cost assessment of water treatment systems," *Science of The Total Environment*, vol. 651, Feb. 2019, doi: 10.1016/j.scitotenv.2018.09.363.

[7] P. Glueckstern, "Cost estimates of large RO systems," *Desalination*, vol. 81, no. 1–3, Jul. 1991, doi: 10.1016/0011-9164(91)85044-U.

[8] F. H. ' Kiang, S. Arasu, W. W. L. Yong, and D. D. Ratnayaka, "Supply of desalinated water by the private sector Singapore's first public-privatepartnership initiative," in *IDA World Conference on Desalination and Water Reuse*, Sep. 2005, pp. 11–16.

[9] A. E. Kabeel, "Performance of solar still with a concave wick evaporation surface," *Energy*, vol. 34, no. 10, Oct. 2009, doi: 10.1016/j.energy.2009.06.050.

[10] T. Arunkumar *et al.*, "An experimental study on a hemispherical solar still," *Desalination*, vol. 286, pp. 342–348, Feb. 2012, doi: 10.1016/j.desal.2011.11.047.

[11] Y. Taamneh and M. M. Taamneh, "Performance of pyramid-shaped solar still: Experimental study," *Desalination*, vol. 291, Apr. 2012, doi: 10.1016/j.desal.2012.01.026.

[12] S. Ravishankara, P. K. Nagarajan, D. Vijayakumar, and M. K. Jawahar, “Phase Change Material on Augmentation of Fresh Water Production Using Pyramid Solar Still,” *International Journal of Renewable Energy Development*, vol. 2, no. 3, Oct. 2013, doi: 10.14710/ijred.2.3.115-120.

[13] P. K. Nagarajan *et al.*, “Performance evaluation of triangular pyramid solar still for enhancing productivity of fresh water,” *Research Journal of Pharmaceutical, Biological and Chemical Sciences*, vol. 5, no. 2, pp. 764–771, 2014.

[14] N. K. Dhiman, “Transient analysis of a spherical solar still,” *Desalination*, vol. 69, no. 1, Jan. 1988, doi: 10.1016/0011-9164(88)80005-5.

[15] B. I. Ismail, “Design and performance of a transportable hemispherical solar still,” *Renewable Energy*, vol. 34, no. 1, Jan. 2009, doi: 10.1016/j.renene.2008.03.013.

[16] A. Ahsan and T. Fukuhara, “Condensation mass transfer in unsaturated humid air inside tubular solar still,” *Annual Journal Hydraulic Engineering, JSCE*, vol. 28, pp. 31–42, 2010.

[17] Z. M. Omara, A. E. Kabeel, and M. M. Younes, “Enhancing the stepped solar still performance using internal reflectors,” *Desalination*, vol. 314, Apr. 2013, doi: 10.1016/j.desal.2013.01.007.

[18] G. N. Tiwari, S. K. Singh, and V. P. Bhatnagar, “Analytical thermal modelling of multi-basin solar still,” *Energy Conversion and Management*, vol. 34, no. 12, Dec. 1993, doi: 10.1016/0196-8904(93)90122-Q.

[19] G. M. Cappelletti, “An experiment with a plastic solar still,” *Desalination*, vol. 142, no. 3, Mar. 2002, doi: 10.1016/S0011-9164(02)00203-5.

[20] M. A. Hamdan, A. M. Musa, and B. A. Jubran, “Performance of solar still under Jordanian climate,” *Energy Conversion and Management*, vol. 40, no. 5, Mar. 1999, doi: 10.1016/S0196-8904(98)00134-4.

[21] M. S. Sodha, A. Kumar, U. Singh, and G. N. Tiwari, “Further studies on double solar still,” *International Journal of Energy Research*, vol. 5, no. 4, 1981, doi: 10.1002/er.4440050405.

[22] A. E. Kabeel, “Water production from air using multi-shelves solar glass pyramid system,” *Renewable Energy*, vol. 32, no. 1, Jan. 2007, doi: 10.1016/j.renene.2006.01.015.

[23] N. Rahbar and J. A. Esfahani, “Experimental study of a novel portable solar still by utilizing the heatpipe and thermoelectric module,” *Desalination*, vol. 284, Jan. 2012, doi: 10.1016/j.desal.2011.08.036.

[24] G. N. Tiwari, Madhuri, and H. P. Garg, “Effect of water flow over the glass cover of a single basin solar still with an intermittent flow of waste hot water in the basin,” *Energy Conversion and Management*, vol. 25, no. 3, Jan. 1985, doi: 10.1016/0196-8904(85)90049-4.

[25] A. A. El-Sebaii, “Thermal performance of a triple-basin solar still,” *Desalination*, vol. 174, no. 1, Apr. 2005, doi: 10.1016/j.desal.2004.08.038.

[26] S. A. El-Agouz, Y. A. F. El-Samadony, and A. E. Kabeel, “Performance evaluation of a continuous flow inclined solar still desalination system,” *Energy Conversion and Management*, vol. 101, Sep. 2015, doi: 10.1016/j.enconman.2015.05.069.

[27] A. A. Badran, I. A. Al-Hallaq, I. A. Eyal Salman, and M. Z. Odat, “A solar still augmented with a flat-plate collector,” *Desalination*, vol. 172, no. 3, Feb. 2005, doi: 10.1016/j.desal.2004.06.203.

[28] S. N. Rai and G. N. Tiwari, “Single basin solar still coupled with flat plate collector,” *Energy Conversion and Management*, vol. 23, no. 3, Jan. 1983, doi: 10.1016/0196-8904(83)90057-2.

[29] S. N. Rai, D. K. Dutt, and G. N. Tiwari, “Some experimental studies of a single basin solar still,” *Energy Conversion and Management*, vol. 30, no. 2, Jan. 1990, doi: 10.1016/0196-8904(90)90026-U.

[30] K. Voropoulos, E. Mathioulakis, and V. Belessiotis, “Experimental investigation of a solar still coupled with solar collectors,” *Desalination*, vol. 138, no. 1–3, Sep. 2001, doi: 10.1016/S0011-9164(01)00251-X.

[31] Y. P. Yadav and A. S. Prasad, “Performance analysis of a high temperature solar distillation system,” *Energy Conversion and Management*, vol. 36, no. 5, May 1995, doi: 10.1016/0196-8904(95)98901-X.

[32] H. Kargar Sharif Abad, M. Ghiasi, S. Jahangiri Mamouri, and M. B. Shafii, “A novel integrated solar desalination system with a pulsating heat pipe,” *Desalination*, vol. 311, Feb. 2013, doi: 10.1016/j.desal.2012.10.029.

[33] S. K. Singh, V. P. Bhatnagar, and G. N. Tiwari, “Design parameters for concentrator assisted solar distillation system,” *Energy Conversion and Management*, vol. 37, no. 2, Feb. 1996, doi: 10.1016/0196-8904(95)00166-B.

[34] Z. S. Abdel-Rehim and A. Lasheen, “Experimental and theoretical study of a solar desalination system located in Cairo, Egypt,” *Desalination*, vol. 217, no. 1–3, Nov. 2007, doi: 10.1016/j.desal.2007.01.012.

[35] B. Chaouchi, A. Zrelli, and S. Gabsi, “Desalination of brackish water by means of a parabolic solar concentrator,” *Desalination*, vol. 217, no. 1–3, Nov. 2007, doi: 10.1016/j.desal.2007.02.009.

[36] G. N. Tiwari and A. Kumar, “Nocturnal water production by tubular solar stills using waste heat to preheat brine,” *Desalination*, vol. 69, no. 3, Jan. 1988, doi: 10.1016/0011-9164(88)80032-8.

[37] G. N. Tiwari and S. Sinha, “Parametric studies of active regenerative solar still,” *Energy Conversion and Management*, vol. 34, no. 3, Mar. 1993, doi: 10.1016/0196-8904(93)90136-X.

[38] S. Kumar and A. Tiwari, “An experimental study of hybrid photovoltaic thermal (PV/T)- active solar still,” *International Journal of Energy Research*, vol. 32, no. 9, Jul. 2008, doi: 10.1002/er.1388.

[39] S. Kumar and G. N. Tiwari, “Estimation of internal heat transfer coefficients of a hybrid (PV/T) active solar still,” *Solar Energy*, vol. 83, no. 9, Sep. 2009, doi: 10.1016/j.solener.2009.06.002.

[40] S. Kumar and G. N. Tiwari, “Life cycle cost analysis of single slope hybrid (PV/T) active solar still,” *Applied Energy*, vol. 86, no. 10, Oct. 2009, doi: 10.1016/j.apenergy.2009.03.005.

[41] G. C. Pandey, “Effect of dried and forced air bubbling on the partial pressure of water vapour and the performance of solar still,” *Solar Energy*, vol. 33, no. 1, 1984, doi: 10.1016/0038-092X(84)90111-7.

[42] V. Velmurugan and K. Srithar, “Solar stills integrated with a mini solar pond — analytical simulation and experimental validation,” *Desalination*, vol. 216, no. 1–3, Oct. 2007, doi: 10.1016/j.desal.2006.12.012.

[43] G. N. Tiwari and S. Suneja, “Performance evaluation of an inverted absorber solar still,” *Energy Conversion and Management*, vol. 39, no. 3–4, Feb. 1998, doi: 10.1016/S0196-8904(96)00227-0.

[44] S. Kumar and K. T. Kurmaji, “Carbon credit earned by some designs of solar stills,” *Desalination and Water Treatment*, vol. 51, no. 22–24, Jun. 2013, doi: 10.1080/19443994.2013.770269.

[45] A. E. Kabeel, K. Harby, M. Abdelgaied, and A. Eisa, “A comprehensive review of tubular solar still designs, performance, and economic analysis,” *Journal of Cleaner Production*, vol. 246, p. 119030, 2020, doi: https://doi.org/10.1016/j.jclepro.2019.119030.

[46] A. W. Jeevadason, S. Padmini, C. Bharatiraja, and A. E. Kabeel, “A review on diverse combinations and Energy-Exergy-Economics (3E) of hybrid solar still desalination,” *Desalination*, vol. 527, p. 115587, 2022, doi: https://doi.org/10.1016/j.desal.2022.115587.

[47] O. Bait and M. Si–Ameur, “Enhanced heat and mass transfer in solar stills using nanofluids: A review,” *Solar Energy*, vol. 170, pp. 694–722, 2018, doi: https://doi.org/10.1016/j.solener.2018.06.020.

[48] O. Bait, “Direct and indirect solar–powered desalination processes loaded with nanoparticles: A review,” *Sustainable Energy Technologies and Assessments*, vol. 37, p. 100597, 2020, doi: https://doi.org/10.1016/j.seta.2019.100597.

[49] V. K. Dwivedi and G. N. Tiwari, “Thermal modeling and carbon credit earned of a double slope passive solar still,” *Desalination and Water Treatment*, vol. 13, no. 1–3, Jan. 2010, doi: 10.5004/dwt.2010.856.

[50] Z. M. Omara, M. H. Hamed, and A. E. Kabeel, “Performance of finned and corrugated absorbers solar stills under Egyptian conditions,” *Desalination*, vol. 277, no. 1–3, pp. 281–287, Aug. 2011, doi: 10.1016/j.desal.2011.04.042.

[51] T. Arunkumar *et al.*, “An experimental study on a hemispherical solar still,” *Desalination*, vol. 286, pp. 342–348, Feb. 2012, doi: 10.1016/j.desal.2011.11.047.

[52] T. Rajaseenivasan and K. Kalidasa Murugavel, “Theoretical and experimental investigation on double basin double slope solar still,” *Desalination*, vol. 319, Jun. 2013, doi: 10.1016/j.desal.2013.03.029.

[53] P. U. Suneesh, R. Jayaprakash, T. Arunkumar, and D. Denkenberger, “Effect of air flow on ‘V’ type solar still with cotton gauze cooling,” *Desalination*, vol. 337, pp. 1–5, Mar. 2014, doi: 10.1016/j.desal.2013.12.035.

[54] Z. M. Omara, A. E. Kabeel, A. S. Abdullah, and F. A. Essa, “Experimental investigation of corrugated absorber solar still with wick and reflectors,” *Desalination*, vol. 381, pp. 111–116, Mar. 2016, doi: 10.1016/j.desal.2015.12.001.

[55] D. G. Harris Samuel, P. K. Nagarajan, R. Sathyamurthy, S. A. El-Agouz, and E. Kannan, “Improving the yield of fresh water in conventional solar still using low cost energy storage material,” *Energy Conversion and Management*, vol. 112, Mar. 2016, doi: 10.1016/j.enconman.2015.12.074.

[56] T. Rajaseenivasan and K. Srithar, “Performance investigation on solar still with circular and square fins in basin with CO 2 mitigation and economic analysis,” *Desalination*, vol. 380, pp. 66–74, Feb. 2016, doi: 10.1016/j.desal.2015.11.025.

[57] P. Pal, P. Yadav, R. Dev, and D. Singh, “Performance analysis of modified basin type double slope multi–wick solar still,” *Desalination*, vol. 422, Nov. 2017, doi: 10.1016/j.desal.2017.08.009.

[58] S. M. Elshamy and E. M. S. El-Said, “Comparative study based on thermal, exergetic and economic analyses of a tubular solar still with semi-circular corrugated absorber,” *Journal of Cleaner Production*, vol. 195, Sep. 2018, doi: 10.1016/j.jclepro.2018.05.243.

[59] P. Pal, R. Dev, D. Singh, and A. Ahsan, “Energy matrices, exergoeconomic and enviroeconomic analysis of modified multi–wick basin type double slope solar still,” *Desalination*, vol. 447, pp. 55–73, Dec. 2018, doi: 10.1016/j.desal.2018.09.006.

[60] K. S. Reddy, H. Sharon, D. Krithika, and L. Philip, “Performance, water quality and enviro-economic investigations on solar distillation treatment of reverse osmosis reject and sewage water,” *Solar Energy*, vol. 173, Oct. 2018, doi: 10.1016/j.solener.2018.07.033.

[61] K. v. Modi and J. G. Modi, “Performance of single-slope double-basin solar stills with small pile of wick materials,” *Applied Thermal Engineering*, vol. 149, Feb. 2019, doi: 10.1016/j.applthermaleng.2018.12.071.

[62] W.-L. Cheng, Y.-K. Huo, and Y.-L. Nian, “Performance of solar still using shape-stabilized PCM: Experimental and theoretical investigation,” *Desalination*, vol. 455, Apr. 2019, doi: 10.1016/j.desal.2019.01.007.

[63] M. S. Yousef, H. Hassan, and H. Sekiguchi, “Energy, exergy, economic and enviroeconomic (4E) analyses of solar distillation system using different absorbing materials,” *Applied Thermal Engineering*, vol. 150, Mar. 2019, doi: 10.1016/j.applthermaleng.2019.01.005.

[64] P. Dumka, A. Jain, and D. R. Mishra, “Energy, exergy, and economic analysis of single slope conventional solar still augmented with an ultrasonic fogger and a cotton cloth,” *Journal of Energy Storage*, vol. 30, p. 101541, 2020, doi: https://doi.org/10.1016/j.est.2020.101541.

[65] H. Sharon, “Energy, exergy, environmental benefits and economic aspects of novel hybrid solar still for sustainable water distillation,” *Process Safety and*

Environmental Protection, vol. 150, pp. 1–21, 2021, doi: https://doi.org/10.1016/j.psep.2021.04.003.

[66] B. Benoudina, M. E. H. Attia, Z. Driss, A. Afzal, A. M. Manokar, and R. Sathyamurthy, “Enhancing the solar still output using micro/nano-particles of aluminum oxide at different concentrations: An experimental study, energy, exergy and economic analysis,” *Sustainable Materials and Technologies*, vol. 29, p. e00291, 2021, doi: https://doi.org/10.1016/j.susmat.2021.e00291.

[67] J. A. Esfahani, N. Rahbar, and M. Lavvaf, “Utilization of thermoelectric cooling in a portable active solar still — An experimental study on winter days,” *Desalination*, vol. 269, no. 1–3, Mar. 2011, doi: 10.1016/j.desal.2010.10.062.

[68] R. Dev and G. N. Tiwari, “Annual performance of evacuated tubular collector integrated solar still,” *Desalination and Water Treatment*, vol. 41, no. 1–3, Mar. 2012, doi: 10.1080/19443994.2012.664715.

[69] Z. M. Omara, M. A. Eltawil, and E. A. ElNashar, “A new hybrid desalination system using wicks/solar still and evacuated solar water heater,” *Desalination*, vol. 325, Sep. 2013, doi: 10.1016/j.desal.2013.06.024.

[70] M. A. Eltawil and Z. M. Omara, “Enhancing the solar still performance using solar photovoltaic, flat plate collector and hot air,” *Desalination*, vol. 349, Sep. 2014, doi: 10.1016/j.desal.2014.06.021.

[71] M. R. Karimi Estahbanati, M. Feilizadeh, K. Jafarpur, M. Feilizadeh, and M. R. Rahimpour, “Experimental investigation of a multi-effect active solar still: The effect of the number of stages,” *Applied Energy*, vol. 137, Jan. 2015, doi: 10.1016/j.apenergy.2014.09.082.

[72] D. B. Singh, J. K. Yadav, V. K. Dwivedi, S. Kumar, G. N. Tiwari, and I. M. Al-Helal, “Experimental studies of active solar still integrated with two hybrid PVT collectors,” *Solar Energy*, vol. 130, Jun. 2016, doi: 10.1016/j.solener.2016.02.024.

[73] B. Praveen kumar, D. Prince Winston, P. Pounraj, A. Muthu Manokar, R. Sathyamurthy, and A. E. Kabeel, “Experimental investigation on hybrid PV/T active solar still with effective heating and cover cooling method,” *Desalination*, vol. 435, Jun. 2018, doi: 10.1016/j.desal.2017.11.007.

[74] O. Bait and M. Si–Ameur, “Numerical investigation of a multi-stage solar still under Batna climatic conditions: Effect of radiation term on mass and heat energy balances,” *Energy*, vol. 98, pp. 308–323, 2016, doi: https://doi.org/10.1016/j.energy.2016.01.017.

[75] K. S. Reddy and H. Sharon, “Active multi-effect vertical solar still: Mathematical modeling, performance investigation and enviro-economic analyses,” *Desalination*, vol. 395, Oct. 2016, doi: 10.1016/j.desal.2016.05.027.

[76] K. S. Reddy and H. Sharon, “Energy-environment-economic investigations on evacuated active multiple stage series flow solar distillation unit for potable water production,” *Energy Conversion and Management*, vol. 151, Nov. 2017, doi: 10.1016/j.enconman.2017.08.064.

[77] A. Kr. Tiwari and A. Somwanshi, “Techno-economic analysis of mini solar distillation plants integrated with reservoir of garden fountain for hot and dry climate of Jodhpur (India),” *Solar Energy*, vol. 160, Jan. 2018, doi: 10.1016/j.solener.2017.11.078.

[78] A. E. Kabeel and M. Abdelgaied, “Performance enhancement of a photovoltaic panel with reflectors and cooling coupled to a solar still with air injection,” *Journal of Cleaner Production*, vol. 224, Jul. 2019, doi: 10.1016/j.jclepro.2019.03.199.

[79] P. Joshi and G. N. Tiwari, “Energy matrices, exergo-economic and enviro-economic analysis of an active single slope solar still integrated with a heat exchanger: A comparative study,” *Desalination*, vol. 443, pp. 85–98, Oct. 2018, doi: 10.1016/j.desal.2018.05.012.

[80] D. B. Singh, “Exergo-economic, enviro-economic and productivity analyses of N identical evacuated tubular collectors integrated double slope solar still,” *Applied Thermal Engineering*, vol. 148, Feb. 2019, doi: 10.1016/j.applthermaleng.2018.10.127.

[81] O. Bait, “Exergy, environ–economic and economic analyses of a tubular solar water heater assisted solar still,” *Journal of Cleaner Production*, vol. 212, Mar. 2019, doi: 10.1016/j.jclepro.2018.12.015.

[82] E. M. S. El-Said, S. M. Elshamy, and A. E. Kabeel, “Performance enhancement of a tubular solar still by utilizing wire mesh packing under harmonic motion,” *Desalination*, vol. 474, Jan. 2020, doi: 10.1016/j.desal.2019.114165.

[83] H. Hassan, M. S. Yousef, M. Fathy, and M. S. Ahmed, “Assessment of parabolic trough solar collector assisted solar still at various saline water mediums via energy, exergy, exergoeconomic, and enviroeconomic approaches,” *Renewable Energy*, vol. 155, pp. 604–616, 2020, doi: https://doi.org/10.1016/j.renene.2020.03.126.

[84] R. Fallahzadeh, L. Aref, N. Gholamiarjenaki, Z. Nonejad, and M. Saghi, “Experimental investigation of the effect of using water and ethanol as working fluid on the performance of pyramid-shaped solar still integrated with heat pipe solar collector,” *Solar Energy*, vol. 207, pp. 10–21, 2020, doi: https://doi.org/10.1016/j.solener.2020.06.032.

[85] S. Shoeibi, N. Rahbar, A. A. Esfahlani, and H. Kargarsharifabad, “Energy matrices, exergoeconomic and enviroeconomic analysis of air-cooled and water-cooled solar still: Experimental investigation and numerical simulation,” *Renewable Energy*, vol. 171, pp. 227–244, 2021, doi: https://doi.org/10.1016/j.renene.2021.02.081.

[86] D. Mevada, H. Panchal, and K. K. Sadasivuni, “Investigation on evacuated tubes coupled solar still with condenser and fins: Experimental, exergo-economic and exergo-environment analysis,” *Case Studies in Thermal Engineering*, vol. 27, p. 101217, 2021, doi: https://doi.org/10.1016/j.csite.2021.101217.

[87] Govind and G. N. Tiwari, “Economic analysis of some solar energy systems,” *Energy Conversion and Management*, vol. 24, no. 2, Jan. 1984, doi: 10.1016/0196-8904(84)90024-4.

[88] A. E. Kabeel, A. M. Hamed, and S. A. El-Agouz, “Cost analysis of different solar still configurations,” *Energy*,

vol. 35, no. 7, Jul. 2010, doi: 10.1016/j.energy.2010.03.021.

[89] M. Sanserwal, A. Kumar Singh, and P. Singh, “Impact of materials and economic analysis of single slope single basin passive solar still: A review,” *Materials Today: Proceedings*, vol. 21, 2020, doi: 10.1016/j.matpr.2019.11.289.

[90] B. K. Sovacool, “Valuing the greenhouse gas emissions from nuclear power: A critical survey,” *Energy Policy*, vol. 36, no. 8, Aug. 2008, doi: 10.1016/j.enpol.2008.04.017.

[91] M. G. J. den Elzen *et al.*, “The Copenhagen Accord: abatement costs and carbon prices resulting from the submissions,” *Environmental Science & Policy*, vol. 14, no. 1, Jan. 2011, doi: 10.1016/j.envsci.2010.10.010.

[92] E. Deniz and S. Çınar, “Energy, exergy, economic and environmental (4E) analysis of a solar desalination system with humidification-dehumidification,” *Energy Conversion and Management*, vol. 126, Oct. 2016, doi: 10.1016/j.enconman.2016.07.064